

239500-5-F

Final Report

MICROWAVE PROPERTY STUDIES OF ARCTIC SEA ICE

Robert Onstott

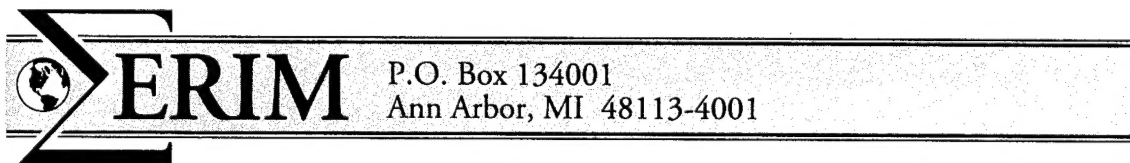
Environmental Research Institute of Michigan
P.O. Box 134001
Ann Arbor, MI 48113-4001

March 1996

Office of Naval Research
Ocean Engineering Division Code 1121 RS
800 N. Quincy Street
Arlington, VA 22217-5000

Attention: Mr. Charles A. Luther

19960424 012



DTIC QUALITY INSPECTED 1

DISTRIBUTION STATEMENT A

Approved for public release;
Distribution Unlimited

REPORT DOCUMENTATION PAGE

Form Approved
OMB No. 0704-0188

Public reporting burden for the collection of information is estimated to average 1 hour per response, including the time for reviewing instructions, searching existing data sources, gathering and maintaining the data needed, and completing and reviewing the collection of information. Send comments regarding this burden estimate or any other aspect of this collection of information, including suggestions for reducing this burden, to Washington Headquarters Services, Directorate for Information Operations and Reports, 1215 Jefferson Davis Highway, Suite 1204, Arlington, VA 22202-4302, and to the Office of Management and Budget, Paperwork Reduction Project (0704-0188), Washington, DC 20503.

1. AGENCY USE ONLY (Leave Blank)	2. REPORT DATE	3. REPORT TYPE AND DATES COVERED	
	March 1996	Final Report	
4. TITLE AND SUBTITLE		5. FUNDING NUMBERS	
MICROWAVE PROPERTY STUDIES OF ARCTIC SEA ICE		N00014-91-C-0127	
6. AUTHOR(S)		7. PERFORMING ORGANIZATION NAME(S) AND ADDRESS(ES)	
Robert Onstott		Environmental Research Institute of Michigan P.O. Box 134001 Ann Arbor, MI 48113-4001	
8. PERFORMING ORGANIZATION REPORT NUMBER		9. SPONSORING/MONITORING AGENCY NAME(S) AND ADDRESS(ES)	
239500-5-F		Office of Naval Research Ocean Engineering Division Code 1121 RS 800 N. Quincy Street Arlington, VA 22217-5000	
10. SPONSORING/MONITORING AGENCY REPORT NUMBER			
11. SUPPLEMENTARY NOTES			
12a. DISTRIBUTION/AVAILABILITY STATEMENT		12b. DISTRIBUTION CODE	
		Unlimited	
13. ABSTRACT (Maximum 200 words)			
<p>The Center for Earth Sciences of the Environmental Research Institute of Michigan (ERIM) continued the fundamental study of the active microwave behavior of Arctic sea ice. Efforts focused on two major activities -- the characterization of microwave properties of sea ice and related modeling activities. The microwave signature study also included the comparison of active and passive microwave data, relating the physical properties of sea ice through laboratory and field studies to SAR signatures, and the study of the capability of polarimetric SAR to improve geophysical property retrievals. We have also made a major contribution to the Office of Naval Research (ONR) and National Aeronautics and Space Administration (NASA) Sea Ice American Geophysical Union Microwave Remote Sensing of Sea Ice Monograph 68.</p>			
14. SUBJECT TERMS			15. NUMBER OF PAGES
CRRELEX, CEAREX,			132
16. PRICE CODE			
17. SECURITY CLASSIFICATION OF REPORT	18. SECURITY CLASSIFICATION OF THIS PAGE	19. SECURITY CLASSIFICATION OF ABSTRACT	20. LIMITATION OF ABSTRACT
Unclassified	Unclassified	Unclassified	Unlimited

CONTENTS

MICROWAVE RESPONSE OF ARCTIC SEA ICE	1
SUMMARY OF THE REPORTING OF RESULTS	8
APPENDIX	11

MICROWAVE RESPONSE OF ARCTIC SEA ICE

The Center for Earth Sciences of the Environmental Research Institute of Michigan (ERIM) continued the fundamental study of the active microwave behavior of Arctic sea ice. Efforts focussed on two major activities -- the characterization of microwave properties of sea ice and related modeling activities. The microwave signature study also included the comparison of active and passive microwave data, relating the physical properties of sea ice through laboratory and field studies to SAR signatures, and the study of the capability of polarimetric SAR to improve geophysical property retrievals. We have also made a major contribution to the Office of Naval Research (ONR) and National Aeronautics and Space Administration (NASA) Sea Ice American Geophysical Union Microwave Remote Sensing of Sea Ice Monograph 68.

Overall Program Goal

The overall objective of this research program is to advance the understanding of the electromagnetic behavior of sea ice and snow and to develop the imaging mechanisms, based upon measurement and theory, from which satellite algorithms for SAR will allow extraction of geophysical information, such as ice type and concentration.

Analysis and Incorporation of Data Acquired Through CRRELEX and CEAREX

Polarimetric data acquired during CRRELEX and the Coordinated Eastern Arctic Experiment (CEAREX) were examined and reported. There are two important results derived from this analysis. The first is the determination of the utility of a polarimetric SAR to improve the accuracy of geophysical properties generated for the Arctic. This is important, in that the Earth Observation System (EOS) SAR team needs to be able to credibly show the utility of polarimetric SAR to justify this capability on the proposed EOS SAR sensor suite. This discussion is a primary focus of the chapter on polarimetry included in the Sea Ice Monograph. The second perspective is that polarimetric measurements provide a complete characterization of the scattered field, therefore these results are impacting our thinking about sea ice scattering by supplying potentially new information and insight, while confirming our original understanding.

The physical properties of sea ice have been related to signatures empirically and through electromagnetic modeling. Data acquired during the CEAREX Cruise have been used in support of this study. In addition, detailed measurements were made of microwave properties of SAR data obtained at 1.25, 5.25, and 9.38 GHz in mapping modes where very large regions (i.e., 200 km x 300 km) are observed using satellite type parameter sets (i.e., ERS-1, J-ERS-1, and RADARSAT). This CEAREX SAR data set is proving to be invaluable due to its excellent coincidence with ground truth of physical ice properties and the unique opportunity to address the relationship of SAR signatures and ice thickness.

Contributions were made to the Sea Ice Monograph and are presented in the chapters on the active microwave / *in situ* observations, thin ice formations, polarimetry and laboratory studies. Citations are included in the reference summary and copies of these chapters are provided in the appendix.

Development of Radar Look-up Tables for Use With Satellite SAR Data

Efforts were completed on the development and refinement of the radar look-up table (RLT) composed of radar scattering cross sections for use with satellite-based geophysical data product applications. Concentration was largely directed to 5.25 GHz, 23 degrees incidence angle and VV antenna transmit-receive polarization due to the launch of ERS-1 which operates with these radar parameter combinations. Efforts were also directed to insure that the RLT is complete and includes other impending radar parameter combinations such as J-ERS-1 (L/HH/23°), EOS (C/POL/20°-50°), and SIR-C (L-C-X/POL/20°-50°). A second aspect of this effort was directed to the future participation in the validation of the ice type products that will be produced by the Alaska SAR Facility Geophysical Processing System Ice Type Discrimination Algorithm. It is important to study the utilization of the RLT in determining ice type, determining what refinements maybe needed, examining the influence of region on accuracy and to determine if there is a need to develop a RLT with regional adaptability, and optimize the manner in which the RLT may be adapted for use in temporal and seasonal studies of ice sheet processes and properties.

Evolution of the Microwave Signature of First-Year Ice

Work continued in the description of the evolution of the microwave signature of first-year ice beginning with the freezing of open water. Improvements have been made by incorporating results obtained from CRRELEX and CEAREX, as well as the other investigations for the case when conditions are winter-like. This work includes a description of the changes in the physical properties of the ice sheet, the snow and frost flower layer, dielectric properties, and surface-roughness statistics. In addition, polarimetric measurements made throughout the evolution process provide for a more complete electromagnetic description of the backscattered field for a wide range of frequencies and angles. Further, the understanding of the backscatter response of new and young sea ice has been improved by the integration of a theoretical dielectric property and scattering models, and the study of the empirical and theoretical responses over a wide frequency range (1 to 35 GHz). Figure 1 is a cartoon which illustrates the change in the scattering coefficient as ice thickness increases from 0 cm to 20 cm based on results obtained in the laboratory. Note that cases where the ice is snow covered or bare, and when an ice sheet has rafted has now been incorporated. There are many facets of this function which are of interest. We have observations which show that the liquid ocean takes on a variety of cross section levels due to wind and fetch conditions. Note that conditions observed in a field of sea ice are different than those observed for the open ocean. New ice is also found to produce a signature which is greater, the same, or below that of the liquid ocean depending on environmental conditions. In the calm conditions often encountered during lead formation, the new ice signature may show an enhancement. As the dielectric constant of the ice sheet reduces (a function of ice thickening), the backscatter intensity will reduce to a point where the lowest backscatter intensity for any ice condition is reached (new ice which is smooth and cold). Frost flowers will form as the ice continues to thicken and may continue to form a dense development if the ice sheet is allowed to grow undisturbed.

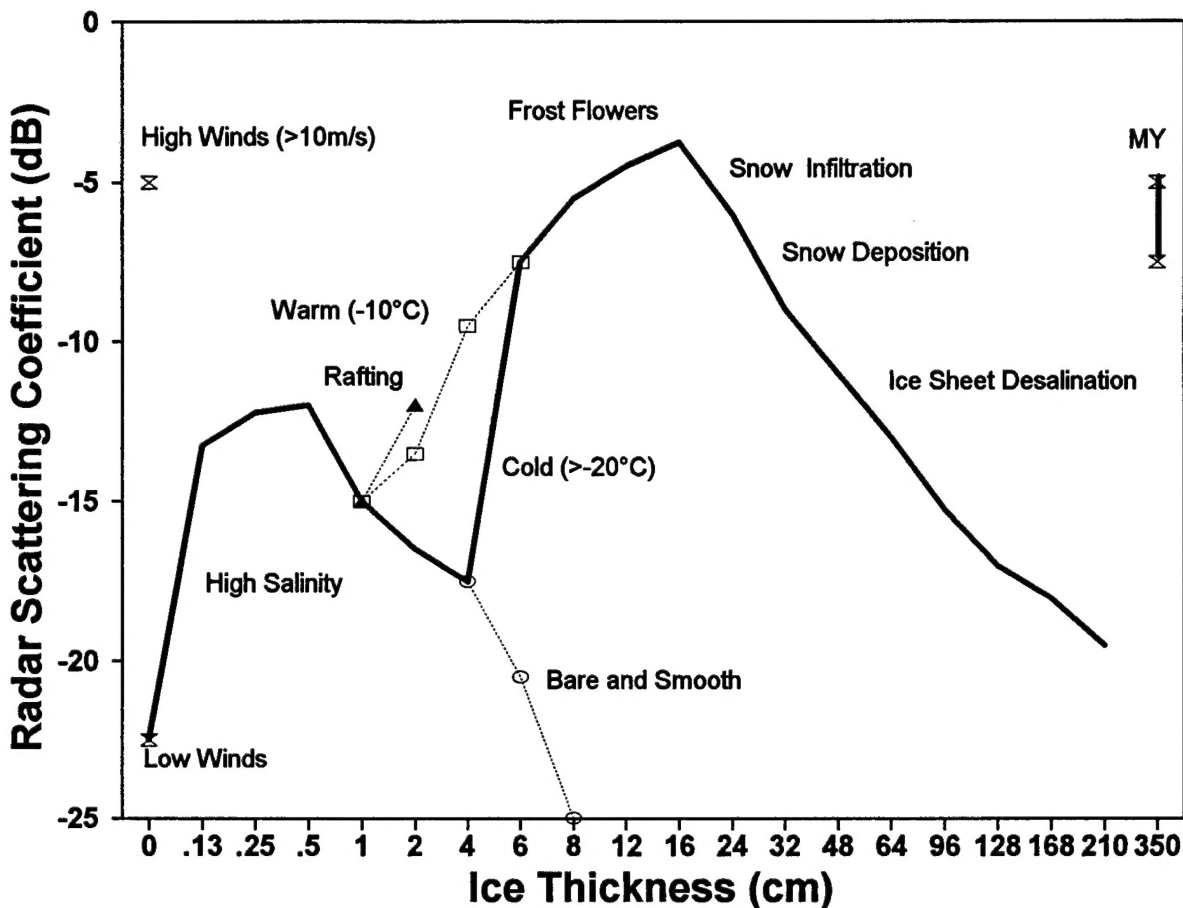


Figure 1. This figure has been assembled to illustrate the change in the scattering coefficient as ice thickness increases from 0 to 350 cm. There are many facets to this function that are of interest. The liquid ocean backscatter cross-section levels are dependent on wind and fetch. New ice produce a signature which is greater, the same, or below that of the liquid ocean depending on environmental conditions. If conditions are calm, the new ice signature may show an enhancement. As the dielectric constant of the ice sheet reduces (a function of ice thickening), the backscatter intensity will reduce to a point where the lowest backscatter intensity for any ice condition is reached (new ice which is smooth and cold). Frost flowers will form as the ice continues to thicken and may continue to form a dense development if the ice sheet is allowed to grow undisturbed. The signature which results is the greatest possible for undisturbed FY ice. It almost attains a level associated with multiyear ice. The infiltration of snow, wind or time result in the disruption of the frost flower structure. In time, the snow and frost flower layer undergo a continual metamorphosis and results in a steady reduction in the backscatter intensity for the ice sheet. Ice sheets grown under cold or warm conditions take two different signature paths if they remain bare and smooth. Rafting dramatically and modifies the signature.

The greatest backscatter intensity for undisturbed first-year ice, almost that of multiyear, may be obtained when the above is true. However, with the infiltration of snow and increasing ice thickness, the structure of the frost flowers will become disrupted. The snow and frost flower layer will undergo a continual metamorphosism which results in a steady reduction in the backscatter intensity for the ice sheet until thicknesses above about 200 cm are reached.

Summary of Accomplishments

- Measurements made during CEAREX'88 have been studied and the impact of fall freeze up on the microwave properties of thin, first year and multiyear ice are described. The thin ice signature was found to be impacted due to the growing conditions associated with mild temperatures. Once air temperatures became cold other ice forms attained winter-like signatures.
- The importance of the upper most properties of a multiyear ice sheet have been studied further. Measurements have been compiled to describe the typical range of properties (density, salinity, gas bubble size, and number of layers). Backscatter responses have been studied to understand sensitivities to property variations.
- The surface roughness statistics for sea ice during summer and winter has been compiled. Statistics for the evolution of open water to grey ice are also now known. In addition, the dielectric properties for this period have been derived from reflectivity measurements for frequencies from 5 to 17 GHz. These results are important because they are based on *in-situ* measurements and provide an accurate description of the change in the electrical properties during this critical period.
- The characterization of the impact of frost flowers on young sea ice both from a physical and electromagnetic perspective is improving. This is being accomplished by the study of previously measured data and newly acquired data (LEADEX). A better understanding of

the change in dielectric properties, the scale of the dielectric roughness attributed to frost flowers, the relationship between frost flower development and ice thickness, and the microwave behavior is becoming better understood.

- The response of the polarization ratio ($\sigma^{\circ}_{vv}/\sigma^{\circ}_{hh}$) versus thickness has been examined.
- The description of the evolution of the microwave signature of first-year ice beginning with the freezing of open water has been improved with the contributions of observations made during CRRELEX and CEAREX, as well as the other investigations for the case when conditions are winter-like. This work includes a description of the changes in the physical properties of the ice sheet, the snow and frost flower layer, dielectric properties, and surface-roughness statistics. In addition, polarimetric measurements have been made throughout the evolution process providing a complete electromagnetic description of the backscattered field for a wide range of frequencies and angles. Further, the understanding of the backscatter response of new and young sea ice has been improved by the integration of a theoretical dielectric property and scattering models, and the study of the empirical and theoretical responses over a wide frequency range (1 to 35 GHz).

Table 1.
RADAR LOOK UP TABLES DEVELOPED FOR ASF-GPS & ERS-1

WINTER TO EARLY SPRING

Ice Type	Thickness - cm -	σ^* - dB -	Standard Deviation - dB -	Slope - dB/* -
MY	> 220	-8.6	2.2	-0.08
TFY	70 TO 220	-11.5	2.1	-0.77
ThFY	20 TO 70	-13.3	1.2	-0.17
OW	0	< -19.7	4.0	-0.04

LATE SPRING

Ice Type	Thickness - cm -	σ^* - dB -	Standard Deviation - dB -	Slope - dB/* -
MY	> 220	-10.7	2.1	-0.27
TFY	70 TO 220	-13.2	1.1	-0.22
OW	0	< -19.7	4.0	-0.04

EARLY SUMMER

Ice Type	Thickness - cm -	σ^* - dB -	Standard Deviation - dB -	Slope - dB/* -
MY SY TFY MFY	> 70	-16.3	1.1	-0.33
ThFY	20 TO 70	-13.1	1.4	-0.16
OW	0	< -19.7	4.0	-0.04

MIDSUMMER

Ice Type	Thickness - cm -	σ^* - dB -	Standard Deviation - dB -	Slope - dB/* -
MY & TFY	> 120	-16.3	1.1	-0.33
MFY	70 TO 120	-14.7	1.5	-0.27
ThFY	30 TO 70	-13.1	1.4	-0.16
OW	0	< -19.7	4.0	-0.04

LATE SUMMER

Ice Type	Thickness - cm -	σ^* - dB -	Standard Deviation - dB -	Slope - dB/* -
MY & TFY	> 120	-16.8	1.8	-0.60
ThFY	30 TO 70	-18.4	2.2	-0.45
OW	0	< -19.7	4.0	-0.04

FALL

Ice Type	Thickness - cm -	σ^* - dB -	Standard Deviation - dB -	Slope - dB/* -
MY	> 150	-10.5	1.7	-0.04
FY	120	-12.5	1.9	-0.21
ThFY & OW	0 TO 30	< -19.7	2.0 to 4.0	-0.04 to -0.63

SUMMARY OF THE REPORTING OF RESULTS

AGU Microwave Remote Sensing of Sea Ice Monograph 68

Drinkwater, M.R., H. Israelson, R. Kwok, R. Onstott, and D. Winnebrenner, "Polarimetry of Sea Ice," Microwave Remote Sensing of Sea Ice, Chapter 5, (ed. by F. Carsey), American Geophysical Union, Washington, D.C., 1993.

Fetterer, F., M.R. Drinkwater, S. Laxon, L. Ulander, and R. Onstott, "Altimeter Backscatter and Processes," Microwave Remote Sensing of Sea Ice, Chapter 7, (ed. by Frank Carsey), American Geophysical Union, Washington, D.C., 1993.

Grenfell, T.C., D.J. Cavalieri, J.C. Comiso, M.R. Drinkwater, R.G. Onstott, I. Rubinstein, K. Steffen, and D.P. Winebrenner, "Considerations for Microwave Remote Sensing of Thin Sea Ice," Microwave Remote Sensing of Sea Ice, AGU Books, Chapter 14, (ed. by Frank Carsey), American Geophysical Union, Washington, D.C., 1993.

Onstott, R.G., "SAR and Scatterometer Signatures of Sea Ice," Chapter 5, Microwave Remote Sensing of Sea Ice (ed. by Frank Carsey), American Geophysical Union, Washington, D.C., 1993.

Swift, T.C., K. St. Germain, K.C. Jezek, S. P. Gogineni, A.J. Gow, D.K. Perovich, T.C. Grenfell, R.G. Onstott, "Laboratory Investigations of the Electromagnetic Properties of Artificial Sea Ice," Microwave Remote Sensing of Sea Ice, AGU Books, Chapter 9, (ed. by Frank Carsey), American Geophysical Union, Washington, D.C., 1993.

Winebrenner, D.P., J Bredow, A.K. Fung, M.R. Drinkwater, N. Drinkwater, An.J. Gow, D.K. Perovich, T.C. Grenfell, H.C. Han, J.A. Kong, J.K. Lee, S. Mudaliar, R.G. Onstott, L. Tsang, and R.D. West, "Microwave Sea Ice Signature Modeling," Microwave Remote Sensing of Sea Ice, Chapter 8, (ed. by Frank Carsey), American Geophysical Union, Washington, D.C., 1993.

Journal Papers

Kwok, R., E. Rignot, B. Holt, R. Onstott, "An Overview of the Geophysical Sea Ice Products Generated at the Alaska SAR Facility," **J. of Geophysical Res.**, 97, C2, 2391-2402, February 1991.

Tucker, W.B., T.C. Grenfell, R.G. Onstott, D.K. Perovich, A.J. Gow, R.A. Shuchman, and L.L. Sutherland, "Microwave and Physical Properties of Sea Ice in the Winter Marginal Ice Zone," **J. Geophysical Research**, vol. 96, no. C3, pp. 4573-4587, 15 March 1991.

Conferences

Jentz, R., C.C. Wackerman, R.A. Shuchman, R.G. Onstott, P. Gloersen, D. Cavalieri, J. Comiso, J. Hollinger, R. Ramseier, R. Rubinstein, NASA, Navy, and AES/York Sea Ice Concentration Comparison of SSM/I Algorithms With SAR Derived Values, **Proc. of IGARSS'91 Symposium**, Espoo, Finland, June 1991

Onstott, R.G., R.A. Shuchman, C.W. Wackerman, Polarimetric Radar Measurements of Arctic Sea Ice During the Coordinated Eastern Arctic Experiment, **Proc. of IGARSS'91 Symposium**, Espoo, Finland, June 1991.

Onstott, R.G. and R.A. Shuchman, An Intercomparison of SAR and Scatterometer Data Collected During CEAREX, **Proc. of IGARSS'91 Symposium**, Espoo, Finland, June 1991.

Onstott, R.G., Active Microwave Observations of Arctic Sea Ice During The Fall Freeze-up, **Proc. of IGARSS'91 Symposium**, Espoo, Finland, June 1991.

Onstott, R.G. and T. Grenfell, Active and Passive Microwave Observations of Arctic Sea Ice During The Fall Freeze-up, **Proc. of IGARSS'91 Symposium**, Espoo, Finland, June 1991.

Onstott, R.G. and R.A. Shuchman, "Arctic Sea Ice Microwave Signature and Geophysical Processes Study," **Proceeding of the First ERS-1 Symposium**, pp. 329-332, Cannes, France, 4-6 November 1992.

Onstott, R.G., "Active Microwave Response of Arctic Sea Ice - A Review Of The Ability To Retrieve Geophysical Information," **Proc. of IGARSS'92 Symposium**, Clear Lake, Texas, May 1992.

Onstott, R.G., "Investigation of the Retrieval of Snow Properties on Arctic Sea Ice Using Active Microwave Radar," **Proc. of IGARSS'92 Symposium**, Clear Lake, Texas, May 1992.

Onstott, R.G., "Polarimetric Radar Measurements of Arctic Sea Ice During the Eastern Arctic Experiment," **Proc. of IGARSS'92 Symposium**, Clear Lake, Texas, May 1992.

Onstott, R.G., "Examination of the Physical, Electrical, and Microwave Evolution Of Water Into Young Sea Ice," **Proc. of IGARSS'92 Symposium**, Clear Lake, Texas, May 1992.

Shuchman, R.A., R.G. Onstott, C.C. Wackerman, C. Russel, L. Sutherland, O. Johannessen, J. Johannessen, S. Sandven, and P. Gloersen, Multi-frequency SAR, SSM/I and AVHRR Derived Geophysical Information of the Marginal Ice Zone, **Proc. of IGARSS'91 Symposium**, Espoo, Finland, June 1991.

Shuchman, R.A. and R.G. Onstott, "ERS-1 SAR Snow and Sea Ice Signatures During LEADEX," ERIM Technical Report 231500-12-T, Environmental Research Institute of Michigan, Ann Arbor, Michigan, August 1992.

Tanis, F. and R.G. Onstott, "Characterization of Intrinsic Optical Properties for Sea Ice and Snow," **Proc. of IGARSS'92 Symposium**, Clear Lake, Texas, May 1992.

APPENDIX

Compilation of AGU Monograph Chapters, Journal Papers, and Conference Papers

EXAMINATION OF THE PHYSICAL, ELECTRICAL, AND MICROWAVE EVOLUTION OF SEA WATER INTO YOUNG ICE

Robert G. Onstott

Environmental Research Institute of Michigan
P.O. Box 134001
Ann Arbor, MI. 48113-4001
(313) 994-1200

ABSTRACT

Knowledge of the interrelationships between ice thickness, its temperature profile, the distribution of salinity, the dielectric property profile, and roughness of the air-ice interface is important to the understanding of the backscatter response of new and young sea ice. Backscatter, physical property, and electrical property measurements made in the laboratory during the first 120 hours of growth aid in describing the evolution of first year ice, in this case open water to grey ice (14.5 cm thick). Results discussed herein describe the evolution response for the case when the ambient air temperature is about -15°C.

INTRODUCTION

Active microwave observations of artificially grown saline ice are presented. Ice which simulates arctic first-year sea ice was grown in a large outdoor tank during an active and passive microwave and ice characterization experiment at a facility located by the U.S. Army Cold Regions Research and Engineering Laboratory, New Hampshire. Radar backscatter measurements were made at 5.2, 9.6, 13.6, and 16.6 GHz. Antenna polarizations include vertical, horizontal, and cross. Angles of incidence range from vertical to 50 degrees. During this investigation the structure and salinity profiles of the ice sheet, the thickness and surface temperature, surface roughness and dielectric properties were examined.

ICE SHEET CHARACTERISTICS

Important electrical characteristics which are sensed with active and passive microwave sensors are attributable to brine inclusions located as between the long vertical ice crystal plates. The size, volume, and concentration of brine in these inclusions is very sensitive to many factors, but mainly the temperature at its locations. The volume of brine in the ice sheet directly impacts its permittivity and influences its ability to scatter and transmit energy. Ice sheet salinities range from 8 ppt when very new, to 2 ppt after 36 days (for an ice thickness of about 33 cm). The ice sheet, grown of undisturbed sea water, which had a salinity of 22 ppt, gave the visual impression of being spatially homogenous. The ice surface was very smooth by appearance and was measured to have an air-ice interface with a roughness of about 0.05 cm rms and a correlation length of 1-to-2 cm.

DISCUSSION

Radar reflectivity and backscatter are found to be frequency sensitive during the first 30 hours of ice growth. During this rapid growth period, frequency sensitivity is attributable largely to the interplay between the dielectric profile of an ice sheet, which is thin, and the radar wavelength. The concept of a bulk dielectric constant aids in the interpretation of the measured results. During this period, the roughness of the ice surface is essentially constant, thereby contributing little to the frequency-time response.

However, after the first 30 hour period the bulk dielectric constant is no longer as frequency sensitive, but backscatter is most modulated by changes associated with the ice-air or ice-snow interface.

A time-series response showing the evolution of open water to grey ice (14.5 cm thick) is provided in Figure 1 for illustration and discussion. This response, obtained at 5.25 GHz, is shown at incidence angles of 0° and 40°, and VV- and HH-polarizations. These observations were made at night so any solar influence is negated. Physical property observations are summarized in Figure 2. Two responses from open water are included; (a) at the beginning of the growth cycle with small ripples present, and (b) a ripples case at the end of the growth cycle.

At the highest microwave frequencies (9-17 GHz) the transition from electrical properties associated with sea water to those more similar to pure ice is dramatic, requiring less than 2 hours, and is achieved prior to an ice thickness of 3 mm (see Figure 3). At a lower microwave frequency (i.e. 5.25 GHz) this transition is much slower, taking 20 hours, by which time the ice thickness became 5 cm. Processes progress further with the final result being a transition from an ice sheet with a high dielectric constant to one with a low dielectric constant. With $T_{air} = -15^{\circ}C$ this occurs within 1 day of the initiation of ice formation and is attained at an ice thickness of 7 cm.

It is found that very new ice undergoes a rapid transition during which the initial ice skim begins with a dielectric constant of sea water and then transitions to a dielectric within a factor twice that of pure ice (3.14). This is illustrated in Figures 4 and 5 which show the predicted and measured response of the magnitude of the bulk dielectric constant. Visual observations suggest that this transition is associated with a change in the structure of the new ice layer, one with stellar crystals interwoven on the surface to one with a thin bubble-and-brine free surface layer. It is observed that new ice grown under calm conditions has a very smooth, ice-air interface. The surface which is very smooth once the ice skim forms becomes extremely smooth, and then roughens due to the deposition of single snow crystals. The influence of increased air temperature (-5°C) and solar heating on a thin ice sheet is shown to produce an enhanced backscatter at all angles. Additional brine liquid is known to be produced with the elevation of ice temperature. There is about a 7.5 dB reduction in the reflectivity (at 5.0 GHz and VV) between ice at 0-to-1 cm and ice of 4-to-7 cm. The magnitude of this reduction is largely determined by the change in the magnitude of the dielectric constant.

The relationship between frequency (5 to 17 GHz) and penetration depth for new ice is important; the average dielectric properties of an ice sheet are defined by this depth. It is understood that longer wavelengths penetrate further into young ice than shorter wavelengths. The importance of this is supported by the results illustrated in Figure 4.

Observations at 9.6 to 16.6 GHz show that very new sea ice attains a dielectric constant much smaller (about 4x) than that of open water at $T = 0^{\circ}$ almost immediately upon the initiation of the ice growth process. These observations argue that brine is gradually being expelled to the surface as the freezing process progresses, that there is a peak in the accumulation (in this study

at 1 cm), and that a large percentage change in the dielectric constant occurs. This occurs prior to the transition into pure-ice-like state. A frequency dependency is seen associated when the lowest dielectric constant is attained.

SUMMARY

Results obtained from the study of the transition of open water into young sea ice has provided insight into the importance of upper ice sheet temperatures, the accompanying dielectric constant response, and the collection of brine and free-water at the air-ice interface on the backscatter response.

ACKNOWLEDGEMENTS

This work is supported by the Office of Naval Research (ONR) Contract N00014-86-C-0469 and the National Aeronautics and Space Administration Grant #2543. The Technical Monitors were Mr. Charles Luther and Dr. Robert H. Thomas.

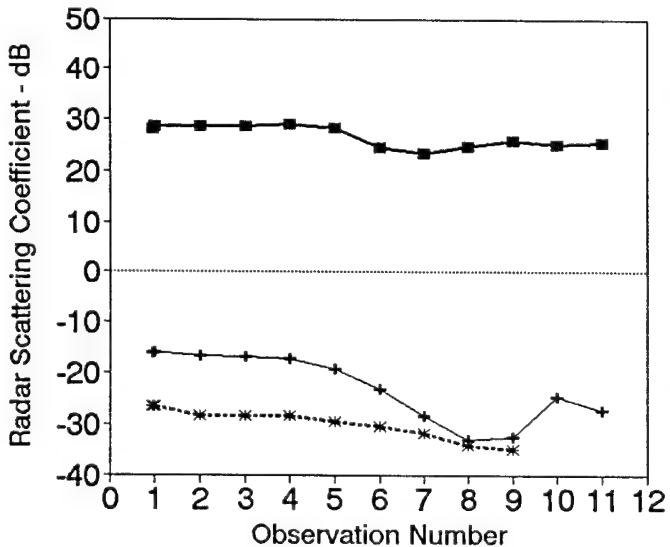


Figure 1. Time Series Response of the Backscatter Response at 5.25 GHz During the Evolution of Open Water to New Ice at Nadir and 40° (VV & HH).

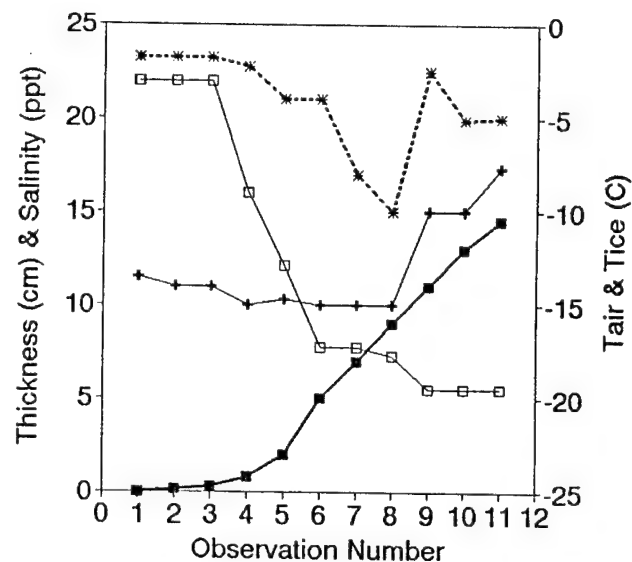


Figure 2. Ice Thickness, Air Temperature, Ice Temperature and Bulk Salinity During the Evolution of Open Water to New Ice.

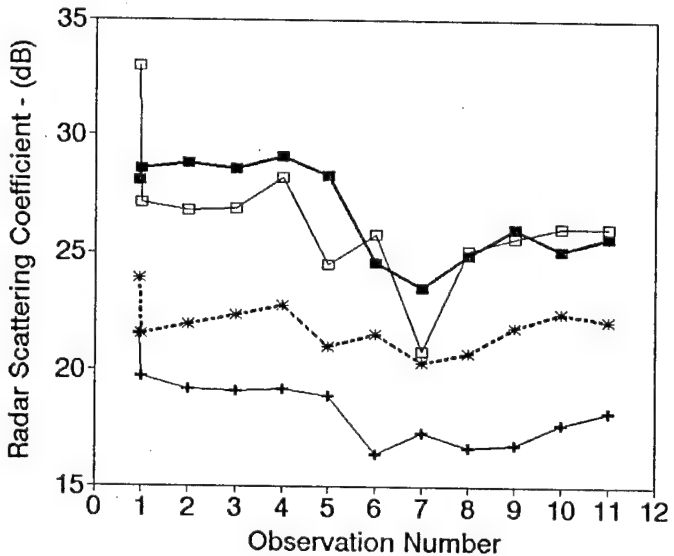


Figure 3. Time Series Response of the Backscatter at Vertical During the Evolution of Open Water to New Ice Shown as a Function from 5.25 GHz to 16.6 GHz.

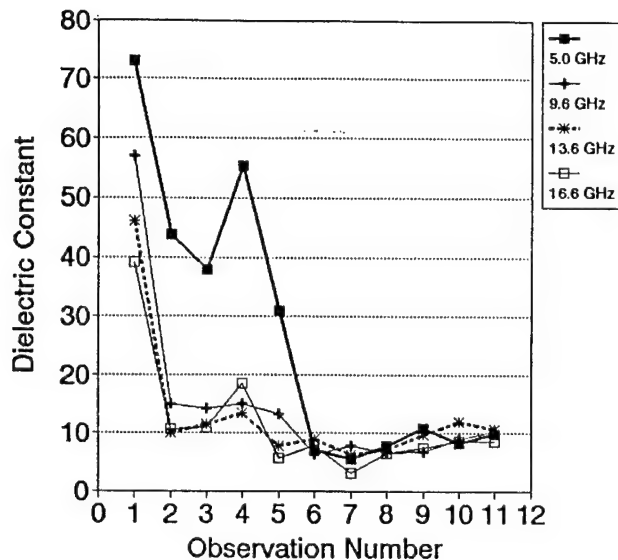


Figure 4. The Magnitude of the Complex Dielectric Constant (ϵ_r^*) as Derived from the Reflectivity Measurements.

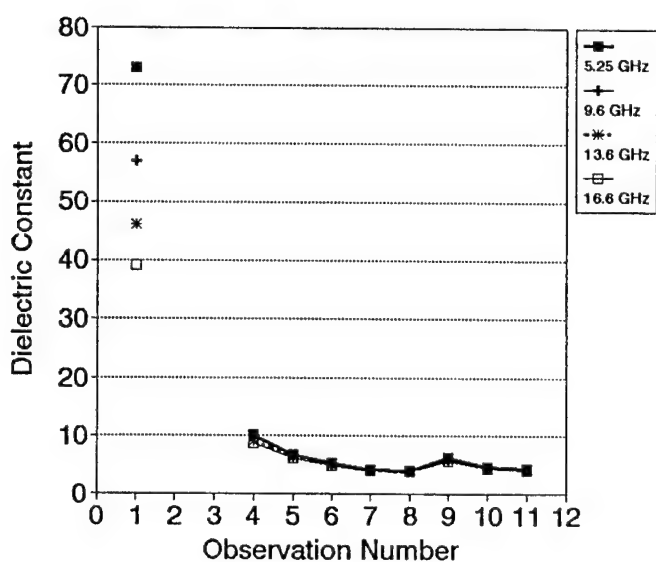


Figure 5. Predicted Magnitudes of the Complex Dielectric Constant (ϵ_r^*).

ACTIVE MICROWAVE OBSERVATIONS OF ARCTIC SEA ICE DURING THE FALL FREEZE-UP

Robert G. Onstott
Center for Earth Sciences
Advanced Concepts Division
Environmental Research Institute of Michigan
P.O. Box 8618 Ann Arbor, MI 48107 USA

ABSTRACT

Near-surface millimeter and microwave measurements were made during September-October, the fall freeze-up period, in regions located to the North and East of Svalbard. Microwave signatures and physical properties were acquired at a large number of stations and included floes composed of multiyear, first-year, young, and nilas sea ice. Systematic variation in the thickness and density of the ice located in the uppermost portion of multiyear ice sheets was observed. In this paper, the measured and predicted backscatter response was examined at 10 GHz. The impact of fall freeze up on microwave signatures is also presented.

Key Words: Sea ice, microwave, radar, and fall.

INTRODUCTION

The characterization of the microwave properties of sea ice was conducted during the September-October 1989 segment of the Coordinated Eastern Arctic Experiment (CEAREX) in regions located to the North and East of Svalbard. During this investigation the ice-strengthened ship R/V *Polarborn* was allowed to freeze within the ice pack next to a vast multiyear ice floe composed of ice of dissimilar origins. In-situ observations of microwave signatures and physical properties were obtained at a large number of stations during this 8-week period when mean air temperatures were in continual decline. Ice forms in the immediate vicinity of the drift station included multiyear-hummock (numerous sites), multiyear-meltponds (numerous sites), very old multiyear ice, typical multiyear ice, second year ice, first year, and a refrozen lead. Variations in the thickness, density, bubble size and roughness associated with the ice located in the uppermost portion of multiyear ice sheets were detected and documented. Selected examples are provided here to illustrate the impact of these combinations of parameters on their microwave signatures. In addition, the impact of fall freeze up on the microwave signatures of four major sea ice types is presented.

The backscattering data described here were collected utilizing a surface-based tower which was positioned at each of the various sites to obtain angular response data. The tower was also transported using a snowmobile to

interconnect these sites so that the inter and intra floe spatial variation in microwave signatures could be addressed further. It is also believed that the physical properties which were sampled discretely may also be extended by their association with their microwave signatures. Polarization diversified data were acquired at 9.38, 18, 35, and 94 GHz over the incidence angle range from 0° to 70°. In this paper, only data at 10 GHz is presented. Sensor specifications are summarized in Table 1.

One of the initiatives of this study is to obtain a better understanding of the mean and variation in the physical properties of sea ice forms and to accompany these observations with their microwave signatures over a wide range of frequencies, polarizations, and angles. Scene variability is important in the context of both geophysical information and physical property retrieval. The data collected are also critical in the validation and development of theoretical sea ice models. For brevity, the discussion presented here is limited to the variation in the properties of the upper-most portion of multiyear ice. In addition, only one of a possible of three major multiyear ice floes will be considered, and only five of a possible ten sites within this floe will be presented.

IMPACT OF FALL FREEZE UP

The impact of fall freeze up has been examined for the time period of about 1 to 15 October when air temperatures ranged from -15°C to -20°C. General results for the four major ice types (multiyear, first year, young, and nilas) are summarized in Table 2. For the cases of multiyear ice, first year ice, and new ice, their signatures are very similar to those obtained during winter conditions. A key factor is that enough cooling has occurred that the cold waves have propagated far enough into the ice sheet so that the above is true. The ice form that is impacted during fall is that of young sea ice. Its physical properties and signature is influenced by slow growing conditions, i.e. the air temperatures are still moderate when compared with winter conditions. The ice in a refrozen lead next to the drift ship did not congeal quickly or thoroughly. The top few centimeters were composed of brine enriched snow (salinity = 26 ppt) and slush. When the sheet became thick enough (35 cm) the upper portion of the lead froze more completely

and a signature enhancement was noted. A discussion of the anatomy of a freezing lead is provided in Gow et al [1].

PHYSICAL AND MICROWAVE PROPERTIES

Five multiyear ice sites have been selected as representative. Four of these sites are from hummocks and one is from a fresh water meltpool. Their physical properties are summarized in Table 3. Important observations will be summarized here. The low density ice (LDI) in the upper portion of the ice sheet is one of the two sources which produce an enhanced backscatter. A pressure ridge which is a topographical feature represents the second. To highlight the importance of the LDI layer, the backscatter response of a hummock and a fresh water meltpool which were separated by fifty meters and were resident on the same multiyear ice floe is provided in Figure 1. The critical difference between these two scenes is the number of discrete scatterers (i.e. gas bubbles) in the top 15 cms of the ice. In addition, the number of scatterers for a given bubble size is related to density. The hummock has a density of 651 kgm^{-3} , while the meltpool has a density of 914 kgm^{-3} , that of pure ice. The lower the density of the LDI layer, the greater is the number of discrete scatterers for the given bubble size. In the incidence angle region from 30° to 60° , the difference ($> 15 \text{ dB}$) between these two multiyear ice responses is striking and the mechanism well-defined.

The interface between snow and LDI may be smooth, moderately rough, or very rough. Rms heights ranged from 0.14 to 1.01 cm. Correlation lengths were very similar with a range from 2.0 to 4.6 cm. It is typically necessary to characterize the LDI layer as a layer of ice with a very low density which is then proceeded by a transitional layer, often composed of large globs, which has a density which falls between that of the upper most LDI layer and that of pure ice. The bulk of the remaining ice sheet also has a density similar to that of pure ice. A cartoon is presented in Figure 2 to illustrate the three ice layers and the range of the critical physical properties for the sites under discussion.

The angular responses of the backscatter response of the four multiyear hummock sites are shown in Figure 3 for like (VV and HH) and cross polarization (VH and HV). The width of the mean angular response interval is about 5 dB for like-polarization, cross-polarization is about one dB wider. A preliminary examination of the ability to predict the ranking between these four sites has been made. Basic "rules of thumb" have been generated for the range of physical property parameters measured during the characterization of these sites and using a radiative transfer model with a rough surface and Rayleigh scatterers [2,3]. The results of a parametric study are summarized here:

- 1) Increasing the bubble diameter from 2 to 3 to 4 mm increases the like-pol return by 5 and 3 dB and the cross-pol return by 8 and 5.5 dB, respectively. Hence, the depolarization ratio decreases from 10 to 7 to 4.5 dB.
- 2) Increasing the rms roughness from 0.125 to .5 causes a reduction in σ^0 of 2 to 3 dB ($\Theta_{inc} = 0^\circ$ to 55°), with the decrease increasing with incidence angle. Increasing the roughness to 1.0 cm causes an additional decrease of 3 to 6 dB.

3) Increasing the density from 500 to 600 to 700 kgm^{-3} causes a reduction in σ^0_{like} of 1 and 1.5 dB, respectively. σ^0_{cross} showed a 2 and 3 dB reduction.

4) If the thickness of the LDI layer is changed from 5 to 10 to 20 cm, then σ^0_{like} increases by 2.5 dB and then 3 dB. σ^0_{cross} increased by 5 dB in each case.

5) Varying the correlation length from 2 to 5 cm produced little effect.

The parameters which appear outstanding for each site are now discussed. The slight salinity in the case of Site DS-4 appears important because the LDI layer was well developed, but the overall return was slightly weaker than two other cases. Site DS-7 may be considered to be typical. Site DS-9 is interesting because it represents the weakest like-pol response in this set. Rms roughness was found to be greater for this site. As was noted in the parametric study an increase in roughness will cause a reduction in the like-pol response with little subsequent reduction in the cross-pol response, except at the largest angles. The cross-pol response for this site falls in the middle of the response range for these sites. Site DS-13 is of particular interest in that it fits in the upper portion of both the like and cross polarization response ranges. Its LDI layer is a bit unique in that the upper most portion is relatively thin, but of very low density (513 kgm^{-3}), and is followed by a very high density layer (929 kgm^{-3}) which contains some extremely large globs (diameters of 1 cm). Large bubbles contribute to large cross-sections and to minimizing depolarization ratios.

SUMMARY

Fall freeze up in mid-October was found to have its greatest impact on the microwave signature of young sea ice. This was attributed to warm temperatures and slow growing conditions when compared to those of winter. Ice signatures for multiyear, first year, and nilas were found to be winter-like. The physical properties of the upper 10 to 20 cm of multiyear ice are shown to control the microwave process. A discussion of property and signature variability was based on measurements obtained from five representative sites.

ACKNOWLEDGEMENTS

This work is supported by the Office of Naval Research (ONR) contract N00014-86-C-0469. The Technical Monitors were Mr. Charles Luther and Dr. Thomas Curtin.

REFERENCES

- [1] A.T. Gow, D.A. Meese, D.K. Perovich, and W.B. Tucker, "The Anatomy of a Freezing Lead," *JGR*, vol. 95, no. C10, Oct. 15, 1990, pp. 18,221-18,232.
- [2] A.K. Fung, and H.J. Eom, "Application of a Combined Rough Surface Volume Scattering Theory to Sea Ice and Snow," *IEEE Trans.*, vol. GE-20,no. 4, October 1982, pp. 528-536.

[3] Y.S. Kim, R.K. Moore, and R.G. Onstott, "Theoretical and Experimental Study of Radar Backscatter from Sea Ice," Univ. of Kansas, Lawrence, Kansas, RSL Tech. Report 331-37, January 1984.

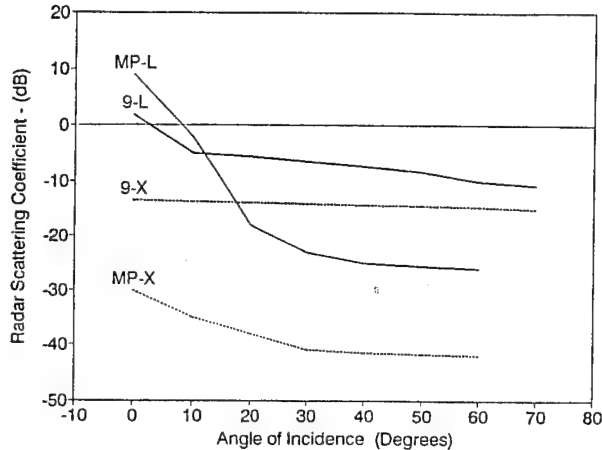


Figure 1. The angular response for the radar scattering coefficient of a multiyear ice hummock and meltpool are shown at 10 GHz. The responses at VV and HH polarizations were nearly identical, as was the case for VH and HV polarizations.

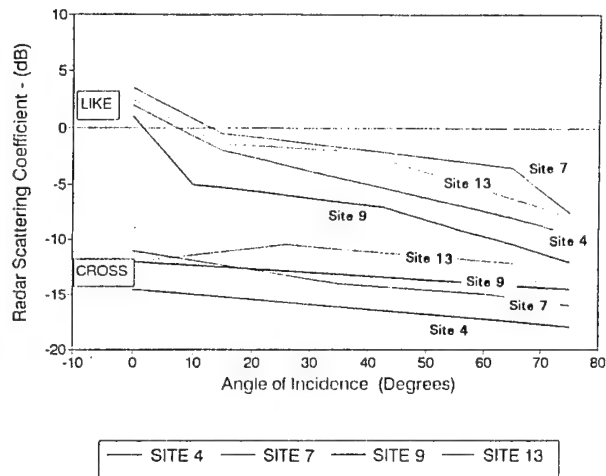


Figure 3. The angular response of the scattering coefficients for four multiyear ice hummocks at 10 GHz and like- and cross- polarizations. The responses at VV and HH polarizations were nearly identical, as were the VH and HV responses.

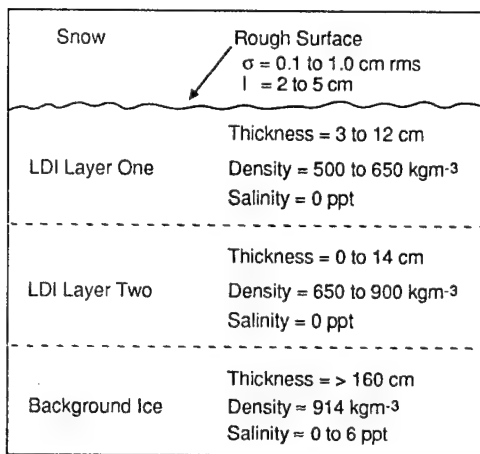


Figure 2. This is a cross-section view of the upper portion of the ice sheet.

Table 1.

CEAREX Surface-Based Radar System Specifications

Type	FM-CW
Frequency (GHz)	10
FM Sweep (Mhz)	1000
Antenna Beamwidth (°)	9
Polarizations ¹	V H X
Height (m)	3
Footprint ² (m)	0.7
N Frequency ³	3.5
N Spatial ⁴	4.7
N Total ⁵	16
σ Precision ⁶ (Db)	±1.9

¹V=VV, H=HH, X=VH or HV

²Footprint at 40°

³Number of Independent Samples via Excess Bandwidth

⁴Independent Samples per Spatial Footprint

⁵Total Number of Independent Samples per Footprint

⁶Precision Based Upon Translating One Footprint Only (90% confidence)

Table 2.

**Preliminary Results for Sea Ice
During Fall Freeze-Up**

Ice Type	Preliminary Results	Comments
Multiyear	Quickly attains winter signature.	1) Only need to cool top 10 cm. 2) $T_{air} = -10^{\circ}\text{C}$ adequate, probably. 3) Ice sheet (bulk) was still near zero in Nov.
First Year	Quickly attains winter signature.	1) Frost flower development slow compared to winter. 2) Transition of bulk dielectric constant (80 to 20 to 4) for top of ice sheet delayed.
Young	Big Impact! Signature evolution impacted by slow growing conditions. Signature not winter-like.	1) Ice does not congeal quickly or thoroughly 2) Top few cms composed of brine enriched snow and slush. 3) Congealed ice sheet produces signature enhancement.
Nilas	Quickly attains winter signature.	1) Only needs to cool top few cms. 2) $T_{air} = -10^{\circ}\text{C}$ adequate, probably.

Table 3.

Upper Ice Sheet Characterizations

Parameter	DS - 4	DS - 7	DS - 9	DS - 13	DS - MP
σ cm rms	$0.23 \pm .05$	$0.14 \pm .02$	$0.77 \pm .12$	$1.01 \pm .31$	$.08 \pm .03$
t cm	$3.5 \pm .3$	2.0 ± 1.3	4.6 ± 1.2	3.2 ± 1.2	2.8 ± 1.9
LDI-1	Thickness - cm -	$12.4 \pm .3$	$5.0 \pm .6$	4.9 ± 1.0	3.0 ± 1.3
	Salinity - ppt -	0.1	0.0	0.0	0.0
	Density - kgm^{-3}	651	457	513	914
	Bubble Dia. - mm	3.3	2.5	2.3	3.3
	Void Dia. - mm	1	8	7	5
LDI - 2	Thickness - cm -	-	$3.5 \pm .4$	$4.9 \pm .4$	$13.6 \pm .4$
	Salinity - ppt -	-	0	0	0
	Density - kgm^{-3}	--	728	728	929
	Bubble Dia. - mm	--	4	4.3	1
	Void Dia. - mm	--	2	0	0

LDI = Low Density Ice Layer

NASA, NAVY, AND AES/YORK SEA ICE CONCENTRATION COMPARISON OF SSM/I ALGORITHMS WITH SAR DERIVED VALUES

R.R. Jentz, C.C. Wackerman, R.A. Shuchman, and R.G. Onstott
Center for Earth Sciences, Advanced Concept Division
Environmental Research Institute of Michigan
Ann Arbor, Michigan 48107 USA

Per Gloersen and Don Cavalieri
Laboratory for Hydrospheric Processes
NASA Goddard Space Flight Center
Greenbelt, Maryland 20771 USA

Joey Comiso
Oceans and Ice Branch
NASA Goddard Space Flight Center
Greenbelt, Maryland 20771 USA

Rene Ramseier and Irene Rubinstein
Atmospheric Environment Service
Centre for Research in Experimental Space Science
York University, North York M3J 3K1 Canada

James Hollinger
Space Sensing Branch
Naval Research Laboratory
Washington, D. C. 20375-5000 USA

ABSTRACT

Previous research studies have focused on producing algorithms for extracting geophysical information from passive microwave data regarding ice floe size, sea ice concentration, open water lead locations, and sea ice extent. These studies have resulted in four separate algorithms for extracting these geophysical parameters. Sea ice concentration estimates generated from each of these algorithms (i.e., NASA/Team, NASA/Comiso, AES/York, and Navy) are compared to ice concentration estimates produced from coincident high resolution Synthetic Aperture Radar (SAR) data. The SAR concentration estimates are produced from data collected in both the Beaufort and Greenland Sea in March 1988 and March 1989, respectively. The SAR data is coincident to the passive microwave data generated by the Special Sensor Microwave/Imager (SSM/I).

KEYWORDS: Sea Ice Comparison, SAR, SSM/I, Sea Ice Concentration, Sea Ice Algorithm Comparison

1.0 INTRODUCTION

The polar research community has been interested in the determination of sea ice products from the arctic region since the launch of the Nimbus 5 Electrically Scanning Microwave Radiometer (ESMR) in 1972, and continued through 1987 with the Nimbus 7 Scanning Multichannel Microwave Radiometer (SMMR). Presently, the polar research community has focused its attention towards the SSM/I which was launched in June of 1987 aboard the Defense Meteorological Satellite Program (DMSP) Spacecraft F8. The SSM/I is the first of seven planned SSM/Is scheduled for launch over the next two decades which will make available passive microwave imagery of the arctic region well into the twenty first century [1].

Since 1972 the polar research community has been developing sea ice product algorithms designed to extract geophysical information about the arctic. The focus of these algorithms has been the generation of ice floe size distributions, open water lead locations, sea ice concentration maps, and sea ice extent (the location of the boundary between open water and the ice pack) which may assist in the generation of global climate models helping us to further understand our biosphere. During this period several research teams have developed algorithms

which produce both the total and fractional sea ice percentages from passive microwave data.

Verification of the results generated from these sea ice concentration algorithms was performed separately by various research teams. Their approach (when ground truth data was not available) has been to compare the results produced from coincident data sets collected by multiple sensors, then try and explain any discrepancies found. High resolution aircraft SAR systems can provide such a verification since the generation of reliable ice concentration estimates can be performed [2]. These studies show that the high spatial resolution associated with SAR imagery provides the ability to delineate individual floes and leads which make the determination of ice concentration easier. The research effort reported here is focused on trying to determine the strengths, weaknesses, and accuracy of several concentration algorithms by adopting the same method. The approach of this analysis is to compare ice concentration estimates generated by four of the most widely used concentration algorithms (i.e. NASA/Team, NASA/Comiso, AES/York, and Navy) to ice concentration estimates produced from coincident high resolution SAR data. Since the potential of imaging radars for discriminating sea ice types has been demonstrated using manual photographic interpretation techniques [3], the SAR concentration estimates are generated manually from a SAR photographic mosaic.

2.0 SYSTEM AND MISSION DESCRIPTION

The current SSM/I is a multichannel passive microwave radiometer built by Hughes Aircraft. It was designed to provide synoptic maps of atmospheric, oceanographic, and selected land parameters on a global scale. The SSM/I contains seven linearly-polarized channels operating at four separate frequencies (i.e., both horizontal and vertical polarization at 19.3, 37.0, and 85.5 GHz and vertical polarization at 22.2 GHz). The SSM/I satellite is in a circular sun-synchronous near-polar orbit at an altitude of approximately 800 km. The orbit period is 102.0 minutes producing 14.1 full orbit revolutions every day. The scanning antenna is tilted at a 45 degree angle to the satellite spin axis and sweeps out a 1400 km wide swath in 1.9 seconds. The resolution, or footprint, of the SSM/I brightness temperatures varies according to the frequency, where the footprint is approximately 55, 49, 32,

and 13 km for the 19.3, 22.2, 37.0, and 85.5 GHz channels respectively [1].

The high resolution SAR data used in this analysis was generated from the Naval Air Development Center (NADC) SAR built by the Environmental Research Institute of Michigan (ERIM), also referred to as the NADC/ERIM P-3 SAR. The NADC/ERIM P-3 SAR is a multifrequency, polarimetric, SAR installed in a U.S. Navy P-3 aircraft. It is a side-looking SAR that operates in both strip-map and spotlight mode. The center frequencies are 9.35 GHz, 5.30 GHz, and 1.25 GHz corresponding to X, L, and C bands respectively. The system is capable of recording polarimetric data corresponding to all of the elements of the polarization matrix (i.e. HH, VV, HV, and VH polarizations) where transmit and receive polarizations can be altered on a pulse-by-pulse basis.

The remote sensing data used in this comparison consists of imagery recorded in the Beaufort Sea on both 18 and 19 March 1988 and in the Greenland Sea on 17 and 20 March 1989. The SAR data was recorded with an azimuth resolution of 2.8 meters (the direction parallel to the flight track) and a range resolution of 3.2 meters (the direction orthogonal to the flight track). This imagery was collected at C-band with VV-polarization and is coincident to the SSM/I overflights.

3.0 ICE CONCENTRATION ALGORITHM DESCRIPTION

The four concentration algorithms included in this study are the NASA/Team, NASA/Comiso, AES/York, and Navy ice concentration algorithms. The NASA/Team algorithm is a multichannel concentration algorithm which generates both the total ice percentage as well as the multiyear ice fraction. It utilizes both the polarization and spectral gradient ratios from the 19.3 and 37.0 GHz channels to determine the percentage of multiyear sea ice [4,5]. The multichannel techniques used by this algorithm were adopted from those developed for the multichannel SMMR sensor which requires a unique emissivity for each of the assumed ice types within the scene. The NASA/Team algorithm uses the "global" set of tie points listed in [4] as the required set of emissivity values. The NASA/Comiso algorithm presented in this analysis is also a multichannel algorithm which produces the total ice percentage only from the 19.3 and 37.0 GHz SSM/I brightness temperatures. However, this algorithm is less rigid than the NASA/Team algorithm. It allows for modification of the tie points representing the emissivity of each ice type taking into account the spatial and temporal variability of the physical characteristics associated with different areas within the arctic [6]. The AES/York algorithm was designed to retrieve not only the basic SSM/I parameter of total sea ice concentration, but also identify first-year, multiyear, thin ice, and open water within the SSM/I footprint. Like the two NASA algorithms it uses both the 19.3 and 37.0 GHz channel data to determine these ice types. It also uses fixed tie points representing the emissivities of each passive microwave ice type signature [7]. The Navy algorithm is a tailored version of the AES/York algorithm. It generates the total ice percentage within an SSM/I footprint along with the predominate ice type where the predominate ice type can be either first-year or multiyear [1]. Like the other algorithms, the Navy

algorithm uses both the 19.3 and 37.0 GHz brightness temperatures to determine the total ice percentage. This algorithm, along with the NASA/Comiso algorithm, is used primarily for determining sea ice extent as well as the first-year/multiyear ice pack boundaries.

4.0 ICE CONCENTRATION ALGORITHM COMPARISON

The SAR ice concentration estimates are derived manually from a photographic mosaic which was produced by optically processing the digital SAR data. The photographic mosaic represents an area of continuous SAR coverage on approximately a 3.0 meter grid. The SAR concentration estimates are produced by dividing the SAR mosaic into a 5.0 km grid and manually interpreting the total ice percentage along with the multiyear, first-year, and open water ice fractions. Sea ice concentration maps are then generated on a 1 km grid for each of the sea ice concentration estimates. These concentration maps are produced using a two dimensional cubic spline interpolation scheme. The SSM/I concentration maps are produced from data collected by multiple orbits of the SSM/I satellite (orbits spanning the same time over which the SAR data was collected). Both the SAR and SSM/I sea ice concentration maps then represent a one-to-one mapping of the fractional ice type over a given latitude and longitude region.

The Beaufort Sea data collected on 18 and 19 March 1988 represent areas of 100% total ice concentrations where the 18 March mosaic crosses the first-year/multiyear ice pack boundary and the 19 March mosaic data was collected in the multiyear ice pack. This is an ideal data set for measuring the strengths of the Navy algorithm which produces a total ice concentration estimate along with the predominate ice type. Figure 1 shows the multiyear sea ice concentration estimates for three of the concentration algorithms (NASA/Team, AES/York, and Navy) along with the SAR estimates plotted as a function of latitude for the 18 March mosaic data (remember the 18 March mosaic crosses the first-year/multiyear ice pack boundary). Notice that the AES/York and Navy algorithm estimates track the SAR estimates close in the first-year ice pack, while the NASA/Team algorithm estimates are closer to the SAR estimates in the multiyear ice pack. Also notice that all three algorithm estimates are higher than the SAR estimates (approximately 40% to 50% higher) and that the NASA/Team estimates are much higher than the SAR within the first-year ice pack (approximately 30% higher). This misclassification of first-year ice by the NASA/Team algorithm is probably due to the pressure ridges associated with first-year ice in the Beaufort Sea. Figure 2 illustrates the corresponding plot of the concentration estimates as a function of latitude for the 19 March mosaic data. The Navy algorithm estimates the entire area as 100% multiyear sea ice, as expected, and the AES/York estimates are all 40% to 50% higher than the SAR estimates. However, the NASA/Team algorithm produced multiyear concentration estimates consistent with the SAR estimates.

The Greenland Sea data collected on 17 and 20 March 1989 represents areas of the Marginal Ice Zone (MIZ) which contains varying amounts of open water, first-year, and multiyear sea ice. This data is good for testing the accuracy of the NASA/Team and AES/York fractional ice type estimates along with the total ice percentage.

Figure 3 is a plot of the total ice concentration estimates versus the Corresponding SAR estimates for the 17 March 1989 data. The key on the plot illustrates a symbol for each of the four algorithms (the NASA Alg. refers to the NASA/Team algorithm and the Comiso Alg. refers to the NASA/Comiso algorithm) along with the slope "a" and y-intercept "b" of the linear regression analysis. Notice that the linear trend corresponding to each of the algorithm estimates is relatively close to the line with slope 1.0 and y-intercept 0.0 (this is the line where $y=x$ representing an exact match between the SAR and SSM/I estimates). The AES/York estimates provide the best match while the NASA/Comiso estimates have a slope very near 1.0 shifted by -9.096. Figure 4 illustrates the corresponding plot for the 20 March 1989 data. Again, this plot shows relatively good results for the NASA/Team, AES/York, and Navy algorithms while the NASA/Comiso algorithm tends to underestimate the total ice concentrations. Figures 5 and 6 show plots of multiyear ice concentrations versus the SAR estimates for the 17 and 20 March 1989 data sets, respectively. These plots show that the Navy algorithm generates ice concentrations that are consistently higher than the SAR. This is expected since this algorithm generates a total ice concentration value. Both the NASA/Team and AES/York algorithms produce multiyear estimates that are consistently lower than the SAR. This is surprising since the multiyear estimates generated for the Beaufort Sea data were consistently higher than the SAR. This might be due to different characteristics in the multiyear ice signatures between the two locations, or possibly the absence of pressure ridges from first-year ice in the MIZ (remember the NASA/Team algorithm misclassified approximately 30% of the first-year ice as multiyear ice on the 18 March 1988 Beaufort Sea data).

5.0 CONCLUSIONS

The NASA/Team algorithm generated multiyear ice concentration estimates similar to the SAR in the multiyear ice pack for the 19 March 1988 Beaufort Sea data (mean difference of approximately 6.5%). It also produced a misclassification error of approximately 30% (due to the pressure ridges) in the first-year ice pack for the 18 March 1988 Beaufort Sea data. The AES/York and Navy algorithms were not affected by the pressure ridges in the first-year sea ice, both produced a 0% multiyear estimate in the first-year ice area. Both the AES/York and Navy algorithms were able to distinguish between the first-year/multiyear ice pack boundaries, but they also overestimate the ice concentrations in the multiyear pack. The total ice concentration estimates derived from the 17 and 20 March 1989 Greenland Sea data are relatively close to the SAR estimates for the NASA/Team, AES/York and Navy algorithms. Each of these algorithms produced a Normalized Standard Error (NSE) less than 0.1, where the NSE is computed as the mean difference between the SSM/I and SAR estimates divided by the mean square of the SAR estimates (NSE equal to zero means no difference between the SAR and SSM/I derived concentration estimates). The NASA/Comiso algorithm underestimated the total ice percentage for the 20 March 1989 data (NSE equals 0.2). However, a much larger discrepancy was found in the multiyear estimates. The Navy algorithm which produces a total ice

estimate containing mostly multiyear sea ice generated NSE values of 0.285 and 0.450 for both the 17 and 20 March Greenland Sea data respectively. The AES/York algorithm generated NSE values of 0.320 and 0.553, and the NASA/Team algorithm NSE values were 0.467 and 0.681 for the 17 and 20 March 1989 Greenland Sea data respectively. This implies that even though the Navy algorithm generates a total ice estimate, the estimates are closer to the SAR estimates than the NASA/Team or AES/York algorithm estimates.

ACKNOWLEDGEMENTS

This research effort was sponsored by the Office of Naval Research (ONR) Contract No. N00014-81-C-0295, N00014-90-C-0148, and N00014-88-C-0680 under the technical guidance of Charles Luther, Robert Thomas at the National Aeronautics and Space Administration (NASA), and Robert Winokur at the Office of the Oceanographer of the Navy.

REFERENCES

- [1] Hollinger, J., "DMSP Special Sensor Microwave/Imager Calibration/Validation," DMSP Final Report Vol. 1, Space Sensing Branch of the Naval Research Laboratory, Washington, D.C., July 1989.
- [2] Burns, B. A., et al., "Computer-Assisted Techniques for Geophysical Analysis of SAR Sea-Ice Imagery", Pro. Nineteenth International Symposium on Remote Sensing of Environment, ERIM, Ann Arbor, MI, pp. 947-959, 1985.
- [3] Gray, A. L., et al., "Simultaneous Scatterometer and Radiometer Measurements of Sea-Ice Microwave Signatures," IEEE J. Oceanic Eng., vol. OE-7, 1982, pp. 20-32.
- [4] Cavalieri, D. J., et al., "Determination of Sea Ice Parameters with the Nimbus 7 SMMR", J. Geophys. Res., vol. 89, pp. 5355-5369, 1984.
- [5] Gloersen, P., et al., "Reduction of Weather Effects in the Calculation of Sea Ice Concentration from Microwave Radiance", J. Geophys. Res., vol. 91, pp. 3913-3919, 1986.
- [6] Comiso, J. C., "Characteristics of Arctic Winter Sea Ice From Satellite Multispectral Microwave Observations", J. Geophys. Res., vol. 91 pp. 975-994, Jan. 1986.
- [7] Ramseier, R. O., "Canadian Validation of The SSM/I and AES/York Algorithms for Sea-Ice Parameters", DSS File No. 62SS.KM168-7-7059, June 1990.

SSM/I Sea Ice Concentrations
March 18 1988

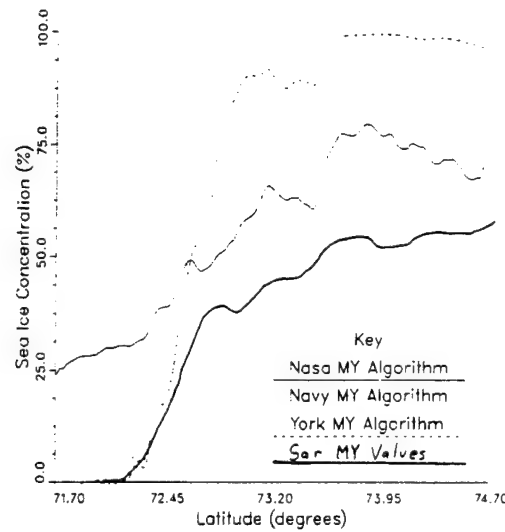


Figure 1. Multiyear Concentration Estimates for NASA/Team, Navy, AES/York and SAR Algorithms using 18 March 1988 Beaufort Sea Data.

Total Ice Algorithm Comparison
March 17 1989 Cearex Data

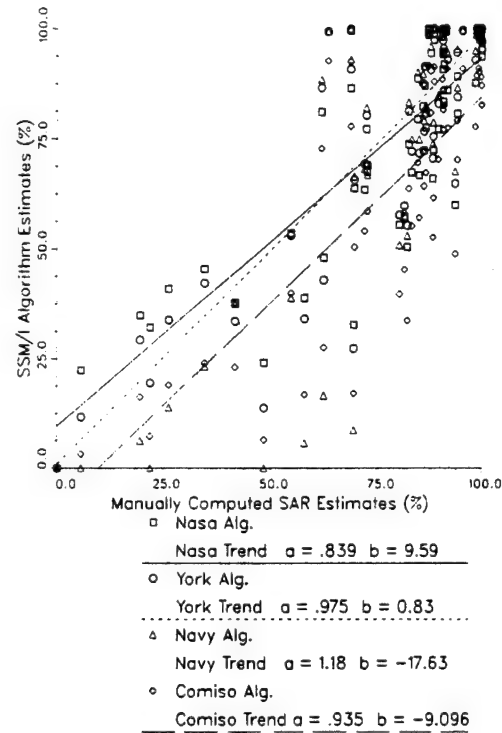


Figure 3. Total Ice Concentration Estimates vs SAR for 17 March 1989 Greenland Sea Data.

SSM/I Sea Ice Concentrations
March 19 1988

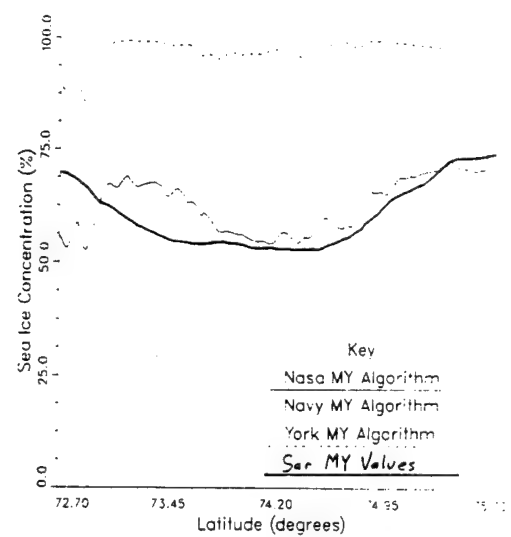


Figure 2. Multiyear Concentration Estimates for NASA/Team, Navy, AES/York and SAR Algorithms using 19 March 1988 Beaufort Sea Data.

Total Ice Algorithm Comparison
March 20 1989 Cearex Data

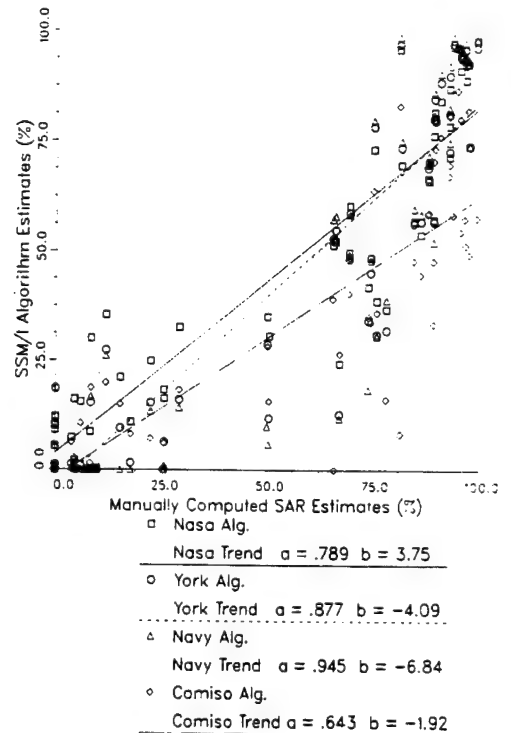


Figure 4. Total Ice Concentration Estimates vs SAR for 20 March 1989 Greenland Sea Data.

MultiYear Algorithm Comparison
March 17 1989 Cearex Data

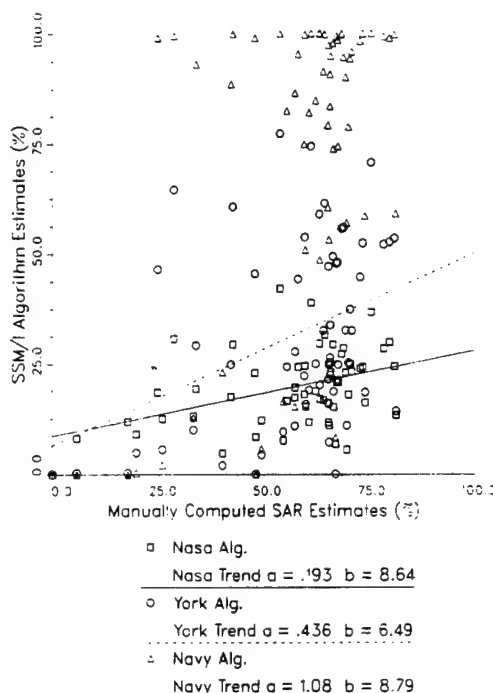


Figure 5. Multiyear Ice Concentration Estimates vs SAR for 17 March 1989 Greenland Sea Data.

MultiYear Algorithm Comparison
March 20 1989 Cearex Data

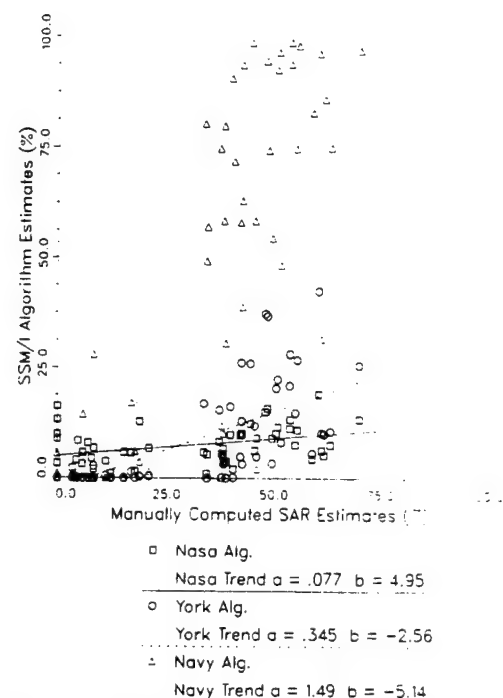


Figure 6. Multiyear Ice Concentration Estimates vs SAR for 20 March 1989 Greenland Sea Data.

POLARIMETRIC RADAR MEASUREMENTS OF ARCTIC SEA ICE DURING THE COORDINATED EASTERN ARCTIC EXPERIMENT

R.G. Onstott, R.A. Shuchman, and C.C. Wackerman
Center for Earth Sciences
Advanced Concepts Division
Environmental Research Institute of Michigan
P.O. Box 8618 Ann Arbor, MI 48107 USA

ABSTRACT

Surface-based scatterometer and airborne synthetic aperture radar (SAR) data of Arctic sea ice in Fram Strait were obtained during March 1989 as part of the Coordinated Eastern Arctic Experiment (CEAREX). Statistics of scattering coefficients, polarization ratios, depolarization ratios, phase differences, and correlation coefficients have been determined at frequencies of 1.25, 2.0, 5.25, 9.38, and 35 GHz to describe the scattering behavior for each of the major ice types. Ice form categories were numerous and included multiyear, first-year, nilas, and the thinnest forms, including very fine spicules of ice in suspension. These statistics have been calculated because they are unique, may be understood theoretically and empirically, and serve as the basis to discriminate image features.

Key Words: sea ice, radar, polarimetry

INTRODUCTION

Polarimetric radar observations were made of sea ice in the Greenland Sea during the March segment of the Coordinated Eastern Arctic Experiment (CEAREX). During this period an intensive series of in-situ observations were made to study several distinct ice types. Aircraft overflights were also conducted. One of the objectives of this investigation is to determine, under winter conditions, the active and passive microwave signatures for a variety of types of ice and to relate these signatures to the physical properties of the ice. A second objective is to determine the utility of a polarimetric synthetic aperture radar (SAR) to improve the accuracy of geophysical properties generated for the Arctic. Also of particular interest is to develop the ability to discriminate open water, new ice, and nilas.

During CEAREX, full complex scattering matrix data were acquired at frequencies in the bands from L to Ka. The purpose in acquiring these data is many fold and includes the improvement in the understanding of the scattering properties of all ice forms by the complete characterization of the scatter field over a very wide range of frequencies. The study of the optimal radar parameter combinations and the determination of the utility of the very robust, polarimetrically capable radars also benefit from these data collections and study. With a polarimetric radar,

information gained is based on the exploitation of the true complex scattering coefficients. This may be obtained from the phase difference between returns at VV and HH polarizations, the differences in the backscatter intensities at the various polarizations (i.e. VV, VH, HH, and VH), and the correlations between these complex scattering coefficients. It is hypothesized that if the full scattering matrix is acquired that physical property information associated with preferred geometric orientations or internal anisotropic physical-dielectric properties will be more accurately obtained. This would then lead to improved ice type discrimination, feature identification, and geophysical property retrievals. This may allow computer algorithms to be simplified because of the ability to select an optimum subset of parameters from the scattering matrix, and possibly the relaxing of SAR resolution requirements while maintaining algorithm performance.

EXPERIMENT DESCRIPTION

Radar backscatter data were acquired at frequencies of 1.8, 5, 10, and 35 GHz from the rail of the ice strengthened ship R/V *Polarbjorn* using a polarimetric scatterometer. The ERIM/NADC P-3 SAR was operated at 1.25, 5.25, and 9.38 GHz to image the regions which were the subject of the intensive in-situ investigations. Sites were located near the open water at the ice edge of the marginal ice zone (MIZ) to the giant floes (diameters greater than 10 km) in the ice pack located a distance of 35 nm from the ice edge. In summary, observations included open water, pancake ice, nilas ice, young ice, first year ice, and multiyear ice. These radar observations were carried out in conjunction with the detailed characterization measurements. A summary of the physical properties for four major ice types is provided in Table 1.

PREDICTED UTILITY

An analysis was performed to determine the ability to exploit the polarization ratio and phase difference for five clutter types including open water, very new ice, new ice, first year ice, and multiyear ice. Response functions derived from the small perturbation scattering model for smooth surfaces were created as a function of incidence angle and

are provided in Figures 1 and 2. Proper dielectric constant values are critical in this study and were derived from previous radar reflectivity measurements. Essential trends are described herein. In the transition from open water to new ice, brine is deposited on the surface of the new ice, hence, its dielectric constant will be higher than that of open water. Within hours, however, the ice thickens and the dielectric constant reduces. By the time grey ice or first year ice has evolved there is an order of magnitude change in dielectric constant. The dielectric constant for multiyear ice (the upper portion of the ice sheet) is about 30% smaller than that for first year ice. Results show that dielectric constant and incidence angle drive these ratios, with the largest differences occurring when there are larger differences in dielectric constant. Ratios among the ice types become larger with increasing incidence angle. Based upon these results and the L, C, X SAR data, it appears that the greatest ability to discriminate new ice and water is obtained at L-band by using the polarization ratio to segment open water and then detecting at VV-polarization the very weak returns produced by the nilas as contrasted to the stronger returns of open water.

DISCUSSION

A set of four SAR images (HH, HV, VH, VV) obtained at 9.38 GHz is provided in Figure 3 to illustrate ice conditions found in the Greenland Sea on 21 March. This scene was selected because it includes open water, nilas, young first year, and multiyear ice which were identified by both helicopter reconnaissance and in-situ sampling. One of the important features in this image set is the extensive lead area, much of which is in open water. Very thin ice was found to form in the shadowed regions of the open water lead which lie close to the vast multiyear ice floe (lower right hand corner). Adjacent to this lead in the lower left hand corner is a band composed of various stages of grey ice. A diagram of sea ice types identified from the SAR imagery is presented in Figure 4.

In general, the information within the four images of different polarizations is very similar, except in the case of the young ice types. Interestingly, the like-pol responses are different enough to have utility, and the comparison between the like- and cross-pol responses are even more dramatic. Hence, polarization diversification for use in separating young ice forms will be examined with interest. The nilas formed in the shadow areas produced a barely detectable enhancement in backscatter return at VV-polarization. The edge between ice and water was delineated. Contrast between these two ice types improved with decreasing frequency (i.e. at C- and L-band). The cluttering between the various young ice forms in the grey ice band suggests a sensitivity to roughness scales at this frequency.

A set of SAR derived products has been generated and is provided in Figure 5. These include σ^0_{VV} , σ^0_{HH} , σ^0_{HV} , span, polarization ratio, depolarization ratio, correlation coefficient, and co-pol phase difference. These results and their interpretation were one of the focusses of the discussion of this presentation. These data were contrasted with preliminary results obtained by the surface-based scatterometer. These results are included in Table 2 for reference.

SUMMARY

A comprehensive collection of data has been obtained to characterize the microwave properties of Arctic sea ice and to allow further refinement of satellite SAR geophysical algorithms. Included is a critical set of data in which areas of open water, new ice, nilas, and young first year have been identified by in-situ observations.

ACKNOWLEDGEMENTS

This work is supported by the Office of Naval Research (ONR) contract N00014-86-C-0469. The Technical Monitors were Mr. Charles Luther and Dr. Thomas Curtin.

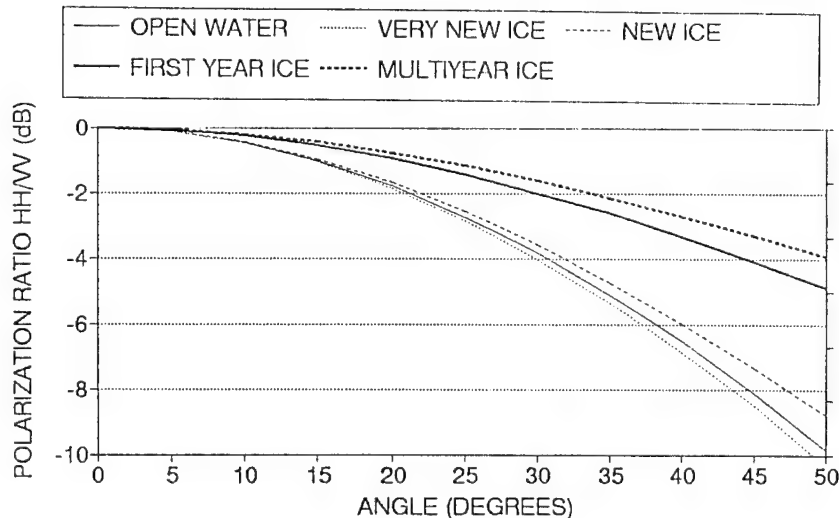


Figure 1. The Polarization Ratio ($\sigma^0_{HH}/\sigma^0_{VV}$) for Open Water, Very New Ice, New Ice, First Year Ice, and Multiyear Ice has Been Calculated Based on the Small Perturbation Model and Measured Dielectric Constants.

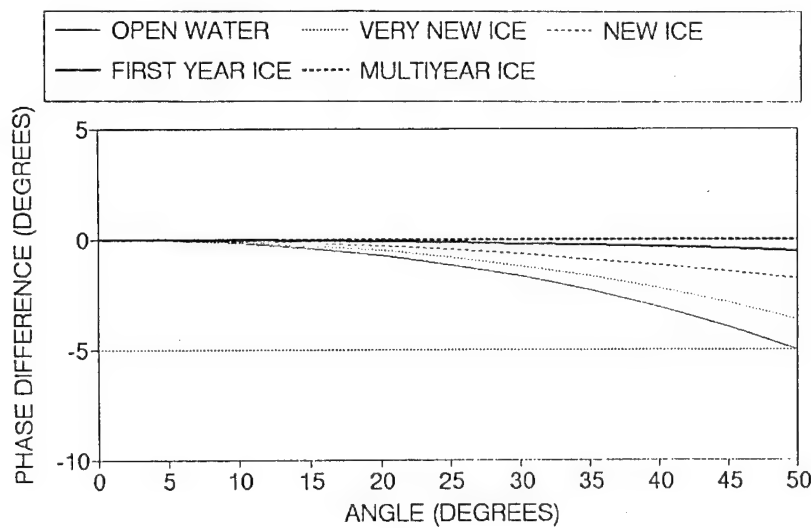


Figure 2. The Phase Difference Ratio (θ_{HHvv}) for Open Water, Very New Ice, New Ice, First Year Ice, and Multiyear Ice has Been Calculated Based on the Small Perturbation Model and Measured Dielectric Constants.

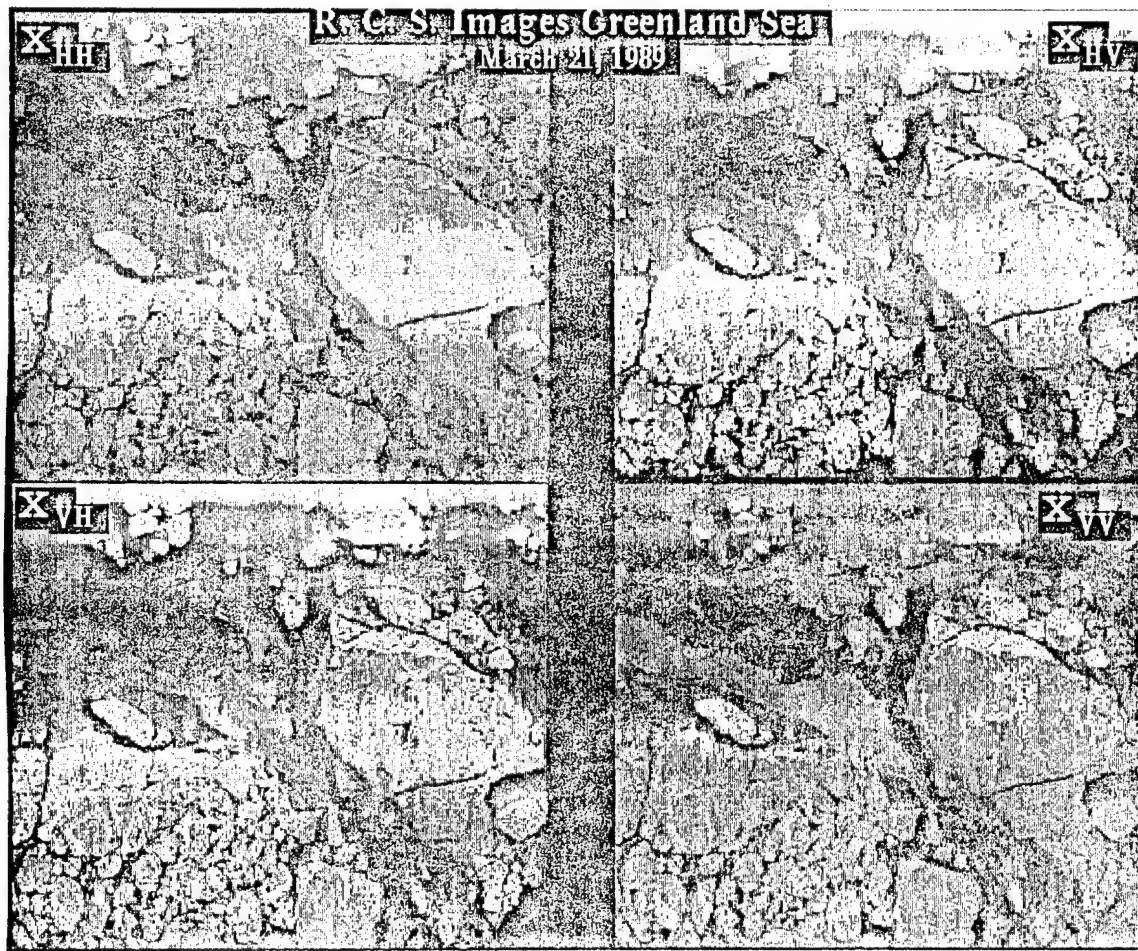


Figure 3. This X-band Quad-Pol SAR image was obtained in March 1989 during the Coordinated Eastern Arctic Experiment in the Greenland Sea.

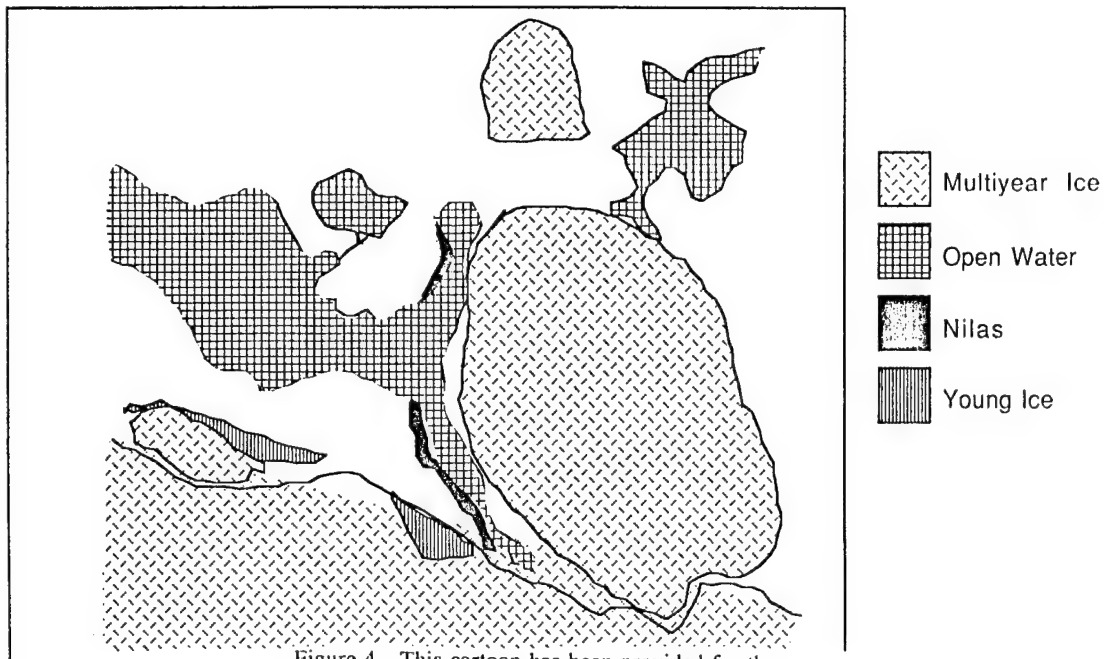


Figure 4. This cartoon has been provided for the identification of the multiyear, young, nilas and open water sites.

Table 1.

Examples of Sea Ice Physical Properties During CEAREX March 1989

Description	Multiyear	Thick First-Year	Young First-Year	Thin First-Year
Ice Thickness - m	$2.55 \pm .64$	1.64	$0.215 \pm .4$	0.42
Snow Thickness - cm	26 ± 19	9.5	8	5
$T_{AIR} - ^\circ C$	-18.3 ± 3.6	-19.7	-17.5 ± 3.5	-25
$T_{ice/Surface} - ^\circ C$	-16.2 ± 3.6	-13.2	-12.0 ± 2.8	-20
Salinity - PPT	$0.17 \pm .19$	8.4 ± 3.0	9.9	7.9
Depth - cm	12	8	6	3
Density - kgm/m ³	$0.716 \pm .19$	$.900 \pm .03$	0.844	0.359
Brine Volume	$0.757 \pm .83$	51 ± 3	35	38

Table 2.

Preliminary Polarimetric Scatterometer Results

Scene	Dielectric Constant	Surface Roughness	$\sigma^{\circ}_{VV}/\sigma^{\circ}_{HH}$	$(\sigma^{\circ}_{VV} + \sigma^{\circ}_{HH})$ $(\sigma^{\circ}_{VV} + \sigma^{\circ}_{HH})$	Correlation Coefficient
Open Water	Large (≈ 40)	$\sigma \approx 0.2 \text{ cm}$ $1 \approx 7 \text{ cm}$	$\approx 4 \text{ dB}$	$\approx 20 \text{ dB}$	≈ 0.99
Nilas (2 cm)	Large	$\sigma \approx 0.05 \text{ cm}$ $1 \approx 1 \text{ cm}$	$\approx 2 \text{ dB}$	$\approx 20 \text{ dB}$	≈ 0.98
Grey (20 cm)	Low (≈ 4)	$\sigma \approx 0.05 \text{ cm}$ $1 \approx 1 \text{ cm}$	$\approx 0 \text{ dB}$	$\approx 16 \text{ dB}$	≈ 0.95
First Year (160 cm)	Low (≈ 4)	$\sigma \approx 0.2 \text{ cm}$ $1 \approx 7 \text{ cm}$	$\approx 1 \text{ dB}$	$\approx 12 \text{ dB}$	≈ 0.80
Multiyear ($>300 \text{ cm}$)	Low (≈ 3)	$\sigma \approx 0.2 \text{ cm}$ $1 \approx 7 \text{ cm}$	$\approx 0 \text{ dB}$	$\approx 9 \text{ dB}$	≈ 0.70

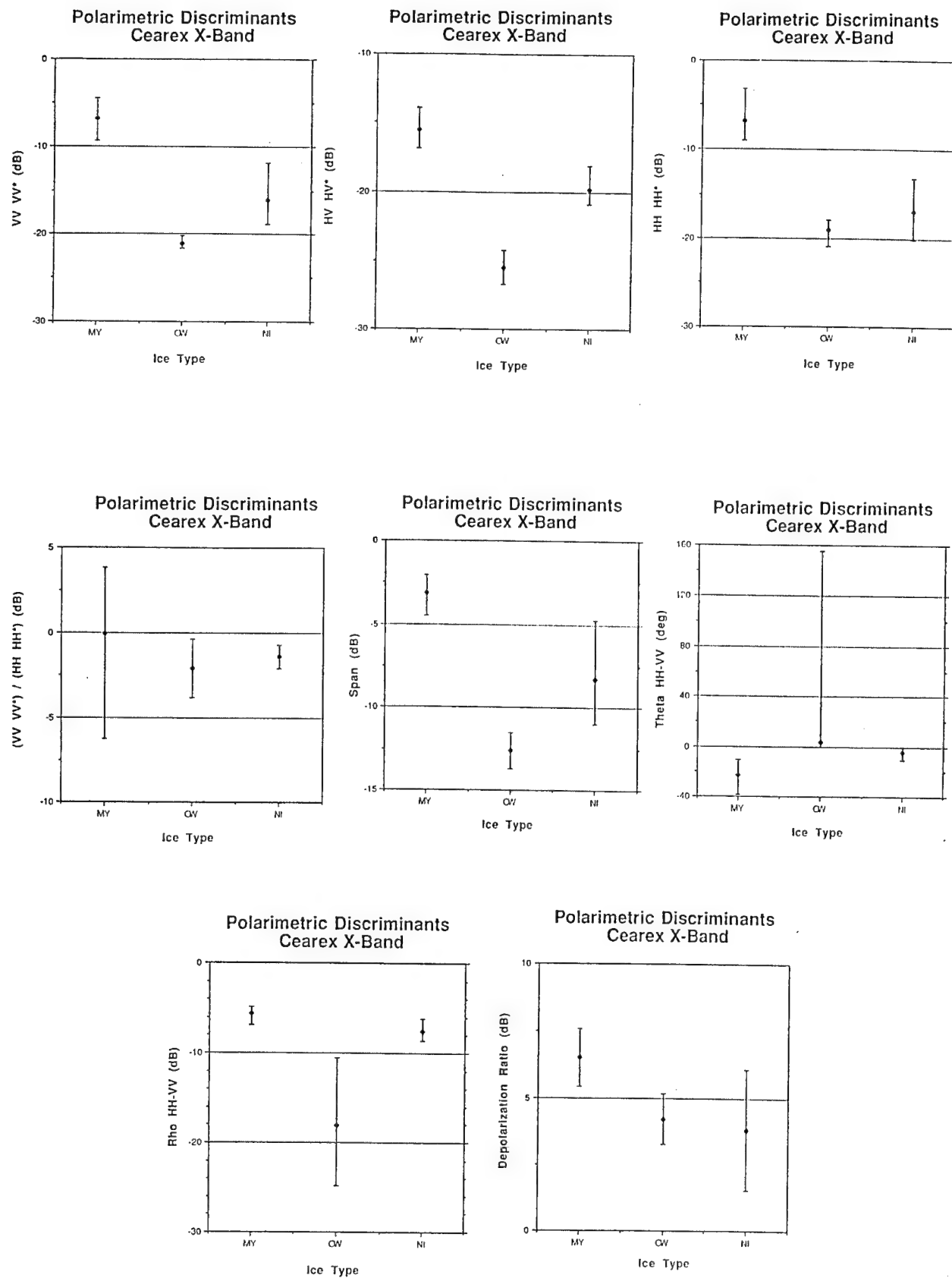


Figure 5. Polarimetric discriminant at X-band calculated for multiyear ice, nilas, and open water for 21 March CEAREX site.

Chapter 5. SAR and Scatterometer Signatures of Sea Ice

ROBERT G. ONSTOTT

Environmental Research Institute of Michigan, P.O. Box 8618, Ann Arbor, Michigan 48107

This chapter discusses the radar measurement of sea ice. The underlying theme is the physics that now make it possible to use active microwave techniques to obtain information about the frozen ocean instead of making direct in-situ measurements and that will ultimately make it possible to use those techniques for continuous, global monitoring. Basic remote-sensing concepts are presented and are followed by discussions of the interaction of electromagnetic energy with various ice types; the discussions include the effects of the environment and of physical-property perturbations. Critical links among ice type and form, physical and electrical properties, and backscatter signature will be highlighted and discussed. The examples used are primarily taken from Arctic research; however, the principles presented are equally applicable to the Antarctic region.

5.1 INTRODUCTION

Active remote sensors that operate in the microwave portion of the electromagnetic spectrum (i.e., radars operating at wavelengths from 2 to 24 cm) provide their own source of illumination and have been used to obtain information pertaining to ice-covered waters. Examples of such instruments include scatterometers and imaging radars.

Knowledge of ice type, thickness, age, and state are of particular interest in the study of the polar oceans. Of these parameters, the Holy Grail is the ability to estimate the distribution of ice thickness accurately, which is particularly critical in supporting climate studies. Figure 5-1 illustrates the key backscatter interactions for multiyear and first-year sea ice, and for open water without wind. Multiyear ice (i.e., ice that has survived a summer melt) can be distinguished from first-year ice by its greater thickness (1.5 m or greater), its lower salinity (2.5‰ versus 7.7‰ for first-year ice), and thicker snow cover (0.4 m versus 0.1 m for first-year ice). The backscatter from multiyear ice is a function of both surface and volume scattering (because of the very low upper-ice salinity, the increased radio wave penetration over time, and a dense population of gas bubbles); whereas backscatter from first-year ice and from the ocean is dominated, in large part, by the roughness of their surfaces (i.e., both are high-loss materials).

Microwave Remote Sensing of Sea Ice
Geophysical Monograph 68
©1992 American Geophysical Union

In-situ observations in the Arctic during the fall freeze-up, late winter, spring, and summer have been conducted to acquire empirical data to describe the microwave properties of sea ice. These data contribute to studies whose goal is to determine the ability of remote sensing to classify ice types and to characterize the physical and electrical parameters that control backscatter intensity. A wide range of frequencies, polarizations, and incidence angles have been employed to determine exactly how backscatter is influenced and to optimize the selection of sensor parameters so as to extract the geophysical parameters of greatest interest.

Results indicate that many features, including ice types, pressure ridges, and other large-scale topographical features, lead (polynya) formations, and icebergs, have unique microwave signatures that may be distinguished by using radar. Hence, it has been shown that backscatter is influenced by different aspects of the sea ice structure. Selection of wavelength, polarization, and viewing angle allows a measure of control over the depth at which the snow and ice are examined and helps in the determination of the dominant scattering mechanisms. These selection options are among the tools the scientist has to capture the desired geophysical information.

Active microwave research on solid oceans began in 1956 with a flight by the Naval Research Laboratory R5D Flying Laboratory. The goal was to determine the scattering characteristics of sea ice in the region near Thule, Greenland, when 0.4 to 10 GHz radars were used and the depression angles were less than 20°. The first attempt to map sea ice with the intent to retrieve information about ice properties was made in the early 1960's by the U.S. Army Cold Regions

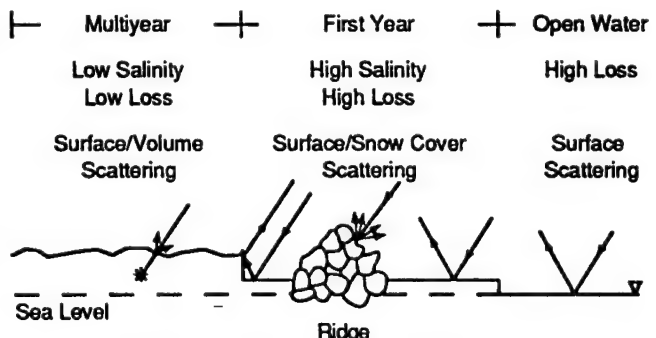


Fig. 5-1. Backscatter interactions for multiyear ice, first-year ice, and smooth open water.

Research and Engineering Laboratory (CRREL) [Anderson, 1966]. Interest in mapping sea ice began with the determination that during winter, first-year and old ice could be distinguished. Water was also found to produce a comparatively weak backscatter, an additional element of this study warranting further investigation. Even though sensors at that time provided little to support a quantitative assessment, these results have propelled research efforts to this day.

Historically, in the 1970's and 1980's, programs centered on determining what information was contained in radar image data of sea ice; often, interpretation of the imagery was based on the intercomparison of radar and optical imagery. The rigor of investigating the backscatter behavior and the mechanisms responsible for it gained momentum in the middle 1970's during a time when in-situ measurements complemented the aerial observation programs. The institution of air and in-situ campaigns was pioneered and promoted by Ramseier et al. [1982] and others, beginning with the 1973 US-USSR Bering Sea Experiment and the 1975-1976 Arctic Ice Dynamics Joint Experiment (AIDJEX) efforts [Campbell et al., 1978]. The addition of in-situ active microwave measurements and ice characterizations was instituted by R. K. Moore (University of Kansas) in 1976. The approaches developed in the 1970's continue today, with refinements in the sets of features sampled, the capabilities of the measurement sensors, and the missions of the experiments.

5.2 SCATTERING MEASUREMENTS

Until the late 1970's, knowledge of the active microwave signature of sea ice was more qualitative than quantitative. This is primarily attributed to difficulty with surface-truthing aircraft radars (which were flown over much greater distances than could be studied easily by surface parties) and to limitations on the size of an in-situ activity and its large logistics cost. Hence, the primary surface-truthing tool was aerial photography. Early radars were rarely designed to provide an absolute measurement, and the utilization of relative backscatter data was difficult even in making pass-to-pass comparisons; it was definitely difficult in making sensor-to-sensor comparisons.

Radar scatterometers were developed to provide accurate measurement of the scattering properties of terrain and ocean surfaces. The radar backscatter is defined in terms of a differential radar cross section per unit area σ^o . This representation is used when backscatter is from an incoherent collection of a very large number of independent scatterers [Ulaby et al., 1982].

Aircraft campaigns began with observations at single frequencies and polarizations. Today, aircraft and in-situ systems have complete polarization diversification and operate at multiple frequencies. Sensors that are fully polarimetric allow the near-simultaneous retrieval of both orthogonal transmit and orthogonal receive polarizations (VV, VH, HV, and HH) and preserve the relative phase difference between channels (see Chapter 24). Side-looking

airborne radars (SLAR's) and synthetic aperture radar (SAR) observe a ground pixel at only one incidence angle. Near-surface scatterometers often allow for a full microwave characterization over a wide range of frequencies, polarizations, and incidence angles. Aircraft scatterometers have a similar capability, but have been limited to a few frequencies and a more difficult absolute calibration.

The measurement programs had two important tasks. The primary task was to provide for the optimum use of existing radar systems and support the development of future satellite and aircraft radars, both aims to be furthered by documenting the mean and variability of the radar backscatter for the various ice forms as functions of season, region, and formation conditions. This description allowed for selection of sensor frequency, angle, and polarization to get the information desired. The second aspect, the primary interest of today, was full characterization of the mechanisms responsible for an ice microwave signature and development of the understanding that would allow the optimum retrieval of geophysical information.

Progress toward this second goal began with the works of Anderson [1966], Dunbar [1969], Ketchum and Tooma [1973], Dunbar and Weeks [1975], and Johnson and Farmer [1971]. Quantitative measurements began with Rouse [1969] and the study of data acquired in May 1967, with the NASA 13.3-GHz (VV) scatterometer on sea ice in the Beaufort Sea. A correlation between ice type and the magnitude of the backscattering coefficient was made. This was extended by Parashar et al. [1977], describing 1970 measurements at 400 MHz and 13.3 GHz, compared with 15-GHz multipolarized images. Gray et al. [1977] suggested that seven ice types could be classified at 15 GHz by using combinations of the magnitude and the angular dependence of the scattering coefficient. Complementary work by Glushkov and Komarov [1971] and Loshchilov and Voyevodin [1972] in the USSR during this period led to the development in the early 1970's of an operational ice surveillance system based on a real aperture radar (RAR) system called Toros that operated at 16 GHz.

5.2.1 Description of In-Situ Data Collections

An increase in scientific and operational interests in the ice-covered regions of the Arctic Ocean resulted in an extensive set of experiments involving the use of radar for monitoring the properties of sea ice. These experiments used aircraft-borne scatterometers, SLAR's, and SAR's, as well as surface-based scatterometers. The goal of these efforts was to gain more information regarding the ice and the radar methods for measuring its properties. The result of the observations has been the documentation of scattering and scene properties for various seasons, regions, ice types, and ice formation conditions.

The in-situ microwave and physical ice property characterizations that serve as the primary basis of this chapter were initiated in 1977. Since that time, there have been observations conducted in the Beaufort Sea, Central Arctic, Greenland Sea, Eastern Arctic Ocean, Labrador Sea, and

Barents Sea. Seasons have included fall freeze-up, early winter, late winter, early spring, and summer. Experiments, locations, seasons, and observations are summarized in Table 5-1.

Sensors for the in-situ measurement programs have been varied. The transportable microwave active spectrometer (TRAMAS) was an important contributor in the late 1970's (see Figure 5-2). Sensor development has continued with the addition of rapid data-acquisition systems that allow efficient operation from both helicopter and ship.

5.2.2 Radar Integral Equation

A radar incorporates a transmitter and receiver. The transmitted energy that returns back to the radar is of great interest; its magnitude is determined by the scattering

properties within the illuminated area. The average received power (P_r) may be obtained by the use of the integral radar equation for distributed targets

$$P_r = \frac{\lambda^2}{(4\pi)^3} \int_A \frac{P_t G^2 \sigma^*}{R^4} \quad (1)$$

where P_t is the power transmitted, G is the antenna gain, λ is the wavelength, R is the range from the radar to the terrain, A is the illuminated area, and σ^* is the radar-scattering coefficient. The radar-scattering coefficient is a function of frequency, incidence angle, and polarization and is an absolute measure of scattering behavior.

TABLE 5-1. Near-surface-based scatterometer investigations.

Mission, year of data collection	Location	Month	Ice types	Frequencies, band
CEAREX, ^a 1989	Fram Strait	January–March	OW–MY	P, L, C, X, Ku, Ka, W
CRRELEX, ^b 1989	Ice tank	January and February	OW–ThFY	L, C, X, Ka (all are fully polarimetric)
CEAREX, 1988	Fram Strait	September–December	OW–ThFY–MY	P, L, C, X, Ku, Ka, W
CRRELEX, 1988	Ice tank	January and February	OW–ThFY	L, C, X (all are fully polarimetric) X, Ku, Ka, W (all are noncoherent)
BEPERS, ^c 1988	Bothnia	March	Brackish	X
MIZEX, ^d 1987	Fram Strait	March	OW–MY	P, L, C, X, Ku, Ka
CRRELEX, 1985	Ice tank	January–March	OW–ThFY	C, X, Ku
MIZEX, 1984	Fram Strait	June and July	OW ThFY–MY	L, C, X, Ku
MIZEX, 1983	Fram Strait	June and July	OW ThFY–MY	L, C, X, Ku
FIREX, ^e 1983	Mould Bay	April	FY SY	C, X, Ku
FIREX, 1982	Mould Bay	June and July	OW TFY MY	L, C, X, Ku
Lab Sea, 1982	Labrador Sea	February	OW NW–ThFY	L, C, X, Ku
Sursat, ^f 1981	Mould Bay	September and October	Gray MY	L, C, X, Ku
YMER, ^g 1980	East Greenland Sea	September	OW FY–MY	L, C, X, Ku
Sursat, 1979	Tuktoyaktuk	March	Brackish FY	L, C, X, Ku
UKansas, ^h 1978	Pt. Barrow	April	FY lake	L, C, X, Ku
UKansas, 1977	Pt. Barrow	May	TFY MY lake	L, X, Ku

^a CEAREX = Coordinated Eastern Arctic Research Experiment

FY = first-year ice

^b CRRELEX = Cold Regions Research and Engineering Laboratory Experiment

MY = multiyear ice

^c BEPERS = Bothnian Experiment in Preparation of ERS-1

ThFY = thin first-year ice

^d MIZEX = Marginal Ice Zone Experiment

TFY = thick first-year ice

^e FIREX = Free-flying Imaging Radar Experiment

SY = second-year ice

^f Sursat = Surveillance Satellite Experiment

OW = open water

^g YMER = a Swedish Experiment

NW = new water

^h UKansas = University of Kansas Experiment

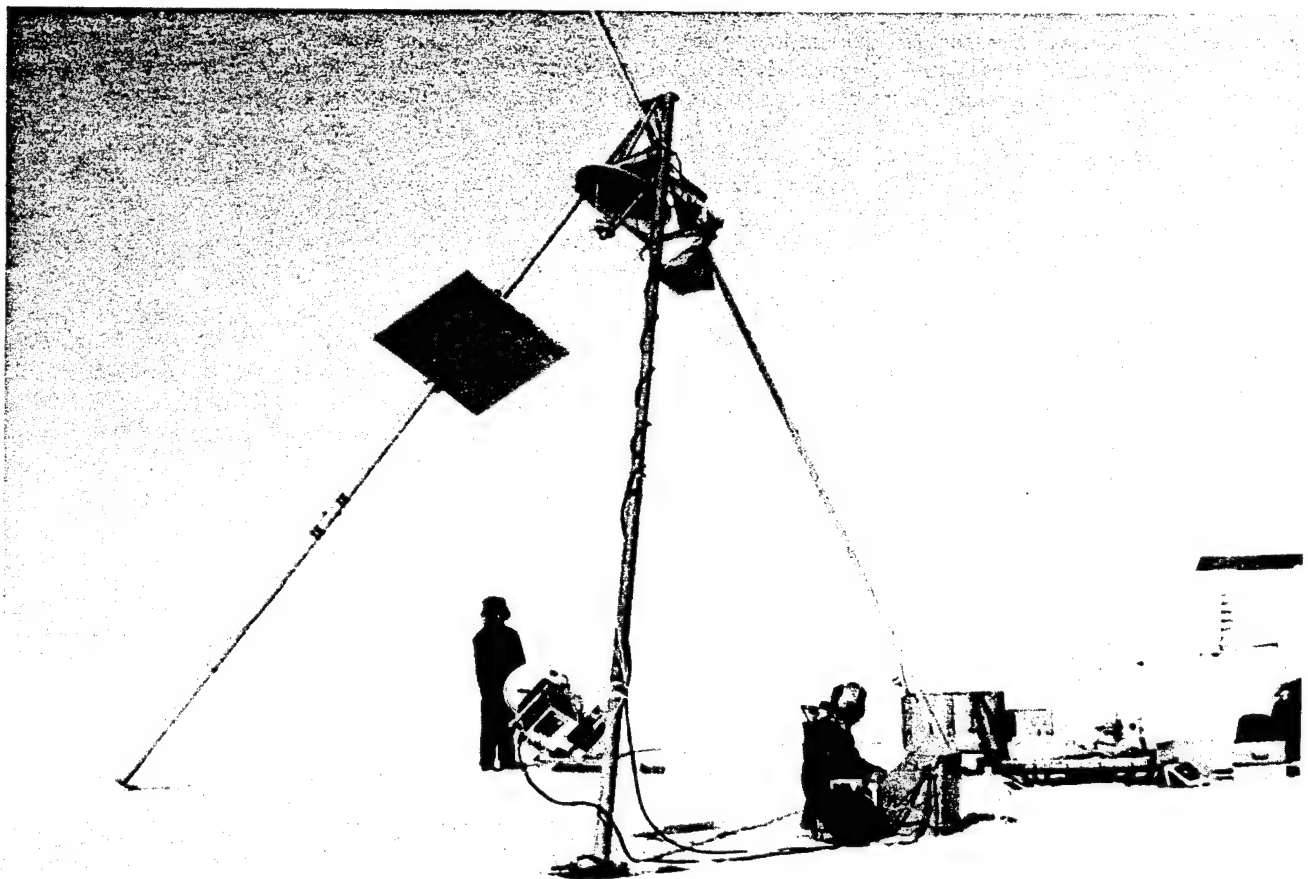


Fig. 5-2. TRAMAS was the first in-situ active microwave system to obtain measurements of sea ice, and was developed in 1976 at the University of Kansas [Onstott et al., 1979].

5.2.3 Origin of Backscatter

What is the origin of the backscatter for sea ice? The basic hypothesis is that backscatter is influenced by the sea ice structure. Questions center on the importance of scatter from the surface of the snow layer, the interior of the snow, the snow-ice interface, the upper portion of the ice sheet, the interior of the ice sheet, and the ice-water interface. The way in which sea ice forms, its history, and its age are important in determining its microwave properties. When ice is young, its surface may be smooth (if it grows undisturbed) or rough (if it is agitated by wave action). Ice may exhibit a thin layer of brine on its surface, thereby limiting electromagnetic wave propagation to depths of a wavelength or less. With the high concentration of brine in its interior, new ice near its freezing point is extremely lossy and, again, penetration is limited.

With age, the volume of brine in first-year ice reduces (see Chapter 2), but the ice remains lossy. During summer, the ice that survives the process of melt has developed additional surface relief, has had the density of the upper portion of the ice sheet reduced, and has desalinated. These

three characteristics contribute to the difference in the microwave signatures of FY and MY ice. A cross-sectional view is provided in Figure 5-3. First-year ice has few internal scatterers, and these are small compared to a wavelength. The penetration depth in multiyear ice may be several wavelengths, and there is a significant number of gas bubbles with diameters of 1 to 3 mm found within this volume. The physical models shown in Figure 5-4 help focus attention on the important aspects of these two ice types.

5.2.3.1. Microwave signature for new, young, and thick first-year ice. The dominant backscatter mechanism associated with first-year ice is surface scattering and/or scattering from the region very near the ice surface. The radar-scattering coefficient may be expressed as

$$\sigma^{\circ}_m(\theta_i) = K \Gamma^2(p, f, \theta_i, \epsilon_r) SF(p, f, \sigma, 1) \quad (2)$$

which is a function of the Fresnel reflection coefficient (Γ), a shape function (SF), and a scaling constant (K). The reflection coefficient is a function of incidence angle (θ_i), the

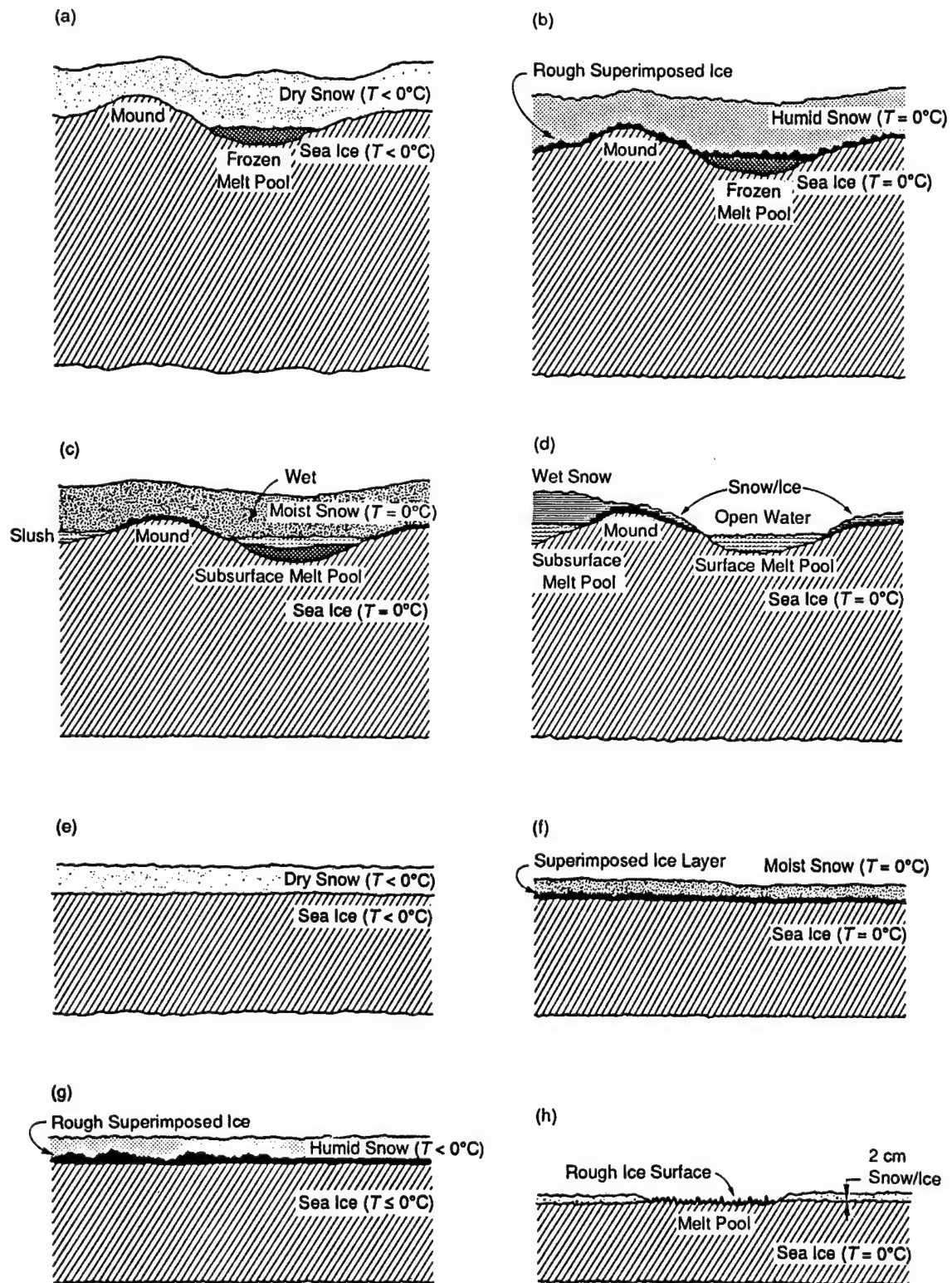


Fig. 5-3. Snow and ice conditions encountered on multiyear ice during (a) winter and early spring, (b) late spring, (c) early summer to midsummer, and (d) midsummer to late summer. Snow and ice conditions encountered on first-year ice during (e) winter and early summer, (f) late spring, (g) early summer to midsummer, and (h) midsummer to late summer [Onstott et al., 1987].

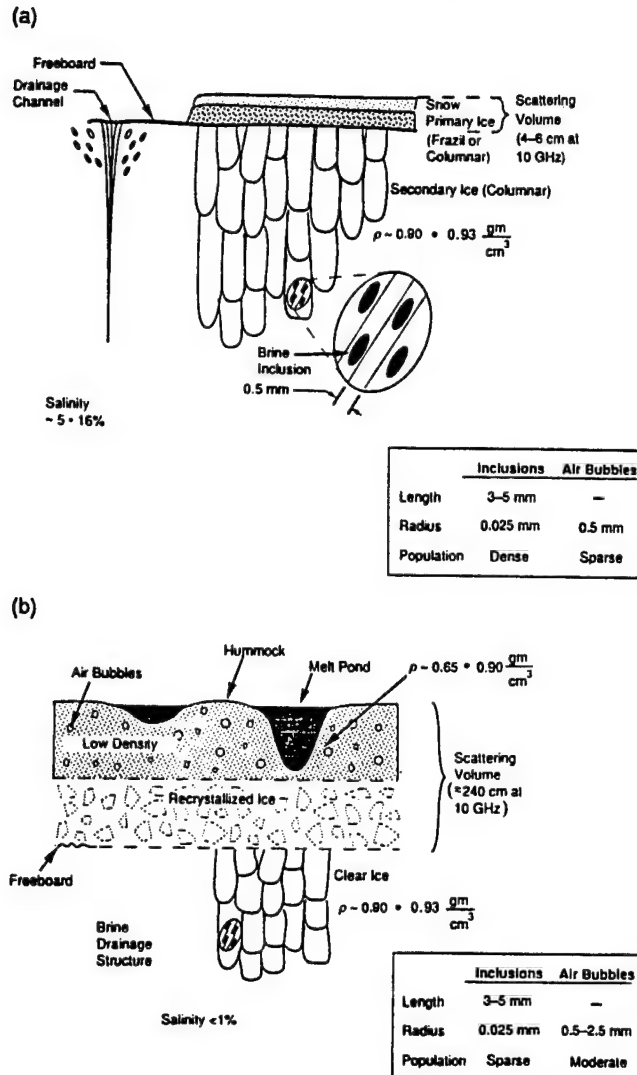


Fig. 5-4. Cross sections of (a) first-year and (b) multiyear sea ice.

transmit-receive antenna polarization (p), frequency (f), and the complex dielectric constant (ϵ_r^*). The shape function is a function of polarization, frequency, the root mean square (rms) surface height (σ), and the surface correlation length (ℓ).

In summary, the important sea ice parameters (primary) are ϵ_r^* , because it acts to set the absolute backscatter level, and the surface-roughness statistics σ and ℓ , because they influence the shape function. They act independently of environmental forcing and have been decoupled to study their impact on the backscatter signature. See Chapters 8 and 9 for additional discussion on the depth of penetration and for comparison of measured and predicted data.

5.2.3.2. Microwave signature for multiyear ice. The backscatter of multiyear ice is attributed to gas bubbles in the upper portion of the ice sheet. (See Chapters 8 and 9.) Propagation through a volume of dielectric discontinuities

or discrete scatterers (i.e., gas bubbles in an ice matrix) may produce volume scattering. These results may be predicted (zero-order) by assuming that each bubble is characterized by a cross section proportional to its radius to the sixth power. The total backscatter is then proportional to the sum of all cross sections [Kim, 1984; Kim et al., 1984a] and may be expressed as the contribution from the surface and the ice volume as given by

$$\sigma_{pp}^0(\theta_i) = \sigma_s^0(\theta_i) + \gamma^2(\theta_i) \sigma_v^0(\theta_i) \quad (3)$$

The surface scattering contribution σ_s^0 is identical to that described earlier. The intensity of the volume backscatter is weighted by the transmission coefficient γ , which is reasonably close to 1. The volume scattering coefficient may be expressed as

$$\sigma_v^0(\theta_i) = N\sigma_b \cos(\theta_i) [1 - 1/L^2(\theta_i)\gamma(2k_e)] \quad (4)$$

where N is the number of particles, σ_b is the scattering cross section per particle, L^2 is the two-way loss factor, and k_e is the extinction coefficient. The number of particles is a function of the density of the layer (ρ) and the radius (r) of the particles cubed and given by

$$N = (1 - \rho/0.926)/(4\pi r^3/3) \quad (5)$$

Hence in the strong volume scattering cases associated with multiyear ice, the backscatter will increase with increasing radii of the gas bubbles and as the total number of discrete scatterers increases. The number of scatterers increases with decreasing density and increasing thickness of the low-density ice (LDI) layer. A cross-sectional view of multiyear ice is shown in Figure 5-5, with ranges of expected thickness, density, salinity, and bubble diameter. In Figure 5-6, the relative contributions of smooth and rough surfaces and of a volume with a smooth and a rough surface are shown as a function of frequency for typical ice characterization values associated with multiyear ice. Note that backscatter intensity increases with increasing frequency in all cases.

5.2.3.3. Empirical observation of the sources of scatter. The measurements of first-year and multiyear ice illustrated in Figure 5-7 were made at 5.25 GHz, VH-polarization, with an incidence angle of 45° [R. G. Onstott, manuscript in preparation, 1992]. Backscatter intensity is plotted as a function of position in the ice and snow (1 m in ice for each 1.75 KHz), and the surface distance moved (40 m).

A multiyear ice sheet is typically composed of three scattering features: hummocks, melt pools, and ridges. The backscatter from the undulating part of the ice sheet (hummocks and melt pools) is considered here because melt pools and hummocks often dominate the response of a multiyear ice floe, and their similarities and differences serve to illustrate the importance of the upper portion of the ice sheet in determining the microwave signature response for

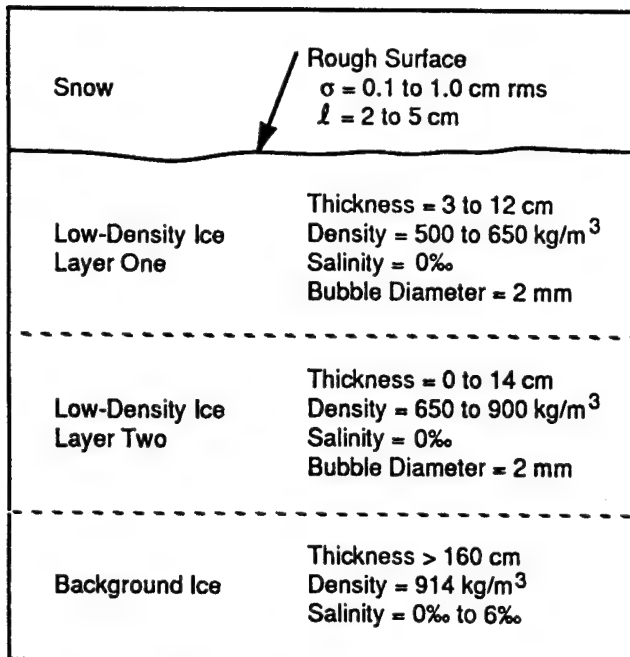


Fig. 5-5. The upper portion of multiyear ice, with a physical property description of the various layers.

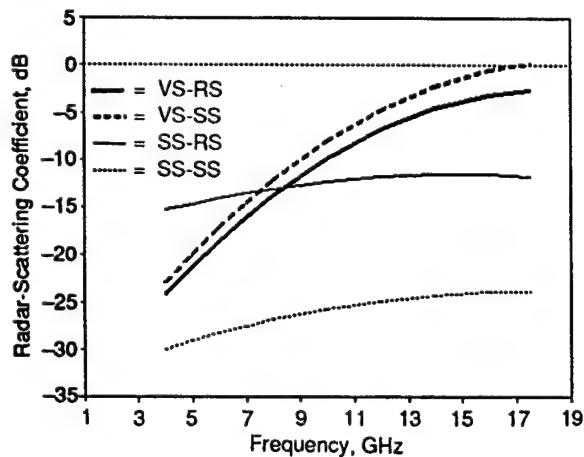


Fig. 5-6. Relative contributions of surface and volume scattering for MY ice [Kim, 1984]. The surface roughness parameters are the correlation length ℓ of 8.6 cm for both smooth and rough surfaces, and height standard deviation σ of 0.81 cm for the rough surface and 0.15 cm for the smooth surface. The ice density is 700 kg/m³, the air bubble radius is 1 mm, and the complex dielectric constant is $3.15 - j0.01$. (VS = volume scatter, RS = rough surface, and SS = smooth surface.)

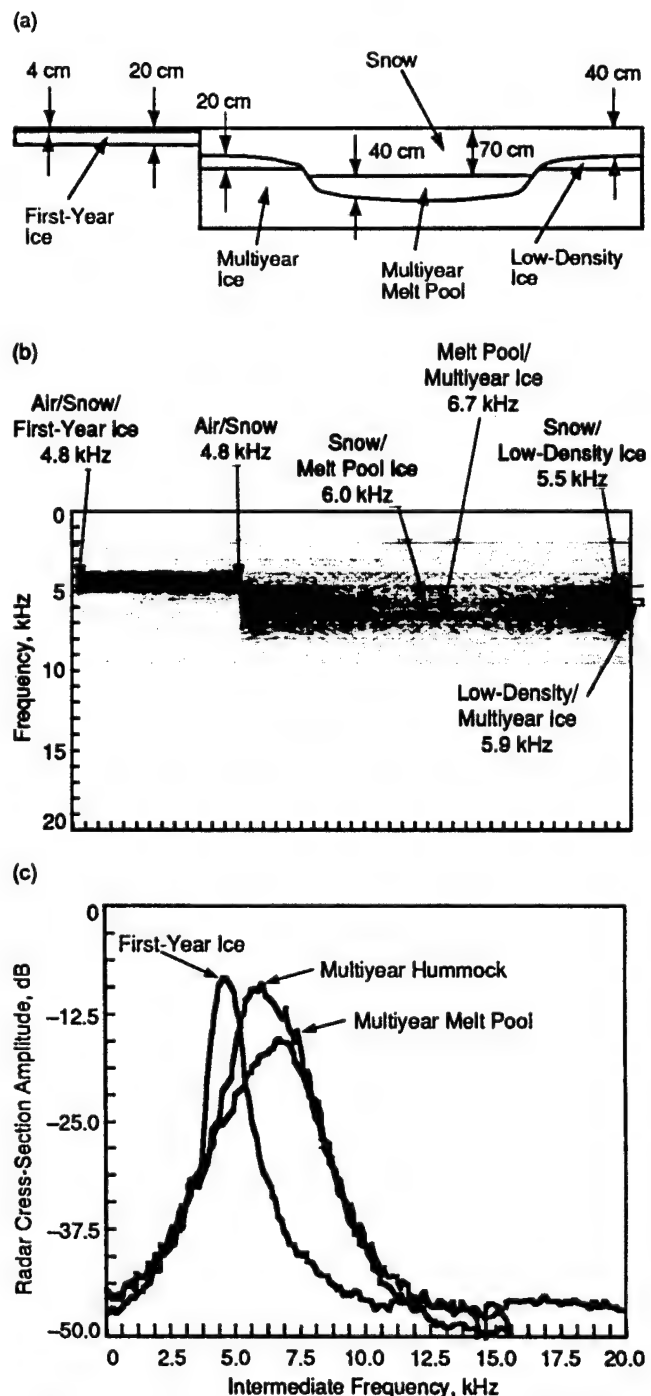


Fig. 5-7. The origin of backscatter in multiyear and first-year ice is illustrated with a probing radar scanned across a 40-m ground track. (a) The surface truth diagram is shown. (b) The backscatter response at 5.25 GHz, 45° incidence angle, and VH-polarization is shown as a function of ground position. (c) Average intensity responses for the first-year ice, hummock, and melt pool versus interior ice position are also shown. Intermediate frequency is proportional to the range at approximately 1750 KHz/m of ice.

multiyear ice. For this ice sheet, there is no distinction between the physical and electrical properties of a multiyear hummock and melt pool (fresh water), except for the ice in the top 20 to 40 cm. Their backscatter characteristics are quite distinct, however, and provide insight into the underlying electromagnetic processes.

These data serve to demonstrate empirically and visually that the physical-property differences in the uppermost portion of a multiyear ice sheet are responsible for the determination of its microwave signature (see Figure 5-7 and Table 5-2). A dense population of gas bubbles (1 to 2 mm in diameter is typical) is required to produce the strong backscatter response associated with multiyear ice. The roughness of the snow–ice interface plays a secondary role.

Melt pools typically have very smooth surfaces and produce weak backscatter. The important observation is that the population of air bubbles trapped in the melt pool ice is too small (the density is approximately that of pure ice) to produce significant backscatter. Penetration of the radar signal to the bottom of the melt pool is apparent, and the centroid of the backscatter response is associated with the pure-ice–sea-ice interface.

There are numerous air bubbles present in the upper portion of hummocked ice (their density is 825 kg/m³), and these are of a size (2 mm in diameter) that may produce an enhanced backscatter return. The backscatter of this hummock and melt pool differs in intensity by a factor of about 32. In addition, the centroid of the hummock response is associated with the center of this low-density ice layer. Also, the response from the snow cover on either the melt pool or the hummock is relatively weak.

Results suggest that the backscatter for first-year ice is limited to the region immediately around the snow–ice interface and that there is no significant penetration in a 20-cm-thick ice sheet. The range extent of this response is explained by the radiation pattern of the radar.

TABLE 5-2. Intercomparison of key physical properties of the melt pool and hummock multiyear ice features.

Parameter	Multiyear melt pool	Multiyear hummock
Ice sheet thickness	3.15 m	3.25 m
Freeboard	5 cm	15 cm
Snow thickness	25 cm	20 cm
Feature thickness	30 cm	20 cm
Feature bulk density	914 kg/m ³	825 kg/m ³
Bubble layer description	Sparse	Abundant
Bubble diameter mean	3 mm	2 mm
Bubble, number/cm ³	0.1	3.3
Salinity, ‰	0	0

5.2.4 Water and Ice Backscatter Discussion

5.2.4.1. Open water. One of the issues of critical importance, especially in navigation and determination of ice concentration, is the discrimination of ice from water. The near-vertical (0° to 10°) backscatter response of water is typically higher than that of ice, whereas the backscatter response falls off quickly as the incidence angle increases beyond 10°. Backscatter for water in the open ocean can be written in a simplified form such as

$$\sigma^*(u, \theta, f, p, \varphi) = C(f, \theta, p, \varphi) u^{\alpha(f, \theta, p, \varphi)} \quad (6)$$

where σ^* is the normalized radar-scattering coefficient, C is the wind-speed scaling constant, u is the equivalent neutral-stability wind speed measured at a 10-m height, α is the wind-speed exponent, θ is the incidence angle, f is the operating frequency, p is the transmit–receive polarization, and φ is the angle between the radar-look direction and wind direction.

The backscatter response is a function of wind speed. Factors that include fetch, air–sea temperature difference (important for determining stability), wave slope, the orientation of the radar to the wind, and wave direction are important in determining the absolute backscatter intensity [Ulaby et al., 1986]. Examples of values for the upwind/downwind case and an angle of 50° are $\approx 6.76 \times 10^{-4}$ for the scaling constant C , and 1.18, 1.53, and 1.64 for the wind exponent α for L-HH, C-VV, and X-VV, respectively [Onstott and Shuchman, 1989].

Water between floes in the marginal ice zone (MIZ) and in the ice pack presents a response dissimilar to that of the open ocean; backscatter values are typically much lower. This has not been fully explored, but is attributed to wave dampening and wind shadowing by floes. Operation at L-VV presents a special situation that has been illustrated in Seasat SAR imagery—especially in cases including large bodies of water (i.e., polynyas). The backscatter intensity is similar to that of ice. Operation at HH-polarization, however, reduces the water response by 5 to 7 dB, enough to provide an improved separation of water and thick ice. This polarization response provides an opportunity to separate new ice from open water (see Chapter 24). Operation at higher frequencies gives more ice–water contrast. This is understandable, since open-water backscatter increases less quickly with increasing frequency than does backscatter from sea ice.

The backscatter responses for water in the open ocean (with wind speeds of 6 to 8 m/s), for moderate sea conditions, and in the MIZ are illustrated in Figures 5-8 and 5-9 for a frequency of 9.6 GHz, HH-polarization, and an angle of 25° [Onstott, 1990a]. The ocean and ice (when either is at 100% concentration) share a similar response level, but water between ice floes has an intensity that is dramatically less (by 13 dB). These data were acquired by a helicopter flying a scan beginning from a position about 16 km from the ice edge in the open ocean to the ice edge, then across the

ocean-ice edge until large floes were encountered near the start of the pack ice, an additional 20 km. Illustrated in these radar data is a transition from the strong backscatter of the open ocean, to the backscatter of a region of calm water (5 km in extent) immediately adjacent to the ice edge, into that of a well-delineated and compact ice edge, into that of a region of 90% ice concentration and large multiyear floes. The weakest returns in the MIZ during summer and winter are associated with the water (or new ice) between ice floes. Ice and water are often difficult to distinguish due

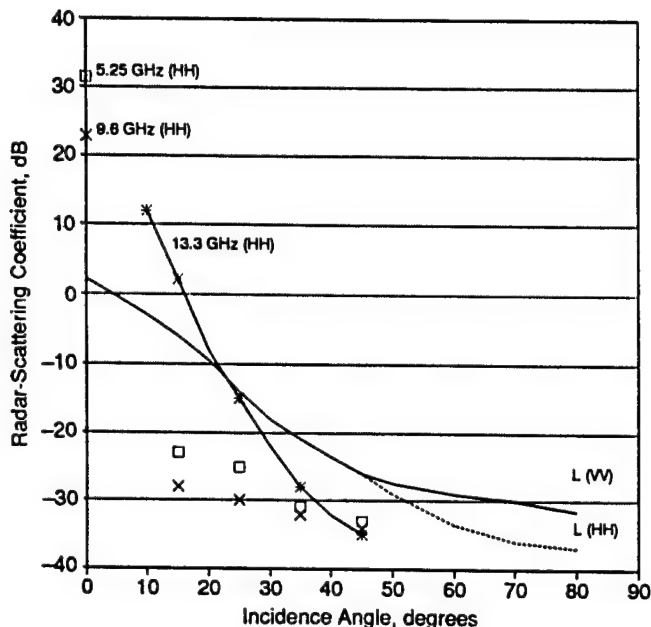


Fig. 5-8. Radar-scattering coefficient data at L-band for a medium sea [Wetzel, 1990], at 13.3 GHz (HH) for a calm ocean [Gray et al., 1982], and 5.3 GHz (HH) and 9.6 GHz (HH) for water between ice floes in the MIZ [Onstott et al., 1987].

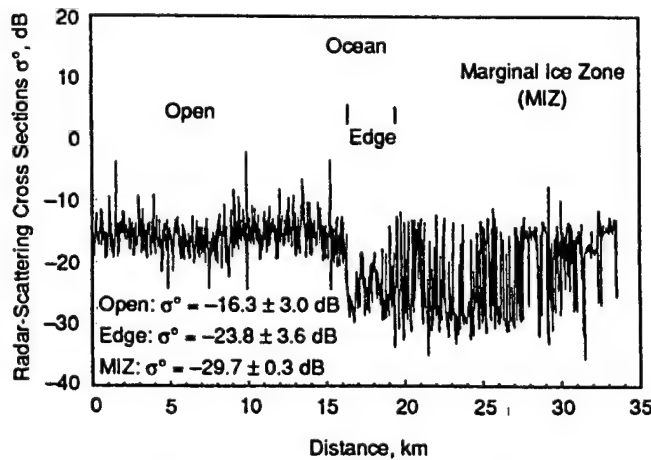


Fig. 5-9. Transect across the ice edge on July 5, 1984, at 9.6 GHz, HH-polarization, and 25° in the marginal ice zone in the Fram Strait [Onstott, 1990a].

to the system noise floor or to the setting of the operating point of the receiver in an attempt to prevent saturation by strong ice returns.

The liquid ocean produced a variety of microwave signatures that, in large part, were influenced by the position of the edge. Observed conditions likely reflect a complicated interaction between the winds, waves, and currents that is due to the effects of cold air from the pack crossing from the cold ocean near the ice edge to the warmer open ocean.

Additional ocean-signature variations were observed and attributed to the dampening of swell and gravity waves by the ice floes. In Figure 5-10, the liquid-ocean signatures are shown as a function of position from the ice edge. Signatures break into four major categories: (a) open ocean, (b) ocean prior to the ice edge and in the MIZ, which is immediately near the edge, (c) ocean in the MIZ, and (d) ocean in the MIZ and the shadows of ice floes.

Discrimination of ice and water may be problematic even at the higher frequencies at the ice edge when on-ice winds are involved. Even at X-band, the open ocean may produce a backscatter response with an intensity similar to that of

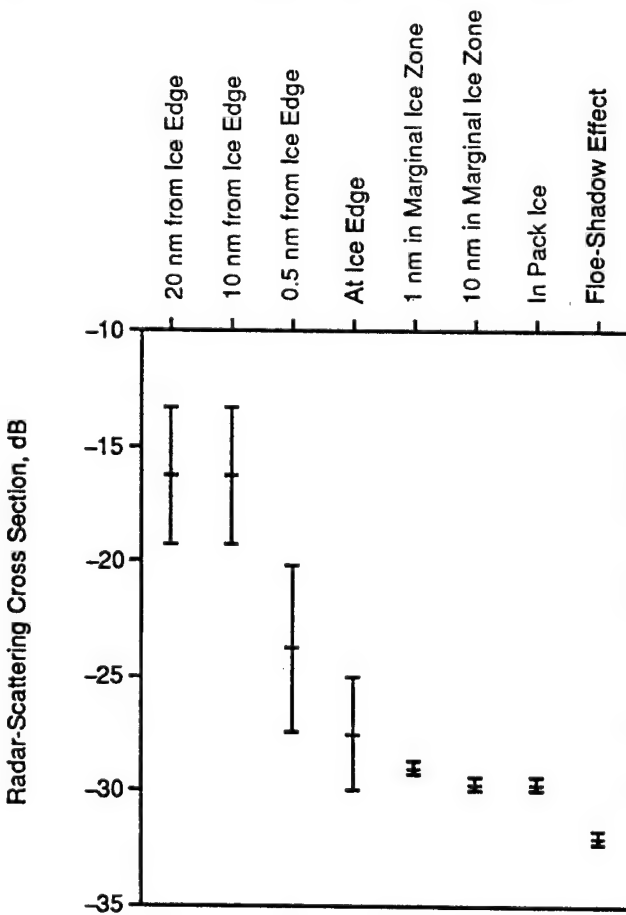


Fig. 5-10. Radar-scattering cross sections of the liquid ocean at 9.6 GHz, HH-polarization, and 25°, obtained as a function of position from the ice edge on July 5, 1984, in the marginal ice zone in the Fram Strait [Onstott, 1990a].

ice. A compacted ice edge prevents the detection of water between floes. Therefore, distinguishing the open ocean from the MIZ may require the exploitation of ice-feature shapes and differences in texture.

Examination of the polarization ratio ($\sigma^{\circ\text{VV}}/\sigma^{\circ\text{HH}}$) is instructive. Measurements show that water has a ratio greater than that of ice. Examination of the ratio of the Fresnel reflectivity coefficients (which represent power) supports this observation. This ratio is driven by the magnitudes of the dielectric constant of the material; the greater the dielectric constant, the larger the ratio at large incidence angles. Ice has a dielectric constant about an order of magnitude less than that of seawater.

5.2.4.2. New ice. The key characteristic of the backscatter from new ice is its weakness. Wind produces ripples (capillary and short gravity waves) on water. The formation of ice crystals (grease) attenuates and impedes the formation of waves. The thicker the crystal layer, the greater the attenuation. The important effect of this process is the production of a surface that is smooth to the radar. In calm conditions, the ice sheet is effectively mirror-like, with only rafting events providing relief. Surface-roughness values are on the order of 0.05-cm rms—a factor of 20 smaller than a radar wavelength at 30 GHz. In addition, it has been observed (see Chapter 9) that the dielectric constant reduces by a factor of at least 4 to 6 from that of seawater. Hence, with the dramatic reduction in both the scale of surface roughness and in dielectric constant, backscatter from new ice is expected to be considerably smaller than that for open water. It may be small enough that it is difficult to measure accurately at the middle and large incidence angles.

5.2.4.3. Nilas and gray ice. Two processes are important in determining the backscatter from nilas and gray ice. These include modification of the surface-roughness statistics and cooling of the upper ice sheet (the sheet cools with increasing ice thickness). New ice grown under calm conditions represents the limiting case of ice with a very smooth surface (except in the case of multiyear ice with melt pools). Any process, especially the formation of rime (e.g., frost flowers that act to wick up brine and then form roughness elements) on a new ice-sheet surface or the deposition of snow crystals, acts to increase surface roughness; there is no turning back! An increase in surface roughness at this stage translates into an increase in backscatter. The formation of frost flowers is the most important contributor in increasing small-scale surface roughness; hence, it is often the controlling backscatter mechanism for young ice. Intensities at microwave frequencies may reach levels almost approaching those of multiyear ice. By the time the gray-white stage is reached, snow has infiltrated and the backscatter intensity decays.

5.3 IMPORTANCE OF ENVIRONMENTAL AND PHYSICAL PROPERTIES

5.3.1 Temperature

5.3.1.1. Multiyear ice. Scattering for multiyear ice has been shown to be determined by the uppermost portion of the ice sheet. The ice there is relatively salt free and may contain large numbers of discrete scatterers. It is not anticipated that backscatter is impacted greatly by temperature variation (for the cases where $T_{\text{ice}} < -5^{\circ}\text{C}$) because penetration through the top 10 to 20 cm is the minimum required to produce a multiyear-ice-like response. The dielectric properties of salt-free ice are relatively insensitive to temperature variations. Temporal observations during September to November have just recently been made (i.e., during CEAREX) and will provide a detailed examination of the temporal response of sea ice and the changes in ice-sheet and snow properties.

5.3.1.2. First-year ice. If the backscatter for first-year ice is largely determined by scattering from the ice surface, the impact of ambient temperature is to change the reflection coefficient of the ice sheet and possibly to promote the further formation of a slush layer. We confine the discussion here to changes in dielectric constant, and radar-scattering coefficients predicted for ice 1-m thick with a 2-cm snow layer for the temperature range of -50° to -2°C are compared with in-situ observations in Figure 5-11. It is

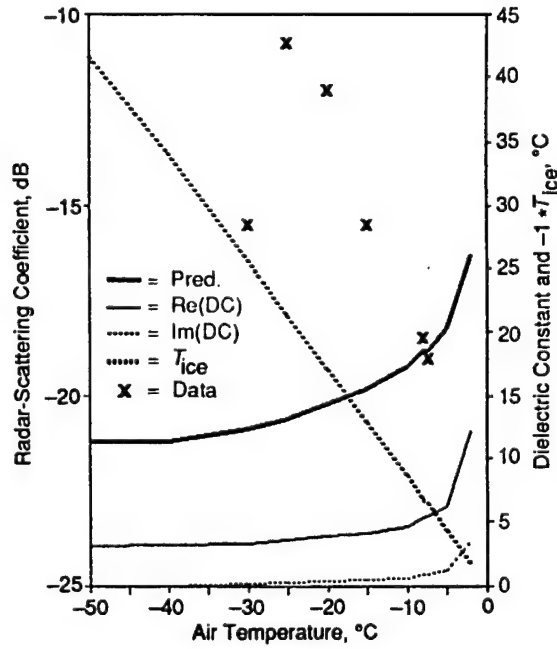


Fig. 5-11 Predicted and measured backscatter for first-year ice (1-m thickness) for air temperature from -50° to -2°C . The frequency is 9.6 GHz and the incidence angle is 40° . (Pred. = predicted, Re(DC) = real part of complex dielectric constant, IM(DC) = imaginary part of complex dielectric constant, and T_{ice} = ice surface temperature.)

shown that dielectric properties increase with rapidly increasing temperatures beginning at -10°C . Based on this knowledge, backscatter (as defined by the physical-optics model) would be expected to increase with an increasing dielectric constant. In addition, the backscatter response would be expected to change by less than 2 dB between the temperatures of -50° and -8°C . However, when compared with in-situ observations, a trend opposite to this is noted. These results suggest that the principal response to low temperature may be the freezing of the slush layer, even though there may be an increase in volume scattering because of an increased depth of penetration (i.e., 7 cm at $T = -50^{\circ}\text{C}$ and 1 cm at $T = -8^{\circ}\text{C}$).

5.3.1.3. Temperature dependence observed in airborne scatterometer data. Livingstone et al. [1983] have compiled observations made over several years and include data obtained at various temperatures. In Figure 5-12, the temperature-dependence data at $\sigma^{\circ}_{\text{HH}}$ and $\sigma^{\circ}_{\text{HV}}$ for an angle of 25° are shown. These data suggest that as temperatures decrease, the backscatter for first-year ice decreases, whereas multiyear ice backscatter increases.

5.3.2 Snow Cover

The importance of snow on sea ice is determined by season (cold or warm) and ice type. The impact of a dry and

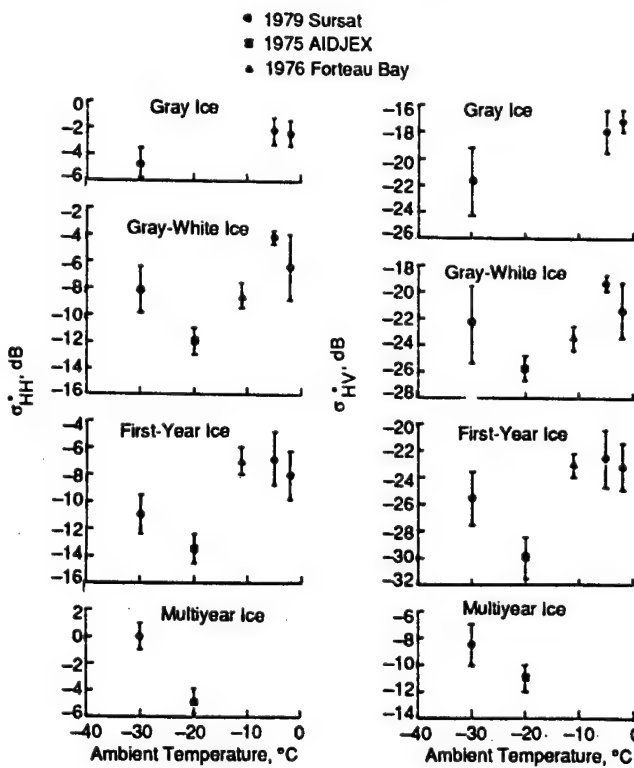


Fig. 5-12. Temperature dependence of $\sigma^{\circ}_{\text{HH}}(\theta = 25^{\circ})$ and $\sigma^{\circ}_{\text{HV}}(\theta = 25^{\circ})$ for gray, gray-white, first-year and multiyear ice [Livingstone et al., 1983].

moist snow layer on first-year and multiyear ice will be discussed.

5.3.2.1. Dry snow. Snow on ice serves as a thermal blanket, since snow has a thermal conductivity much less than that of sea ice. In addition, it may provide an impedance-matching (electromagnetic) function. The scene reflectivity is determined by the combination of the dielectric and scattering properties of the snow and the ice sheet. The snow may improve the matching between the atmosphere and the ice sheet and also reduce the effect of surface roughness. The snow may also facilitate the transfer of brine from the ice sheet and produce a collection of slush at the ice-snow interface. The impact of a developing slush layer with a high liquid content may be (a) to reduce ice sheet surface roughness (i.e., through fill-in) when the surface is rough, (b) to create a dielectrically rough surface (i.e., a vertically variable boundary between dry and saturated snow), (c) to increase the dielectric constant contrast at the ice-snow interface, or (d) to provide a transitional dielectric layer between snow and ice. The dominant mechanism has not been fully defined, but, in all cases, observations suggest that the backscatter is weak in an absolute sense.

5.3.2.2. Dry snow on multiyear ice. When compared with that of multiyear ice, the volume scattering of a thin layer of snow is small. In addition, the impact of raising the ice-surface temperature is small because the upper portion of the ice sheet is relatively brine free, hence absorption does not change greatly with increasing temperature. A calculation made to determine the impact of a 10-cm layer of dry snow with $T_{\text{air}} = -20^{\circ}\text{C}$ and $T_{\text{ice}} = -13.7^{\circ}\text{C}$ shows that the overall effect on the volume scatter coefficient of the multiyear ice is to lower σ by about 0.3 dB [Kim et al., 1984b].

5.3.2.3. Dry snow on first-year ice. Observations show that snow plays an important role in determining the backscatter response for first-year ice [Onstott et al., 1982]. Dramatic increases in ice-surface temperature, especially when the ice is thin, may cause an increase in the complex dielectric constant and the production of brine slush at the snow-ice interface. If the snow burden is too great, the ice sheet may submerge and flood with seawater. All of these actions often produce very similar backscatter intensities.

Measurable signal differences have been observed between ice that is snow covered and ice that is barren. On the average, thick first-year ice with up to 8 cm of snow cover was reported to have backscattering coefficients 1 to 5 dB higher than thick first-year ice that was snow free. The effect was small at L-band (about 0.5 dB), and variable at frequencies from 9 to 17 GHz (a high of about 5 dB and a low of about 1 dB). Results from an examination of snow on smooth first-year ice are presented in Figure 5-13 for frequencies from 1.5 to 17 GHz. The data presented here represent an average derived from backscatter at 20° to 60° . It is interesting to note that the response for frequencies

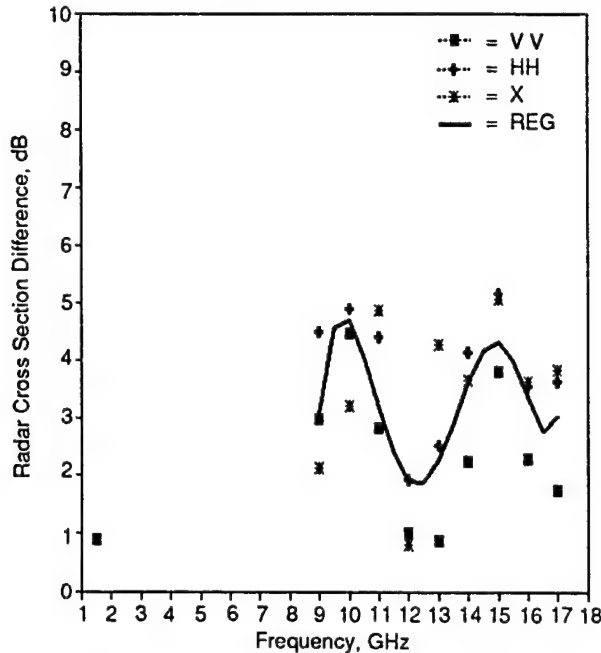


Fig. 5-13. The difference in radar-scattering coefficients for the case of thick first-year ice with and without an 8-cm snow layer. These data represent the average backscatter difference for angles between 20° and 60°. (X = cross-polarization.)

from 9 to 17 GHz is apparently oscillatory about a mean of 3 dB. This suggests that an interference process is responsible. Such a process can occur when a thin dielectric separates two semi-infinite dielectric media (e.g., air and ice). The amplitude of the response also appears to be polarization dependent. This result is of interest because it suggests that coherent radar responses may be observed in nature and are not necessarily dominated by physical-property variation (i.e., thickness of layers) and radar signal scintillation (i.e., fading). Other radar observations of this type have probably been all but ignored based on the above two premises. Coherence effects have been observed in the passive microwave observation of snow on terrain [J. Kong, personal communication, 1989]. The effect of snow on sea ice is shown as a function of snow depth in Figure 5-14 at 8.6 and 17.6 GHz for an angle of 50° [Kim et al., 1984b]. The backscatter predicted for a semi-infinite half space of snow, for both a snow layer on a smooth surface and snow on a rough surface, is also presented. These predictions, based on empirical measurements and a zero-order model, indicate that snow on ice with a smooth surface is an important contributor to backscatter (and is increasingly important with increasing frequency), whereas snow on a rough surface may contribute little, except at high frequencies. These predictions do not take into account potential interference effects, which may explain the close agreement between measurements and prediction seen in the case at 8.6 GHz and the much poorer agreement at 17.6 GHz. Figure 5-13 shows that the data at 8.6 and 17.6 GHz appear to represent data near a peak and a null.

5.3.2.4. Moist snow. During summer, snow is undergoing melt; water may be percolating through the snow and collecting into subsurface melt pools that are in transition and becoming surface melt pools. For the first half of the summer, the most important sea ice characteristic is the presence of a moist snowpack. Measurements of drained snow indicate that the bulk wetness of the snowpack is from 5% to 6% by volume during peak melt and that the majority of the snowpack is old and has a density of 400 to 500 kg/m³ [Onstott et al., 1987]. The electrical properties of dry and wet snow are very different; the electrical properties of dry snow are nearly independent of frequency, whereas moist snow has properties that are very much a function of frequency. The penetration depths calculated for the peak melt conditions described above are about 4.5, 1.8, 1.5, and 1.3 cm for 5.25, 9.6, 13.6, and 16.6 GHz, respectively. Up to midsummer, the snowpack on multiyear ice may be at least 40 cm (i.e., there are many penetration depths between the air-snow and the snow-ice interfaces). It is very important to note that at the higher microwave frequencies, such as 13.6 GHz, only 1 to 3 cm of snow are required before the snow layer completely dominates the backscatter response, because for each penetration depth the incident signal experiences a 9-dB round-trip loss. It has been documented [Onstott et al., 1987] that operation at the longer wavelengths (e.g., 6 cm) allows ice type discrimination during the first two weeks of summer (i.e., to June 20) and that during peak melt (a period often centered around July 7), longer wavelengths (e.g., 24 cm) allow some ice type discrimination due to the ability to penetrate the snow cover and sense the evolving layer of superimposed ice at the snow-ice interface of the thinner first-year ice. In Figures 5-14(c) and (d), the expected behavior for moist snow is presented for small moisture values characteristic of snow in early summer.

5.3.3 Surface Roughness

The small-scale roughness of the air-ice or ice-snow interface is important in the determination of the backscatter intensity for both first-year and multiyear ice, as is shown in Figure 5-6. Since roughness is often the primary backscatter mechanism for first-year ice, except, possibly, at very cold temperatures and when the ice is thick, the first-year ice response to roughness changes is the most dramatic of the two major ice categories. Given that first-year ice may have very smooth to very rough surfaces, the range of backscatter responses may be large and variations of 10 to 15 dB may be observed. In Figure 5-15, the angular responses for smooth first-year ice (thickness of 1.37 m), thick first-year (TFY) ice of pancake-ice origin (pans of 2 to 3 m with 4-cm-high rims, and an ice thickness of 1.65 m), and pancake ice (1- to 2-m pans and a thickness of about 10 to 15 cm) are illustrated. The response shown for the TFY ice cases is typical. As roughness increases, the near-vertical response decreases and the middle- and large-angle backscatter increases. The pancake ice example is shown because it represents a case where the roughness and

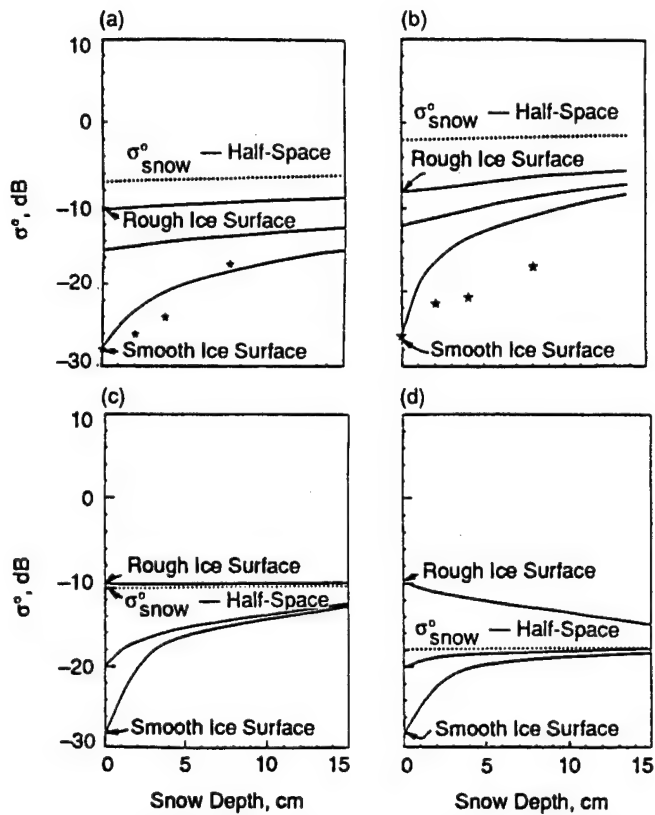


Fig. 5-14. The effect of a dry snow cover on sea ice is shown as a function of snow depth at (a) 8.6 GHz, and (b) 17.6 GHz for an angle of 50°. The solid lines are predicted σ^0 for snow cover and can be very low (smooth ice) or close to that of a half space of dry snow (rough ice). The effect of wet snow on sea ice is shown for a liquid water content of (c) 1% and (d) 3% for 8.6 GHz for an angle of 50° [Kim, 1984; Kim et al., 1984a].

dielectric constant are great and produce responses with intensities that may be confused with the responses and intensities produced by multiyear ice. A further examination of the importance of surface roughness for first-year ice is provided in the discussion of laboratory measurements (see Chapter 9).

Additionally, in-situ observations by Onstott [1991] show that multiyear ice with a smooth snow-ice interface produces up to 4 dB greater backscatter than multiyear ice with a rough interface, which confirms theoretical predictions [Kim et al., 1984a] shown in Figure 5-6. It is also observed that a relatively smooth interface is typical. The importance of surface roughness is further examined in the sections discussing the properties of the low-density ice layer of multiyear ice (Sections 5.3.6 and 5.3.7). Measured roughness statistics are compiled in Table 5-3 to illustrate the variation in roughness observed for sea ice grown in the laboratory and for in-situ observations.

5.3.4 Dielectric Constant and Salinity

The dielectric constant of ice in the upper portion of the ice sheet is known to be one of the key parameters that set the

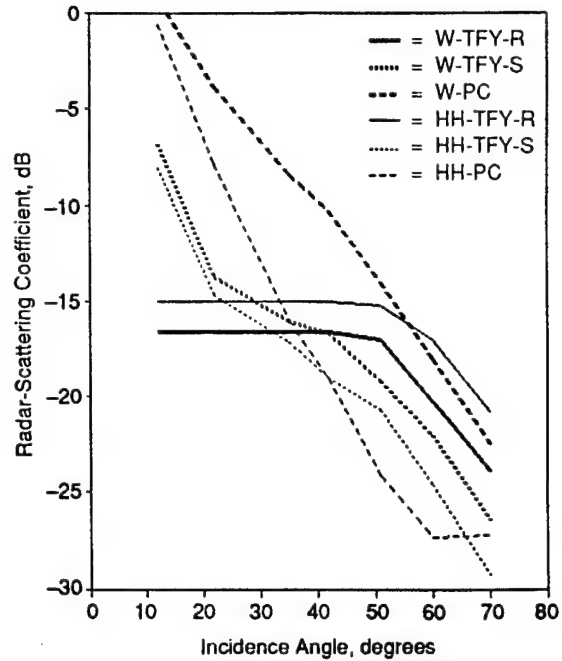


Fig. 5-15. The radar backscatter response is shown as a function of angle for smooth first-year ice of pancake origin (pans of 2- to 3-m diameters, 4-cm-high rims, and a thickness of 1.65 m), and of pancake ice (1- to 2-m pans and a thickness of 10 to 15 cm). These observations were made at 9.6 GHz. (W = water, R = rough, S = smooth, and PC = pancake ice.)

absolute backscatter level. Observations suggest that once first-year ice attains an ice thickness greater than about 10 cm during cold conditions, the differences between the dielectric properties of first-year and multiyear ice become of secondary importance, since the ice types become more similar than different. It is also observed that surface roughness and the presence of a large number of discrete scatterers (of sizes within an order of magnitude of the radar wavelength in the medium) near the ice-snow interface begin to dominate and account for the differences in backscatter level. Additional discussions of the importance of the dielectric constant are found throughout this chapter and in the discussion of laboratory measurements (see Chapter 9).

Differences in dielectric constant may be exploited through the examination of the polarization ratio $P_{vv} = \sigma^0_{vv}/\sigma^0_{HH}$. This ratio is expected to have a value of 1 (0 dB) at an incidence angle of 0° and to increase with increasing incidence angle. In addition, the larger the dielectric constant, the larger the possible polarization ratio for observations of calm open water, new ice (5.5 cm), thin first-year ice (24 and 42 cm), and multiyear ice during winter. (See Figure 5-16.) These data were obtained during March for CEAREX'89. The average rms deviation for these data is 0.7 dB. The complex dielectric constant is related to the salinity. The greater the salinity, the greater the dielectric constant. In a less rigorous sense, the polarization ratio is shown to respond to salinity—the largest ratio being associated with the entity

TABLE 5-3. Measured surface-roughness statistics.

Summer/ Winter	Thickness, cm	Ice type	RMS roughness, cm	Correlation length, cm	Lab or field	Sample length, cm	Comments
W	0.3	C-FY	0.065	—	L	—	Estimated from backscatter response
W	0.8	F-FY	0.032±0.002	0.740±0.391	L	60	
W	1.0	F-FY	0.038±0.008	1.000±0.410	L	180	
W	1.5	C-FY	0.020±0.002	0.490±0.159	L	44	
W	2.6	F-FY	0.033±0.019	1.717±0.771	L	125	After 7-cm snowfall
W	3.0	C-FY	0.069±0.006	0.454±0.030	L	66	
W	5.0	C-FY	0.038±0.010	2.69±2.180	L	68	
W	5.2	F-FY	0.031±0.012	1.261±0.807	L	120	
W	6.5	C-FY	0.048±0.001	0.745±0.109	L	44	
W	7.1	F-FY	0.077±0.0245	1.527±0.692	L	100	
W	7.5	C-FY	0.096	1.1112	L	30	
W	9.0	C-FY	0.233±0.032	1.742±0.466	L	75	
W	10.0	C-FY	0.119±0.018	1.447±1.235	L	50	
W	12.0	C-FY	0.059±0.001	1.70±0.580	L	40	
W	15.0	C-FY	0.026±0.000	0.694±0.259	L	34	
W	20.0	C-FY	0.340±0.031	3.652±0.922	L	40	Desalinated first-year ice
W	150	C-FY	0.053	1.736	F	58	Formed under calm conditions
S	200+	C-FY-R	0.766	7.75	F	1000	Early summer (6/13): still cold
S	200+	C-FY-S	0.108	0.538	F	150	Early summer (6/13): still cold
S	200+	C-FY-R	0.493	2.778	F	400	Summer (6/20): showing superimposed ice
W	200+	Typical SY-HM	0.277±0.120	5.651±3.88	F	85	Formation site same as on 6/13: smooth
W	200+	SY-HM-WD	0.262±0.204	6.015±5.44	F	111	
W	200+	SY-MP-S	0.075±0.159	2.402±0.728	F	102	
W	200+	Cusped SY-MP	0.209±0.090	3.479±3.2	F	150	
W	200+	MY-HM-S	0.185±0.035	2.75±1.05	F	60	
W	200+	MY-HM-R	0.890±0.170	3.90±6.20	F	60	
W	200+	MY-MP-S	0.080±0.030	2.8±1.9	F	60	

C = congelation ice

HM = hummock

R = rough

F = frazil ice

MP = melt pool

S = smooth

WD = well-developed

with the highest salinity (i.e., seawater), and the smallest ratio being associated with the entity with the lowest salinity (i.e., the pure uppermost portion of multiyear ice). The result shown for the multiyear ice has an additional twist that is equally important. Given that the responses for VV and HH are nearly identical, the discrete scatterers in the upper ice sheet must be dominated by spherical gas bubbles (i.e., there is no polarization preference). This result is expected and is based on examining the bubble shapes by studying numerous thin sections of ice.

5.3.5 Brine Surface Layer and Brine-Enriched Slush

A brine surface layer may form through the expulsion of brine from the upper ice sheet to the surface, through the melting of the ice surface (by warming or solar heating), or through the process of dehydration. A brine-enriched slush layer will form through the wicking action of snow on an ice surface. Quantifying the contributions of each of these processes is difficult and is the subject of laboratory study. The impact of the surface layer and slush is also discussed in Chapter 9. In the case of young ice, questions arise as to the importance and the relationship of the thickness of a brine surface layer and backscatter response. First-year ice is often observed to have a surface wet with brine. In the case of either a bare or snow-covered surface, the presence of brine does not necessarily dominate the backscatter process by presenting a semi-infinite half-space with a high dielectric. Measured bulk dielectric constants are biased toward values approaching those of pure ice, rather than those of seawater.

5.3.6 Importance of Low-Density Ice Layer for Multiyear Ice Backscatter Characterization

Microwave signatures and physical properties have been acquired at a large number of multiyear sea ice stations in order to examine the physical-property variation in the

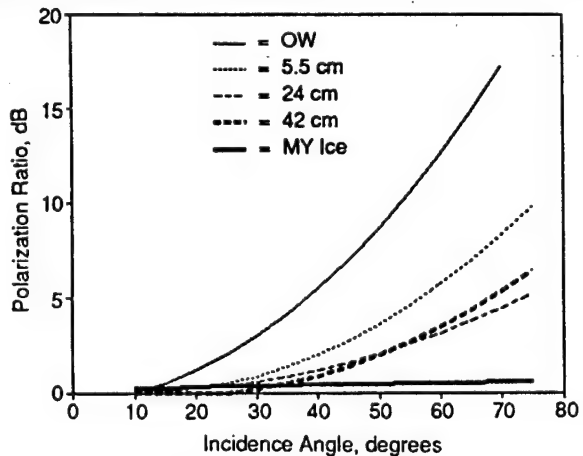


Fig. 5-16. The measured polarization ratio $P_r = \sigma_{VV}/\sigma_{HH}$ at 5.25 GHz is shown as a function of incidence angle for open water, 5.5-, 24-, and 42-cm-thick first-year ice, and multiyear ice. The average rms deviation for these data is 0.7 dB.

uppermost portion of the ice sheets [Onstott, 1991]. Variations in the thickness, density, bubble size, and roughness associated with ice of low density located in the uppermost portion of multiyear ice sheets were detected and documented. Selected examples are provided in Table 5-4 to illustrate the impact of these combinations of parameters on microwave signatures.

5.3.7 Physical and Microwave Properties of Multiyear Ice

Five multiyear ice sites have been selected for discussion. Four of these sites are from hummocks and one is from a freshwater melt pool. The low-density ice in the upper portion of the ice sheet is one of two sources that produce an enhanced backscatter. The pressure ridge, which is a topographical feature, is the second. To highlight the importance of the LDI layer, the backscatter response of three hummock areas (DS-7, DS-9, and DS-13) and a freshwater melt pool (DS-MP) that were within a 50-m radius and were resident on the same multiyear ice floe will initially be considered. Later, a fourth hummock case will be added to complete this discussion.

The critical difference between multiyear ice hummocks and melt pools is the number of discrete scatterers (i.e., gas bubbles) in the top 15 cm of the ice. In addition, the number of scatterers of a given bubble size may also be related to the density of the ice. The hummocks have densities of 457 to 517 kg/m³, while the melt pool has a density of 914 kg/m³ (i.e., the density of pure ice). As the LDI layer decreases, the number of discrete scatterers for the given bubble size increases. In the region from 30° to 60°, the difference in backscatter (>15 dB) between these two multiyear ice features is striking, and the dominant scattering mechanism becomes apparent.

The interface between snow and LDI may be smooth, moderately rough, or very rough. The rms heights range from 0.14 to 1.01 cm. Correlation lengths were very similar and range from 2.0 to 4.6 cm. It is necessary, typically, to characterize the LDI transitional layer, which is often composed of large globs and has a density that falls between the uppermost LDI layer and the pure ice below. Figure 5-5 illustrates the three ice layers and the range of the critical physical properties for the sites under discussion.

The angular responses of the backscatter for the three multiyear hummock sites discussed above are shown in Figure 5-17 for like- (VV and HH) and cross-polarizations (VH and HV). The width of the mean angular response interval for the drift station (DS) hummocks is about 5 dB for like-polarization; for cross-polarization, it is about one decibel wider. An examination of the ability to predict the ranking of these four sites according to absolute backscatter intensity has been performed. Basic rules of thumb have been derived for describing the impact on backscatter intensity for the range of physical-property parameters that were measured during the characterization of these sites. These rules have been supported through the use of a radiative transfer model of multiyear ice with a rough surface and embedded Rayleigh scatterers [Fung and Eom, 1982; Kim

TABLE 5-4. Characterization of the upper sheet of multiyear ice.

Parameter	Alpha-35	DS-7	DS-9	DS-13	DS-MP
σ , cm rms	0.33 \pm 0.2	0.14 \pm 0.02	0.7 \pm 0.12	1.01 \pm 0.31	0.08 \pm 0.03
τ , cm	4.7 \pm 0.21	2.0 \pm 1.3	4.6 \pm 1.2	3.2 \pm 1.2	2.8 \pm 1.9
LDI-1					
Thickness, cm	14	5.0 \pm 0.6	4.9 \pm 1.0	3.0 \pm 1.3	5.2 \pm 3
Salinity, ‰	0.0	0.0	0.0	0.0	0.0
Density, kg/m ³	815	457	513	513	914
Bubble diameter, mm	1.6	2.5	2.3	3.3	1.3
Void diameter, mm	0.5	8	7	5	0
LDI-2					
Thickness, cm	—	3.5 \pm 0.4	4.9 \pm 0.4	13.6 \pm 0.4	4.8 \pm 0.3
Salinity, ‰	—	0	0	0	0
Density, kg/m ³	—	728	728	929	919
Bubble diameter, mm	—	4	4.3	1	0
Void diameter, mm	—	2	0	0	0

Alpha-35, DS-7, DS-9, and DS-13 are hummock areas, DS-MP is a freshwater melt pool, and τ = correlation length.

et al., 1984a]. The results of a parametric study are summarized:

- Increasing the bubble diameter from 2 to 3 or 4 mm increases the like-polarization return by 5 and 8 dB and the cross-polarization return by 8 and 13.5 dB, respectively. Hence, the depolarization ratio ($\sigma^o_{\text{like}}/\sigma^o_{\text{cross}}$) decreases from 10 dB to 7 and 4.5 dB, respectively.
- Increasing the rms roughness from 0.125 to 0.5 causes a reduction in σ^o of 2 to 3 dB ($\theta_i = 0^\circ$ to 55°), with the decrease increasing with incidence angle. Increasing the roughness to 1.0 cm causes an additional decrease of 3 to 6 dB.
- Increasing the density from 500 to 600 or 700 kg/m³ causes a reduction in σ^o_{like} of 1 and 1.5 dB, respectively. For the same increases, σ^o_{cross} showed 2 and 3 dB reductions.
- If the thickness of the LDI layer is changed from 5 to 10 or 20 cm, then σ^o_{like} increases by 2.5 to 5.5 dB, respectively, and σ^o_{cross} increases by 5 and 10 dB, respectively.
- Varying the correlation length from 2 to 5 cm produces little effect.

The parameter set for Site DS-7 may be considered typical. Site DS-9 produced the weakest like-polarization response in the hummock set (DS-7, DS-9, and DS-13); this is largely attributed to its greater rms roughness. As is noted in the parametric study, an increase in surface roughness will cause a reduction in the like-polarization response, but little reduction in the cross-polarization response, although some reduction in the cross-polarization response occurs at the largest angles. The cross-polarization response for this site falls in the middle of the response range for these sites. Site DS-13 fits in the upper portion of both the like- and cross-polarization response ranges. Its LDI layer is unique in that the uppermost portion is relatively thin, but is of very low density (513 kg/m³), and is followed by a layer very high in density (914 kg/m³) that contains some extremely large globules (diameters of 1 cm). Its ranking is attributed to bubbles that are 30% larger than those found at Sites DS-7 and DS-9 and that contribute to large cross sections and reduced depolarization ratios.

Site Alpha-35 represents a case where the LDI thickness is large (15 cm), but of high density (815 kg/m³). Bubble diameters are 50% smaller than the typical case. Both the high density and the smaller bubbles suggest a reduced backscatter intensity. This combination results in a backscatter that is 10 dB or more weaker than those of the multiyear hummocks described earlier.

In a simplistic sense, what these five responses show is that the backscatter intensity increases with decreasing density (i.e., the increase in the volume of discrete scatterers) in the upper portion of the ice (it is assumed that all other parameters are held constant). The development of the LDI layer is observed [R. G. Onstott, field observations, 1982] to be associated with either thick snow layers or snow

drifts. During summer melt, these areas are the last to melt, or they melt more slowly. Areas of thin snow melt quickly and produce melt pools. Water is then free to drain from the drift areas into the surrounding melt pool strings, further slowing the melt process and allowing a transition to a layer with larger ice crystal diameters and lower density. It is reasonable to say that this layer is produced by a joint process that includes the metamorphosis of snow and the simultaneous erosion of the upper ice sheet.

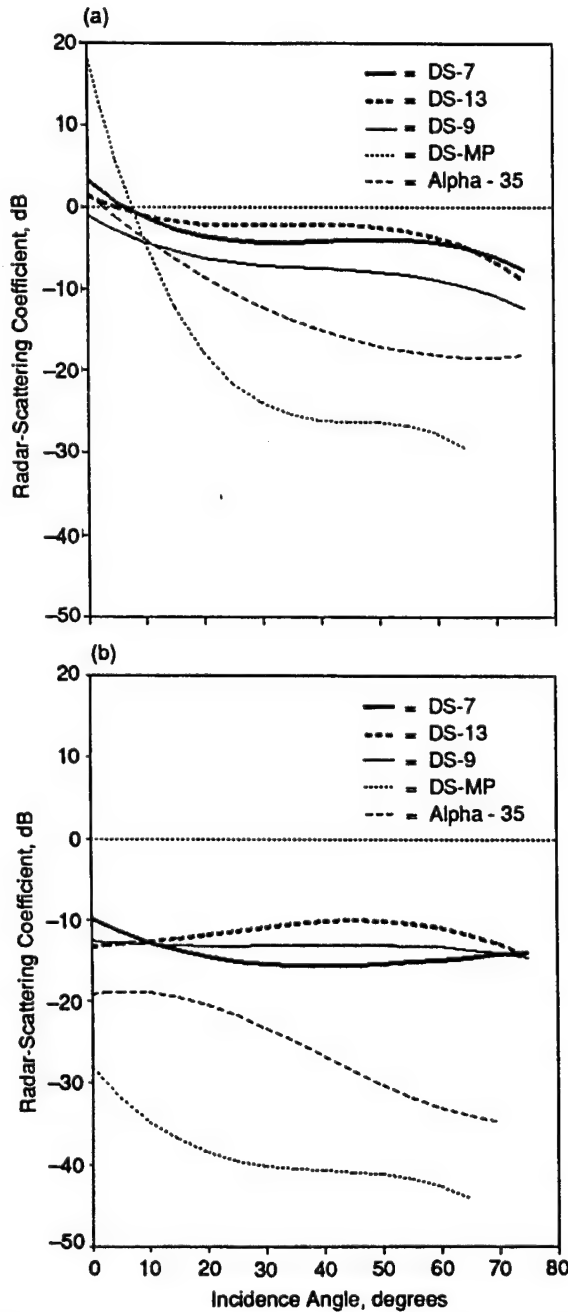


Fig. 5-17. The angular response of the scattering coefficients for four multiyear ice hummocks and a melt pool at 10 GHz and at (a) like- and (b) cross-polarizations. The responses at VV- and HH-polarizations are nearly identical, as are the VH and HV responses.

5.4 ICE TYPE BACKSCATTER SUMMARY

In this section the active microwave behavior of sea ice is discussed further in terms of its response with angle and frequency time to evolution, season, and region.

5.4.1 Angle and Frequency Behavior

During winter, the microwave signatures of multiyear ice are clearly different from those of the more highly saline first-year ice. The situation in summer is more complex: Summer is the time of melting snow and ice, of melt pool formation, and desalination. In winter, the active microwave backscatter of first-year and multiyear ice increases linearly with increasing frequency (see Figure 5-6). This is true for ice surfaces that are smooth and rough, and for ice with air bubbles in its upper layers. Multiyear and first-year ice can be distinguished independent of frequency between 5 and 35 GHz. Discriminating between ice types becomes more difficult with the introduction of moisture into the snow and the warming of the ice sheets (see Figures 5-18, 5-19, and 5-20).

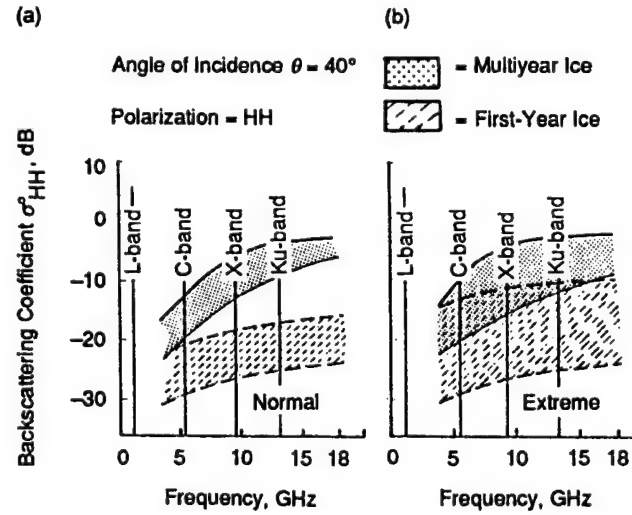


Fig. 5-18. Frequency dependence of the backscatter coefficient for first-year and multiyear ice at 40°. Theoretical σ^0 for sea ice under (a) normal-winter and (b) extreme-summer conditions.

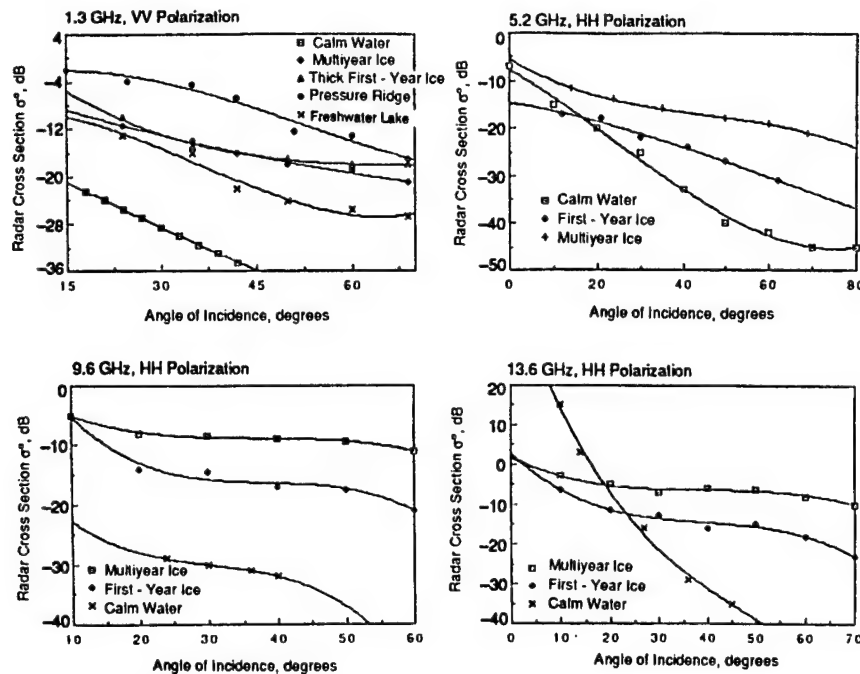


Fig. 5-19. Radar backscatter cross sections at L-, C-, X-, and Ku-bands during winter, illustrating the contrast in ice type and water signatures as a function of frequency and incidence angle.

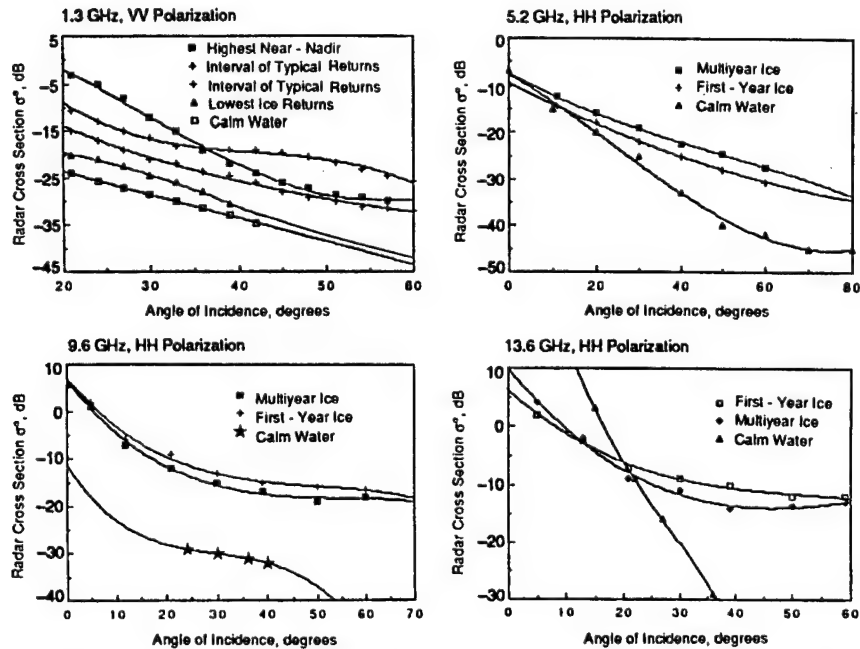


Fig. 5-20. Radar backscatter cross sections at L-, C-, X-, and Ku-bands during summer, illustrating the contrast in ice type and water signatures as a function of frequency and incidence angle.

5.4.2 Evolution of the Microwave Signature of First-Year Ice

The description of the evolution of the microwave signature of first-year ice begins with the freezing of open water and continues through the duration—up to nine months, at which time thicknesses of 200+ cm may be attained. Changes have been noted in the physical properties, the dielectric properties, and the surface-roughness statistics of an ice sheet, as well as the snow and frost flower layer. Figure 5-21 illustrates the change in the scattering coefficient as ice thickness increases from 0 to 200+ cm. Many facets of this function are of interest. The liquid ocean may take on a variety of cross-section levels due to wind and fetch conditions. New ice may produce a signature that is greater, the same, or less than that of the liquid ocean, depending on the environmental conditions at the time. In the calm conditions often encountered during lead formation, the new-ice signature may show an enhancement. As the dielectric constant of the ice sheet decreases (a function of ice aging), the backscatter intensity will reduce to a point where the lowest backscatter intensity for any ice condition (i.e., new ice that is smooth and cold) is reached. Within a few days, nilas transforms into young sea ice. When air temperatures are cold, ice crystals form as clumps (frost flowers) on the surface of the thin ice sheet. The colder the temperature, the thicker the ice becomes, and the more rapid the formation of frost flowers. As the ice sheet continues to thicken with time, the density (spatial) of frost flowers will increase, and the clumps of crystals may continue to increase in size until heights of about 3+ cm are attained. Brine from the thin ice sheet is wicked into the clumps, thereby producing a feature that has a dielectric constant similar to or higher than that of the ice sheet. These features represent roughness elements on a previously smooth dielectric plane. The temporal change in surface roughness (from smooth to very rough) appears to be linked to age and meteorological conditions (the nature of the temporal change is the topic of ongoing research) and provides the opportunity to use synthetic aperture radar (SAR) to obtain improved thickness

information for young sea ice. The greatest backscatter intensity for undisturbed first-year ice, almost that of multiyear ice, may be obtained when the frost flower layer is fully developed. However, with time and the eventual infiltration of snow and wind, the structure of the frost flowers becomes irreversibly altered. This has been observed to occur when a thickness of about 35 cm is reached [R. G. Onstott, field observations, 1987]. The snow and frost flower layer then undergoes a restructuring, which results in a steady reduction in the backscatter intensity for the ice sheet until thicknesses near 200 cm are reached.

5.4.3 Seasonal Evolution

The microwave signatures of sea ice may change dramatically with the season. With the continual monitoring of backscatter intensity levels, the determination of the physical state of ice sheets may be possible. This includes obtaining knowledge of the initiation of summer melt, the progression and intensity of summer melt, the duration of the melt cycle, the initiation of fall freeze-up, and the cooling of the ice sheets in late fall and winter (see Chapter 17). In Figures 5-22 and 5-23, a partial compilation of results from the many measurements presented in Table 5-1 is presented for both multiyear and first-year ice at 1.5, 5.25, and 9.5 GHz at an angle of 40° and at like-polarization (VV and HH are very similar in value). During late fall, winter, spring, and early summer, there is a significant separation between the scattering coefficients of multiyear and first-year ice at 5.25 and 9.5 GHz, whereas at 1.25 GHz there is little separation. For summer, however, the input of meltwater into the snowpack promotes a rapid merging of multiyear and first-year ice signatures at about June 15 [Onstott et al., 1984, 1987; Onstott and Gogineni, 1985; Livingstone et al., 1987b]. A period of indistinguishable ice signatures continues until midsummer. By midsummer, snow thickness is reduced to about half the year's high, allowing penetration of the radar signal to the snow–ice interface, which has experienced an important transformation. Percolation of free water onto an ice surface during late spring and early summer results in a superimposed ice layer, and processes associated with melt combine to enhance the small-scale surface roughness dramatically (Figure 5-24). The microwave response at midsummer marks a key backscatter trend reversal (see Figures 5-19, 5-20, and 5-25). The snow on multiyear ice is still thick and moist, and it dominates the backscatter process. In the case of first-year ice, the snow is thin and the surface is rough, producing a backscatter enhancement. Absorption losses decrease with increasing wavelength. Operation at 1.5 GHz was found to be optimal for discriminating between thin and thick ice types at this time. After midsummer, multiple contrast reversals may be observed. These are associated with melt and drain cycles. In a melt cycle, free water pools abundantly on an ice sheet. In a drain cycle, the ice sheet becomes less wet. By the end of summer, backscatter from multiyear ice once again becomes greater than that of first-year ice. However, this achievement is not associated with

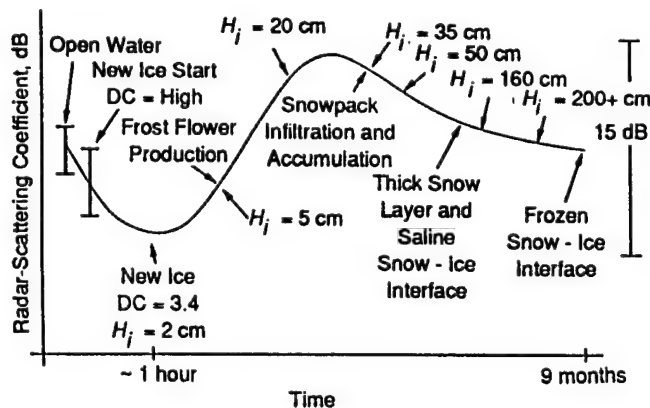


Fig. 5-21. The evolution of the microwave signature of first-year ice. (DC = dielectric constant and H_i = ice thickness.)

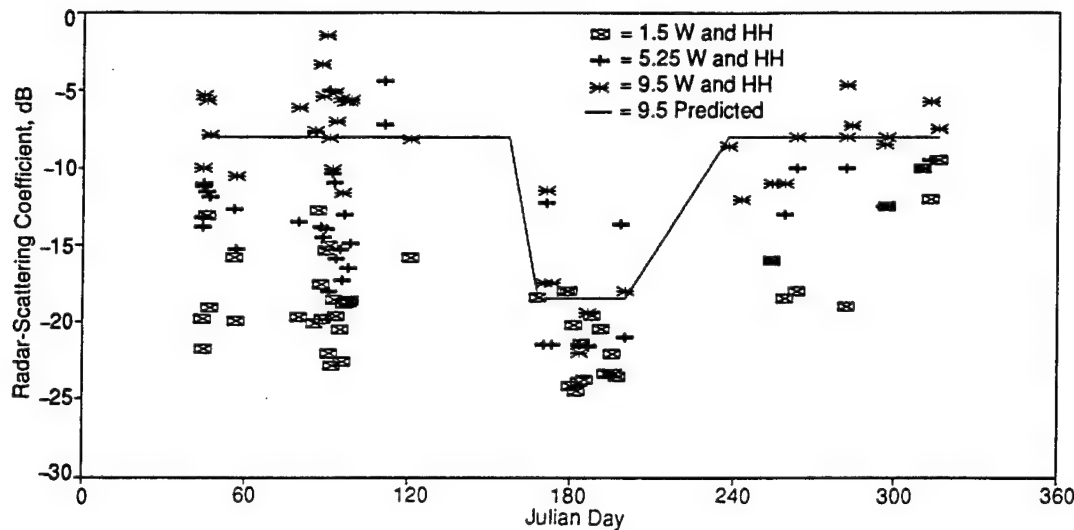


Fig. 5-22. Seasonal backscatter response for multiyear sea ice at 1.5, 5.25, and 9.5 GHz, an angle of 40° , and like-polarization (VV or HH). (W = water.)

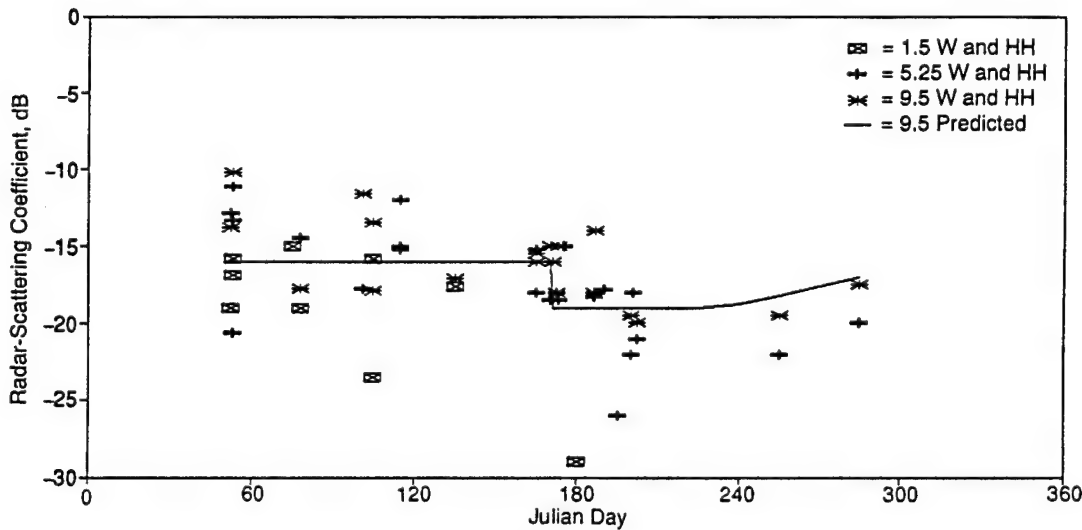


Fig. 5-23. Seasonal backscatter response for first-year sea ice at 1.5, 5.25, and 9.5 GHz, an angle of 40° , and like-polarization (VV or HH).

the return of volume scatter, as is the case in winter. On the small scale, the erosion effect of melt works to smooth exposed ice surfaces. First-year ice has large-scale surface undulations that are smaller in scale than the well-developed undulating topography of multiyear ice. A scene composed of many large-amplitude and rolling surfaces and edges has the potential to produce greater backscatter than a smoother scene. The transformations in the physical scene are illustrated in cross-sectional views provided in Figure 5-3.

Observations of the process of freeze-up during the fall show that by October, the signatures of first-year and multiyear ice are similar to those found during winter [Kim,

1984; Kim et al., 1984a; Onstott et al., 1984; Livingstone et al., 1987a; Onstott, 1990b, 1991]. However, the signature of young ice is greatly impacted. The lack of the severe cold temperatures characteristic of winter causes the congelation process to be disturbed and delayed and to become influenced by the accumulation of snow. This results in an ice sheet without a distinct snow-ice interface [Gow et al., 1990].

5.4.4 Regional Variation

Formation conditions impact the backscatter response of sea ice. For instance, first-year ice grown under calm conditions has a very smooth ice surface, whereas first-year

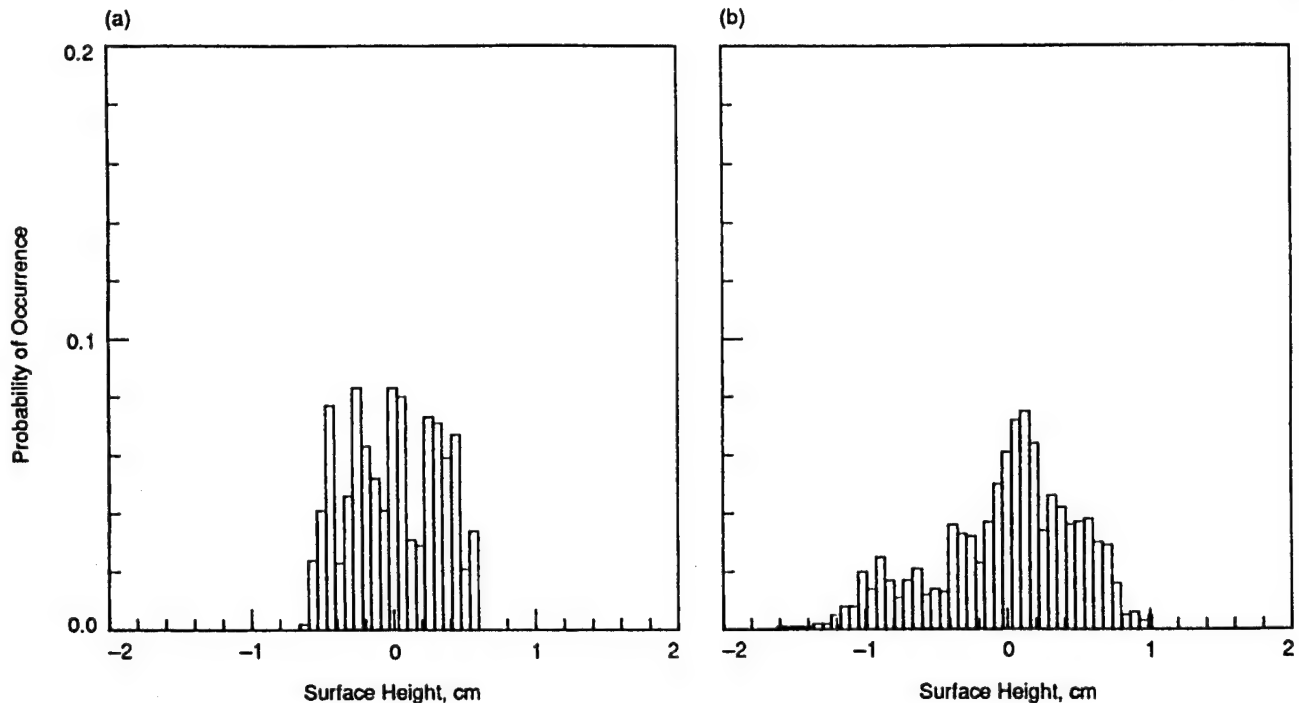


Fig. 5-24. First-year surface height histograms for a homogeneous ice sheet. (a) Data acquired June 14 are typical of early summer pre-melt, late fall, winter, and spring conditions. Height range, variance, and skewness were 0.932 cm, 0.044 cm^2 , and 0.0003, respectively. (b) Data acquired June 20 are typical of early summer melt conditions. Superimposed ice increases the height range to 2.778, the variation to 0.243, and skewness to -0.588 [Onstott and Gogineni, 1985].

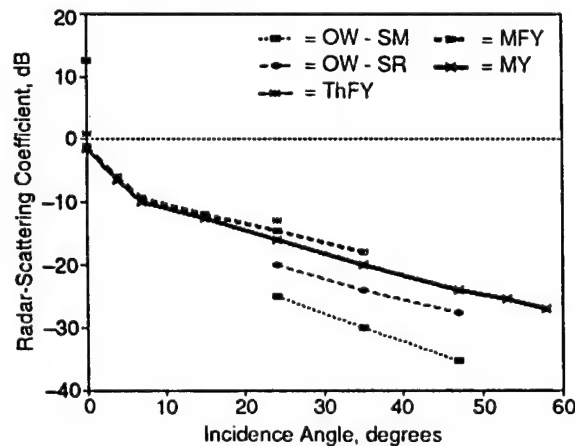


Fig. 5-25. The angular response at 5.25 GHz and HH-polarization for midsummer shown for open water, thin first-year (ThFY), medium first-year (MFY), and multiyear ice. The letters OW-SR indicate open water that is slightly rough, whereas OW-SM indicates open water that is smooth.

ice that began as pancake ice has a very rough surface. Their two backscatter responses are correspondingly different. In general, it is not well understood how or if the physical properties of a given ice type vary from region to region.

Passive microwave satellite data suggest that microwave property differences may be significant. Scatterometer observations have been carried out in five different geo-

graphical regions during both cold (winter-like) and warm (summer-like) conditions. In general, it is found that a given type of ice is more similar than different in the various regions. Subtle differences are not always easily detected because of the limited number of observations. Observations over many years may be required to determine if region plays a critical role. It is anticipated that temporal weather fluctuations will play a dominant role in determining ice properties and signatures, except in regions (e.g., the Bering, Labrador, and Barents Seas) that are dynamic and characterized by deformation features. Moreover, major climatic differences may be important. For instance, the ice in the Antarctic Weddell Sea has so much snow that negative freeboards are common, and these affect radar backscatter.

5.5 SAR OBSERVATIONS

A large number of sea ice observations made by imaging radars were interpreted to determine the radars' ability to obtain geophysical information. It should be noted, precisely as was stressed by Moore [Ulaby et al., 1982], that these conclusions are based on a specific radar parameter set; one that is very often limited. In addition, the ability to obtain surface truth of these sensors is logically difficult. This was especially true from 1956 to 1975. Much of the work to that point was qualitative and mainly supported by correlation with aerial photography.

The value of radar was noted, however. It was shown to be a significant tool and had an especially important prop-

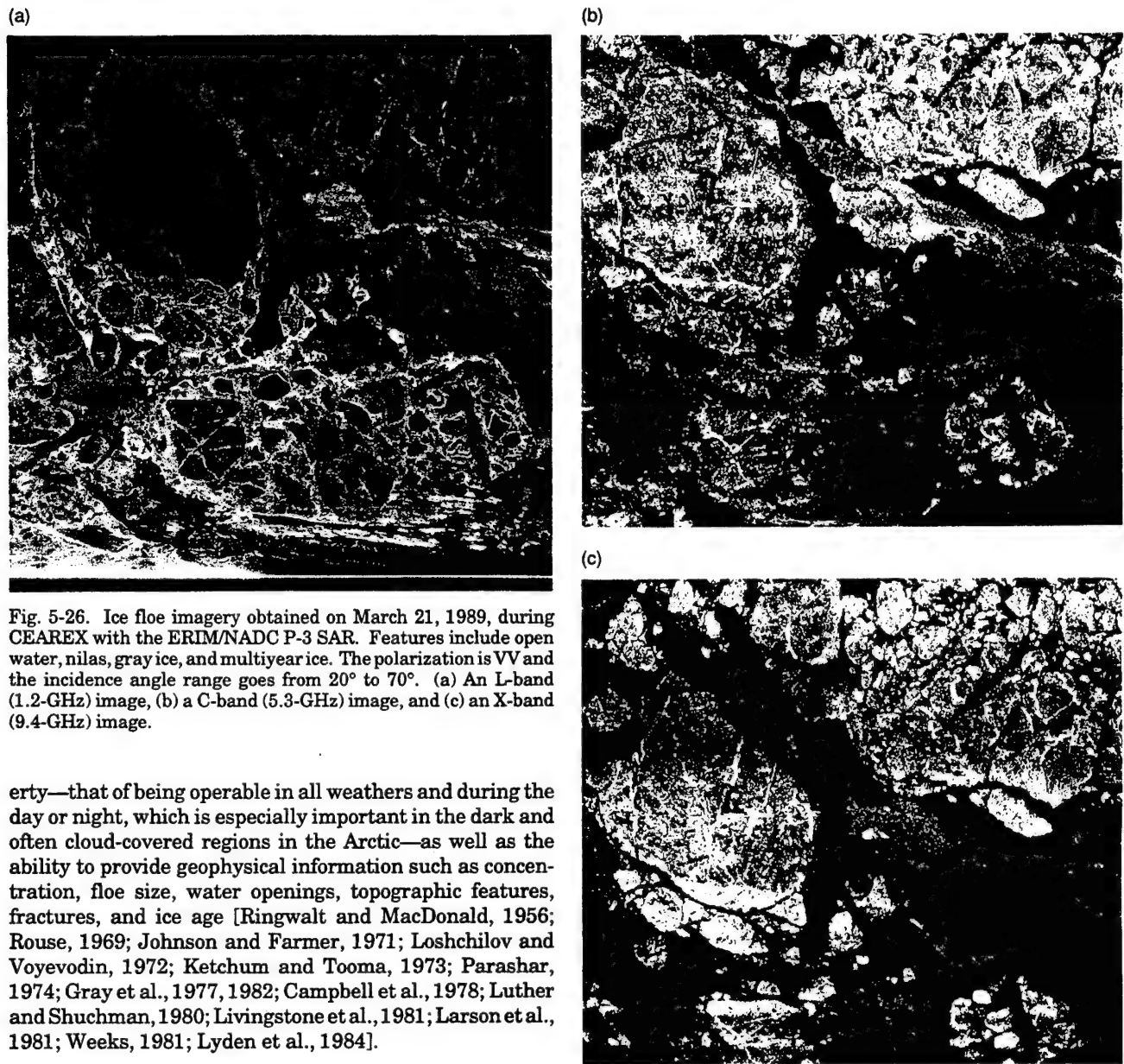


Fig. 5-26. Ice floe imagery obtained on March 21, 1989, during CEAREX with the ERIM/NADC P-3 SAR. Features include open water, nilas, gray ice, and multiyear ice. The polarization is VV and the incidence angle range goes from 20° to 70°. (a) An L-band (1.2-GHz) image, (b) a C-band (5.3-GHz) image, and (c) an X-band (9.4-GHz) image.

erty—that of being operable in all weathers and during the day or night, which is especially important in the dark and often cloud-covered regions in the Arctic—as well as the ability to provide geophysical information such as concentration, floe size, water openings, topographic features, fractures, and ice age [Ringwall and MacDonald, 1956; Rouse, 1969; Johnson and Farmer, 1971; Loshchilov and Voyevodin, 1972; Ketchum and Tooma, 1973; Parashar, 1974; Gray et al., 1977, 1982; Campbell et al., 1978; Luther and Shuchman, 1980; Livingstone et al., 1981; Larson et al., 1981; Weeks, 1981; Lyden et al., 1984].

5.5.1 Examples of SAR Imagery

5.5.1.1. Sea ice during winter. A three-frequency (L-, C-, and X-band) image set is provided in Figure 5-26. These data were obtained in the Fram Strait during March when air temperatures were about -20°C . The instrument used was the Environmental Research Institute of Michigan/Naval Air Development Center (ERIM/NADC) P-3 SAR, which has a resolution of about 1.8 m; incidence angles ranged from 20° to 70°, and the area coverage of an image was about 10 km.

5.5.1.2. L-band. Beginning with the L-band image, the features that stand out most strikingly are those associated with large-scale topographic features, which include pres-

sure ridges, ridge lines, fractures, and rubble. Other features include the open-water region (wind speed was about 5 m/s), the dark return from nilas, the bright return from some of the gray-ice areas, and the featureless return from homogeneous multiyear ice. The utility of an L-band radar [Onstott et al., 1991] to aid in the discrimination of open water, new ice, and nilas may be limited by the sensitivity of the radar ($\sigma^0_{\min} = -35$ dB), not the ice physics. Precise determination of the open water areas may require study or the utilization of HH-polarization data (water return areas are weaker than ice return areas by 5 to 7 dB). Determination of floe boundaries is often less precise at L-band than at other frequencies. The linear features seen in the 4-km

multiyear floe are pressure ridges. Pressure ridges are composed of blocks of ice with tilted surfaces, and they may produce strong backscatter due to scattering from individual facets, multiple-facet scattering, and, in some cases, enhanced volume scattering due to a transition into a very low-density ice form [Gogineni, 1984; Livingstone et al., 1983].

5.5.1.3. C-band. Most striking in this image is the fact that floe boundaries are more defined and the old ice now has a much stronger backscatter than is the case at the lower frequency. This illustrates the important role volume scattering plays in the backscatter from sea ice. The areas that produce weak backscatter are either first-year ice or open water. The region of gray ice that runs diagonal in the image produces a moderate backscatter that is reasonably homogeneous and shows few ridge lines. It may be difficult to see from this image, but the open water provides the weakest backscatter and the nilas produces a slightly greater backscatter. Based on this image, it may be inferred that the calculation of the multiyear fraction may be obtained accurately.

5.5.1.4. X-band. Probably the most striking characteristic of this image is the similarity to C-band. It takes careful study to detect differences. It is not known what role the presentation (i.e., the normalization used in the preparation of the image) has played here, but scatterometer measurements have shown that backscatter at C- and X-band are more similar than different, with X-band showing a few decibels more dynamic range between ice types, but also a few decibels more variance.

5.5.1.5. Nilas and young ice. An image (Figure 5-27) obtained on March 20, 1989, during CEAREX at C-band (5.3 GHz) shows features that include open water, nilas, multiyear ice, and gray ice. The majority of the image is composed of gray ice of various ages and thicknesses that has the distinction of appearing like panes of broken glass. The brighter the image intensity, the thicker the gray ice in this case. The polarization is VV, and the incidence angle range goes from 20° to 70°. A vast floe located in the lower right-hand corner of the image moved at a drift rate different from that of the surrounding ice. Thin ice of various ages is found near the leeward side of this floe. The floes with linear boundaries and of similar sizes making up much of the center portion of this image are composed of young ice with thickness in the range of 5 to 50 cm. Their backscatter intensity is related directly to the development of frost flower formations and the infiltration of snow. The results of the CEAREX study will aid in determining if a continuum of ice thickness values may be retrieved. At present, only four major ice-type categories (open water, thin ice, first-year ice, and multiyear ice) are expected to be discriminated using satellite data [Kwok et al., 1991].

An image (Figure 5-28) obtained during a study of the fall freeze-up also shows that the contrast between the various ice types is very similar during winter and fall. As deter-



Fig. 5-27. Ice floe imagery obtained on March 20, 1989, during CEAREX with the ERIM/NADC P-3 C-band (5.3-GHz) SAR. Features include open water, nilas, gray ice, and multiyear ice. The majority of the image is composed of gray ice of various ages and thicknesses. The brighter the image intensity, the thicker the ice sheet. The polarization is VV, and the incidence angle range goes from 20° to 70°.

mined during CEAREX, the important forcing condition is a few days of cold weather. As noted above, during fall, nilas and young ice may present various backscatter intensities.

5.5.1.6. Sea ice during summer. With the input of free water into the snowpack during summer, microwave signatures may become progressively less variable. In Figure 5-29, three images (taken as part of MIZEX'84 on June 29) are presented to illustrate the character of sea ice at peak melt. The composition of the large multiyear floe includes an area where the snow was homogeneous (and thick) with no signs of surface pooling, areas with subsurface pooling of free water, and areas of first-year ice. The variability that is present is due to different degrees of surface wetness and different amounts of snow cover. By early summer to midsummer, the snowpack had experienced considerable melt, and depressions in the ice or snow with a low freeboard had collected varying quantities of meltwater. Fully open melt pools appear as "no return" areas, not dissimilar to the response of open water between floes, at both 1.2 and 9.4 GHz. In areas of melt pool formation and in areas where snow is being transformed into mixtures of snow, ice, and water, strong returns appear. For areas of thick and drained snow, weak returns appear at both frequencies, and the ice surface topography is well masked. As the frequency decreases, the contrast between areas with heavy and thin snow cover increases. In areas where melting has

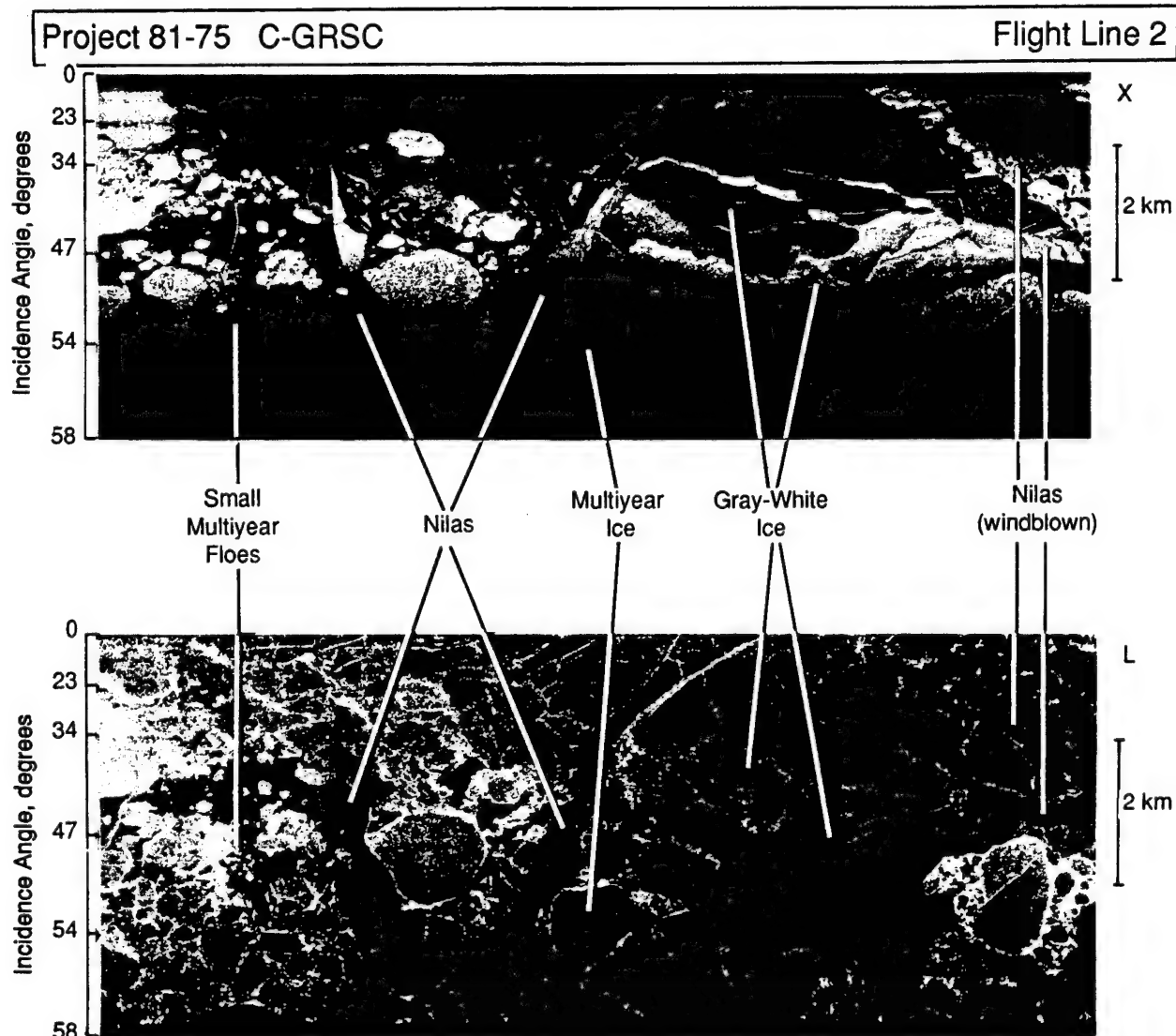


Fig. 5-28. Ice floe imagery obtained on November 1, 1981, during the Beaufort Sea Project at X-band (9.4 GHz) and L-band (1.2 GHz). Features include nilas, gray-white ice, and multiyear ice. The incidence angle range goes from 0° to 58°.

produced both a thin snow cover and enhanced small-scale surface roughness (on the order of 1 to 3 cm for first-year ice), strong returns are produced, especially at 1.2 GHz. Thus, later in summer, as the ice surface is exposed and surface melt ponds drain, the radar backscatter again reflects ice type differences [Onstott et al., 1987; Livingstone et al., 1987a, b; Cavalieri et al., 1990]. It was also determined that pressure ridges were very difficult to detect at mid-summer, due to the heavy snow burden. At X-band, the brightest features detected at the multiyear floe were associated with thin first-year ice. Here, the presence of a thin snow cover and superimposed ice contribute to a relatively

strong backscatter. This is also apparent in the aerial photograph from the features that are gray in color. It should be noted that floes designated as multiyear ice are actually composites of multiyear and first-year ice of various ages. The first-year ice in effect welds the multiyear fragments together. This structure is apparent from further examination of the aerial photograph. The areas on a multiyear ice floe that experience the greatest melt are the first-year ice areas.

5.5.1.7. Post-peak melt. At the point after midsummer when 50% to 60% of the snow cover has melted, open-water

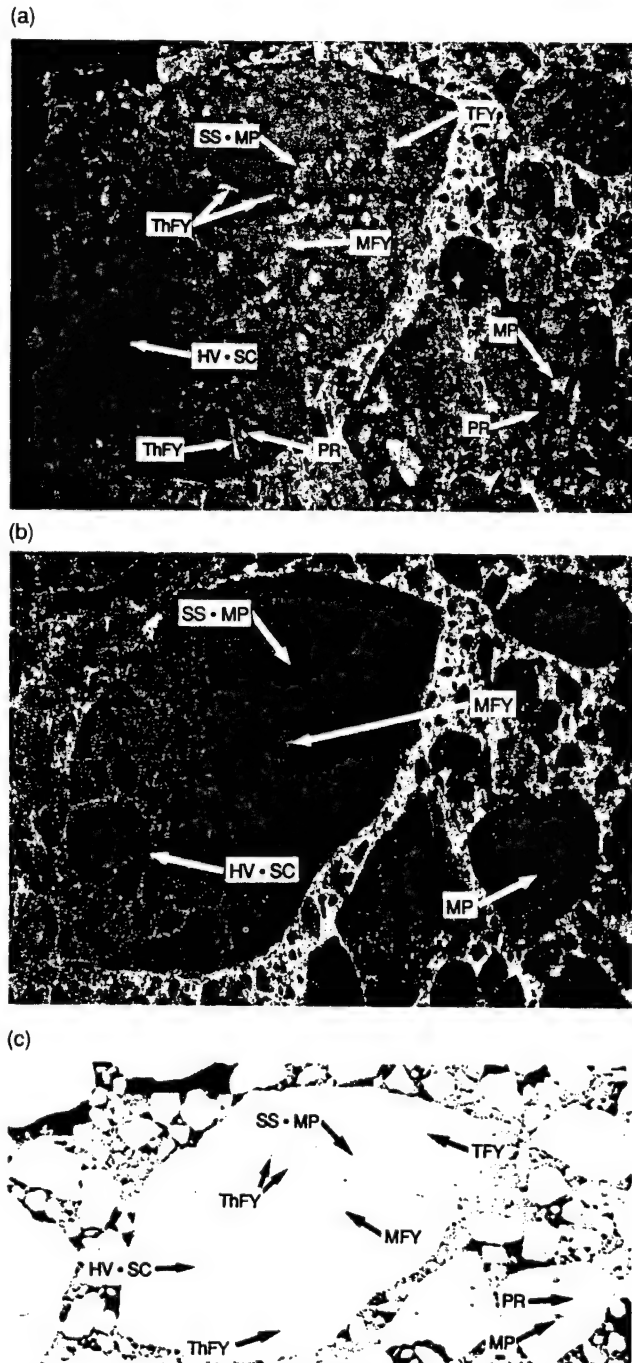


Fig. 5-29. Ice floe imagery obtained on June 29, 1984, during MIZEX'84 at (a) X-band (9.4 GHz), (b) L-band (1.2 GHz), and (c) with an aerial camera. Surface features include snow-covered ice (SC); heavily snow-covered ice (HV•SC); thick (TFY), medium (MFY), and thin first-year (ThFY) ice; pressure ridges (PR); subsurface melt ponds (SS•MP); and melt pools (MP).

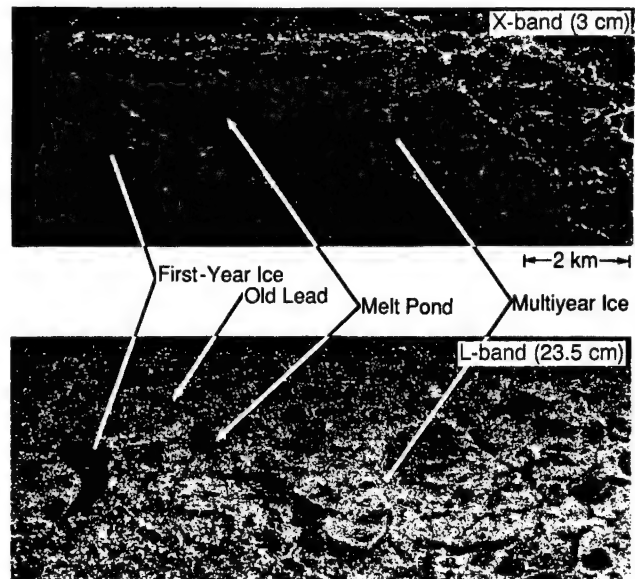


Fig. 5-30. Ice floe imagery obtained in July 1983, during MIZEX'83 at X-band (9.4 GHz) and L-band (1.2 GHz). Surface features include first-year ice, an old refrozen lead, a melt pond, and multiyear ice.

melt pools become common on thick ice. For the thin ice, the snowpack has now eroded into a 2-cm-thick granular snow-ice layer, and former melt pools consist of collections of candled ice tips that rise up to 1 cm above the freeboard of the thin, saturated ice sheet. Backscatter from multiyear ice is greater than or equal to that from first-year ice; a contrast reversal has taken place. After midsummer, first-year ice roughness elements have been eroded by melt to a point where they are small in relation to the radar wavelength; the surface appears smooth and produces weak backscatter (see Figure 5-30). Multiyear ice remains topographically rough and has many tilted surfaces and a complex mixture of ice, snow, and water features that provide a strong surface scatter. At X-band, the image presented is almost featureless. First-year ice, an old lead, and multiyear ice produce similar backscatter levels. This indicates that the small-scale roughness for each of these features is very similar. Only the melt pool feature stands out. In the L-band image, first-year ice produces a weak backscatter (a trend reversal), but not as weak as that produced by open water between floes. It is spatially more homogeneous than the areas with probable subsurface pooling.

5.5.1.8. Tone and texture. To date, the primary exploitation of backscatter information is associated with intensity (tone) and standard deviation. The exploitation of spatial variation has been elusive to date, even though visual examination of imagery gives one the sense that it should be exploitable [Guindon et al., 1982; Burns and Lyzenga, 1984; Holmes et al., 1984; Barber, 1989; Shokr, 1990; Wackerman,

1991]. The spatial variability of physical and microwave properties for multiyear ice is considerable. The constituents that contribute to the signature of multiyear ice include pressure ridges, rubble areas, individual and strings of melt pools, and refrozen first-year leads. The spatial variability of first-year ice is primarily influenced by the distribution of pressure ridges, ridge lines, and fracture lines. Since there is no prescribed order to the physical characteristics of either first-year or multiyear ice, texture measures may be image dependent and not easily extrapolated. In addition, since many features are small in extent, the resolution impacts the results obtained. However, visual analysis uses textural clues, as well as floe shape, to establish ice-type information, with the requirement that the data are obtained at moderate resolution.

5.5.1.9. Pressure ridges. Multiyear ice ridges have cross sections only 3 to 4 dB greater than the background ice [Gray et al., 1982; Livingstone et al., 1983, 1987b]. First-year ridge returns are typically brighter than the background, with the probability that they scatter as strongly as the ridge returns of multiyear ice. Pressure ridges are characterized as long, linear features composed of blocks of broken ice. Strong backscatter is associated with tilted surfaces. It has been observed that old multiyear pressure ridges may be most easily detected if observed broadside and may not be detectable if observed along track. This may be attributed to the weathering of a ridge to a point where the backscatter is dominated by volume scattering, which is much less sensitive to the local incidence angle. This suggests that the reflection off the flat ice adjacent to an old ridge may be important in providing the needed backscatter enhancement that distinguishes the ridge from the background ice. The geometry is such that when the radar is aligned parallel to the ridge, this forward-scattering contribution is not present. In Figures 5-26 to 5-30 a number of ridges are identifiable. Note especially that during summer, the tilted blocks are coated with moist snow, which masks the backscatter from tilted blocks that is so important in winter. In addition, pressure ridges are more likely to be identified during this period as long, linear features of weak return surrounded by strings of melt pools.

5.6 SAR-SCATTEROMETER COMPARISONS

A number of SAR and scatterometer intercomparisons have been made [Parashar, 1974; Livingstone et al., 1987a; Shuchman et al., 1989; Onstott and Shuchman, 1990]. These have included comparison of relative change between ice types, as well as of absolute change levels. One of the more important differences in these intercomparisons has to do with the sampling. Scatterometer observations are often conducted over homogeneous regions; for instance, for multiyear ice, a decision may be made to differentiate between pressure ridges and flat ice and to separate them into two populations. This is also true to a lesser extent in SAR analysis, and probably only for the prominent ridges. Melt pools and hummocks are often combined together. In

general, the results from aircraft and in-situ observations are in agreement. Aircraft data often acquire more of a synoptic view of ice conditions, whereas in-situ observations obtain more detailed information, but at fewer locations.

5.7 OPTIMUM FREQUENCY, POLARIZATION, AND INCIDENCE ANGLE

Many questions arise in the discussion of the optimum choices of frequency, polarization, and incidence angle. What if multiple frequencies and polarizations can be utilized? Furthermore, what if the coherent properties of clutter may be exploited? What then is optimum? Season and the set of ice types to be discriminated among may also have a bearing. At present, there is difficulty in specifying the best set of radar parameters. A general discussion of what appears reasonable follows.

5.7.1 Optimum Frequency

During winter, the critical mechanism in separating first-year and multiyear ice is discriminating backscatter dominated by volume scattering from that dominated by surface scattering. This works because the surface roughness for each of these ice types is similar. Observations suggest that surface scattering may increase with frequency squared. It has been shown [Kim, 1984; Kim et al., 1984a] that multiyear ice may be well modeled by spherical scatterers. In somewhat simplistic terms, this suggests that the optimum frequency will be one that exploits the fact that volume scattering dominates. Rayleigh-scattering cross sections increase with λ^6 (but losses reduce the overall effect to λ^4), so one should choose a wavelength λ such that surface scattering remains the principal backscatter mechanism for first-year ice; also, the wavelength should be short enough for strong multiyear ice volume scatter.

Frequency responses for frequencies from 1 to 100 GHz are shown in Figure 5-31 for multiyear and first-year ice. These data suggest that the contrast increases with increasing frequency and that a minimum occurs at frequencies below 2 GHz. The upper limit is not well-defined. A family of theoretical predictions (using radiative transfer theory) has been developed to examine the optimum frequency for the case of HH-polarization and an incidence angle of 40°. These results are presented in Figure 5-18. Measurement data are also included to provide a comparison of a typical backscatter response with the range of responses possible for observed physical-property values. This work suggests that the optimum frequency may occur in the Ku- or Ka-band portion of the microwave region. Observations and predictions argue that discrimination at C-band will be much better than at L-band, and that results at X-band will be similar to those at C-band, but with additional dynamic range.

During summer, it was shown [Onstott and Gogineni, 1985; Livingstone et al., 1987a, b; Onstott et al., 1987] that at high frequencies, the moist snowpack produced sea ice

images that were essentially featureless, except that open water could easily be distinguished from sea ice. The ability to discriminate improved with decreasing frequency, with the greatest separation at L-band. The underlying process was attributed to the ability to penetrate and sense the rough ice-snow interface. For all-season capability, selection of a C-band frequency is a very reasonable choice when satellite operation is limited to one frequency.

5.7.2 Optimum Polarization

The choice of the optimum polarization is less obvious than the choice of the optimum frequency. For many ice forms, VV and HH are very similar. However, for open water and calm conditions, the cross section at VV-polarization is 5 to 7 dB greater than at HH-polarization. For very thin ice, VV-polarization may have a cross section 2 to 3 dB greater than that of HH-polarization. Cross-polarization has been shown to increase the range between multiyear and first-year returns by an additional 3 dB [Parashar, 1974; Onstott et al., 1979; Livingstone et al., 1983]. This is attributed to the very weak depolarization that occurs for smooth and slightly rough surfaces. Volumes composed of discrete scatterers or dielectric discontinuities give rise to a strong depolarization component. This is well illustrated by comparing a multiyear hummock (many discrete scatterers) and a melt pool (few discrete scatterers). However, the discrimination among young ice types is hampered if cross-polarization is used, because intensity differences due to surface scatter are suppressed. The choice of polarization is often driven more by system considerations, such as ease of antenna design or the amount of available transmitter power. An intercomparison of the contrast between multiyear ice, first-year ice, and thin ice is shown in Figures 5-32 to 5-34 for VV-, HH-, and VH-polarizations.

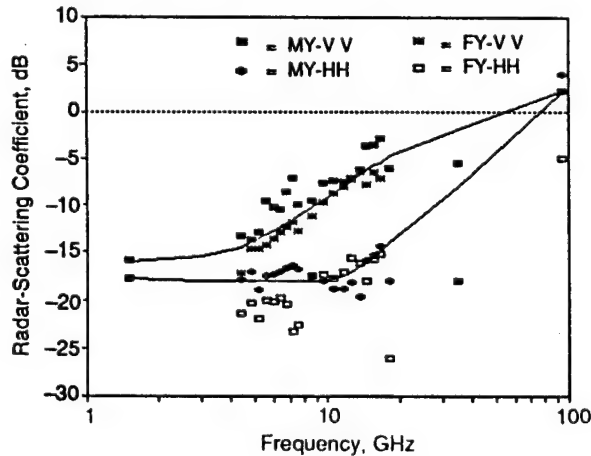


Fig. 5-31. The radar-scattering coefficients of multiyear and first-year ice are shown as a function of frequency and polarization, and at an angle of 40°. This response is for winter conditions.

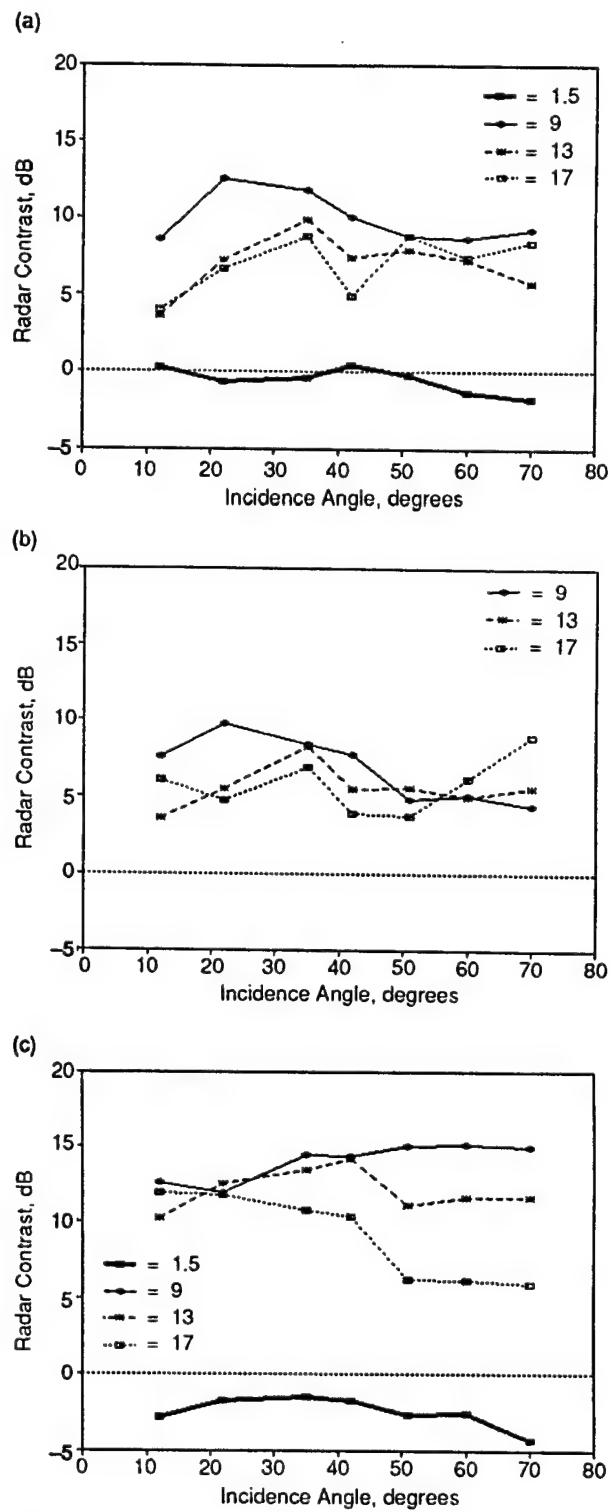


Fig. 5-32. The contrast in scattering coefficients of multiyear and first-year ice is shown as a function of polarization, angle, and frequency. In (a) the polarization is VV, in (b) it is HH, and in (c) it is VH.

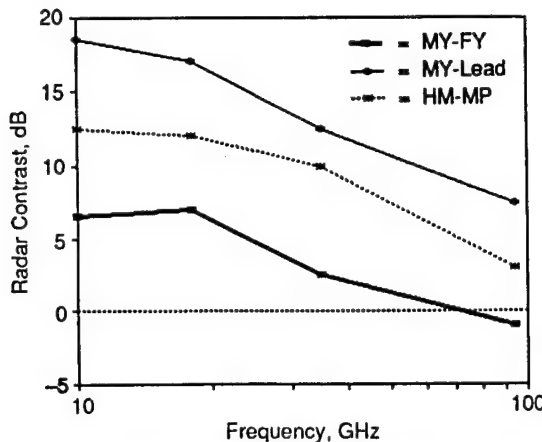


Fig. 5-33. The differences between radar-scattering coefficients of multiyear ice, first-year ice, lead ice (30-cm thick), and a multiyear hummock and melt pool are shown for fall conditions. The incidence angle is 40°, and the polarization is VV.

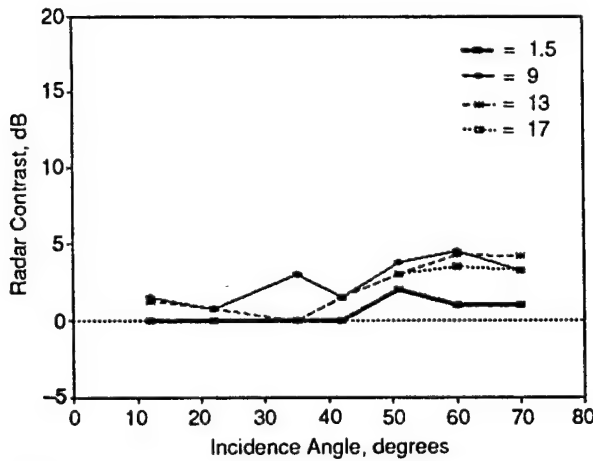


Fig. 5-34. The contrast in the scattering coefficient of gray-white ice and first-year ice is shown as a function of frequency. The polarization is VV.

TABLE 5-5. Radar lookup tables developed for ASF GPS and ERS-1.

Ice season	Description	Period
Winter and early spring	Cold conditions	November–April
Late spring	Warming conditions	May and June
Early summer	Moist snow	June
Midsummer	Peak melt	Late June and July
Late summer	Post-peak melt	July and August
Fall	Freezing conditions	September and October

5.7.3 Optimum Incidence Angle

Based purely on backscattering phenomena, the optimum incidence angle range is from 20° to 70° (the middle angles), with the implication that the optimum angle may be polarization and ice-type sensitive. Angles near vertical are dominated by surface scattering and coherence effects. In the angle region from 10° to 15°, the various scattering responses intersect, causing confusion. At the small grazing angles, backscatter originates from topographical features, if it occurs at all. An example of the polarization response for the contrast between multiyear and first-year ice for winter conditions is presented in Figures 5-32 and 5-33. In Figure 5-34, gray-white ice is contrasted with thick first-year ice.

5.8 RADAR LOOKUP TABLES FOR ASF GPS

The results of the in-situ scatterometer observations have culminated in providing a set of tables that contain scattering coefficients for three to four ice-type combinations. There are tables for six seasons that have been identified according to changes produced in ice backscatter. They include winter to early spring, late spring, early summer, midsummer, late summer, and fall. The seasons, the ice state conditions, and the time periods are provided in Table 5-5. Tables have been produced for the European Space Agency's Remote Sensing Satellite (ERS-1 operates at C-VV-23°), the Japanese Earth Resources Satellite (JERS-1 operates at L-HH-35°), and the NASA Earth Observing System satellite (EOS is designed to operate at X-HH-25°, as well as other frequencies and polarizations). Entries in the tables include major ice-type categories, the thickness range associated with each category, and radar-scattering coefficients described by means, standard deviations, and slope (e.g., for 20° to 26° in the case of the ERS-1 radar lookup table [RLT] series). Tables 5-6, 5-7, and 5-8 are used in conjunction with the Alaska Synthetic Aperture Radar Facility (ASF) Geophysical Processor System (GPS) to discriminate among ice types. Clutter categories are segmented, statistics of each segment (mean σ^0 and its standard deviation) are compared with values contained in the lookup tables, and a decision is made as to ice type (see Chapter 19).

The validation of ASF GPS ice-type products began in March 1992. Study of the accuracy of ice-type discrimination done with ERS-1 data and by using the ASF GPS is the subject of a major validation campaign. Questions such as the influence of region on accuracy, the need to develop RLT's with regional adaptability, and the approach in selecting RLT's for use in temporal and seasonal studies of ice sheet processes are topics under consideration. Efforts at improving ice-type discrimination will consider the use of ancillary data (such as air temperature, snowfall predictions, and time of year), the incorporation of electromagnetic models for absolute-level adjustment, and the exploitation of temporal SAR data.

TABLE 5-6. Radar lookup tables developed for ASF GPS and ERS-1.

Ice type	Thickness, cm	σ^o , dB	Standard deviation, dB	Slope, dB/deg
<i>Winter to early spring</i>				
MY	>220	-8.6	2.2	-0.08
TFY	70 to 220	-11.5	2.1	-0.77
THFY	20 to 70	-13.3	1.2	-0.17
OW	0	<-19.7	4.0	-0.04
<i>Late spring</i>				
MY	>220	-10.7	2.1	-0.27
TFY	70 to 220	-13.2	1.1	-0.22
OW	0	<-19.7	4.0	-0.04
<i>Early summer</i>				
MY SY TFY MFY	>70	-16.3	1.1	-0.33
THFY	20 to 70	-13.1	1.4	-0.16
OW	0	<-19.7	4.0	-0.04
<i>Midsummer</i>				
MY and TFY	>120	-16.3	1.1	-0.33
MFY	70 to 120	-14.7	1.5	-0.27
THFY	30 to 70	-13.1	1.4	-0.16
OW	0	<-19.7	4.0	-0.04
<i>Late summer</i>				
MY and TFY	>120	-16.8	1.8	-0.60
THFY	30 to 70	-18.4	2.2	-0.45
OW	0	<-19.7	4.0	-0.04
<i>Fall</i>				
MY	>150	-10.5	1.7	-0.04
FY	120	-12.5	1.9	-0.21
THFY and OW	0 to 30	<-19.7	2.0 to 4.0	-0.04 to -0.63

MFY = medium first-year ice

TABLE 5-7. Radar lookup tables developed for ASF GPS and JERS-1.

Ice type	Thickness, cm	σ^o , dB	Standard deviation, dB	Slope, dB/deg
<i>Winter to early spring</i>				
MY	>220	-7.0	TBD	-0.28
TFY MFY THFY	20 to 220	-23.4	TBD	-0.67
OW	0	<-30.7	TBD	-0.53
<i>Late spring</i>				
MY	>220	-15.5	TBD	-0.28
TFY	70 to 220	-23.4	TBD	-0.67
OW	0	<-30.7	TBD	-0.53
<i>Early summer</i>				
MY SY TFY MFY	>70	-15.1	TBD	-0.15
ThFY	20 to 70	TBD	TBD	TBD
OW	0	<-30.7	TBD	-0.53
<i>Midsummer</i>				
MY	>220	-22.7	2.0	-0.54
TFY MFY	70 to 220	-19.8	TBD	-0.55
OW	0	<-30.7	TBD	-0.53
<i>Late summer</i>				
MY and TFY	>120	-21.9	TBD	-0.54
ThFY	30 to 70	-28.1	TBD	-0.67
OW	0	<-30.7	TBD	-0.53
<i>Fall</i>				
MY	>150	-17.3	TBD	-0.43
FY	30 to 120	-18.4	TBD	-0.43
OW	0	<-30.7	TBD	-0.53

TABLE 5-8. Radar lookup tables developed for ASF GPS and EOS X-HH-23°.

Ice type	Thickness, cm	σ^0 , dB	Standard deviation, dB	Slope, dB/deg
<i>Winter to early spring</i>				
MY	>220	-3.6	1.9	-0.25
FY	20 to 220	-14.2	1.8	-0.10 to -0.31
OW	0	<-29.7	0.3	0
<i>Late spring</i>				
MY	>220	TBD	TBD	TBD
TFY	70 to 220	TBD	TBD	TBD
OW	0	<-29.7	0.3	0
<i>Early summer</i>				
MY SY TFY MFY	>70	-15.9	0.7	-0.42
ThFY	20 to 70	-15.1	0.4	-0.11
OW	0	<-29.7	0.3	0
<i>Midsummer</i>				
MY and TFY	>70	-15.7	0.7	-0.11 to -0.42
ThFY	20 to 70	-14.7	0.35	-0.11
OW	0	<-29.7	0.3	0
<i>Late summer</i>				
MY and TFY	>120	TBD	TBD	TBD
ThFY	30 to 70	TBD	TBD	TBD
OW	0	<-29.7	0.3	0
<i>Fall</i>				
MY	≥ 150	-6.9	2.4	-0.05
FY	>70	-13.5	0.9	-0.31
ThFY	30 to 70	-14.4	1.2	-0.10

5.9 FUTURE OPPORTUNITIES AND ISSUES

The ability to obtain temporal information about the polar regions is now becoming a reality. The polar regions in the United States have only been the subject of active microwave observation on an occasional basis, and then only for a few weeks at a time. This is beginning to change. Observations with moderate resolutions (i.e., about 10 m) will become commonplace rather than the exception. The European Space Agency launched the ERS-1 SAR on July 17, 1991. Japan's National Space Development Agency launched the JERS-1 SAR on February 11, 1992. The Canadian Space Agency has a 1994 launch scheduled for its Radarsat SAR (C-HH-30° to 50°). The United States is considering a multifrequency and multipolarization SAR for 2005. The former USSR launched a series of X-band RAR's (Kosmos/Okean), starting in 1983, and S-band SAR's (ALMAZ) in 1987. With the potential of numerous sensors in space at once, it appears possible to have multifrequency, multiple polarizations, and multiple angle views. In addition, the frequency of coverage may allow for global mappings in enormous detail. The potential for retrieving very useful and timely information is upon us.

Future efforts will be directed toward the use of multi-parameter and multitemporal data. As suggested above, to obtain global coverage, various sensors may be used, with probable differences in operating parameters. In the past, work has centered on the exploitation of a single image at a time. This will change. Both the study of the seasonal response (microwave and physical property) of sea ice and

the availability of multitemporal SAR data allow for a very large next step, that is, exploitation of *time evolution*. With such an assessment, the ability to reduce signature ambiguities is possible, especially if multiple frequencies, polarizations, and angles are included. Given the proper information (including ancillary data) and continuous coverage, ice-thickness, mass-balance, and heat-transfer estimates will improve.

At present, discrimination between ice forms is by ice type, rather than by thickness. Ice thickness has been suggested to be an important indicator of global change and is known to be important in heat-mass balance predictions. Future research efforts will be directed to improving this ability to determine thickness. It is hypothesized that a continuum of thickness values will be retrieved by incorporating an understanding of the evolution of first-year ice (with links between microwave signatures, physical properties, and environmental conditions). This, coupled with temporal SAR data, certainly promises an exciting future and dramatic improvements in the retrieval of geophysical information about our polar regions.

REFERENCES

Anderson, V. H., High altitude, side looking radar images of sea ice in the Arctic, *Proceedings of the Fourth Symposium on Remote Sensing of the Environment*, pp. 845-857, Willow Run Laboratory, Ann Arbor, Michigan, 1966.

Barber, D. G., *Texture Measures for Sea-Ice Discrimination: An Evaluation of Univariate Statistical Distributions*, Report ISTS-EOL-TR89-005, Department of Geography, University of Waterloo, Waterloo, Ontario, Canada, 1989.

Burns, B. A. and D. R. Lyzenga, Textural analysis as a SAR classification tool, *Electromagnetics*, 4, pp. 309-322, 1984.

Campbell, W. J., J. Wayneberg, J. B. Ramseyer, R. O. Ramseier, M. R. Vant, R. Weaver, A. Redmond, L. Arsenault, P. Gloersen, H. J. Zwally, T. T. Wilheit, T. C. Chang, D. Hall, L. Gray, D. C. Meeks, M. L. Bryan, F. T. Barath, C. Elachi, F. Leberl, and T. Farr, Microwave remote sensing of sea ice in the AIDJEX main experiment, *Boundary-Layer Meteorology*, 13, pp. 309-337, 1978.

Cavalieri, D. J., B. B. Burns, and R. G. Onstott, Investigation of the effects of summer melt on the calculation of sea ice concentration using active and passive microwave data, *Journal of Geophysical Research*, 95(C4), pp. 5359-5369, 1990.

Dunbar, M., *A Glossary of Ice Terms (WMO Terminology)*, *Ice Seminar, Special Volume 10*, pp. 105-110, The Canadian Institute of Mining and Metallurgy, 1969.

Dunbar, M. and W. Weeks, *The Interpretation of Young Ice Forms in the Gulf of St. Lawrence Using Radar and IR Imagery*, DREO Report 711, Research and Development Branch, Department of National Defense, Ottawa, Canada, 1975.

Fung, A. K. and H. J. Eom, Application of a combined rough surface volume scattering theory of sea ice and snow, *IEEE Transactions on Geoscience and Remote Sensing*, GE-20(4), pp. 528-536, 1982.

Glushkov, V. M. and V. Komarov, Side-looking radar system Toros and its application to the study of ice conditions and geological exploration, *Proceedings of the Seventh International Symposium on Remote Sensing of the Environment*, 1, p. 317, Willow Run Laboratory, Ann Arbor, Michigan, 1971.

Gogineni, S. P., *Radar Backscatter From Summer and Ridged Sea Ice, and the Design of Short-Range Radars*, Ph.D. dissertation, The University of Kansas, Lawrence, Kansas, 1984.

Gow, A. J., D. A. Meese, D. K. Perovich, and W. B. Tucker, The anatomy of a freezing lead, *Journal of Geophysical Research*, 95(C10), pp. 18,221-18,232, 1990.

Gray, A. L., R. O. Ramsier, and W. J. Campbell, Scatterometer and SLAR results obtained over Arctic sea ice and their relevance to the problem of Arctic ice reconnaissance, *Proceedings of the Fourth Canadian Symposium on Remote Sensing*, pp. 424-443, 1977.

Gray, A. L., R. K. Hawkins, C. E. Livingstone, L. D. Arsenault, and W. M. Johnstone, Simultaneous scatterometer and radiometer measurements of sea ice microwave signatures, *IEEE Journal of Oceanic Engineering*, OE-7(1), pp. 20-33, 1982.

Guindon, B., R. K. Hawkins, and D. G. Goodenough, Spectral-Spatial analysis of microwave sea ice data, *Proceedings of the IGARSS'82*, 2, pp. 4.1-4.8, Munich, 1982.

Holmes, Q. A., D. R. Nuesch, and R. A. Shuchman, Textural analysis and real-time classification of sea-ice types using digital SAR data, *IEEE Transactions on Geoscience and Remote Sensing*, GE-22, pp. 113-120, 1984.

Johnson, J. D. and L. Farmer, Use of side-looking radar for sea ice identification, *Journal of Geophysical Research*, 76, pp. 2138-2155, 1971.

Ketchum, R. D., Jr., and S. G. Tooma, Jr., Analysis and interpretation of air-borne multifrequency side-looking radar sea ice imagery, *Journal of Geophysical Research*, 78, pp. 520-538, 1973.

Kim, Y. S., *Theoretical and Experimental Study of Radar Backscatter From Sea Ice*, Ph.D. dissertation, University of Kansas, Lawrence, Kansas, 1984.

Kim, Y. S., R. K. Moore, and R. G. Onstott, *Theoretical and Experimental Study of Radar Backscatter From Sea Ice*, Remote Sensing Laboratory Technical Report 331-37, University of Kansas, Lawrence, Kansas, 1984a.

Kim, Y. S., R. G. Onstott, and R. K. Moore, Effect of snow cover on microwave backscatter from sea ice, *IEEE Journal of Oceanic Engineering*, OE-9(5), pp. 383-388, 1984b.

Kwok, R., E. Rignot, B. Holt, and R. Onstott, An overview of the geophysical sea ice products generated at the Alaska SAR Facility, *Journal of Geophysical Research* 97(C2), pp. 2391-2402, 1991.

Larson, R. W., J. D. Lyden, R. A. Shuchman, and R. T. Lowry, *Determination of Backscatter Characteristics of Sea Ice Using Synthetic Aperture Radar Data*, 110 pp., ERIM Final Report 142600-1-F, Environmental Research Institute of Michigan, Ann Arbor, Michigan, 1981.

Livingstone, C. E., R. K. Hawkins, A. L. Gray, K. Okamoto, T. L. Wilkinson, S. Young, L. D. Arsenault, and D. Pearson, Classification of Beaufort Sea ice using active and passive microwave sensors, *Oceanography From Space*, pp. 813-826, edited by J. F. R. Gower, Plenum, New York, 1981.

Livingstone, C. E., R. K. Hawkins, A. L. Gray, L. Drapier, L. D. Arsenault, K. Okamoto, T. L. Wilkinson, and D. Pearson, *The CCRS/Sursat Active-Passive Experiment 1978-1980: the Microwave Signatures of Sea Ice*, Canada Centre for Remote Sensing, Ottawa, 1983.

Livingstone, C. E., R. G. Onstott, L. D. Arsenault, A. L. Gray, and K. P. Singh, Microwave sea-ice signatures near the onset of melt, *IEEE Transactions on Geoscience and Remote Sensing*, GE-25(2), pp. 174-187, 1987a.

Livingstone, C. E., K. P. Singh, L. D. Arsenault, and A. L. Gray, Seasonal and regional variations of active/passive microwave signatures of sea ice, *IEEE Transactions on Geoscience and Remote Sensing*, GE-25(2), pp. 159-173, 1987b.

Loshchilov, V. S. and V. A. Voyevodin, Determining elements of drift of the ice cover and movement of the ice edge by the aid of the Toros aircraft lateral scan radar station, *Problemy Artiki i Antarktiki*, 40, pp. 23–30, 1972.

Luther, C. A. and R. A. Shuchman, *The Proceedings of the Final Sursat Ice Workshop Summary Report*, 11 pp., edited by R. O. Ramseier and D. J. Lapp, Atmospheric Environment Service, Toronto, 1980.

Lyden, J. D., B. A. Burns, and A. L. Maffett, Characterization of sea ice types using synthetic aperture radar, *IEEE Transactions on Geoscience and Remote Sensing*, GE-22(5), pp. 431–439, 1984.

Onstott, R. G., MIZEX'84 multifrequency helicopter-borne altimeter observations of summer marginal sea ice, *Proceedings of the IGARSS'90 Symposium*, pp. 2241–2244, College Park, Maryland, 1990a.

Onstott, R. G., Near surface microwave measurements of Arctic sea ice during the fall freeze-up, *Proceedings of the IGARSS'90 Symposium*, pp. 1529–1530, College Park, Maryland, 1990b.

Onstott, R. G., Active microwave observations of Arctic sea ice during the fall freeze-up, *Proceedings of the IGARSS'91 Symposium*, pp. 821–824, Espoo, Finland, 1991.

Onstott, R. G. and S. P. Gogineni, Active microwave measurements of Arctic sea ice under summer conditions, *Journal of Geophysical Research*, 90(C3), pp. 5035–5044, 1985.

Onstott, R. G. and R. A. Shuchman, Scatterometer measurements of wind, waves and ocean fronts during NORSEX, *Proceedings of the IGARSS'89 Symposium*, pp. 1084–1088, Vancouver, Canada, 1989.

Onstott, R. G. and R. A. Shuchman, Comparison of SAR and scatterometer data collected during CEAREX, *Proceedings of the IGARSS'90 Symposium*, pp. 1513–1516, College Park, Maryland, 1990.

Onstott, R. G., R. K. Moore, and W. F. Weeks, Surface-based scatterometer results of Arctic sea ice, *IEEE Transactions on Geoscience and Electronics*, GE-17, pp. 78–85, 1979.

Onstott, R. G., R. K. Moore, S. Gogineni, and C. V. Delker, Four years of low altitude sea ice broadband backscatter measurements, *IEEE Journal of Oceanic Engineering*, OE-7(1), pp. 44–50, 1982.

Onstott, R. G., Y. S. Kim, and R. K. Moore, *Active Microwave Measurements of Sea Ice Under Fall Conditions: The Radarsat/FIREX Fall Experiment*, Technical report 331-30/578—Final, University of Kansas Remote Sensing Laboratory, Lawrence, Kansas, 1984.

Onstott, R. G., T. C. Grenfell, C. Mätzler, C. A. Luther, and E. A. Svendsen, Evolution of microwave sea ice signatures during early and midsummer in the Marginal Ice Zone, *Journal of Geophysical Research*, 92(C7), pp. 6825–6835, 1987.

Onstott, R. G., R. A. Shuchman, and C. C. Wackerman, Polarimetric radar measurements of Arctic sea ice during the Coordinated Eastern Arctic Experiment, *Proceedings of the IGARSS'91 Symposium*, pp. 93–97, Espoo, Finland, 1991.

Parashar, S. K., *Investigation of Radar Discrimination of Sea Ice*, Ph.D. dissertation, CRES Technical Report 185-13, University of Kansas Center for Research, Inc., Lawrence, Kansas, 1974.

Parashar, S. K., R. M. Haralick, R. K. Moore, and A. W. Briggs, Radar scatterometer discrimination of sea ice types, *IEEE Transactions on Geoscience and Electronics*, GE-15, pp. 83–87, 1977.

Ramseier, R., P. Gloersen, W. Campbell, and T. Chang, Mesoscale descriptions for the principal Bering Sea Experiment, *Proceedings of the Final Symposium on the Results of the Joint Soviet-American Expedition*, pp. 231–236, edited by Y. Kondratyev et al., A. A. Balkema, Rotterdam, Netherlands, 1982.

Ringwalt, D. L. and F. C. MacDonald, *Terrain Clutter Measurements in the Far North*, Report of NRL Progress, Naval Research Laboratory, Washington, DC, 1956.

Rouse, J. W., Arctic ice type identification by radar, *Proceedings of the IEEE*, 57(4), pp. 605–611, 1969.

Shokr, M. E., On sea-ice texture characterization from SAR images, *IEEE Transactions on Geoscience and Remote Sensing*, 28(4), pp. 737–740, 1990.

Shuchman, R. A., C. C. Wackerman, A. L. Maffett, R. G. Onstott, and L. L. Sutherland, The discrimination of sea ice types using SAR backscatter statistics, *Proceedings of the IGARSS'89 Symposium*, pp. 381–385, Vancouver, Canada, 1989.

Ulaby, F. T., R. K. Moore, and A. K. Fung, *Microwave Remote Sensing—Active and Passive, Vol. II: Radar Remote Sensing and Surface Scattering and Emission Theory*, Addison-Wesley Publishing Company, Reading, Massachusetts, 1982.

Ulaby, F. T., R. K. Moore, and A. K. Fung, *Microwave Remote Sensing—Active and Passive, Vol. III: From Theory to Applications*, Artech House, Inc., Dedham, Massachusetts, 1986.

Wackerman, C. C., *Optimal Linear Combinations of Statistics and Texture Measures for SAR Sea Ice Classification*, presented at the IGARSS'91 Symposium, Espoo, Finland, 1991.

Weeks, W. F., Sea ice: The potential for remote sensing, *Oceanus*, 4(3), pp. 39–47, 1981.

Wetzel, L. B., *Sea Clutter, Radar Handbook*, pp. 13.12–13.40, edited by M. Skolnik, McGraw-Hill, New York, 1990.

Chapter 9. Laboratory Investigations of the Electromagnetic Properties of Artificial Sea Ice

CALVIN T. SWIFT AND KAREN ST. GERMAIN

Department of Electrical and Computer Engineering, University of Massachusetts, Amherst, Massachusetts 01003

KENNETH C. JEZEK

Byrd Polar Research Center, 1090 Carmack Road, The Ohio State University, Columbus, Ohio 43210

S. PRASAD GOGINENI

Radar Systems and Remote Sensing Laboratory, University of Kansas Center for Research, Inc., 2291 Irving Hill Drive, Campus West, Lawrence, Kansas 66045

ANTHONY J. GOW AND DONALD K. PEROVICH

Cold Regions Research and Engineering Laboratory, 72 Lyme Road, Hanover, New Hampshire 03755

THOMAS C. GRENFELL

Department of Atmospheric Sciences, University of Washington, Seattle, Washington 98195

ROBERT G. ONSTOTT

Environmental Research Institute of Michigan, P. O. Box 8618, Ann Arbor, Michigan 48107

9.1 INTRODUCTION

The electrical properties of sea ice growing on the open ocean are determined by the mechanical and thermodynamical influences of the ocean and atmosphere. Winds, currents, and air and water temperatures, among other variables, contribute to the eventual roughness, texture, chemical composition, and temperature gradient through the seaice. These latter properties tend to be inhomogeneous over relatively short length scales (tens of meters horizontally and tens of centimeters vertically at best) and they tend to evolve with time as the boundary conditions and internal composition of the ice pack change. For these reasons, the analyses of electromagnetic data collected by spaceborne instruments over sea ice have tended to rely on empirical relationships between limited ranges of an electromagnetic variable (e.g., brightness temperature) and a geophysical property of the ice. Numerous papers document the success of this analysis approach for estimating sea ice concentration and sea ice motion (e.g., Swift and Cavalieri [1985]; Zwally et al. [1983]; Parkinson et al. [1987]). Yet for these same reasons, attempts to obtain a deeper understanding of the electromagnetic properties of naturally growing sea ice can be complicated. For example, it is logically difficult to measure and sample young sea

ice. Some features such as the onset of flooding are transient phenomena, lateral inhomogeneity makes sampling difficult, and the opportunities to view a particular type of ice or even the same piece of ice throughout the seasonal cycle have been rare. Individually, almost all of these problems can and have been overcome by field investigators. But, taken together, there seems to be a strong argument for designing a new approach to answering fundamental questions about sea ice electromagnetic properties, namely, what are the important scattering and absorption mechanisms in sea ice and how are these mechanisms related to ice properties. It was felt that an approach could be found in the laboratory.

The Cold Regions Research and Engineering Laboratory (CRREL) Experiments were designed to confront some of the difficulties encountered in field work by growing sea ice in a carefully constrained, laboratory environment. Microwave experiments were conducted under an overarching set of principles that included: a uniform ice sheet of limited and well-documented physical properties could be grown and maintained; multiple sensors could collect data simultaneously from the same ice; and the interpretation of all electromagnetic observations of the ice with the measured ice physical properties has to be considered. As the experiments progressed, it also became apparent that two more facets needed to be added to the CRREL Experiment (CRRELEX). First, data relevant to a range of electromagnetic models (Chapter 10) needed to be collected. Second, time series data needed to be collected, partly because of initial observations that showed measurable changes in

electrical properties at every stage of ice development. That CRRELEX could document this evolution is viewed as one of the more important contributions of this work.

9.2 SCOPE

As originally conceived, CRRELEX was designed to study the microwave response of young thin (10 to 20 cm) sea ice that forms on open leads. Facilities were constructed towards this objective and included a saline-water-filled pond fitted with a plastic liner (Figure 9-1). The pond was 12 m long, 5 m wide, and 1 m deep. These dimensions were chosen to accommodate the planned remote sensing instruments. For example, at a width of 5 m, negligible antenna beam spillover occurs at nadir for a C-band radiometer, which has the largest footprint of the remote sensing instruments used. The 12 m length allowed observations at incidence angles up to 50° and provided for acquiring several independent samples with the radars used. An enormous tent could be rolled on and off the pond to protect against changes in weather. Air-conditioning units were installed inside the tent to preserve the ice during inevitable warm temperature periods, but these units were only

rarely used and later were abandoned. Paving tiles placed around the perimeter of the pond allowed an instrumented gantry to be moved over the ice. Later, a second, concrete-lined pond 10 m long, 10 m wide, and 1 m deep was outfitted with an instrument shelter, a refurbished movable bridge, and a movable roof. Finally, an indoor test facility used to grow a sea ice simulant from an urea solution and a small refrigerated pit ($8 \times 5 \times 1$ m) were used at the later stages of CRRELEX. The two indoor facilities proved to be extremely valuable in achieving the controlled environmental conditions initially set forth as a CRREL objective. However, the enclosures themselves limited the observations to range-gated radar measurements.

Use of the outdoor facilities placed constraints on the range of simulated ice properties and the duration over which any one ice property could be studied. Thin ice could be grown in an essentially undisturbed fashion for periods of several days. When grown under quiescent conditions, CRRELEX ice sheets exhibited physical properties similar to those found for thin Arctic ice. Depending on whether the ice was seeded with a fine spray of supercooled water or was left undisturbed to develop spontaneously, the upper centimeter of the ice sheet would be composed of smaller or larger

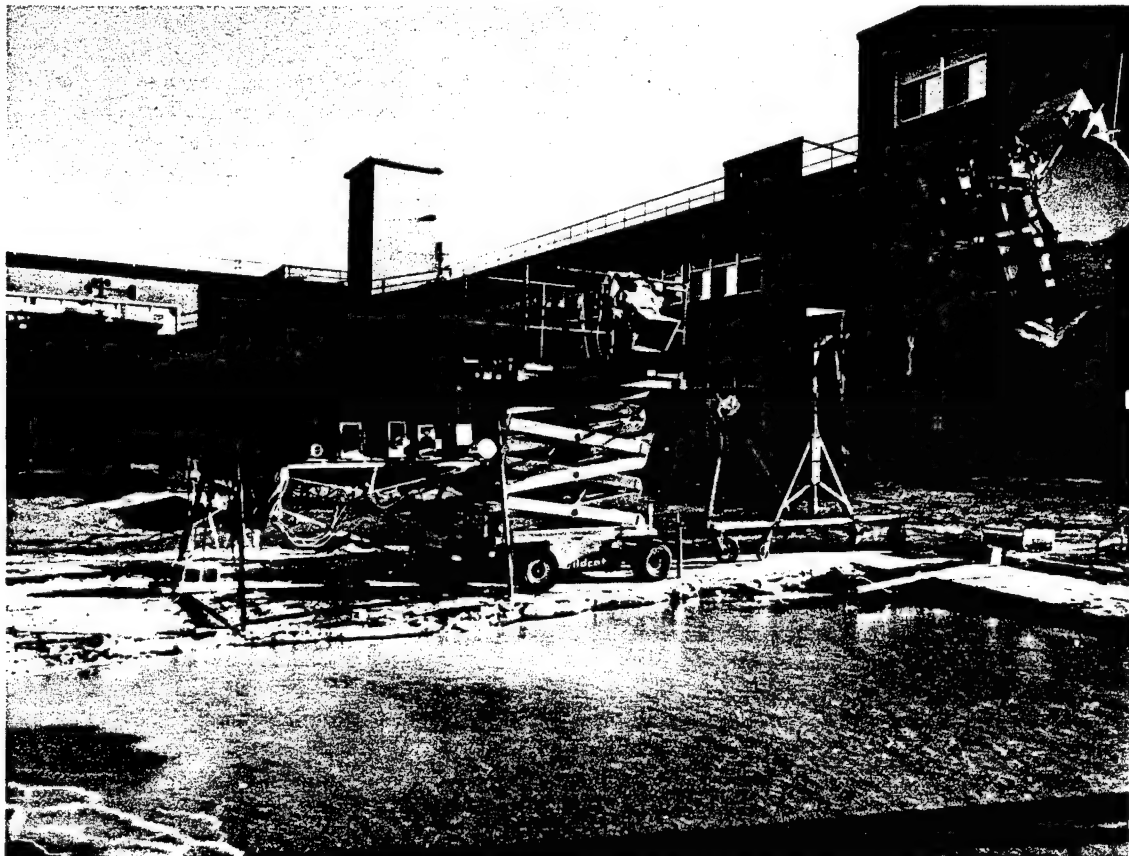


Fig. 9-1. Typical experiment arrangement at the outdoor facility at the Cold Regions Research and Engineering Laboratory. Pictured from the left are five single-frequency radiometers, the Stepped Frequency Microwave Radiometer, and a cluster of radar systems.

crystals with vertical *c*-axes [Gow, 1986]. A transition in ice properties occurred at a 1 to 2 cm thickness. At that point the *c*-axes reorient toward the horizontal, and columnar organization of ice crystals, characteristic of Arctic congelation ice, becomes dominant (Figure 9-2).

Congelation ice sheets were routinely grown during CRRELEX with maximum thicknesses ranging from about 10 to 30 cm, depending on the experimental requirements. In each case, the ice was closely monitored for salinity, crystal structure, brine pocket distribution, and, as possible, surface roughness. An example of the structural and salinity characteristics of an ice sheet monitored from

initial growth to decay is presented in Figure 9-3. In this particular case, ice growth was initiated in January 1985, and for the first month this ice sheet exhibited typical C-shaped salinity profiles, Figure 9-4(a). Subsequent pooling of snow melt and rain on top of the ice sheet in late February to early March 1985 led to significant downward percolation of the water and concomitant desalination of the ice before the pooled water refroze to produce the salinity and structural characteristics of ice depicted in Figure 9-3. At this stage, the ice contained few brine inclusions and the outlines of crystals had become rounded, a situation similar to multiyear Arctic ice [Gow et al., 1987].

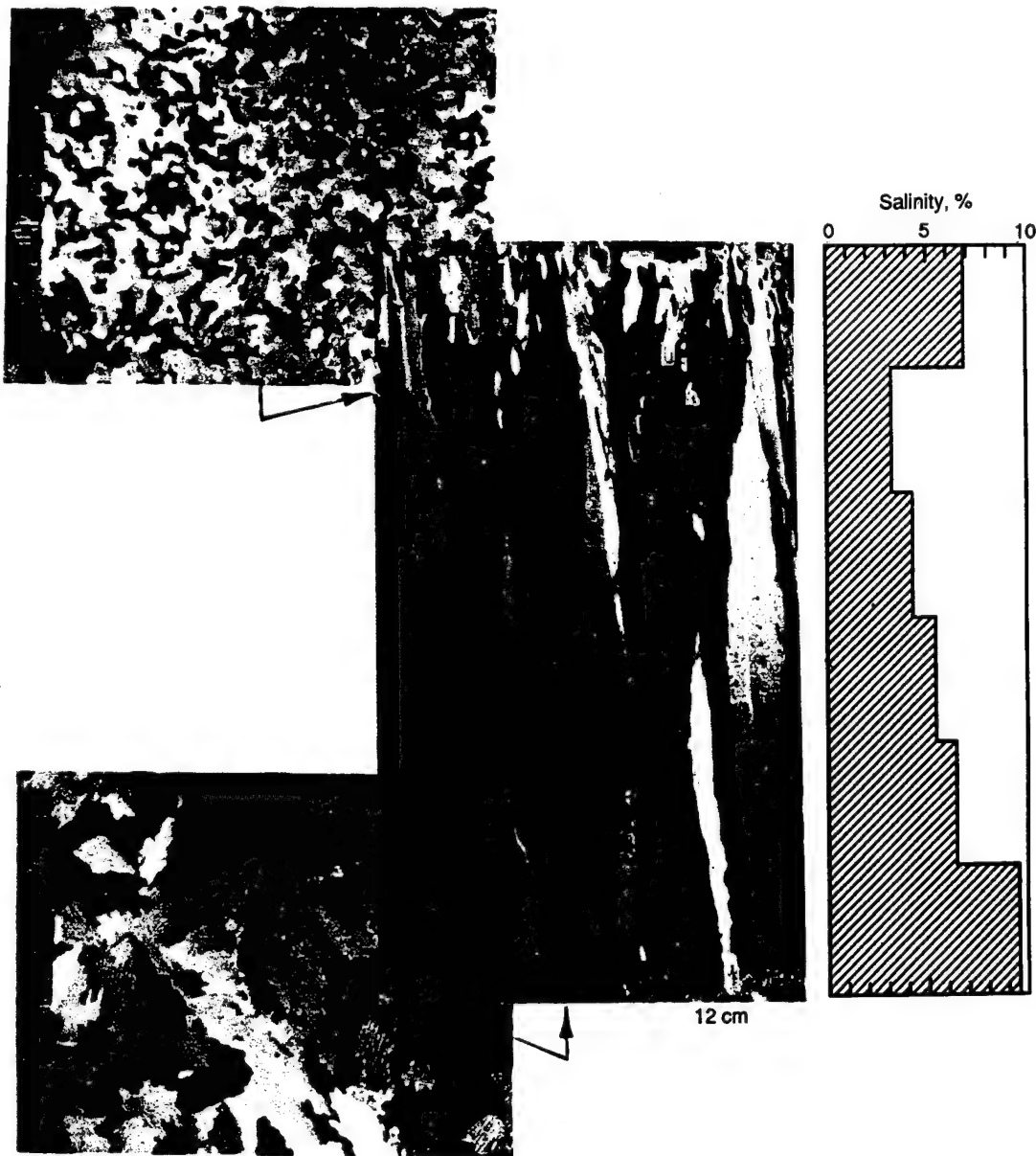


Fig. 9-2. The ice shown in these vertical and horizontal thin-section photographs and salinity profile is freshly grown saline ice from the CRREL test pond. Structurally, this ice closely simulates young Arctic sea ice. Scale subdivisions in horizontal sections measure 1 mm.

Salinity profiles documenting the progressive desalination of the January to March 1985 CRREL saline ice sheet are shown in Figure 9-4(b). Desalinated ice was also produced by cutting a pre-existing ice sheet into blocks and placing the blocks on wooden pallets. The blocks were allowed to weather and desalinate under ambient conditions. At the end of this process, the blocks were overlain on a second ice sheet growing in the pond; block salinities did not exceed 0.35‰.

Figure 9-5 documents salinity, temperature, brine volume, and crystalline structure more typical of 10 to 15 cm thick congelation ice sheets grown on the outdoor ponds at

CRREL. Temperatures increase linearly with depth. Brine volumes are nearly constant (about 3%) in the upper 75% of the ice. Below that level, brine volumes increase rapidly in the region where the ice develops a more open dendritic structure. A characteristic C-shaped salinity profile is found in this ice with a maximum value at the surface of about 8‰ (averaged over three cm) and a minimum of 5.4‰ at a depth of 10 cm. Salinity increases below 10 cm again because of the structure of the dendritic layer. The horizontal distribution of brine pockets was quantified by digitizing horizontal thin sections taken at various levels through the ice sheet.

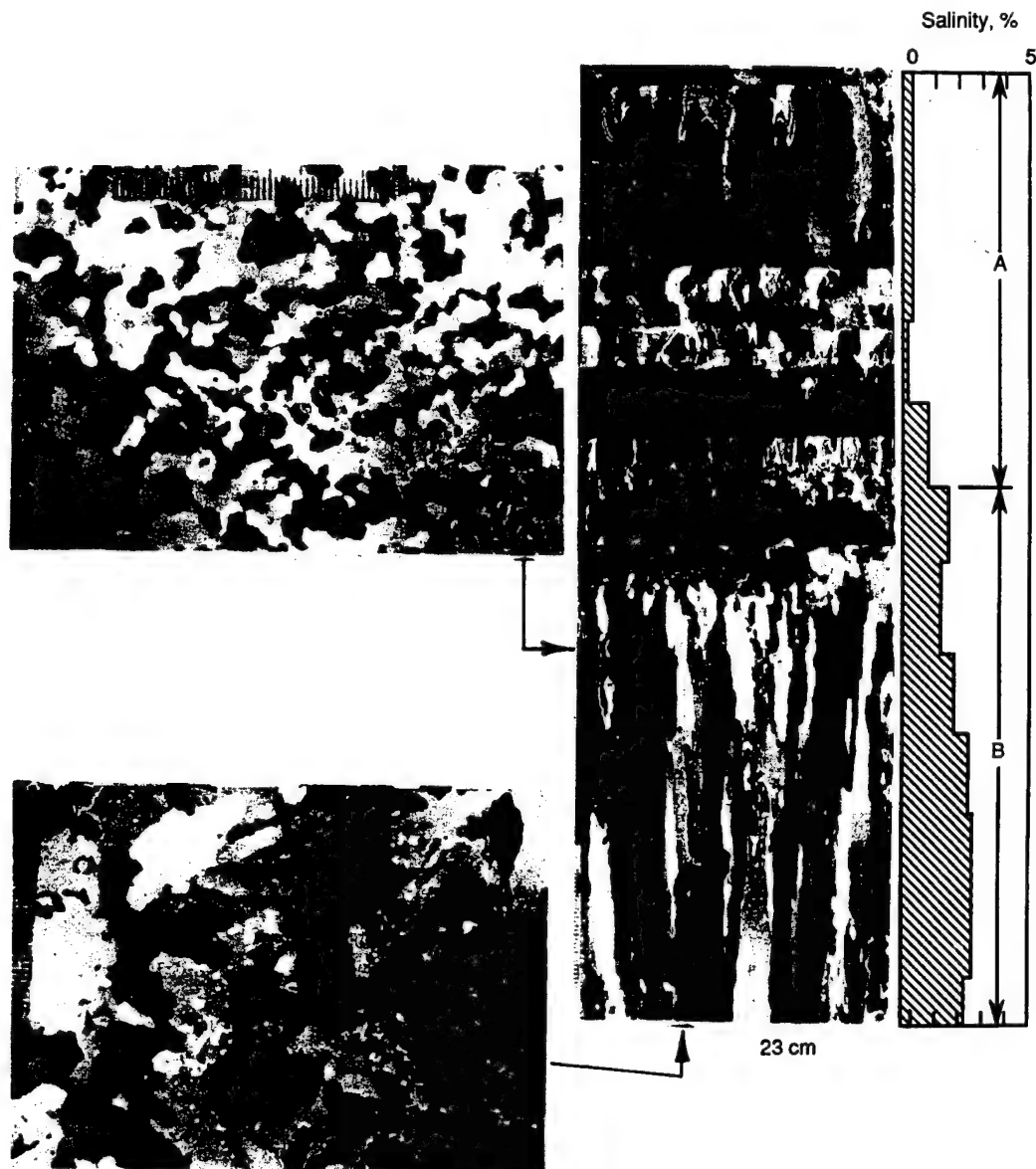


Fig. 9-3. Crystalline structure and salinity characteristics of ice desalinating in the CRREL test pond. In this example, several layers of melt pond ice (A) overlie desalinated columnar saline ice (B). Scale subdivisions in horizontal sections measure 1 mm.

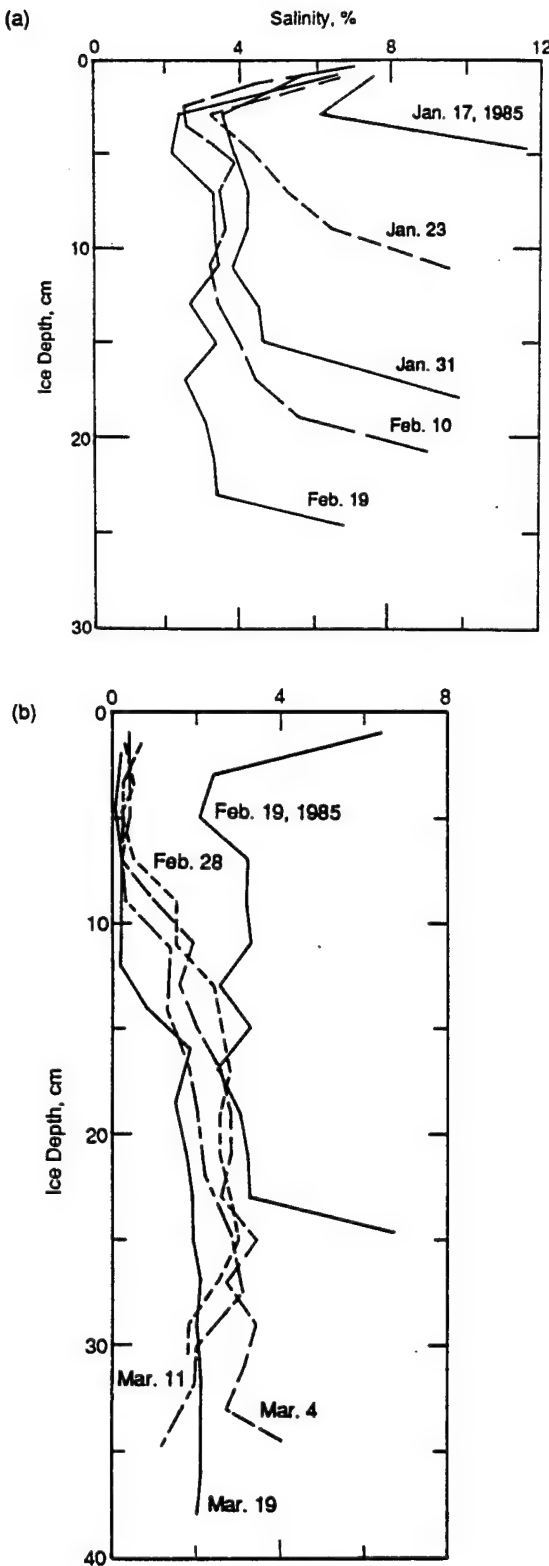


Fig. 9-4. (a) Salinity profiles at different stages of growth of sea ice grown in an outdoor pond at CRREL. Profiles closely simulate those found in Arctic first-year ice. (b) Transformation from a new ice to desalinated ice salinity profile in the outdoor pool at CRREL.

With additional experimentation, it was found that several other physical properties and ice-growth processes could be simulated in the laboratory. Varying surface roughness was introduced either by manually raking the ice surface or by spreading a layer of small chunks of ice on the growing ice sheet. In a few instances, larger blocks of ice were assembled into simulations of ridges. Other classes of complementary experiments could be included during each CRRELEX, and high-frequency acoustic [Stanton et al., 1986; Jezek et al., 1990] and optical frequency propagation measurements were often conducted simultaneously with the microwave observations.

Frazil ice, which forms in turbulent seas and has a granular texture, was simulated in three different ways. Snowfall onto the surface of the unfrozen pool produced a slush cover. Frozen slush results in an ice cover with salinity and structural characteristics very similar to frazil ice. Granular, frazil-like ice sheets up to 8 cm thick were produced in this manner. The second method for producing frazil ice involved a submersible pump to induce frazil crystal nucleation in the pool and the herding of crystals into a layer up to 4 cm thick. A third method simulated both frazil production and the agglomeration of frazil platelets into pancake ice. Here a wave generator consisting of a motor-driven panel was positioned at one end of the pond. Turbulence and wave action converted the semiconsolidated frazil ice sheet into a field of pancakes with pans measuring 20 to 30 cm in diameter and several centimeters thick. The vertical structure of a typical pancake including a salinity profile is presented in Figure 9-6.

Snow-covered ice was studied on the outdoor ponds and also under more controlled conditions in the indoor pit. Analyses of snow-covered ice is complicated by the subtle modification of the ice-snow surface when thin layers of snow are applied. A snow layer is absorbent and, over time, tends to wick surface brine up into the snow layer. This process seems to result in a dielectric roughening of the interface, although direct measurements of the amount or degree of roughening have yet to be made. A sufficient snow load will depress the ice surface below the unloaded freeboard, causing the surface to flood. Flooding was studied in the laboratory by loading a slab of ice with snow and then cutting the slab free from the restraining walls of the tank.

Finally, it is worth mentioning that frost flowers routinely developed in the indoor test basin and cold pit. Preliminary radar measurements were made on freshwater ice sheets completely covered by frost flowers and on urea and saline ice sheets with a low density of frost flowers.

As mentioned, many of the early CRRELEX's were exercises in learning about the ice. As each experiment was completed, it seemed possible to more clearly articulate several questions that drove the development of subsequent experiments:

- What are the microwave absorption and scattering coefficients of thin sea ice? How do they change with time?

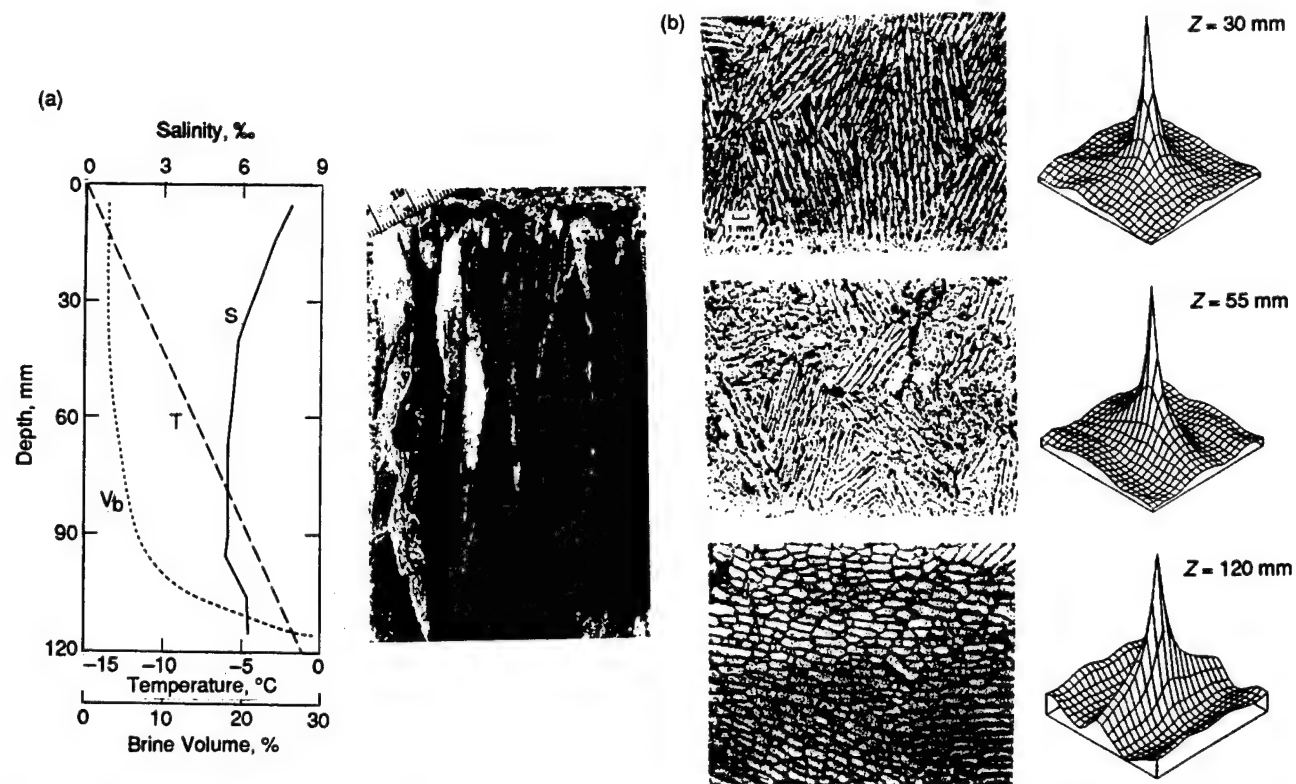


Fig. 9-5. Vertical profiles of temperature (T), salinity (S), and brine volume (V_b) for young sea ice. The vertical thin section shows that the ice structure is predominantly columnar with a thin surface layer of frazil. Also shown are horizontal thin sections from the top, middle, and bottom of the ice sheet with corresponding correlation functions [Perovich and Gow, 1991].

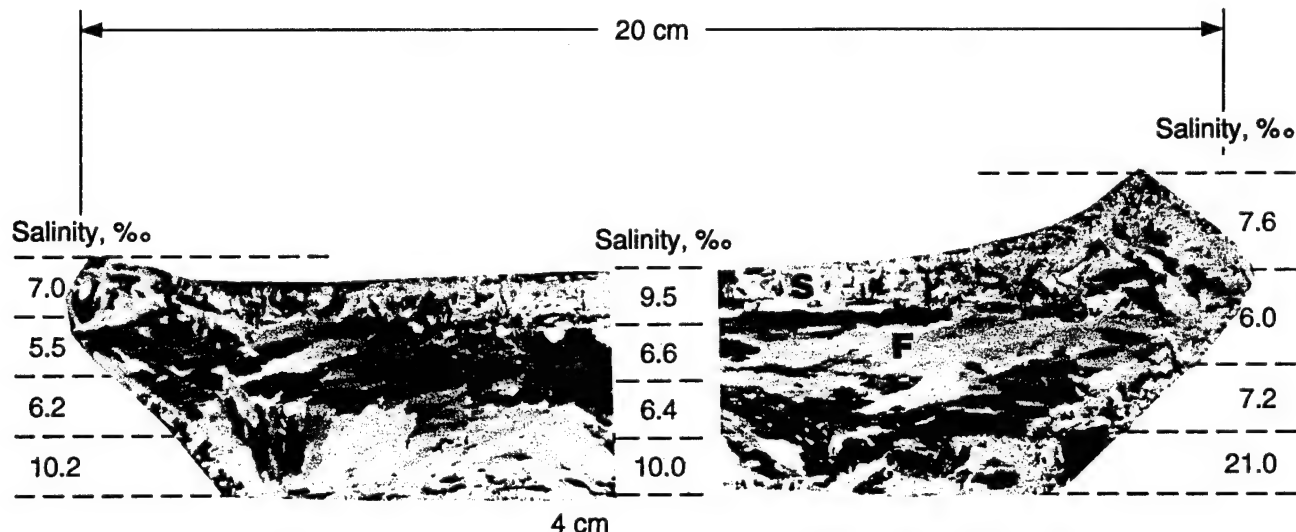


Fig. 9-6. Vertical thin-section structure and salinity profiles from a 4 cm thick pancake from CRRELEX'90. The sequence of ice textures from top to bottom of the pan is slush ice (s) underlain by platey frazil ice (f).

- To what thickness and in what fashion does the ice-water interface and the dendritic layer control electromagnetic response at a particular frequency?
- How important are the shapes, orientation, density, and distribution of brine pockets on the microwave response?
- Given that different classes of surface roughness are associated with different ice formation scenarios, which are the most important roughness classes; which classes dominate over, are equivalent to, or are less than volume scatter effects? Does the sequence of steps in the development and destruction of particular morphologies (e.g., frost flowers) result in a characteristic sequence of microwave responses?
- Does snow play a role in coupling electromagnetic energy between the air, snow, and ice? Is the modification of the ice surface due to the presence of thin snow an important effect? What happens to electromagnetic signatures when snow is sufficiently thick to cause flooding?
- Do thin ice, snow-covered ice, deformed ice, and ridges display azimuthal electromagnetic response? If so, why?
- How and why do signatures change when thin ice warms and desalinates and how is this related to the changing internal structure of the ice?

9.3 GROWTH PHASE OF THIN SALINE ICE

Microwave backscatter, transmission, and brightness temperature measurements were made by the CRRELEX team on saline ice during the winters from 1984 to 1989. Results from all measurements on undeformed congelation ice are similar. Results of representative experiments from this period are used to illustrate the range of measured responses.

Figure 9-7 shows the variation with time of the backscatter coefficient at 5.3 GHz as the surface evolves from open water to grey ice (14.5 cm thick) [Gogineni et al., 1990].

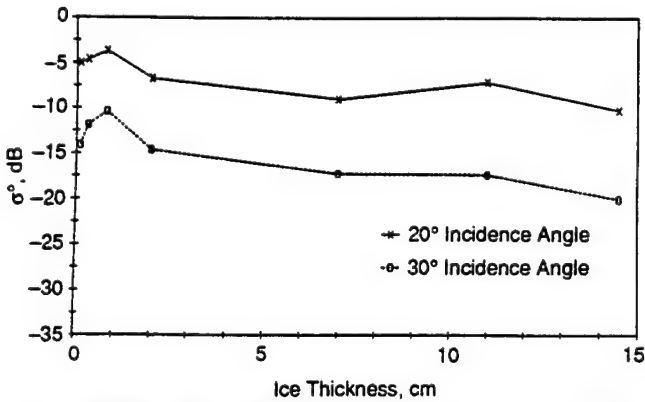


Fig. 9-7. Effects of ice growth on vertical polarization σ_0 at 5.3 GHz.

Vertically polarized data from 1984 are shown at 20° and 30° angles of incidence. For ice thicknesses greater than 3 cm, the scattering coefficients remained nearly constant, and possibly decreased when the ice thickness exceeded 12 cm. A more complicated response was observed for very thin ice during the transition from horizontal to vertical crystallographic orientation. The scattering coefficient increased immediately subsequent to ice formation, reached a maximum value at about 1 cm thickness, and then decreased, reaching a stable value after about 2 cm of growth. A similar behavior has been observed for measurements performed at 13.9 GHz on an ice sheet growing from an urea solution in the laboratory. Two mechanisms may contribute to the thin ice response: a high surface dielectric constant and surface roughening (e.g., frost flowers). Frost flowers or other macroscopic surface phenomena were not observed during the experiment. Although surface roughness changes cannot be ruled out on the basis of available observations, it seems more probable that a high dielectric constant explains the data. During initial ice growth, brine is expelled onto the ice surface and surface salinities as large as 70% have been reported [A. Kovacs, personal communication, CRREL, Hanover, New Hampshire, 1988].

Figures 9-8, 9-9, 9-10, and 9-11 show both the changing microwave signatures and the changing physical properties of the ice sheet for the 1985 experiments [Onstott, 1991]. Data were obtained at several frequencies and are shown at both like polarizations and at 0° and 40° angles of incidence. Two responses from open water were measured: at the beginning of the growth cycle with small ripples present and a rippleless case at the end of the growth cycle. Both open water points appear at the beginning of the time series.

In this experiment, at an oblique incidence angle (Figure 9-8), there is no evidence of a rise or fall in the thin ice backscatter response, though there is a weak suggestion of

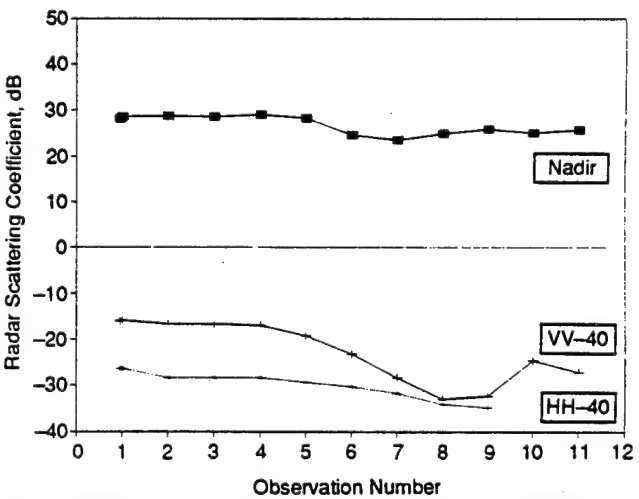


Fig. 9-8. The time series response of the backscatter coefficient at 5.0 GHz during the evolution of open water to new ice at nadir and 40° (VV and HH).

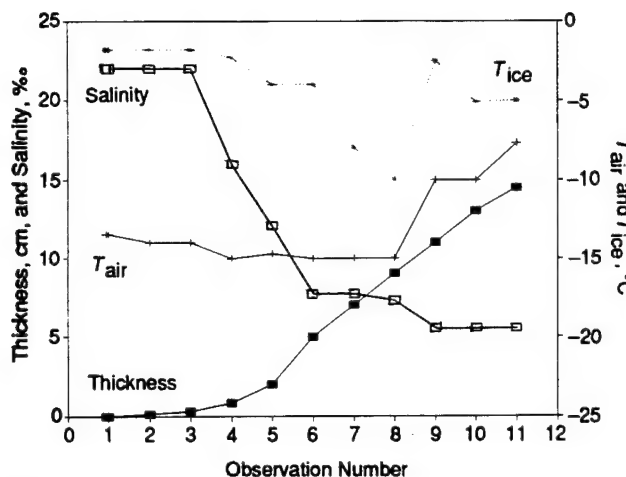


Fig. 9-9. Ice thickness, air temperature, ice temperature, and bulk salinity during the evolution of open water to new ice.

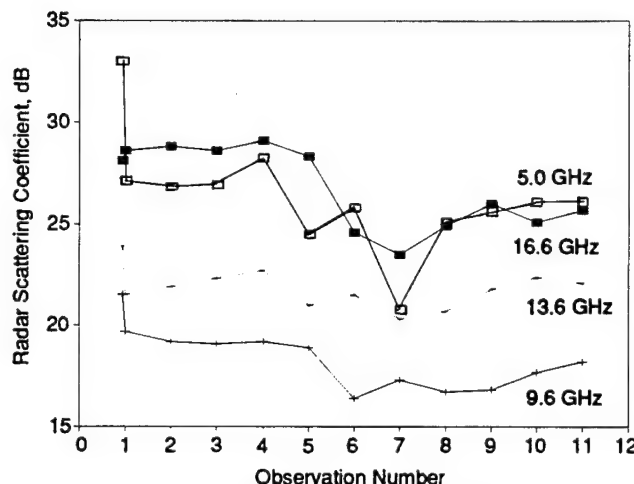
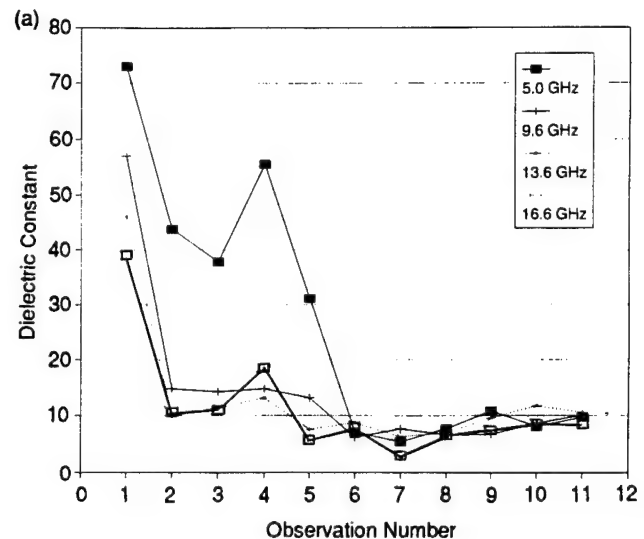


Fig. 9-10. The time series response of backscatter at vertical incidence during the evolution from open water to new ice shown as a function of frequency from 5.0 to 16.6 GHz.

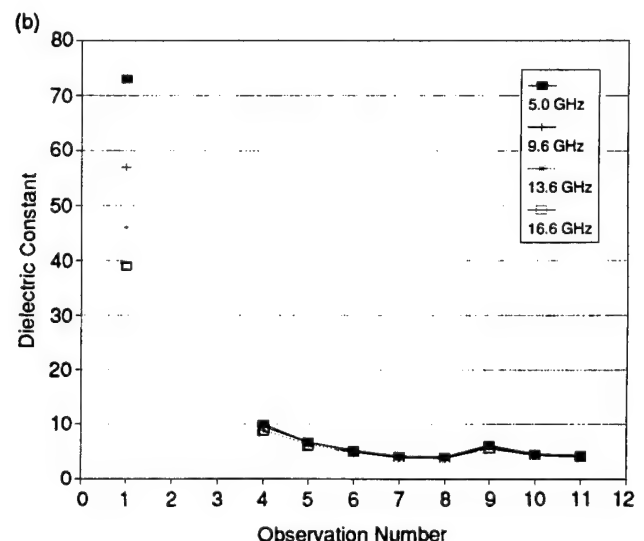


Fig. 9-11. The magnitude of the complex dielectric constant $|\epsilon_r^*|$ (a) as derived from the measurement of reflectivity and (b) by prediction.

that phenomenon at normal incidence angles (Figure 9-10). The backscatter is relatively constant (a slope of 0.05 with a mean square error of 0.4 dB) in the ice thickness range from 0 to 2 cm. Immediately subsequent to formation, the ice was very smooth visually, and measurements made later in the experiment indicated roughnesses of 0.05 cm root mean square (rms) with typical correlation lengths of 1 to 2 cm. The magnitude of the complex dielectric constant calculated from the scattering coefficient at nadir and at 5 GHz is (assuming a smooth surface) 42 ± 9 (Figure 9-11). This high value for the dielectric constant is consistent with the inferences made from the data in Figure 9-7.

Near-surface ice temperatures and bulk salinities decreased as the ice thickened. A change in both ice physical

properties and microwave properties is evident at about OB5. The crystallographic orientation and growth process has undergone a transformation at this point. Evidently, the change in bulk properties and processes is driving a change in the electromagnetic response.

Even under relatively controlled conditions, the ice sheet surface will undergo a metamorphosis with time. Single snow particles blown onto the ice sheet (OB8–OB11) increase the roughness of new ice by creating an “orange peel” surface. Onstott [1991] observed that when snow particles are deposited onto new ice, brine is wicked from the ice layer and deposited about the snow particles. The particles melt, dilute the brine solution, and then refreeze. This process creates small roughness elements that modify the backscat-

ter response. Bredow [1991] also investigated the relative contributions of volume scattering from brine pockets and scattering from the surface of thin saline ice. Modeled and predicted variations of X-band backscatter strength with incidence angle agreed well with a Kirchoff scattering model. Bredow also compared the measured radar pulse shape with simulations and found that the pulse shapes were primarily governed by surface scatter along with a weak volume scatter component that caused a slight broadening of the received pulse. At C-band, Bredow found that volume and surface scattering contribute about equally to the ice signature, presumably because of increasing penetration depth.

Linearly polarized radiometers operating at 10, 18, 37, and 90 GHz were used to observe the changing brightness temperature during the growth phase of thin ice. The variation in ice emissivity versus thickness during the growth phase is shown in Figure 9-12 for frequencies of 18, 37, and 90 GHz. The signature is characterized by a rapid increase in emissivity with increasing ice thickness up to a saturation level. Similar results at 10, 18, 37, and 90 GHz, vertical polarization and 50° incidence angle, are reported by Grenfell and Comiso [1986]. They show that emissivity increased from 0.525 to 0.95 at 10 GHz during the initial 50 mm of growth. They also found that emissivity at higher frequencies increased more rapidly with increasing ice thickness.

Results of concurrent radiometer measurements taken at C-band are shown in Figures 9-13 and 9-14. As expected, the emissivity at C-band saturates at substantially thicker ice than would be the case for higher frequencies. As discussed in the next section, the general shape of the curve

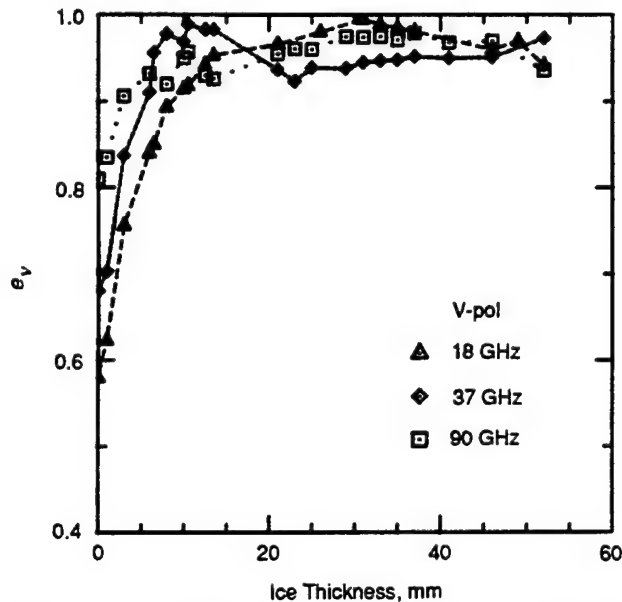


Fig. 9-12. Ice emissivity versus thickness for 18-, 37-, and 90-GHz vertical polarizations during initial growth of congelation ice [Grenfell et al., 1988].

is as would be predicted by a model that only allows for the incoherent addition of energy propagating through the ice. However, the excursion observed during the initial growth phase is undoubtedly a coherent effect associated with the first half of an interference fringe. Figure 9-14 demonstrates that a change in wavelength influences the periodicity of the first minimum.

Grenfell and Comiso [1986] compare the degree of polarization P (defined as the ratio of the difference between the

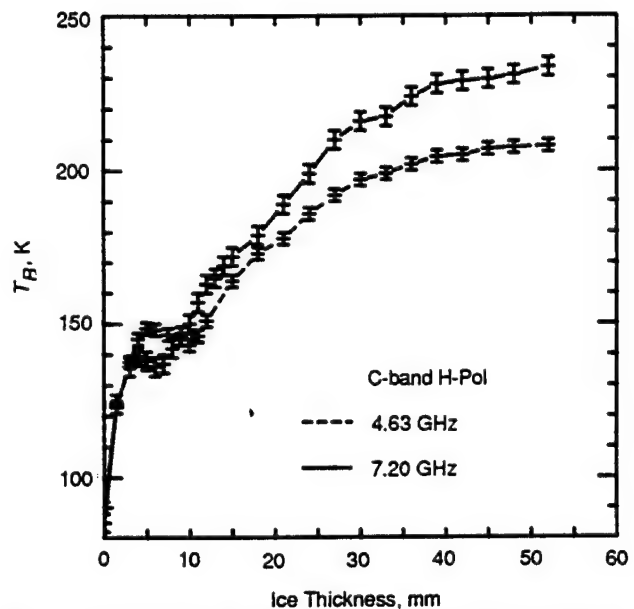


Fig. 9-13. Brightness temperature versus thickness during initial growth at two C-band frequencies and horizontal polarization. These observations cover the same ice sheet as in Figure 9-12 [Grenfell et al., 1988].

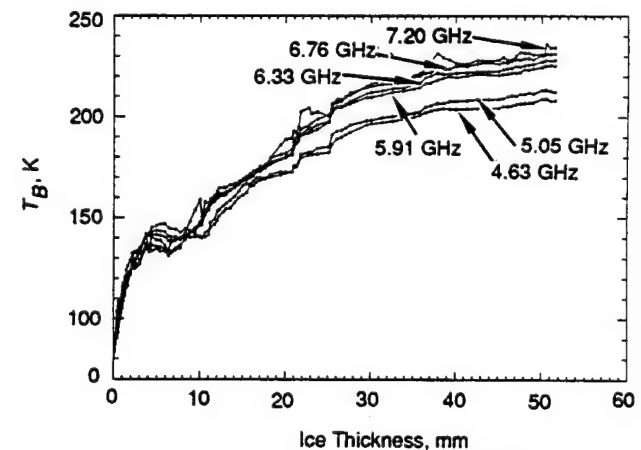


Fig. 9-14. Brightness temperature of CRRELEX'88 sheet 1B versus thickness at the six C-band frequencies of the Stepped Frequency Microwave Radiometer. The measurements were taken at horizontal polarization and a 35° incidence angle. Data from Figure 9-13 are included here without the associated uncertainty bars.

two linear polarizations divided by their sum at a single frequency), during the early growth stages. Polarization decreased by about 60% at 18 GHz as the ice grew to a thickness of about 20 to 25 mm—somewhat less than was required for the emissivity to reach a comparable saturation level.

Arcone et al. [1986] discussed a series of transmission measurements on ice samples extracted from the CRREL pond, as well as in-situ observations acquired by placing antennas above the slab and in the water below the ice slab. Data were evaluated to estimate real and imaginary parts of the dielectric constant. Each experiment required that the ice maintain mechanical integrity and hence the minimum ice thickness sampled was about 7 cm, for which a well-ordered columnar structure was established. Slabs removed from the pond to a refrigerated laboratory were subjected to cyclic cooling and warming.

Loss was measured in situ at 4.5, 4.8, 8.9, 9.0, 9.15, and 10 GHz and was found to vary between 4.1 and 8.7 dB/cm. Higher loss rates were associated with higher frequencies. The highest loss rates were also associated with the thinnest ice. Such ice would be relatively warm and hence would have the highest brine volume fraction. Arcone et al. [1986] reported real permittivities for samples removed from the pond. Values ranged from a maximum of about 4.5 for a slab temperature of -4°C to about 3.2 for cold slabs. The authors modeled the permittivity of high salinity thin ice and concluded that the real part varied from about 10 to about 4 for the temperature range -2° to -10°C in the frequency range 4.8 to 9.5 GHz. In general, Arcone et al. found that both the real and imaginary parts varied linearly with brine volume.

9.3.1 Thin Ice Data Interpretation

Variations in radar backscatter and microwave emission data during thin ice growth seem to be associated with a transition in ice physical properties. The onset of freezing is characterized by the formation of a thin skim of ice that quickly evolves into a complex of stellar crystals. The optical axis of these ice crystals is horizontal, their crystalline texture looks granular in vertical cross section, and brine is expelled onto the ice surface. This upper, transitional layer of thin ice tends to be brine-free and bubble-free. After 1 or 2 cm of growth, a columnar structure develops wherein brine is expelled downward or is trapped within isolated pockets.

These evolving ice processes force progressive changes in the ice sheet's electrical properties. In particular, Figure 9-11 shows that very new sea ice has a dielectric constant much smaller (about 75%) than that of open water. Between thicknesses of 1 and 2 cm, the dielectric constant reaches a maximum value. Consequently, the backscatter response at normal incidence increases with the largest changes at higher frequencies (Figure 9-10). These radar observations are consistent with the facts that: brine is gradually being expelled to the surface as the freezing process progresses; brine accumulation peaks (in this study

at 1 cm ice thickness); and a large percentage change in the dielectric constant occurs.

At 2 cm thickness (OB5), Figure 9-8, backscatter response for VV-40 decreased significantly while the backscatter at nadir remained within about 1 dB. This indicates that multiple processes were at work. The nadir response at 5 GHz directly tracked the change in dielectric constant, while the responses at oblique incidence were sensitive to both the change in dielectric constant and changes in surface roughness statistics.

After the ice is about 2 cm thick, growth proceeds by the accretion of ice to the base of columnar crystals. Based on the normal incidence backscatter data, the magnitude of the dielectric constant after columnar growth is initiated was about 7 (OB6 in Figure 9-11) and reached a minimum about 6 hours later [Onstott, 1991]. The surface roughness at this point was 0.05 cm rms and the ice surface temperature had cooled to -4°C . By accounting for the change in the dielectric constant between the transitional ice growth phase and columnar growth, the roughness for the initial skim was determined to be about 0.065 cm rms. This estimate was based on predictions using the small perturbation model.

As ice growth continues, ice nearest the surface cools and the surface brine layer dissipates. The thickening layer of highly emissive ice shields the radiometrically colder water. This causes brightness temperatures to elevate at a rate proportional to their frequency. Dissipation of the thin, highly concentrated brine layer at the surface of the ice sheet will result in an additional emissivity increase. Also, as Arcone et al. [1986] pointed out, lower temperatures decrease the bulk dielectric constant, which in turn causes a decrease in the backscatter response. Figure 9-10 reveals a 7.5-dB reduction in backscatter (5.0 GHz and VV) between ice 0 to 1 cm thick and ice 4 to 7 cm thick.

To examine the frequency dependence during the transition to a columnar ice structure, the average value of the dielectric constant for OB1 through OB5 and the minimum value measured immediately at the beginning of columnar growth are used, Figure 9-11(a). Associated changes in backscatter are 5, 3, 2, and 2 dB at 5.0, 9.6, 13.6, and 16.6 GHz, respectively. Since cooling is a top-down process, changes at higher frequencies are expected to occur first. This is verified by correlating the physical observations in Figure 9-9 with the reflectivity response at ice thicknesses between 0 and 2 cm. The time at which the drop in dielectric constant occurs is frequency dependent. This level was reached at a thickness of 5 cm (OB6) for 5.0 and 9.6 GHz, and 2 cm (OB5) for 13.6 and 16.6 GHz. This trend further illustrates that the magnitude of the backscatter response is driven by the dielectric constant and that an effective bulk dielectric constant is determined by penetration depth, both of which are frequency dependent.

A modified version of a model developed by Kovacs et al. [1986] was used to predict dielectric profiles so that penetration depths and bulk dielectric constants could be calculated at each frequency. For comparison, these results are included in Figure 9-11(b). The C-shaped salinity

profile further modulated the effective dielectric constant, especially at high frequencies, because of an increase in the brine volume in the uppermost portion of the ice sheet. Examination of the penetration depths provided in Table 9-1 shows that the backscatter response at 5.0 GHz was influenced by the entire dielectric layer for thicknesses from 0 to 2 cm. In contrast, at 16.6 GHz, the top 0.5 cm sets the absolute level of the backscatter response.

New ice grown under very calm conditions has a very smooth ice-air interface; however, the surface may become slightly roughened with the deposition of single snow crystals. This observation and Bredow's [1991] result at C-band that volume and surface scattering contribute about equally to the ice signature for very smooth ice argue that backscatter data at C-band and higher frequencies provide information about the upper layers of the ice. Radiometric results presented in Figures 9-12, 9-13, and 9-14 argue that at C-band frequencies and lower, brightness temperature data represent an integration of effects distributed throughout the thin ice sheet. In particular, Figure 9-14 shows an oscillatory dependence of brightness temperature of young sea ice with frequency and ice thickness. This dependence indicates that microwave emission from young sea ice also includes a coherent process.

Apinis and Peake [1976] derive an expression for coherent emission from a slab:

$$\varepsilon = 1 - r = \frac{(1 - r_i)(1 - Ar_w)}{(1 + Ar_i r_w + 2\sqrt{Ar_i r_w} \cos 2B\ell)} \quad (1)$$

where r is the composite power reflection coefficient
 r_i is the power reflection coefficient at the air-ice interface
 r_w is the power reflection coefficient at the ice-water interface
 $A = \exp(-4\alpha\ell)$
 α is the attenuation coefficient in ice
 B is the phase constant in ice
 ℓ is the radiation path length

This expression shows that the emissivity is a damped, periodic function of ice thickness. Of course, interface roughness will destroy coherence and, if the surface is sufficiently rough, the average emissivity is given by

TABLE 9-1. Predicted penetration depths for sea ice with thicknesses from 1 to 8 cm [Onstott, 1991].

Ice thickness, cm	Penetration depth, cm, for given frequencies			
	5.25 GHz	9.6 GHz	13.6 GHz	16.6 GHz
1	>1	0.8	0.5	0.4
2	2.0	1.0	0.7	0.5
4	3.3	1.6	1.0	0.8
8	3.7	1.6	1.0	0.8

$$\langle \varepsilon \rangle \approx \frac{(1 - r_i)(1 - Ar_w)}{(1 - Ar_i r_w)} \quad (2)$$

This very simple expression depends only on the reflection coefficients at the two interfaces and the product of the attenuation coefficient and path length. Therefore, if the bulk electrical properties are known, the total incoherent emissivity is a function only of the slab's mean thickness. The monotonic increase in emissivity predicted by Equation (2) is supported by data for ice with significant surface roughness [Swift et al., 1986]. (Equation (2) does not reduce to the proper value for zero slab thickness. An empirical equation has been introduced by Swift et al. [1986] to correct this limitation.)

Variations in emissivity shown in Figures 9-12 and 9-14 can be understood in terms of incoherent and coherent processes. The signatures in Figure 9-12 are characterized by rapid increases in emissivity with increasing ice thickness up to a saturation level—this is the functional form predicted by the incoherent propagation model. The frequency, ice thickness, and ice extinction coefficients will determine when the saturation level will be reached. To show this relationship more clearly, the attenuation coefficient, A , can be expressed as

$$A = e^{-4\alpha\ell} = \exp\left(\frac{-8\pi n_i d_0}{\lambda_0}\right) \quad (3)$$

where n_i is the imaginary part of the refraction index of sea ice. Because n_i is expected to be reasonably constant over the microwave band of frequencies, Equation (3) shows that the attenuation increases as the frequency of observation increases. This result agrees with the data trends in Figure 9-12, which indicate that for a given ice thickness, the emission from the underlying water decreases as the operating frequency increases.

The results of concurrent measurements taken at C-band are shown in Figure 9-14. Since the C-band wavelength is much larger, saturation is reached at substantially thicker ice. This signature is very similar to that predicted by the incoherent model, except for the excursion noted during the initial growth phase. This is undoubtedly a coherent effect associated with the first half-wave interference fringe. The interference patterns at 4.63 and 7.20 GHz are distinct. From Equation (1), we expect to observe a maximum when $1/\lambda_i = 0.25$ and a first minima at $1/\lambda_i = 0.5$.

Because the ice thickness was frequently measured, the data can be used to solve for the average dielectric constant of the ice layers. St. Germain and coworkers [St. Germain, K. M., C. T. Swift, and T. C. Grenfell, Determination of dielectric constant of young sea ice using microwave spectral radiometry, submitted to the *Journal of Geophysical Research*] derived a relationship between the real part of the dielectric permittivity and ice thickness given by

$$\epsilon_r' = \frac{1}{2} \left\{ \left(\frac{c\ell}{d_0 f \lambda_i} \right)^2 \pm \sqrt{\left(\frac{c\ell}{d_0 f \lambda_i} \right)^4 - 4 \left(\frac{c\ell}{d_0 f \lambda_i} \right)^2 \sin^2 \theta_i} \right\} \quad (4)$$

Table 9-2 presents a listing of thicknesses that correspond to the first and second quarter-wave interference fringes. Using data from Table 9-2 along with Equation (4) allows one to solve for the dielectric constant of ice. Results are presented in Figure 9-15, where a linear regression has been plotted through the data points. This figure shows that the dielectric constant of ice during the first centimeter of growth is approximately three times larger than results quoted for thick first-year ice, which is consistent with results reported above. St. Germain and coworkers evaluated the frequency dependence of the dielectric constant and found that n_i is equal to about 0.038 ($\epsilon = 0.215$).

TABLE 9-2. Mean ice thicknesses measured at the first maximum $d/\lambda = 0.25$ and the first minimum $d/\lambda = 0.50$ in the time series brightness temperature data for each frequency.

Frequency, GHz	$d_0 [d = \lambda/4]$, mm	$d_0 [d = \lambda/2]$, mm
4.63	5.0	10.5
5.05	4.5	10.0
5.91	4.0	9.0
6.33	4.0	8.0
6.76	3.5	7.5
7.20	3.0	7.0

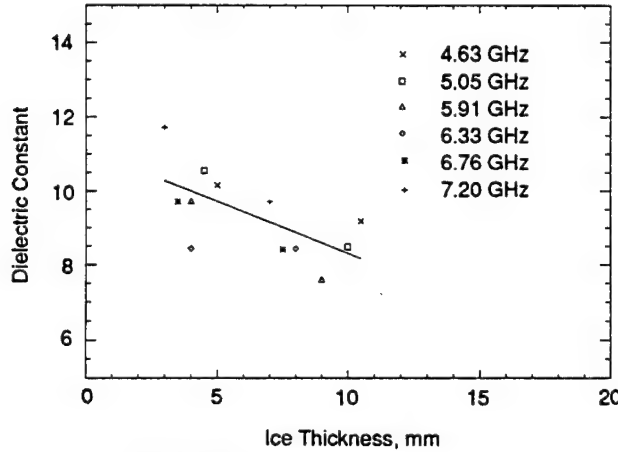


Fig. 9-15. Calculated dielectric constant as a function of the ice thickness.

9.4 UREA ICE

Urea ice is structurally identical to saline ice [Gow, 1984]. Under calm conditions it develops a columnar structure characterized by thin plates of pure ice that separate vertical planes of pockets filled with urea solution. Because urea is a covalent molecule, an urea solution is less conductive than brine. Nevertheless, at frequencies above 10 GHz and at temperatures near 0°C, the imaginary parts of the dielectric constant of saline water and even fresh water are identical [Ulaby et al., 1982, p. 2023]. The real part of the dielectric constant of saline water is a few percent less than that for fresh water. The complex permittivity of both fresh and saline water is strongly frequency dependent over 1 to 100 GHz.

Radar backscatter measurements of urea ice were acquired because urea is noncorrosive and, hence, large quantities can be easily managed in an indoor facility. Data were collected with 13.9 and 35 GHz polarimetric scatterometers during the growth and evolution of several urea ice sheets.

Normalized radar cross sections of smooth urea ice at different angles of incidence greater than 20° and at like and cross polarizations are shown in Figure 9-16 at 35 GHz. Figure 9-17 shows like-polarization cross sections at 13.9 GHz corrected for antenna beamwidth effects for both smooth urea ice and saline ice. Both figures show a strong, exponential decrease in cross section with increasing incidence angle although there is almost a 20 dB difference

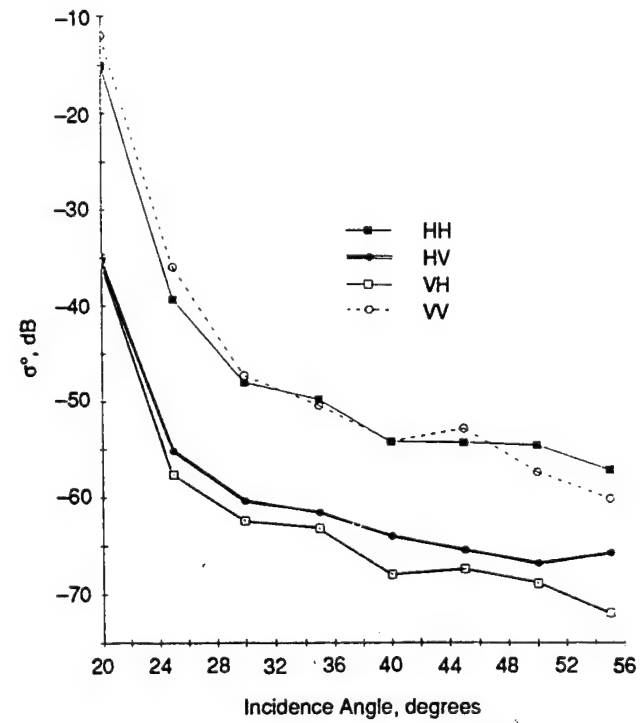


Fig. 9-16. Polarimetric normalized radar cross section (σ^0) of smooth urea ice at 35 GHz [Colom, 1991].

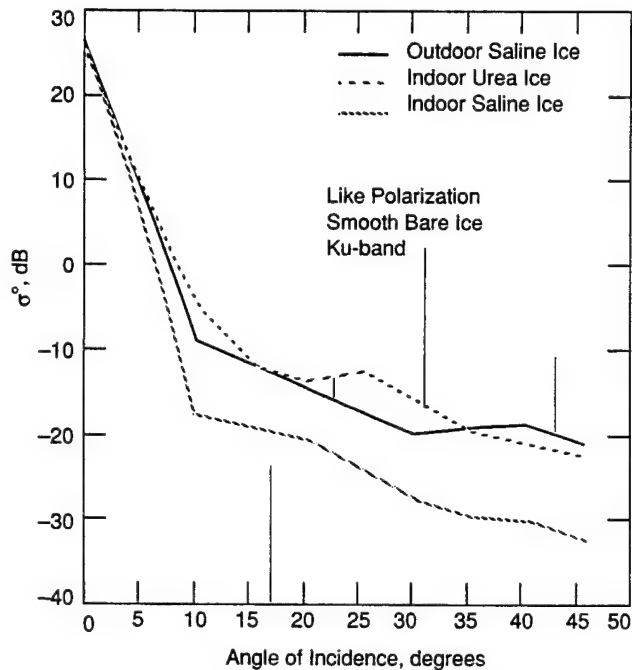


Figure 9-17. Beamwidth corrected backscatter coefficients for two saline ice sheets and an urea ice sheet. One of the saline sheets and the urea ice sheet were grown indoors. The second saline sheet was grown on an outdoor pond.

between the 13.9 and 35 GHz data at large angles at like polarization. Also at larger angles, the 13.9 GHz urea ice data are about 10 dB lower than those for saline ice, possibly because of the difference in dielectric constant between the two materials. Because the ice was smooth and there was no distinction between the HH- and VV-polarization components, any residual power at 13.9 GHz is attributable to volume scattering. The low power levels at large incidence angles indicate that the inclusions must be small compared to a wavelength.

An experiment was conducted to discriminate between surface and volume scattering. A smooth sheet of urea ice was grown indoors until it was 30.5 cm thick. The surface was smooth enough so that surface scattering was negligible. The temperature of the room was slowly raised over a period of 48 hours to observe any change in the resultant backscatter. It was anticipated that any changes could be primarily attributed to volume scattering. Figure 9-18(a) shows the results of this experiment at 35° and 45° of incidence where σ was plotted versus ice temperature. The trends shown are also consistent for each of the four polarizations plotted in Figure 9-18(b). As expected, σ is lower for a larger incidence angle. The value of σ is also low for the smooth ice at temperatures of approximately -9° and -8° C. The value of σ increases slowly until it reaches a maximum around -1° C and then drops off. During the experiment, air bubbles 2 to 5 mm wide were observed near the surface for a temperature range of -2° to 0° C. Bubbles formed because pockets of urea solution drained, leaving cavities partially or completely filled with air. The ice sheets free of

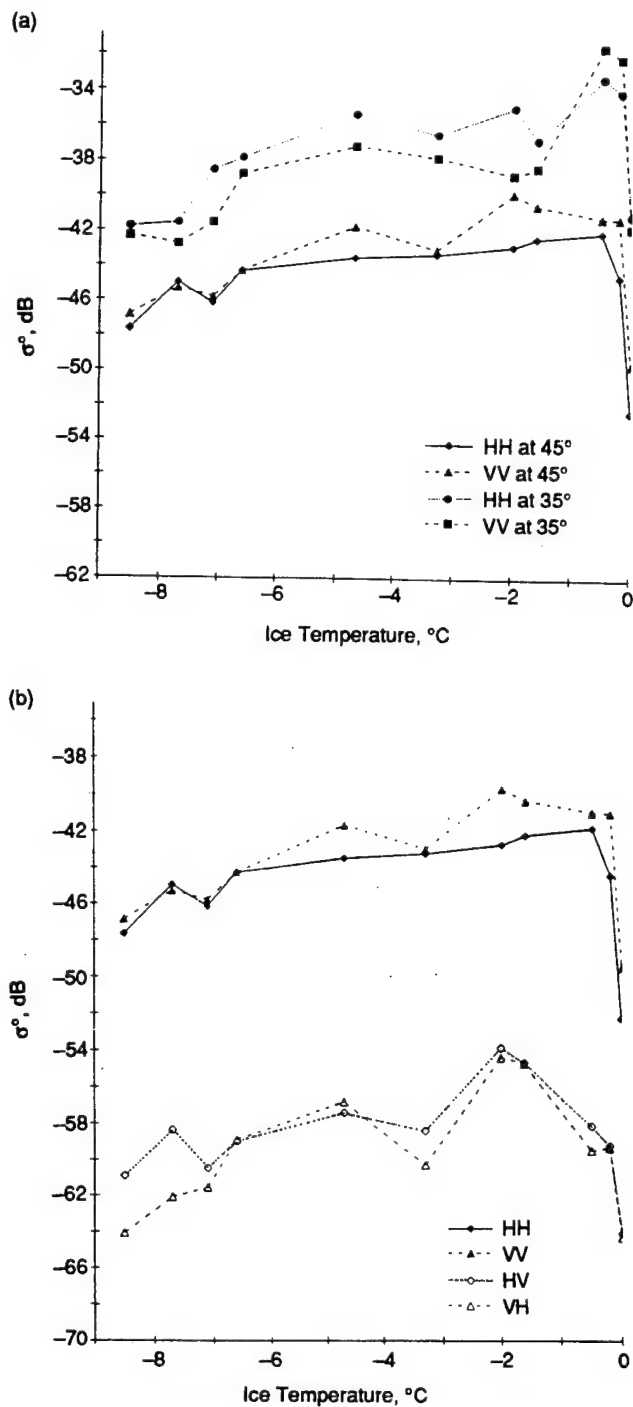


Fig. 9-18. Normalized radar cross section (σ^0) versus ice temperature at (a) 35° and 45°, and (b) polarimetric cross sections at 45° [Colom, 1991].

an urea solution present low loss to the microwave signal, scattering more energy and explaining the maximum at about -1° C. Eventually, water filled the air pockets and covered the ice sheet, masking the scatterers located below the surface. Indeed, the scattered signal decreased considerably at 0° C.

9.5 DESALINATED ICE

Ice sheets were left in place on the outdoor pond at CRREL for up to several months. One ice sheet, grown in January 1988, grew to a thickness of 16 cm, at which point ice cubes were distributed on the surface to simulate roughness. The ice sheet was left undisturbed until late January when unseasonably warm air temperatures caused the surface to melt. Fresh water so formed flushed much of the brine from the ice sheet. Periods of growth and melt followed until late February, when the ice was about 31 cm thick. The salinity of the ice in the top 5 cm of the ice sheet was less than 0.5‰. The density in the top 10 cm of the ice was about 0.89 mg/m³.

Measurements were made in 1989 on the desalinated ice blocks as mentioned in Section 9.2 [Gogineni, S. P., J. W. Bredow, A. J. Gow, T. C. Grenfell, and K. C. Jezek, Microwave measurements over desalinated ice under quasi-laboratory conditions, submitted to *IEEE Transactions on Geoscience and Remote Sensing*, 1992]. Salinities in the upper 5 cm were less than 1.0‰ with densities in the upper 10 cm varying between 0.84 and 0.87 mg/m³. Ice characteristics from both the 1988 and 1989 experiments appear in Table 9-3.

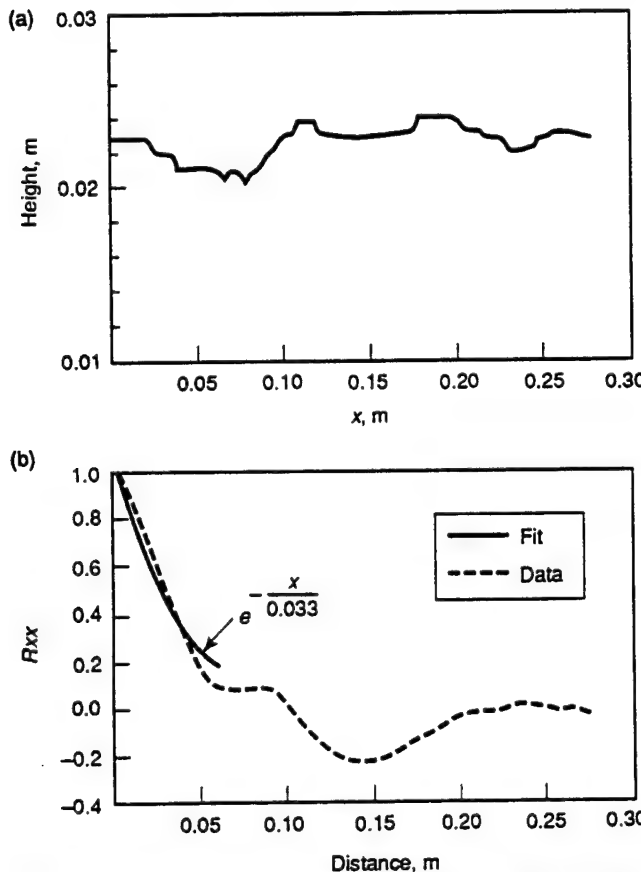


Fig. 9-19. For desalinated ice blocks studied during CRRELEX'89: (a) surface profiles, and (b) computed autocorrelations and minimum-mean-square-exponential fits.

TABLE 9-3. Ice surface and internal characteristics.

Year	RMS height, cm	Standard deviation, cm	Correlation length, cm
1988	0.18	0.07	2.5
1989	0.08	0.15	3.3
Year	Bubble size, mm	Correlation length, mm	Bulk density
1988	0.5	—	—
1989	0.45	1.5–2.0	0.844

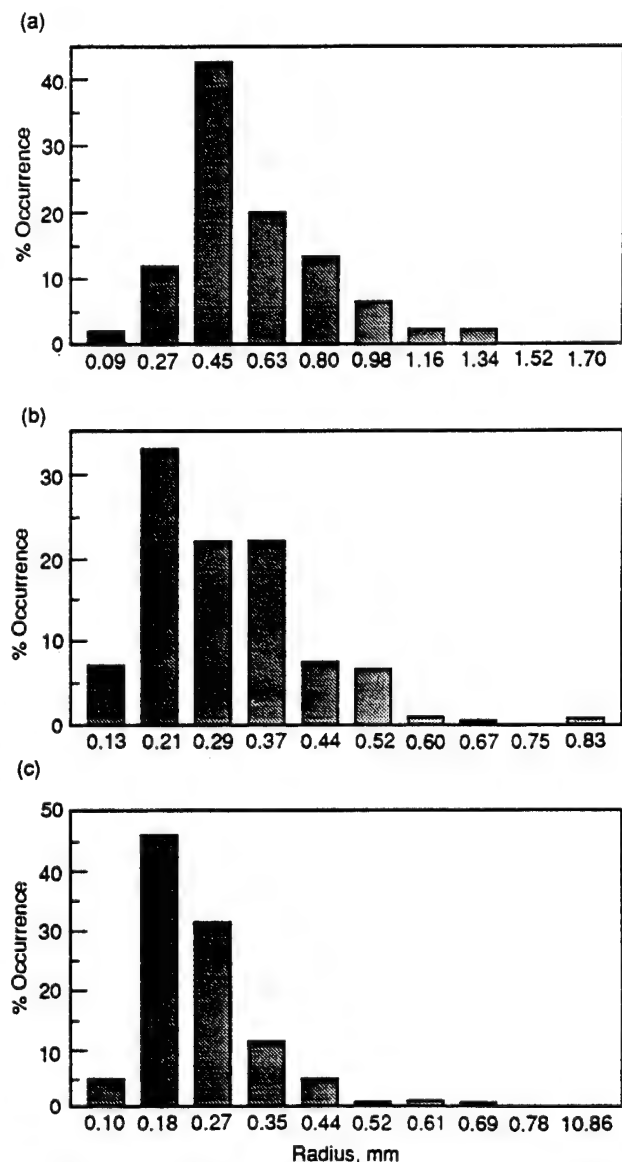


Fig. 9-20. Air-bubble size distribution from the (a) top, (b) middle, and (c) bottom of a block of desalinated ice studied during CRRELEX'89.

Figure 9-19(a) shows a typical surface roughness profile obtained using a contour gauge. The corresponding autocorrelation function is shown in Figure 9-19(b). Bubble size and distribution were determined from photographs of vertical and horizontal thin sections taken from the desalinated blocks. Bubbles were highlighted and the images digitized. Figure 9-20 shows a typical bubble distribution obtained from the desalinated ice.

Figure 9-21 shows the results of radar backscatter measurements made on the desalinated ice at C-band. The bars represent the total uncertainty in the scattering coefficient estimate resulting from random and systematic errors. The upper curve is the maximum value of σ obtained by increasing the rms height by one standard deviation and reducing the correlation length by one standard deviation. The minimum values of σ , represented by the lower dashed curve, were determined by decreasing the rms height by one standard deviation and increasing the correlation length by one standard deviation. The decay of σ with incidence angle is similar to that observed on saline ice. This decay indicates that surface scattering is the dominant source of scattering. To confirm this, data were collected over a 24-hour period to determine the temperature dependence of the scattering coefficient (Figure 9-22). At X-band, scattering from the ice sheet decreased by more than 10 dB when the ice temperature increased from about -5° to -3°C . There was negligible change at C-band. The decrease in scattering at X-band can be attributed to the presence of moisture on the surface, which reduced the volume contribution. However, because we did not observe a corresponding reduction at C-band, we concluded that scattering at C-band is dominated by the ice surface.

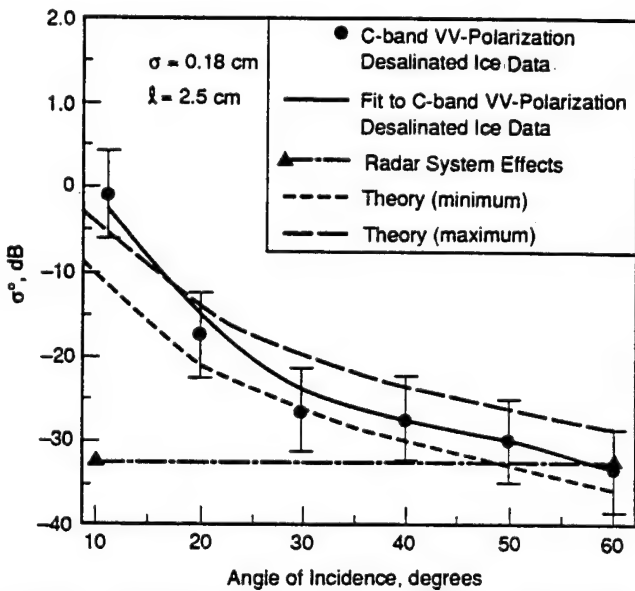


Fig. 9-21. Backscatter cross section of desalinated ice sheet at C-band, as determined from data obtained during CRRELEX'88, compared with predictions of the Small Perturbation Method.

The dependence of emissivity on frequency and nadir angle are shown in Figure 9-23 for the desalinated ice measured during February 1988. The error bars indicate the standard deviation of the results of twelve sets of observations. The resulting frequency spectrum, Figure 9-23(a), shows a very weak frequency dependence. The emissivity spectra measured on the desalinated blocks created in 1989 show more structure (Figure 9-24). The maxima at 6 and 37 GHz are suggestive of interference fringes, however, the variation with incidence angle is quite weak (Figure 9-25). The differences between the 1988 and 1989 ice sheet simulations are pronounced. Removal of the blocks in 1989 no doubt allowed brine to drain from the entire slab. Low block salinities would have resulted in a decrease in the optical thickness of the ice. That the ice sheet was left in place in 1988, would suggest there was still substantial brine in the lower part of the ice slab. Higher salinities in the lower portion of the ice sheet could have caused sufficient attenuation to eliminate fringe effects.

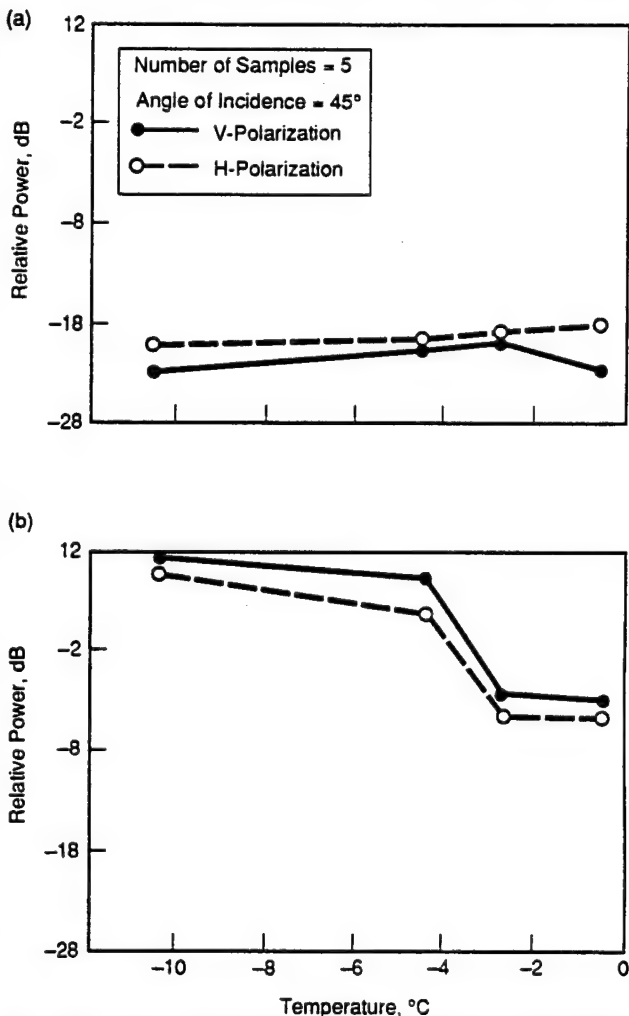


Fig. 9-22. Effect of temperature on backscatter from desalinated ice at (a) C-band and (b) X-band as determined from data obtained during CRRELEX'88.

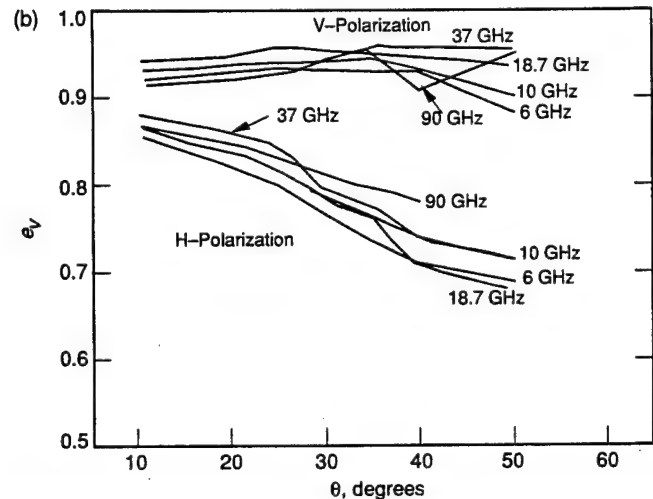
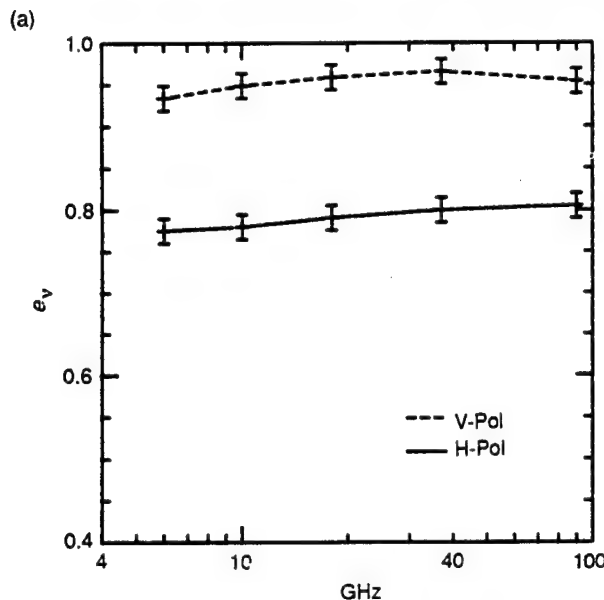


Fig. 9-23. (a) Emissivity spectra from 6 to 90 GHz of a desalinated ice sheet at V- and H-polarizations. (b) Microwave emissivity versus incidence angle for the desalinated pond ice. Curves give the results for the five observation frequencies.

9.6 PANCAKE ICE

Pancake ice was simulated by installing a wave-generating paddle at one end of the outdoor pond. Pancakes were formed with thicknesses of about 7 cm. The surface emissivity increased as the ice froze, but never achieved the values previously recorded for congelation ice. C-band observations indicated that the increase in brightness temperature was linear with thickness, contrary to the nonlinear relationships discussed earlier. This linear variation existed because the brightness temperature was being modulated more strongly by varying concentrations of ice and slush-water. As time and thickness increased so could the concentration of ice, however no quantitative method

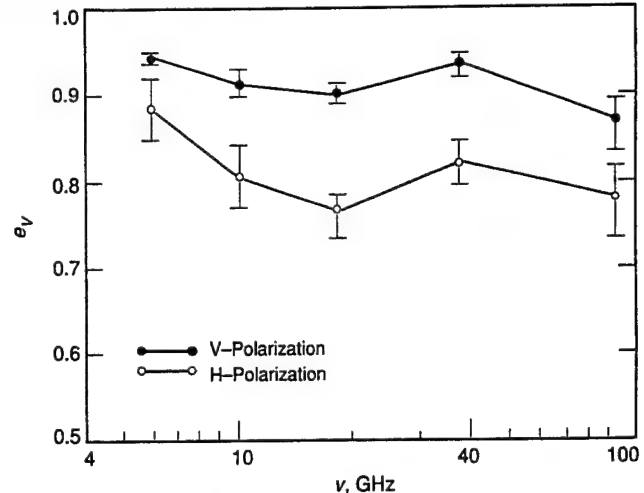


Fig. 9-24. Microwave emissivity versus frequency for the desalinated blocks in January 1989. The error bars denote the standard deviation for four independent samples.

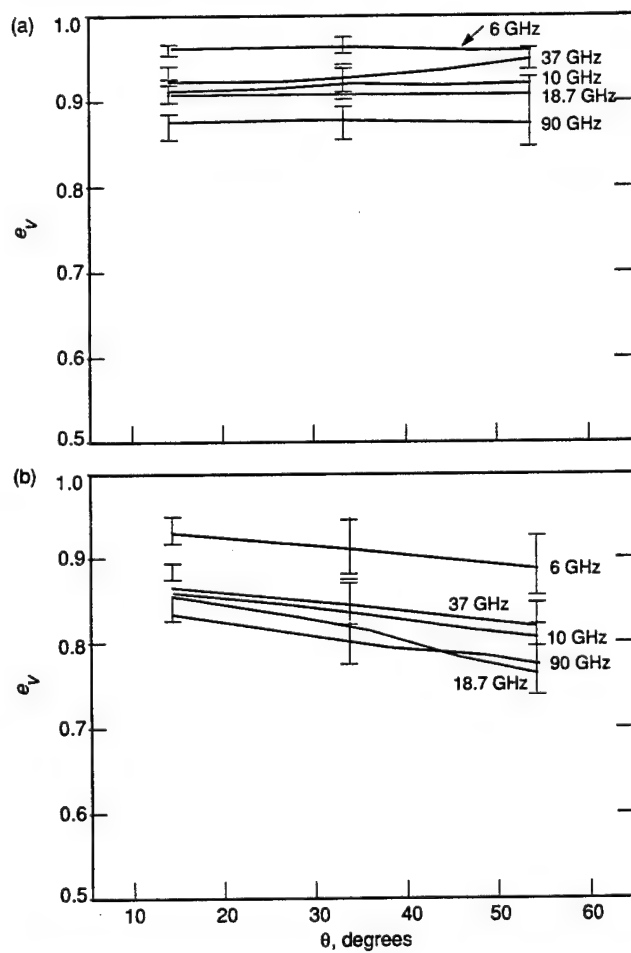


Fig. 9-25. Microwave emissivity versus incidence angle (a) V and (b) H polarizations for the desalinated blocks.

for estimating the relative percentage of ice and slush was available.

9.7 SURFACE EFFECTS

The vertical distribution of brine changes rapidly as the ice sheet grows from the melt. As evidenced by the above results, this early redistribution of brine and the formation of brine pockets within the ice has a primary influence on microwave signatures. As the ice sheet continues to age, secondary metamorphic processes begin to rework the surface. Natural processes such as mechanical deformation, frost flowers, and snow cover will each produce different but characteristic scales of surface roughness and near-surface inhomogeneities that modify, and may eventually dominate, the electromagnetic response.

Several types of surface processes were duplicated in the indoor and outdoor laboratories. Results of those experiments are discussed in the following sections.

9.7.1 Roughened Surface

A roughened ice sheet was simulated by mechanically raking and gouging the ice surface. This produced an irregular texture with 2- to 3-cm height variations. Figure 9-26 shows the angular dependence of the backscattering coefficient for smooth, rough, and snow-covered ice at 9.6 GHz (HH-polarization). Roughening causes the scattering coefficient to increase by about 10 dB over the results for smooth ice at incidence angles greater than 20°. The shape of the backscattering curve is indicative of surface scattering. However, a volume contribution may be comparable to the surface term at large incidence angles because a volume term must be included to model the scattering from smooth saline ice. Of course, as the surface gets rougher, the volume term becomes less and less important.

Radiometer data were collected on the same ice sheet. Before roughening, the ice sheet was optically thick and there was no clear dependence of emissivity on frequency

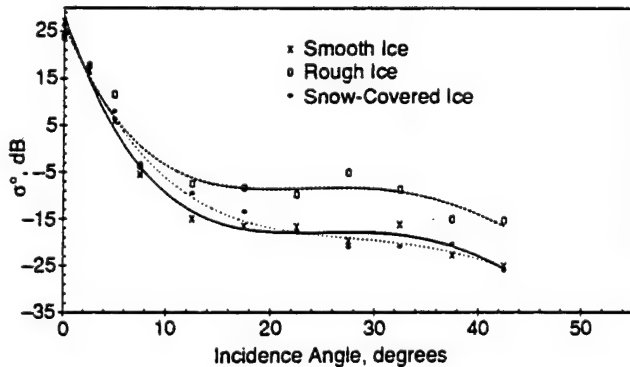


Fig. 9-26. Effects of surface conditions on backscatter angle response at 9.6 GHz and HH polarization.

and incidence angle at vertical polarization. At horizontal polarization, the undisturbed ice showed the usual frequency and incidence angle dependence [Grenfell and Comiso, 1986]. After roughening, all of the horizontal observations at 18 and 37 GHz showed a large increase in emissivity (Figure 9-27). For vertical polarization, the 10- and 90-GHz emissivities decreased while the 18-GHz emissivity increased at 40° and 50° incidence. The 37-GHz emissivity increased at 60°. Grenfell and Comiso [1986] argued that the results at 18 and 37 GHz were explained by the fact that the scale of roughness was close to the wavelengths at these frequencies. All other results were within the range of expected values from conventional scattering and emission theory of rough surfaces [Ulaby et al., 1982]. When the rough layer was scraped off, the emissivities decreased further, suggesting that a thin liquid skim had formed on the smooth surface.

9.7.2 Rubble Surface

A rubbed ice surface was created by spreading fresh ice chunks on top of an 8-cm thick ice sheet. At this thickness, the physical properties of the ice sheet are only slowly changing, so sequential microwave observations essentially view the same material. The ice sheet grown for this experiment was very smooth (0.05 cm rms) and was snow-free. Ice surface temperatures prior to application of the ice chunks were about -16°C. Warmer air temperatures later in the experiment and after the chunks were applied caused the ice surface temperature to rise to about -8°C. The rubble layer was about 2.5 cm thick and photographs of vertical thick sections are shown in Figure 9-28. Environmental descriptions of bare and rubble-covered ice sheets are listed in Table 9-4. The scale of roughness simulated here is similar to that observed for pancake ice. Roughnesses greater than this are usually associated with large-scale deformation processes (i.e., strewn blocks and rubble).

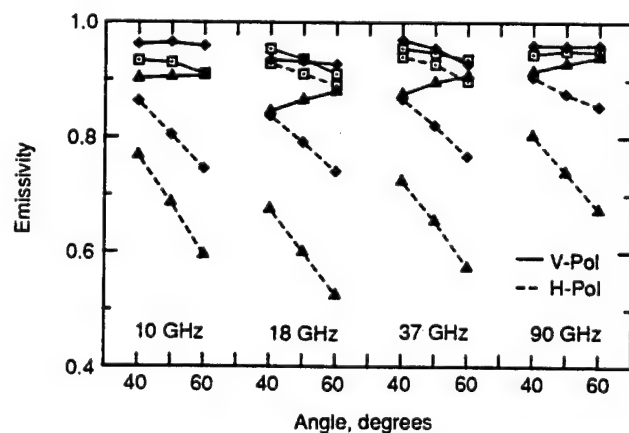


Fig. 9-27. Comparative spectra showing the effects of surface roughness for the natural surface (diamonds), the same surface after roughening (squares), and after the rough upper surface was scraped off (triangles) [Grenfell and Comiso, 1986].

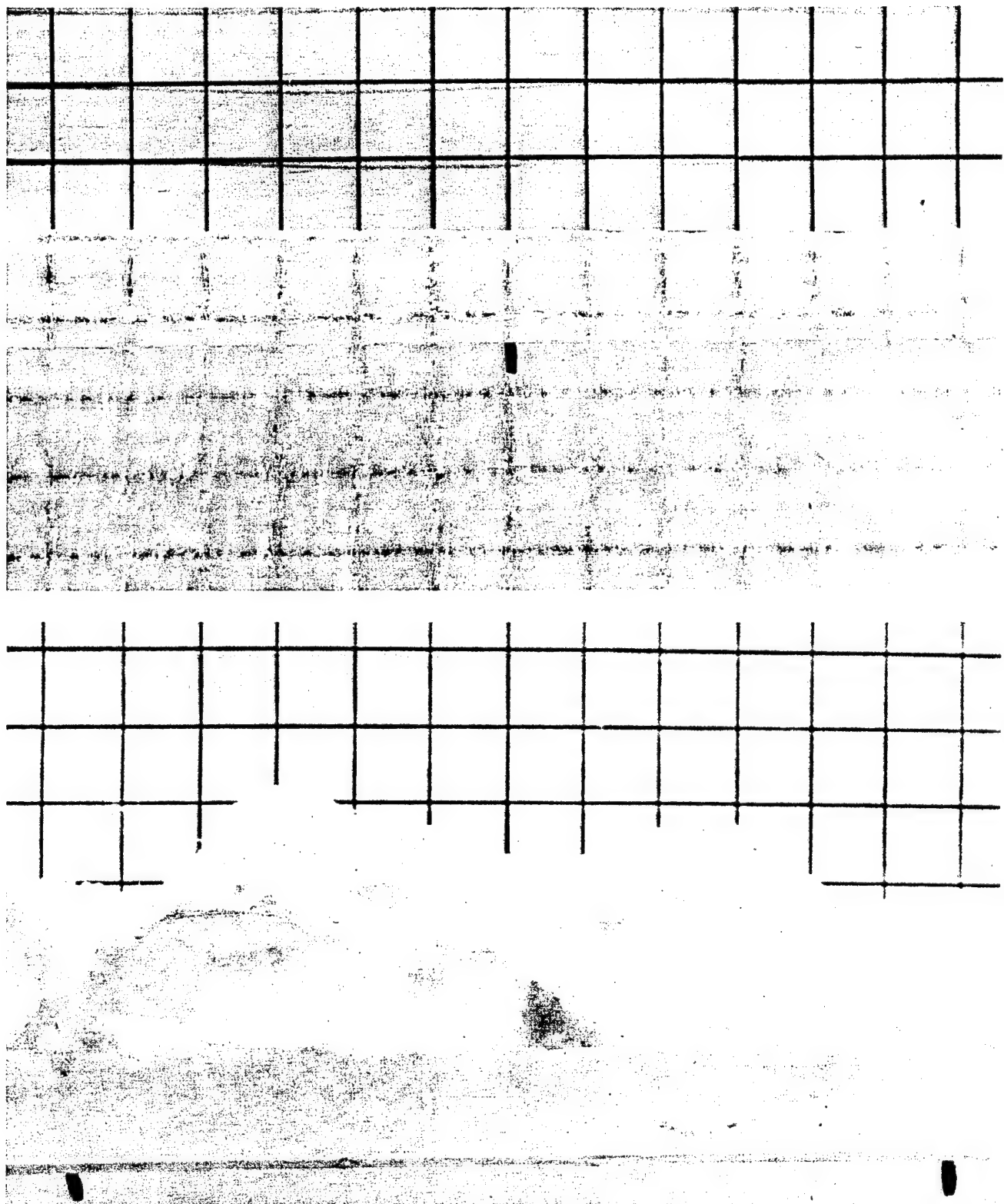


Fig. 9-28. Vertical thick sections showing the air-ice interface for (a) slightly rough and (b) very rough grey ice. The grid spacing is 1 cm.

TABLE 9-4. Summary of the physical property observations for a grey ice sheet with a smooth and rough surface [Onstott, 1990].

Description	Grey ice smooth	Grey ice rough
Ice age	70 hours	100 hours
Ice thickness	7.5 cm	8.3 cm
Snow cover	none	none
$\sigma_{\text{roughness}}$	0.048 cm rms	0.544±0.053 cm rms
$\ell_{\text{correlation.length}}$	0.669 cm	1.48 ± 0.334 cm
T_{air}	-23.5 to -26.6°C	-14.6 to -18.1°C
T_{ice}	-16°C	-8°C
Bulk salinity	10.1‰	10.1‰ (ice sheet)
Top 5 cm		0‰ (roughness elements)

A few comments are necessary before presenting and comparing data. First the magnitude of the dielectric constant of bare ice is about twice that of fresh ice. Consequently, the backscatter cross sections from rough ice require an increase of about 3.7 dB to account for this difference. Relative to the radar wavelength, there is almost an order of magnitude change in surface roughness between the bare and rubble-covered ice sheets (Figure 9-29). At 5 GHz and like polarization, backscatter increases by about 19 dB at 40°, while at 10.0 GHz it increases about 22 dB after the surface has been roughened.

Passive microwave observations of the same scene yielded results similar to those reported earlier for raked surfaces. At 6 GHz and vertical polarization, the emissivity was constant before and after addition of the rubble layer. As shown in Figure 9-30, the emissivity decreased at the higher frequencies after the rubble was added. This response is likely explained by the fact that the rubble layer is rough at higher frequencies but smooth at C-band. Horizontal polarization observations showed that the emissivity at low frequencies rose slightly, but decreased at higher frequencies. As presented in Figure 9-31, the C-band data between 4.9 and 7.2 GHz included a maximum at the low frequency and a minimum at the high frequency, consistent with a first-order fringe pair from a 2-cm layer with a dielectric constant of 1.15.

A rubble layer was deposited on the surface of an urea ice sheet. Chunks of urea ice 2 to 5 cm square were spaced over a new, smooth urea ice sheet. Figure 9-32 shows backscatter coefficients for rough ice versus the angle of incidence. As expected, backscatter is stronger for this case than for the smooth ice case (Figure 9-16), especially at large incidence angles.

9.7.3 Snow-Covered Surface

Snow cover is ubiquitous over sea ice and can significantly affect the microwave backscatter or emissivity [Kim

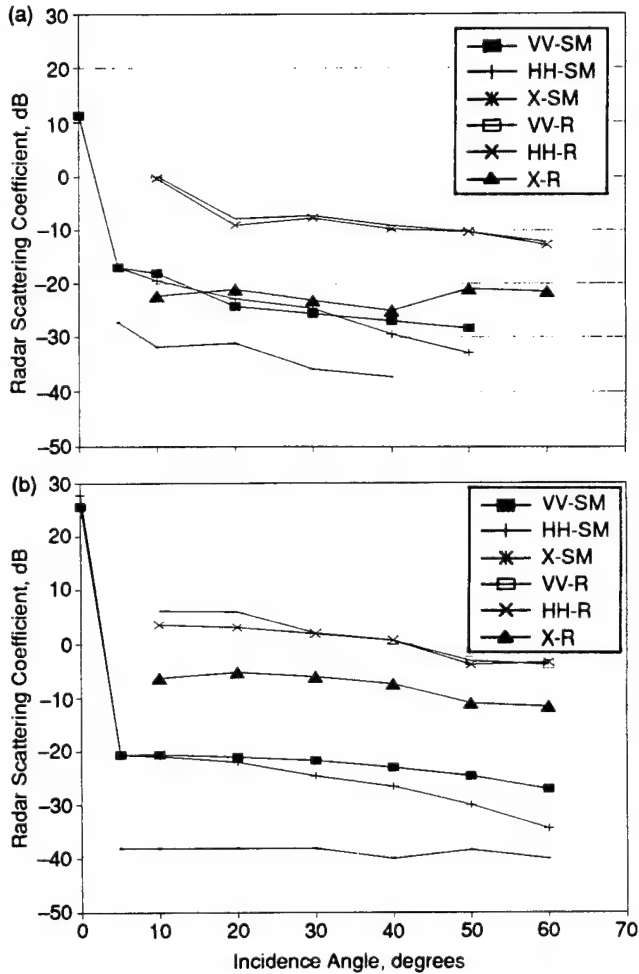


Fig. 9-29. Radar scattering coefficient response for ice with a rough (R) or smooth (SM) surface. The response is shown at (a) 5.0 and (b) 10.0 GHz.

et al., 1984; Comiso et al., 1989]. Snow cover overtly modifies the electromagnetic signature of sea ice simply by addition of another layer of scattering particles. But the influence of snow cover on sea ice is also more subtle. Snow acts as an insulator and a mechanical load. This combination serves to release brine from just below the ice surface. The brine is subsequently wicked up into the snow layer [Grenfell and Comiso, 1986]. If the snow is thick enough, the load can be sufficient to depress the ice sheet below its natural freeboard, and flooding will occur. Several laboratory experiments were carried out to assess the effects of a snow cover over sea ice and the subsequent flooding and refreezing of a basal slush layer on active and passive microwave signatures.

Naturally falling, dry snow accumulated on a saline ice sheet grown on the outdoor pond. The snow layer reached a thickness of 4.5 cm. Snow-covered and smooth ice returns at 9.6 GHz were similar in magnitude, indicating that thin snow cover has negligible effect on backscattering from

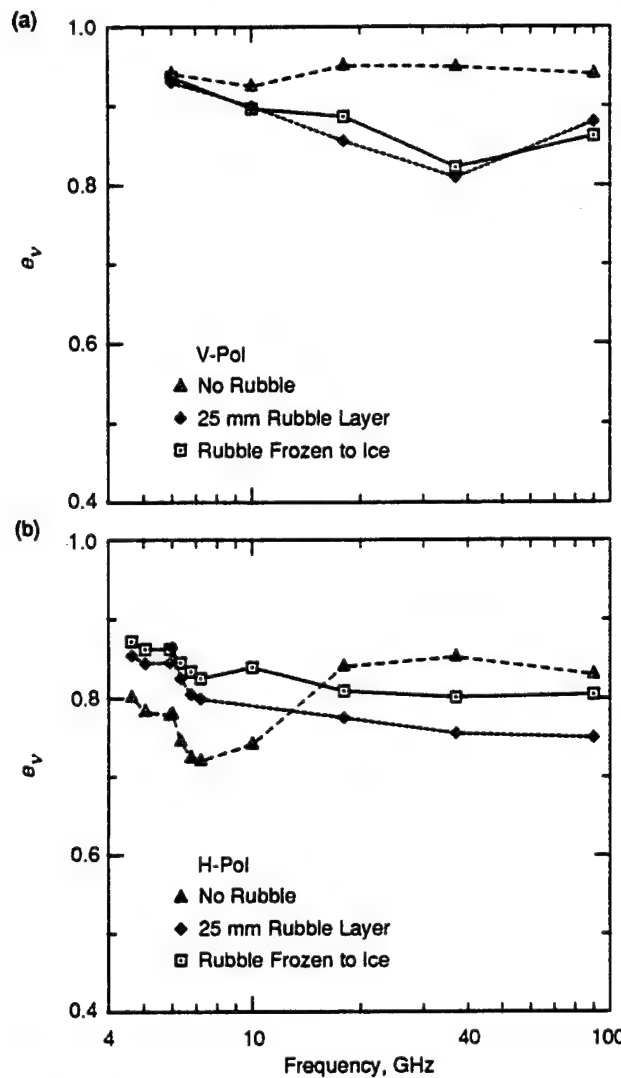


Fig. 9-30. Emissivity spectra of 150-mm-thick ice before and after the addition of a 25-mm layer of ice rubble at (a) vertical and (b) horizontal polarizations [Grenfell et al., 1988].

saline ice [Bredow, 1991]. However, backscatter coefficients of snow-covered ice at 13.6 GHz were about 3 dB higher than those of smooth ice at incidence angles greater than about 20° (Figure 9-33). Radiometer measurements of snow-covered saline ice recorded an increase in polarization and a decrease in emissivity, with a stronger decrease occurring at higher frequencies [Grenfell and Comiso, 1986]. Measurements at C-band (Figure 9-34) indicated the possibility of an interference effect, which, because of the snow depth, appeared to cause a spectral emissivity inversion to occur.

Lohanick [1992] conducted a series of detailed radiometric observations of snow-covered saline ice. Data were acquired at 10 and at 85 GHz before and for several weeks after a single snowfall event. A time series of 45° incidence-

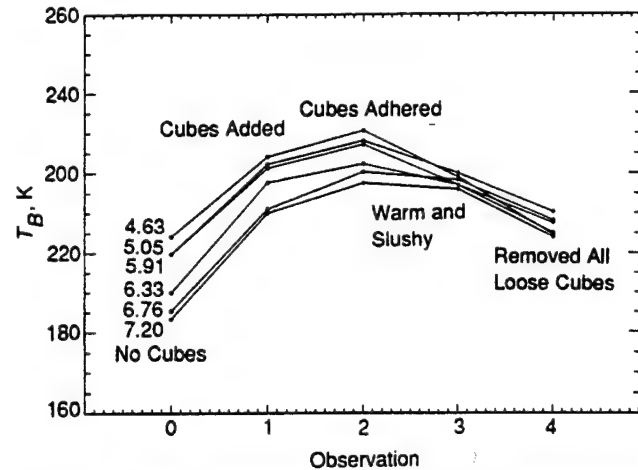


Fig. 9-31. C-band brightness temperature with varying surface roughness. Observation 1 was made immediately after adding approximately 2.5 cm of ice cubes to a 13.2-cm-thick ice sheet. Observation 2 was made the following morning, after most cubes had become frozen to the ice surface. Three hours later, the surface temperature had increased to -4°C for observation 3. Finally, for the last observation, the surface was raked to remove all loose cubes.

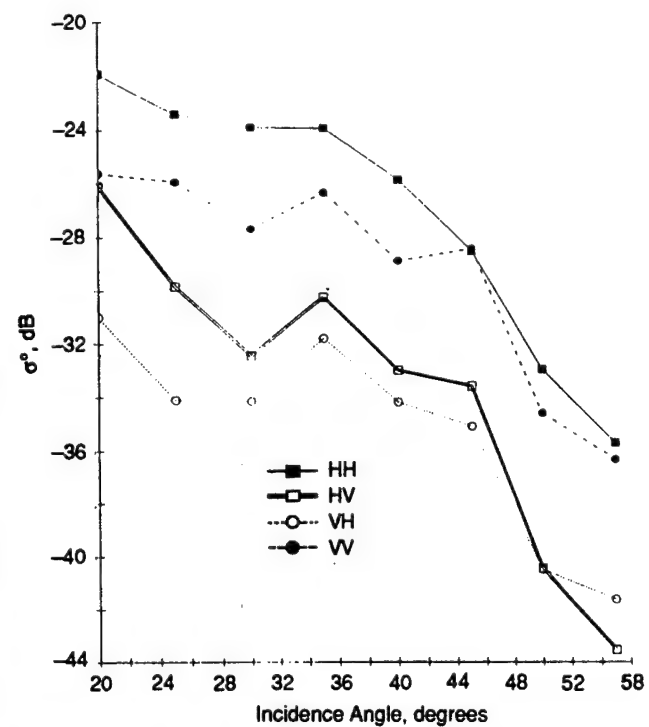


Fig. 9-32. Normalized radar cross section of rough ice at 35 GHz [Colom, 1991].

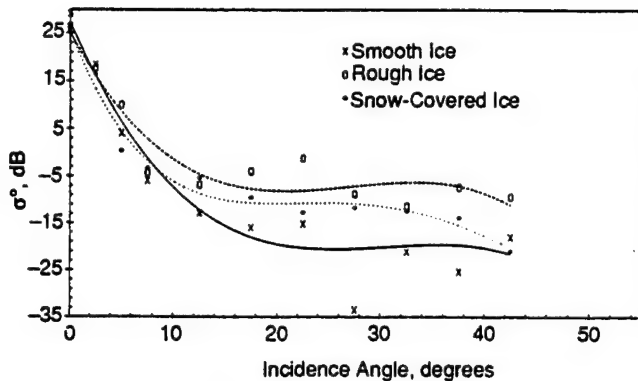


Fig. 9-33. Effects of surface conditions on backscatter angle response at 13.6 GHz and HH polarization.

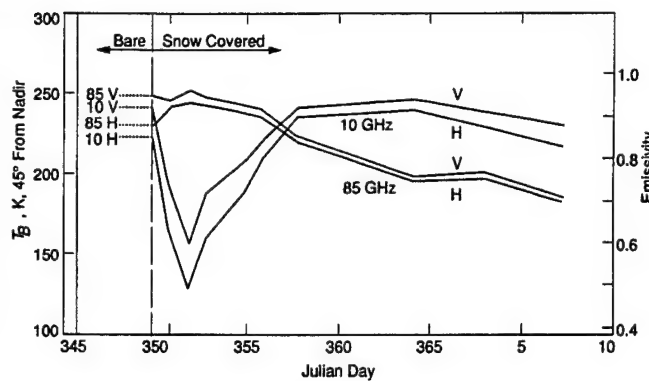


Fig. 9-35. Brightness temperatures and emissivities at 10 and 85 GHz and 45° incidence angle before and after the development of a snow cover on top of a saline ice sheet [Lohanick, 1992].

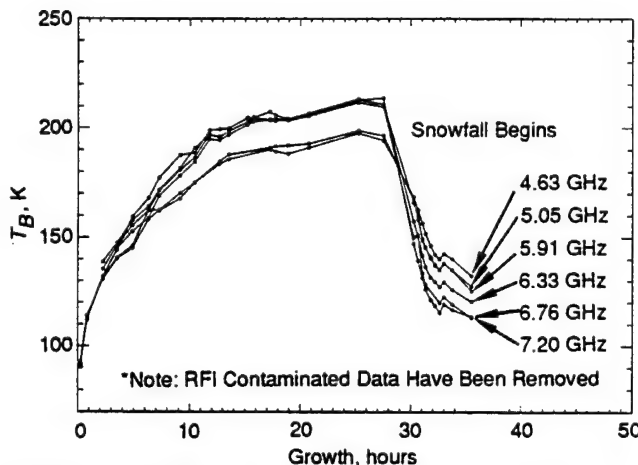


Fig. 9-34. C-band brightness temperature measurements illustrate the effect of light snowfall on a sheet of frazil ice. The snow thickness reached only 1 cm and became very moist over time.

angle radiometric temperature and emissivities for 10 and 85 GHz is shown in Figure 9-35. Snow fell late on Julian day 349. Dotted lines in Figure 9-35 show bare ice brightness temperatures. Emissivities at 10 GHz were calculated by dividing the brightness temperature by 268 K, the measured ice surface temperature; 85-GHz emissivities were calculated by dividing brightness temperature by snow surface physical temperature.

Figure 9-35 shows a significant drop (100 K) in 10-GHz brightness temperatures after snow deposition. Lohanick [1992] argued that the formation of a slush layer at the base of the snow was responsible for the behavior of the low frequency data. Brine wicked upwards into the snow caused a slush layer to form. This layer behaved radiometrically as a rough water interface. As the layer froze, it evolved to look more like water-saturated snow and finally a near perfect emitter at 10 GHz.

The 85-GHz data apparently were affected only by the snow layer. The 85-GHz brightness temperatures slowly dropped during the experiment and its polarization re-

mained constant. This suggested an explanation relying on increased volume scatter in the snow due to increased snow grain size.

A similar sequence of observations was made on urea and saline ice sheets growing in an indoor laboratory [Lytle, V. I., K. C. Jezek, R. Hosseinmostafa, and S. P. Gogineni, Laboratory backscatter measurements over urea ice with a snow cover at Ku-band, submitted to *IEEE Transactions on Geoscience and Remote Sensing*]. The 13.9-GHz radar backscatter observations were acquired during the growth phase and until the ice was approximately 9 cm thick (Figure 9-36). At that point, snow previously stored in a cold room was applied in three successive layers. Events 22, 23, and 24 represent the addition of three layers of snow that in total were 6.3, 11.2, and 14.8 cm thick, respectively. Event 25 represents the moment at which the snow-covered ice was freed from the restraining walls of the tank and began to flood. Event 35 represents the point at which the flooded snow layer was refrozen. Ice growth to 9 cm took about three days. The snow experiments, including flooding, were distributed over about 12 hours. The refrozen slush was measured about 15 hours after the initial flooding event.

As with the outdoor experiments, the snow caused the nadir return to decrease by about 4 dB, while oblique incidence returns increased by about 10 dB. Backscatter coefficients were essentially invariant with the thickness of the snow layer, which varied from 6 to 15 cm. Lytle and coworkers concluded that these observations could not be explained by volume scattering effects. Instead, and as concluded by Lohanick [1992], they attributed the observations to a metamorphosis of the snow-ice interface that caused additional surface scattering. The lower portion of the snow pack was observed to be wet because of the wicking phenomenon described earlier. Using a Kirchoff model, they found that an effective interface roughness of about 0.5 cm rms and a correlation length of 15 cm explained the observations.

After a 15-cm thick snow layer was applied to the ice surface, the section of the ice sheet covered with snow was freed from the restraining walls of the tank. The ice surface

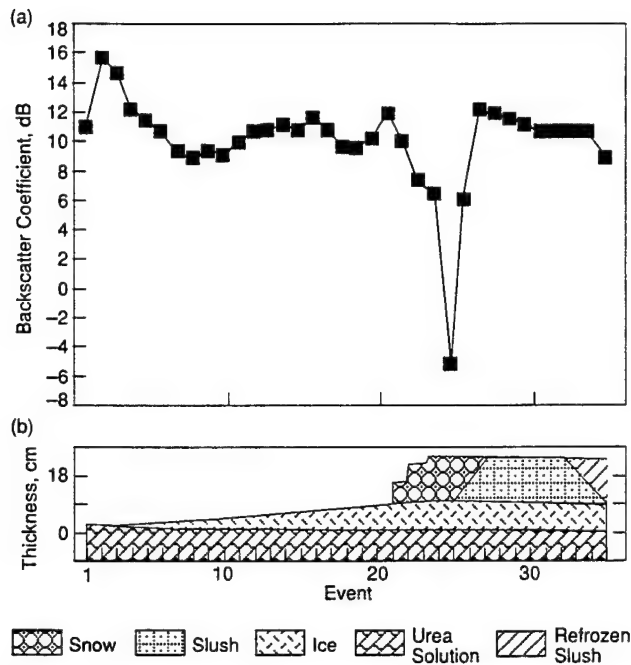


Fig. 9-36. (a) Evolution of backscatter coefficient with successive, controlled changes in ice sheet properties. Data were collected with a 13.9-GHz radar operating at normal incidence over an indoor tank filled with an urea solution. (b) The initial formation of ice from the melt (event 1) through the point at which the ice was about 9 cm thick (event 21) is shown. Events 22, 23 and 24 represent the addition of three snow layers. Event 25 represents the moment at which flooding begins.

depressed below the water level and the snow layer quickly flooded with urea solution. The entire column of snow eventually saturated with liquid. As soon as flooding occurred, normal incidence backscatter decreased by about 11 dB, but then rapidly increased to a level about 4 dB higher than backscatter measured prior to flooding. At 20° incidence angle, backscatter remained constant as the slush layer started to form; as the snow layer saturated the backscatter increased by about 5 dB. Increase in backscatter at all angles was attributed to the increased reflection coefficient at the flooded interface. Upon refreezing, backscatter at 20° incidence angle decreased 5 dB, similar to the level associated with an unflooded snow layer. This similarity was not unexpected. Although the overlying snow had been replaced by refrozen slush, the physical characteristics of this surface were expected to be similar to the ice–snow surface before flooding occurred.

Similar results have been derived from indoor laboratory measurements of snow-covered saline ice, and all observations are summarized in Figures 9-37(a), (b), and (c). These figures show that the backscatter coefficient consistently decreases at nadir with the application of a snow layer. They also show a consistent increase at oblique angles of incidence. Figures 9-38(a), (b), and (c) support the argument that interface roughness rather than volume scattering is the explanation for these data. These figures show the time domain response at 13.9 GHz over bare and snow-

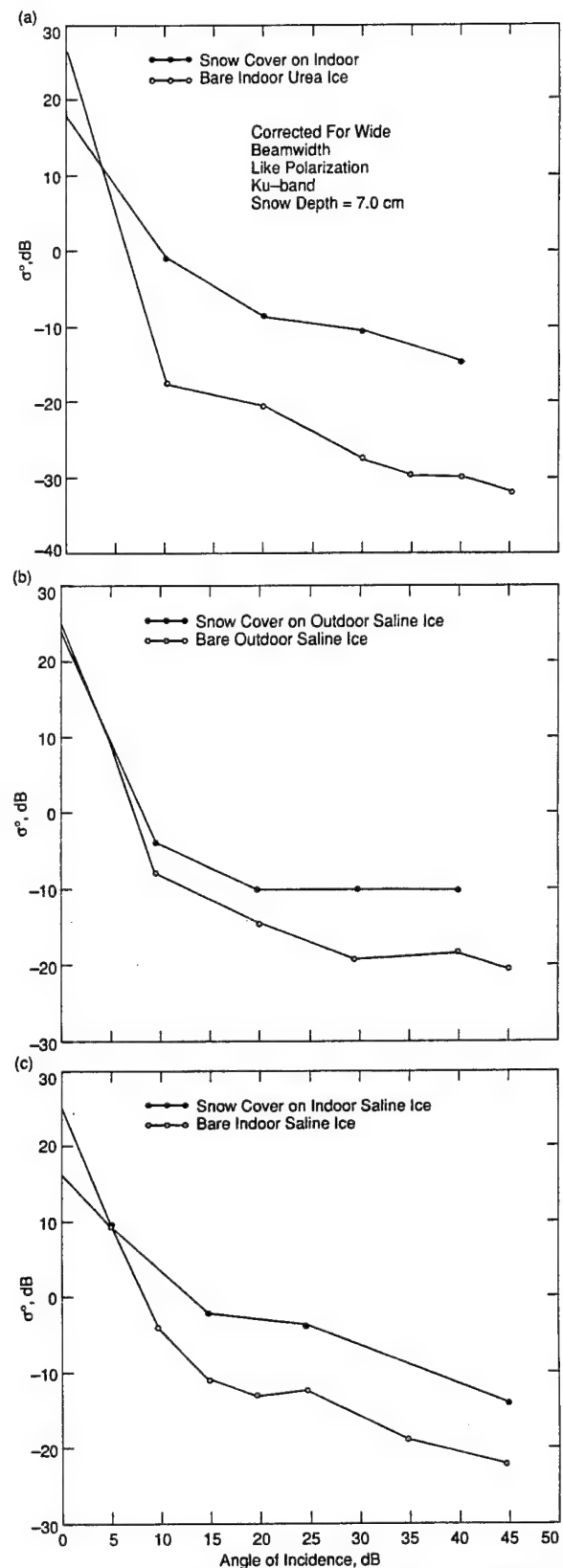


Fig. 9-37. Angular response of the backscatter coefficient at 13.9 GHz for three different bare and then snow-covered ice sheets: (a) urea grown indoors; (b) saline grown outdoors; and (c) saline grown indoors.

covered saline ice. The nadir signal from the ice surface is the large peak near the far left-hand side of Figure 9-38(a). Notice that application of a snow layer decreases the magnitude of the response, but application of additional snow does not change the pulse amplitude. Also there is no noticeable pulse broadening. At 45° incidence angle, the snow-covered return is about 10 dB higher than the equivalent bare ice result.

9.8 SIGNIFICANCE OF CRRELEX RESULTS

Experiments using the outdoor and indoor test facilities at CRREL demonstrated that saline ice with a predefined range of physical properties can be grown. These saline ice types include thin ice with varying crystalline textures and salinity gradients, roughened ice that includes a range of roughness elements, desalinated ice, and snow-covered ice. That selected ice properties can be isolated, duplicated, and studied in the laboratory is an important achievement. This achievement has been exploited to better understand the relationship between particular saline ice properties and microwave propagation phenomena. For example, there is excellent agreement between the dielectric constant of thin ice as determined from radar backscatter, radar transmission, and microwave emission observations. Moreover, changes in the dielectric constant are clearly seen to be related to the complex distribution of brine and the migration of brine through the ice sheet as the ice ages. Similarly, snow cover was found to have a profound effect on both active and passive microwave observations. Again, multisensor data could be interpreted consistently in terms of the dielectrically rough, slushy layer that develops at the snow-ice interface.

The unique combination of attributes that were part of CRRELEX makes it seem unlikely that equivalent insight into the specific microwave properties of saline ice could be obtained from field observations alone. Many of these new insights are very exciting, still, interpretation must be tempered by the broader objective of studying sea ice growing on the polar oceans. Growth in the natural ocean environment occurs under the influence of many competing effects. In turn, these effects integrate to yield a complex physical structure and associated microwave response. This natural integration reveals the basic limitation of CRRELEX, namely, that it is difficult, perhaps impossible, to simulate simultaneously all the processes that drive the formation of natural sea ice. For example, while desalinated ice of a particular composition could be grown in the laboratory, experimental techniques are far from duplicating the complete properties of even first-year ice. The CRRELEX experiences have established a new methodology for combining laboratory research that tests specific hypotheses using field measurements to evaluate the significance of a particular phenomenon in a complex environment.

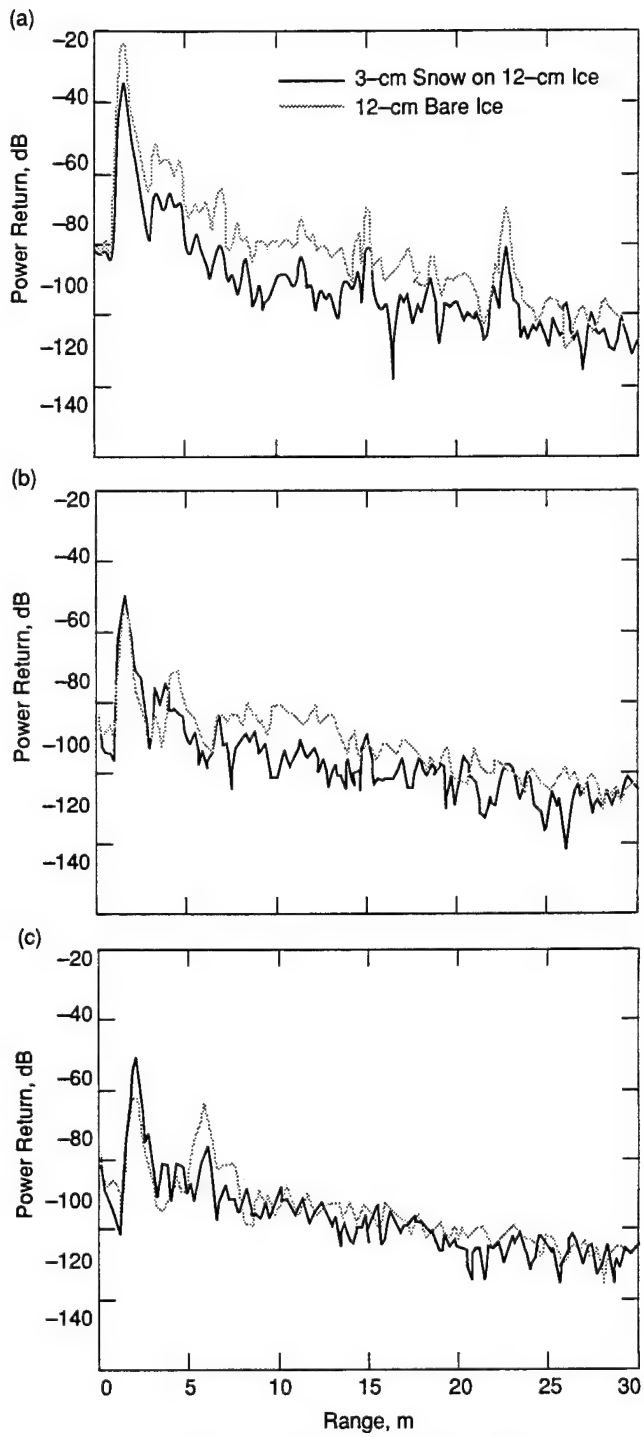


Fig. 9-38. Time domain response for a 13.9-GHz radar over bare and snow-covered saline ice. (a) The nadir signal from the ice surface corresponds to the large peak near the far left side. At (b) 25° and (c) 45° incidence angles, the backscattered signal with a slight time delay at oblique incidence also appears on the left side of each figure.

REFERENCES

Apinis, J. J. and W. H. Peake, *Passive Microwave Mapping of Ice Thickness*, Ohio State University Electrosciences Report 3892-2, Columbus, OH, 1976.

Arcone, S. A., A. J. Gow, and S. McGrew, Microwave dielectric structural and salinity properties of simulated sea ice, *IEEE Transactions on Geoscience and Remote Sensing*, GE-24(6), pp. 832-839, 1986.

Bredow, J. W., *A Laboratory Investigation Into Microwave Backscattering From Sea Ice*, University of Kansas, Lawrence, Kansas, 173 pp., 1991.

Colom, J. G., *Development of a 35-GHz Network Analyzer Based Polarimetric Scatterometer*, University of Massachusetts, Amherst, Massachusetts, 107 pp., 1991.

Comiso, J. C., T. C. Grenfell, D. L. Bell, M. A. Lange and S. F. Ackley, Passive microwave in situ observations of winter Weddell sea ice, *Journal of Geophysical Research*, 94(C8), pp. 10,891-10,905, 1989.

Gogineni, S. P., R. K. Moore, P. Wang, A. J. Gow, and R. G. Onstott, Radar backscatter over saline ice, *International Journal of Remote Sensing*, 11(4), pp. 603-615, 1990.

Gow, A. J., *Crystalline Structure of Urea Ice Sheet Used in Modelling Experiments in the CRREL Test Basin*, CRREL Report CR84-24, CRREL, Hanover, New Hampshire, 1984.

Gow, A. J., W. Tucker, and W. Weeks, *Physical properties of summer sea ice in the Fram Strait, June-July*, CRREL Report 87-16, U.S. Army Cold Regions Research and Engineering Laboratory, Hanover, New Hampshire, 1987.

Grenfell, T. C. and J. C. Comiso, Multifrequency passive microwave observations of first year sea ice grown in a tank, *IEEE Transactions on Geoscience and Remote Sensing*, GE-24, pp. 826-831, 1986.

Jezek, K. C., T. K. Stanton, A. J. Gow and M. A. Lange, Influence of environmental conditions on acoustical properties of sea ice, *Journal of the Acoustical Society of America*, 88(4), 1903-1912, 1990.

Kim, Y.-S., R. G. Onstott, and R. K. Moore, The effect of a snow cover on microwave backscatter from sea ice, *IEEE Journal of Oceanic Engineering*, OE-9(5), pp. 383-388, 1984.

Kovacs, A., R. M. Morey, G. F. N. Cox, and N. C. Valleau, *Modelling the Electromagnetic Property Trends in Sea Ice and Example Impulse Radar and Frequency Domain Electromagnetic Ice Thickness Sounding Results*, Technical Report, CRREL, Hanover, New Hampshire, 1986.

Lohanick, A. W., Microwave brightness temperatures of laboratory grown undeformed first-year ice with an evolving snow cover, *Journal of Geophysical Research*, in press, 1992.

Onstott, R. G., *Active Microwave Observations of the Formation Process of Simulated Sea Ice*, Technical Report 239500-2-T, Environmental Research Institute of Michigan, Ann Arbor, Michigan, 1991.

Parkinson, C. L., J. C. Comiso, H. J. Zwally, D. J. Cavalieri, P. Gloersen, and W. J. Campbell, *Arctic sea ice, 1973-1976: Satellite passive-microwave observations*, NASA SP-489, 296 pp., National Aeronautics and Space Administration, Washington, DC, 1987.

Perovich, D. and A. J. Gow, A statistical description of the microstructure of young sea ice, *Journal of Geophysical Research*, 96, 16,943-16,953, 1991.

Stanton, T. K., K. C. Jezek, and A. J. Gow, Acoustical reflection and scattering from the underside of laboratory grown sea ice: Measurements and predictions, *Journal of the Acoustical Society of America*, 80, 1486-1494, 1986.

Swift, C. T. and D. J. Cavalieri, Passive microwave remote sensing for sea ice research, *Eos, Transactions of the American Geophysical Union*, 66, 1210-1212, 1985.

Swift, C. T., D. C. Dehorter, and A. B. Tanner, Passive microwave spectral emission from saline ice at C-band during the growth phase, *IEEE Transactions on Geoscience and Remote Sensing*, GE-24(6), pp. 840-848, 1986.

Ulaby, F. T., R. K. Moore, and A. K. Fung, *Microwave Remote Sensing—Active and Passive, Vol. II: Radar Remote Sensing and Surface Scattering and Emission Theory*, Addison-Wesley Publishing Company, Reading, Massachusetts, 1982.

Zwally, H. J., J. C. Comiso, C. L. Parkinson, W. J. Campbell, F. D. Carsey, and P. Gloersen, *Antarctic Sea Ice, 1973-1976: Satellite Passive-Microwave Observations*, 206 pp., NASA SP-459, National Aeronautics and Space Administration, Washington, DC, 1983.

Chapter 14. Considerations for Microwave Remote Sensing of Thin Sea Ice

THOMAS C. GRENFELL

Department of Atmospheric Sciences, University of Washington, Seattle, Washington 98195

DONALD J. CAVALIERI AND JOSEFINO C. COMISO

Laboratory for Hydrospheric Processes, Goddard Space Flight Center, Greenbelt, Maryland 20771

MARK R. DRINKWATER

Jet Propulsion Laboratory, California Institute of Technology, 4800 Oak Grove Drive, Pasadena, California 91109

ROBERT G. ONSTOTT

Environmental Research Institute of Michigan, P. O. Box 8618, Ann Arbor, Michigan 48107

IRENE RUBINSTEIN

Ice Research and Development, York University, 4700 Keele Street, North York, Ontario, M3J 1P3, Canada

KONRAD STEFFEN

Cooperative Institute for Research in Environmental Sciences, University of Colorado, Boulder, Colorado 80309-0449

DALE P. WINEBRENNER

Polar Science Center, Applied Physics Laboratory, University of Washington, 1013 NE 40th Street, Seattle, Washington 98105

14.1 INTRODUCTION

Thin ice, consisting of the World Meteorological Organization's (WMO's) group of types for new and young sea ice less than about 0.3 meters in thickness, is of considerable importance both for the energy exchange between the atmosphere and ocean in the polar regions and for the dynamics of the sea ice cover. Integrated over the annual cycle, thin ice can be found over an area of at least $8 \times 10^6 \text{ km}^2$ and $16 \times 10^6 \text{ km}^2$ in the Arctic and Antarctic, respectively, and the maximum instantaneous coverage is estimated at about $1 \times 10^6 \text{ km}^2$. The brightness temperatures, emissivities, and radar scattering cross sections of thin ice evolve during growth. Their behavior for thin ice is determined by its bulk dielectric properties, but can be strongly modified by the presence of snow and by the properties of the near surface layers, where the salinity can be very large.

In this chapter, we will show that surface-based radiometric results and principal component analysis indicate that some thin ice types can be resolved under favorable circumstances. Mixtures of thick ice and open water, however, can still give rise to ambiguities in ice type

identification in available satellite data. Initial comparisons of concurrent radiometric and radar data show the potential to improve discrimination of thin ice on the basis of emitted and backscattered intensities. We expect the ability to distinguish thin ice using satellite imagery will improve considerably with the combination of Special Sensor Microwave/Imager (SSM/I) data, high-resolution results from the First European Remote Sensing Satellite (ERS-1), and microwave models of the ice.

The spatial and temporal distribution of thin ice plays a central role in both the thermodynamics and dynamics of the world's sea ice. Thin ice refers to all sea ice types younger than first-year ice and less than 0.3 meters thick. The polar packs consist of complex mixtures of many different thicknesses. A typical mesoscale region can be expected to contain open water, new ice, and young ice in varying proportions, depending on season and geographic location. Because of thermodynamic mass changes and dynamic motions that rearrange existing ice, the area covered by any particular thickness category undergoes continual change. Given sufficient data about the velocity field and mechanical properties of the ice and the energy fluxes at the upper and lower boundaries one can calculate the magnitude of these changes using thickness-distribution-dependent dynamical models [Rothrock, 1975; Thorndike et al., 1975]. Reviews by Rothrock [1986] and Thorndike [1986] show

that the ice thickness distribution plays a central role in controlling the large-scale dynamics of the ice and that thin ice is particularly important. Observational verification of such modeling, however, is not yet available in sufficient detail to know how well the amount of thin ice is predicted.

Many properties of sea ice are strongly dependent on its thickness, including surface temperature, strength, growth rate, salinity, and dielectric constant. Thus, some knowledge of the way in which ice thickness is distributed in a particular part of the ice pack in a particular season is needed before its large-scale behavior can be predicted accurately. The extent and distribution of the areas covered by open water and thin ice are of special concern in modeling heat exchange with the atmosphere and the salinity balance of the upper ocean. In the central Arctic, open water appears to make up no more than 1% of the ice pack during the winter, but estimates from submarines of the amount of ice less than 1 m in thickness give a range from 8% to 12% [Wittman and Schule, 1966], about an order of magnitude greater. These latter estimates are consistent with independent theoretical calculations [Thorndike et al., 1975]. For the southern ocean [Wadhams et al., 1987; Lange and Eicken, 1991], up to 7% of thin ice is associated with floes, but, because of logistical limitations, this is an underestimate that does not include new ice.

Modeling of heat transport through young sea ice [Maykut, 1978, 1982] predicts that in the central Arctic during the cold months, the net heat input to the atmosphere from ice in the 0 to 0.4 m range is between one to two orders of magnitude larger than that from perennial ice. Maykut concludes that with the present estimates of ice thickness distribution in the central Arctic, total heat input to the atmospheric boundary layer from regions of young ice is equal to or greater than that from regions of open water or thick ice.

Similar considerations hold for the salt and buoyancy fluxes in the ocean [Smith et al., 1990; Morison et al., 1991]. The rejection of salt due to the growth of thin ice significantly enhances convection in the mixed layer and affects the oceanic heat flux to the bottom of the ice. In certain areas of the marginal ice zones (MIZ) and areas of persistent polynyas, the salt flux appears to be influential in generating oceanic bottom water. Over the Arctic Ice Dynamics Joint Experiment (AIDJEX) array, thin ice rather than open leads had the greatest influence on ice production, heat input to the atmosphere, and salt input to the ocean.

In the Antarctic and in the northern MIZ areas, there is often greater divergence and even more open water and thin ice than in the central Arctic. Cruise results from the Antarctic [Wadhams et al., 1987; Eicken and Lange, 1989; Worby and Allison, 1991] indicate that much of the winter Antarctic ice pack is highly dynamic, drifting at speeds of tens of kilometers per day, and that this motion is often divergent, leading to a large percentage of new ice within the pack. Under these conditions, the larger areas (even as low as 80%) of thin ice result in greater turbulent heat loss than from open water.

Microwave imagery from aircraft and satellites provides monitoring on intermediate to large geographic scales and has already demonstrated its usefulness for understanding the behavior of the global sea ice cover. Because of limitations in spatial resolution and the small relative area covered by freezing leads and polynyas, however, thin ice determination has proved difficult. Techniques to refine our knowledge of the thickness distribution of new and young ice are still being developed. This chapter aims to review the present state of the art.

14.2 TERMINOLOGY AND CLASSIFICATION

Because of the diversity of conditions that can accompany the formation and growth of thin ice, its physical properties can cover a range that is wide even for ice in a particular thickness interval. The WMO division into the subcategories of new and young ice based on visual appearance is useful. The visually distinct surface forms often appear to be accompanied by differences in their dielectric properties.

The WMO system defines the categories usually used to distinguish various stages of evolution for both calm and wavy conditions. This sequence is shown diagrammatically in Figure 14-1, adapted from Weeks [1976], along with the approximate range of thicknesses associated with each category. A certain amount of crossover is possible if calm conditions become wavy or vice versa. For example, grease ice can quickly develop into nilas if the waves subside, and nilas can be broken up into small pieces that quickly form

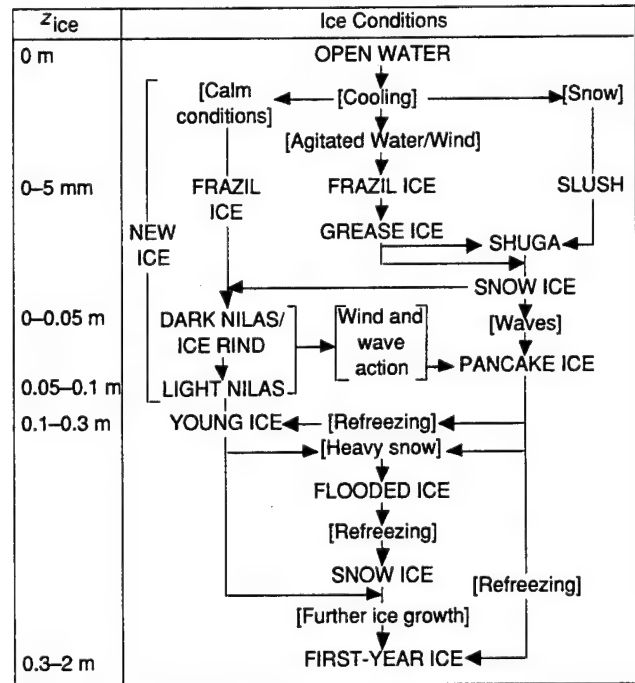


Fig. 14-1. Evolutionary sequence for thin sea ice. Ice types are shown in capital letters and related environmental processes are enclosed in square brackets.

pancakes. Young ice develops both from the consolidation and thermal growth of pancake ice and from light nilas. The snow cover is quite variable and is often thick enough to make visual identification of the underlying ice difficult.

Since the WMO system is based on the visible albedo and morphology of the ice, in general it will not have a one-to-one relationship with the microwave characteristics. For example, variations in snow cover can easily confuse a particular visible categorization while they may have a much smaller effect on microwave signatures. This sort of situation could be exploited to allow greater discrimination of ice types using a combination of sensors. The quantities we wish to determine by remote sensing are the physical properties of the ice (e.g., thickness, salinity, temperature, density, and snow cover characteristics) and the attendant environmental conditions, rather than WMO types per se. The ultimate evaluation of any classification system is based on how well it succeeds in doing this.

14.3 GEOGRAPHICAL AND TEMPORAL DISTRIBUTION OF THIN ICE

Thin ice must occur during the freeze-up phase in seasonal sea ice zones—those areas covered by ice in the winter, but free of ice in summer. It is also formed in polynyas and leads throughout the winter in the perennial ice. Consequently, thin ice will occur over large areas of the polar regions, but because the growth of new and young ice tends to be rapid, a smaller area would in general be covered with thin ice at any one time. An overview of the subject by Maykut [1986] indicates that, as a result of freezing alone, ice will form and grow to 0.3 m in thickness in approxi-

mately 5 to 10 days if $T_{\text{air}} = -30^{\circ}\text{C}$ and in about 7 to 15 days if $T_{\text{air}} = -20^{\circ}\text{C}$. Then, for a satellite sampling rate of once every three days, a given area of thin ice would be observable between one and five times before developing into another type of ice. Consequently, we would expect that in many places the area covered by thin ice would not appear as a persistent or static feature.

Microwave satellite imagery has greatly refined our knowledge of the extent and cycling of the seasonal sea ice zones (SSIZ) of both the Northern and Southern Hemispheres since 1973 [Zwally et al., 1983; Parkinson et al., 1987; Parkinson and Cavalieri, 1989; Parkinson, 1991]. This has in fact provided the most precise identification and discovery of many areas of thin ice. In the SSIZ regions, thin ice occurs in abundance and can be readily delineated from the seasonal information provided by passive satellite imagery. These regions are shown in Figures 14-2 and 14-3 for the Arctic and Antarctic, respectively, from four-year averages of Electrically Scanning Microwave Radiometer (ESMR) data. The greatest area is around Antarctica, where the SSIZ covers $16 \times 10^6 \text{ km}^2$, but large areas are also found around the margins of the Arctic Basin, in the Bering Sea, and in the Sea of Okhotsk covering $8 \times 10^6 \text{ km}^2$.

Cracking and divergence of the pack continually provide new areas of ice formation and growth. Large areas where this occurs, polynyas and major lead systems, have been detected by microwave satellite imagery in many places throughout the Arctic and Antarctic Sea ice zones [Martin and Cavalieri, 1989].

A striking and recurrent winter feature in the Greenland Sea is the Odden, a large tongue of sea ice jutting out from

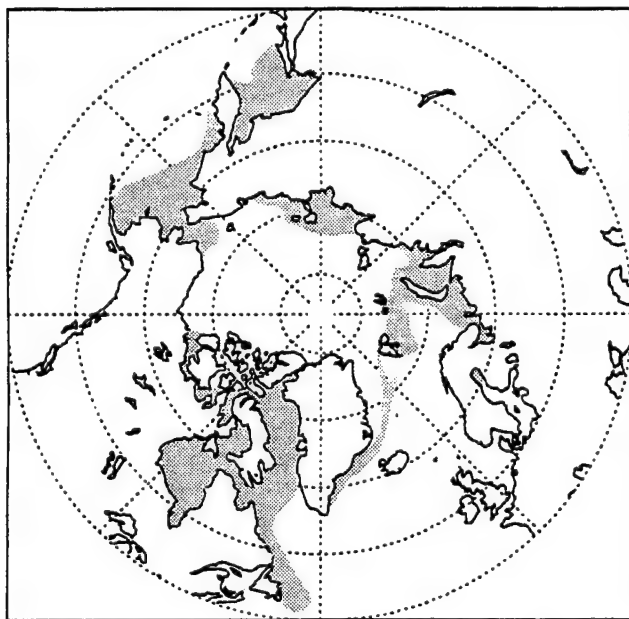


Fig. 14-2. Approximate boundaries of the seasonal sea ice zones of the Northern Hemisphere derived from ESMR satellite imagery [Parkinson et al., 1987].

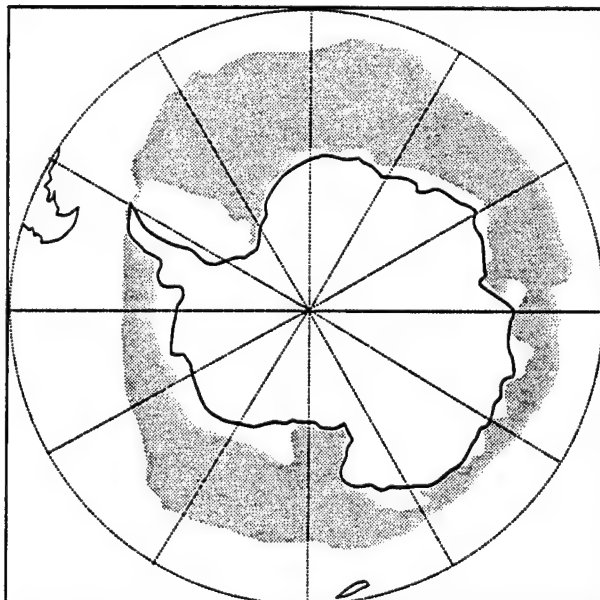


Fig. 14-3. Approximate boundaries of the seasonal sea ice zones of the Southern Hemisphere derived from ESMR satellite imagery [Zwally et al., 1983].

the thick ice of the east Greenland drift stream, which has routinely been detected by the Scanning Multichannel Microwave Radiometer (SMMR) and SSM/I. This feature can cover an area of more than 10^5 km^2 and can appear and dissipate within a few days to a week. Ship-based observations during recent field experiments have shown that the Odden is made up in large part of thin ice. The rapid appearance and disappearance of the Odden reflects fluctuations in the delicate balance between the atmospheric and oceanic heat fluxes in the region; indeed this may be a region of considerable importance in the ventilation of the deep ocean [Gascard, 1990].

Estimates of the amount of thin ice in the central Arctic have been made on the basis of empirical growth rate formulae from Anderson [1961] and from the results of dynamic and thermodynamic model results by Maykut [1982]. They give regional percentages of thin ice of 20% during fall freeze-up, 1.4% to 4% in midwinter, and 10% in midsummer. Corresponding estimates for the Antarctic [Weller, 1980] give wintertime concentrations of 20% for the inner zone and 60% for the outer zone.

For the entire Arctic and Antarctic, including the peripheral seas, an independent estimate can be made directly using satellite imagery to determine rates of change in total

ice area [Zwally et al, 1983; Comiso and Zwally, 1984; Parkinson and Cavalieri, 1989]. These are then integrated over the lifetime of thin ice to give areal coverage at a particular time. Figure 14-4 shows the resulting estimates for each month, assuming that it takes 7 days on average for the ice to become 0.3 m thick during growth and that no ice grows during summer breakup. Estimated areas are as high as 0.5×10^6 to $1 \times 10^6 \text{ km}^2$ (about 5 and 25% of minimum extent) in the Arctic and Antarctic, respectively. The current estimates are only approximate, but thin ice is clearly present in substantial quantities in both hemispheres.

14.4 MICROWAVE SIGNATURES OF THIN ICE

The concept of microwave signatures for thin ice and its subcategories implies a well-defined relationship between some aspect of the physical properties of the ice and an appropriate combination of brightness temperatures, emissivities, and/or scattering coefficients that will identify that ice type. The first case to consider is that of an instantaneous image where the signature makes it possible to extract the distribution of a particular ice type in the image.

14.4.1 Radiometry

Because of the coarse resolution of satellite passive microwave sensors to date, thin ice has been difficult to identify in the imagery and can be easily confused with mixtures of thick ice and open water. However, even though thin ice may be difficult to identify, the ice types in this category do have significantly different microwave signatures than open water or thicker ice. Thus, the effects of thin ice must be present in the satellite record and the above distribution estimates suggest that the effects should be significant under appropriate circumstances.

Representative emissivity spectra for thin ice types, from surface and aircraft-based observations, are presented in Chapter 4. These show that thin ice has emissivity spectra that lie between the values for open water and those of first-year ice and have different slopes. Figure 14-5 shows laboratory measurements illustrating the progression of emissivity with ice thickness for calm growth conditions [Grenfell and Comiso, 1986]. A complication associated with near-surface observations is the contribution of interference fringes. These are due to multiple reflections from layering in spatially homogeneous areas of ice and snow, and they generate T_B fluctuations in small-scale observational results (Chapter 9). In aircraft or satellite studies, the footprints are much larger, usually enough to include many different ice conditions and to average out the fringes.

For ice growth under both calm and wavy conditions, the rate at which the emissivities evolve with ice thickness depends strongly on the development of the dielectric properties of the ice. This is determined by the distribution of brine in the ice. In calm water, this is determined by the

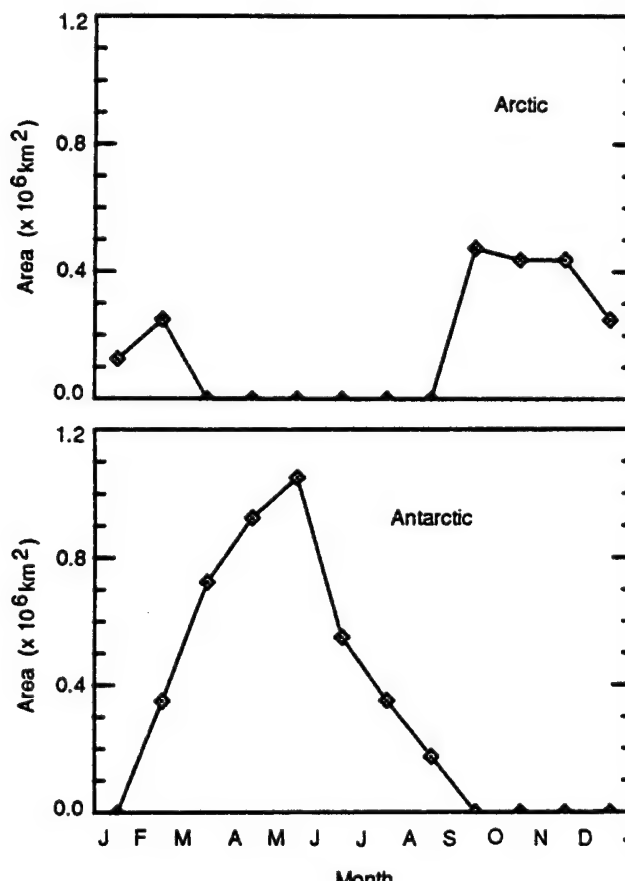


Fig. 14-4. Estimates of areal coverage by thin sea ice in both the Arctic and Antarctic based on ESMR data.

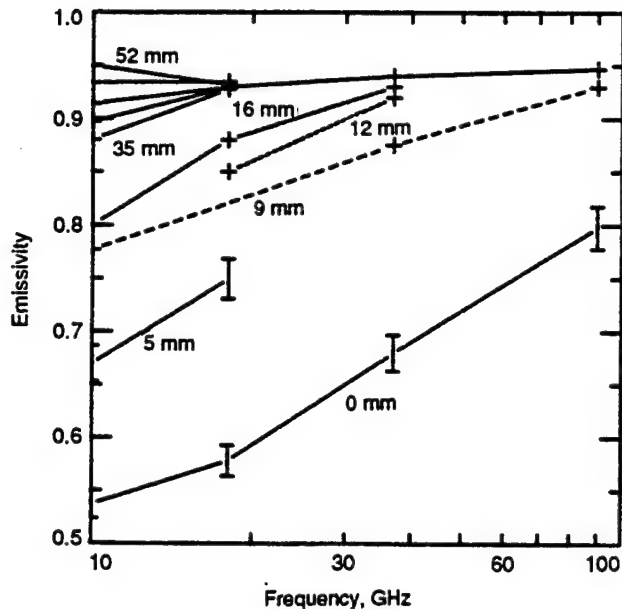


Fig. 14-5. An example of the progression of emissivity versus frequency at vertical polarization of thin ice from open water to young ice. Each curve gives the ice thickness. Maximum thickness for this set of observations is about 100 mm. V-pol observations are at a nadir angle of 50°.

growth rate of the ice and the salinity of the water [Weeks and Ackley, 1986]. Laboratory observations [Grenfell, 1986; Grenfell and Comiso, 1986; Wensman, 1991] show that the ice becomes optically thick at physical thicknesses between 50 and 80 mm for 10 GHz, decreasing with increasing frequency to about 10 mm for 90 GHz. Beyond this point, the high reflectivity of the underlying water no longer makes a significant contribution to the emitted radiation. Subsequent emissivity changes then arise primarily from changes in the distribution of brine in the uppermost layers.

For grease ice and pancake ice, the situation is quite different. Salt entrapment is not due to growth at a planar interface, but involves the consolidation of a crystal slurry that results in entrapment of brine throughout the slurry's volume. After consolidation, flushing of the surface continues through the development of pancake ice and further modifies the salinity distribution. Since the mechanisms of brine entrapment, drainage, and expulsion are different than those associated with congelation ice growth, we would in general expect differences in the microwave signatures.

A cluster plot of observations from the Marginal Ice Zone Experiment (MIZEX) 1987 (Figure 14-6) shows results for thin ice types grown under wavy conditions. The brightness temperatures (T_B 's) span the range from open water to thick first-year (FY) ice. Since the footprint size for each of these observations was about 5 m across, small but decreasing amounts of open water between the pancakes were included in the radiometer's field of view. Observed signature development thus combines changes due to ice growth with changes due to increasing ice concentration.

Corresponding observations were carried out during an experiment in the Weddell Sea [Comiso et al., 1989] over areas where bare, rafted, and snow-covered nilas covered most of the area around the ship. The emissivities for nilas were within 0.05 to 0.2 of the values for FY ice, consistent with laboratory results. The results at 18 and 90 GHz, for example, showed several clusters associated with thin ice (Figure 14-7, labeled new ice) that were due to undisturbed and rafted areas with different amounts of snow cover. In this case, the brightness temperatures were tightly grouped rather than spread out evenly between open water and first-year ice as in Figure 14-6.

The polarization ratio, $PR(v) = [T_B(v, V\text{-pol}) - T_B(v, H\text{-pol})]/[T_B(v, V\text{-pol}) + T_B(v, H\text{-pol})]$, where H- and V-pol denote horizontal and vertical polarization, respectively, is also used to indicate thin ice in SMMR and SSM/I imagery. It was selected on the basis of observed differences between open water and thick ice. During new or young ice growth PR_V decreases from open water values near 0.3 to young ice values of about 0.1 [Grenfell and Comiso, 1986]. This is shown in detail in Chapter 9, and is determined by the relative contributions to the total reflectivity of the upper and lower surfaces of the ice. Both surface and aircraft observations in the Bering Sea (Figure 14-8) show a similar behavior [Cavalieri et al., 1986] as do satellite results from the Chukchi Sea and northern Baffin Bay [Steffen and Maslanick, 1988; Carsey and Pihos, 1989; Steffen, 1991].

SSM/I data from the Bering Sea [Cavalieri, 1988] shown in Figure 14-9 indicate clustering in the circled region,

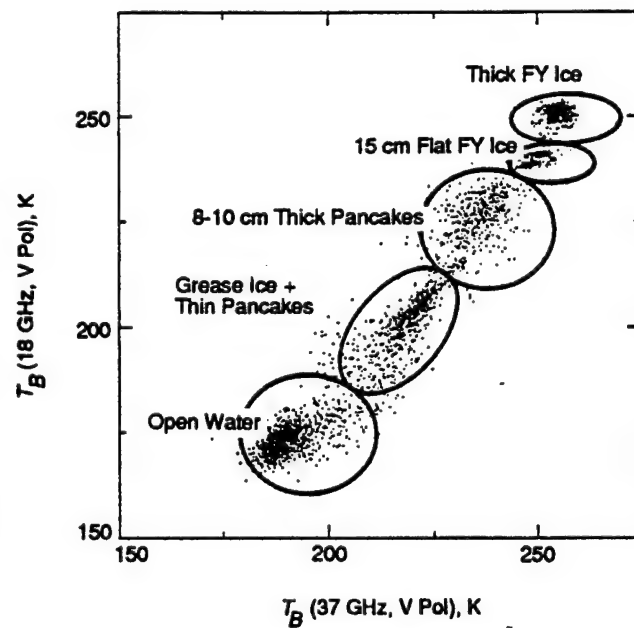


Fig. 14-6. Cluster observations of some thin ice types and first-year ice from MIZEX'87 in the northern Greenland Sea [Grenfell, T. C. and D. L. Bell, unpublished, University of Washington, Seattle, Washington, 1988]. V-pol observations are at a nadir angle of 50°.

where $GR(v1, v2) = [T_B(v2, V\text{-pol}) - T_B(v1, V\text{-pol})]/[T_B(v2, V\text{-pol}) + T_B(v1, V\text{-pol})]$. The density of points in this cluster is higher during the presence of polynyas and appears to indicate the presence of young ice. A recent analysis of thin ice [Wensman, 1991] gives growth trajectories of undisturbed young ice, for which representative results are shown in Figure 14-10. Growing ice passes quickly through the early phase, but moves much more slowly toward the end of the sequence just when the signatures lie within the area defined by the oval in Figure 14-9. Although young ice

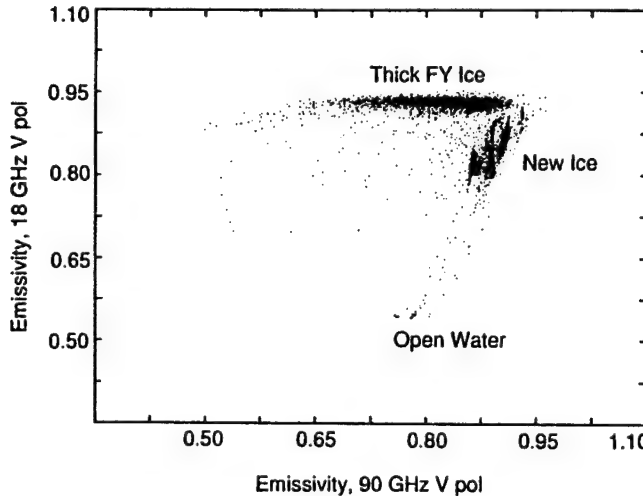


Fig. 14-7. Scatter plot of emissivities for thin ice obtained during the winter of 1986 in the Weddell Sea. New ice indicates nilas in different stages of development—undisturbed and overthrusted with and without snow cover.

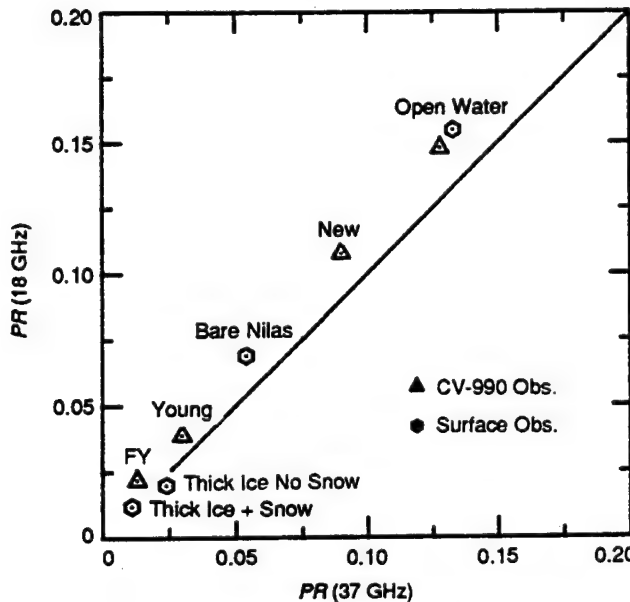


Fig. 14-8. Polarization ratio for combined aircraft-based and surface observations in the Bering Sea [Cavalieri et al., 1986]. The nadir angle is 45°.

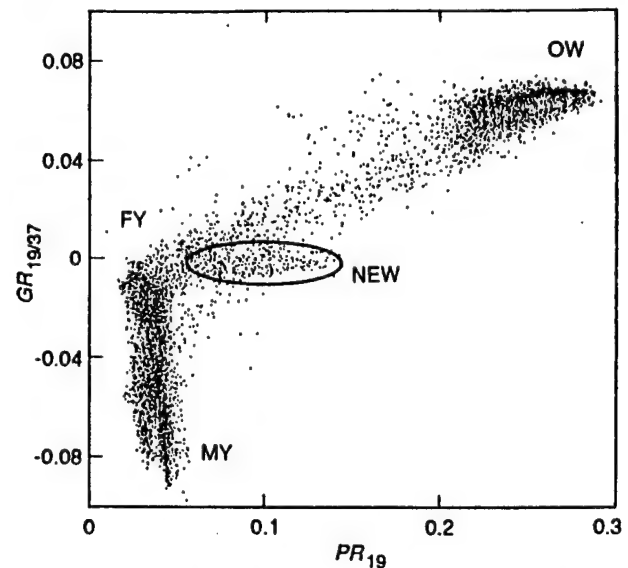


Fig. 14-9. Cluster plot of preliminary data from SSM/I during January. The cluster of points in the oval are from the Bering Sea in January 1988.

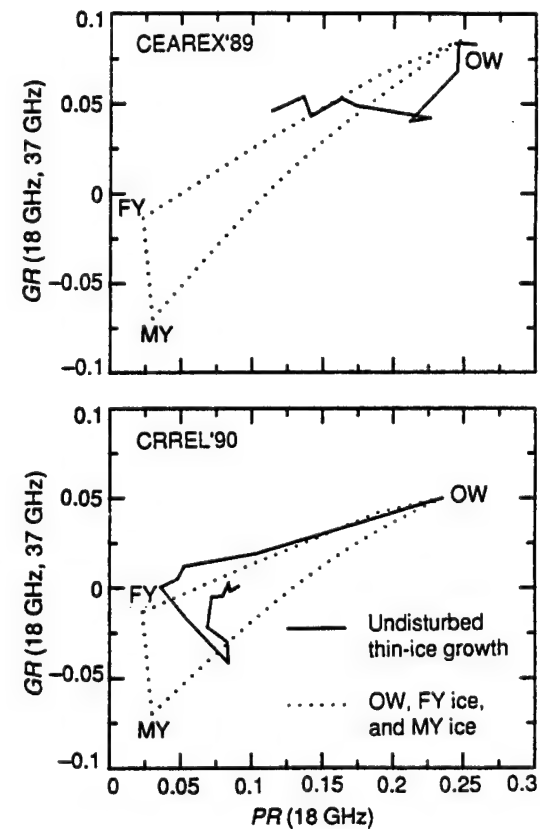


Fig. 14-10. Results for new ice from the northern Greenland Sea (CEAREX'89) and for young ice at the CRREL pond (CRREL'90).

may not account for all the points within the oval, it apparently clusters there. A recent aircraft study also found a similar result over the Beaufort Sea for 100% ice concentration [Drinkwater et al., 1991a].

The work by Wensman [1991] also presents a supervised principal component analysis that strongly suggests that under favorable conditions both young and new ice can be distinguished using passive microwave data. The separation of new and young ice in principal component space is illustrated in Figure 14-11 based on data from the Cold Regions Research and Engineering Laboratory (CRREL) pond experiment and Coordinated Eastern Arctic Research Experiment (CEAREX). A thin ice algorithm based on this analysis and applied to SSM/I data appears to explain quite well the ice distribution for a test case from the Bering Sea. Further development is needed, however, before this technique can be used operationally.

14.4.2 Radar

Studies of radar signatures of thin ice have also become available recently. Figure 14-12(a) shows combined results from a progression of surface-based backscatter cross sections at C- and X-bands from open water through thick ice covering a dynamic range of about 20 dB [R. G. Onstott,

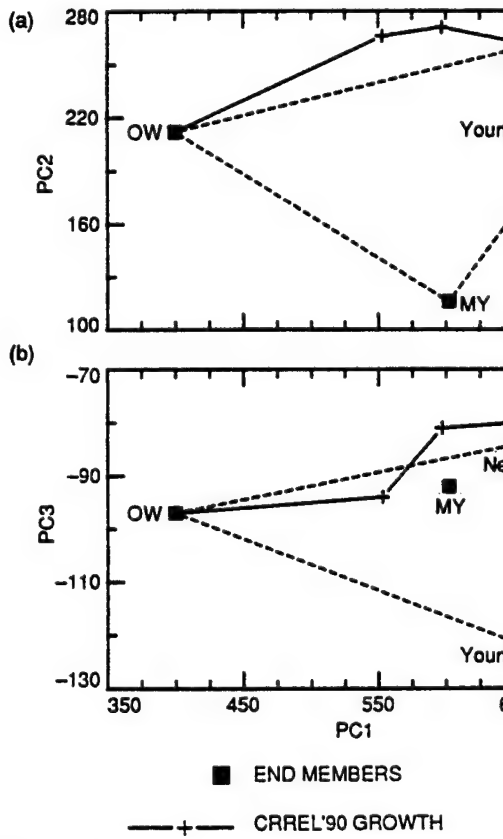


Fig. 14-11. Principal components derived from a 10-channel data set consisting of dual-polarization brightness temperatures from 6 to 90 GHz.

personal communication, 1991]. Minima are found for grease and frazil ice about 0.02-m thick and for medium first-year ice, and there is a strong maximum for 0.05- to 0.3-m thick ice, which spans the range from light nilas to young ice. Corresponding results from Soviet satellite observations using the X-band side-looking real aperture radar on Cosmos 1500 [Nazirov et al., 1990] are shown in Figure 14-12(b) for the eastern Arctic. These results depict the optical density of the imagery that is approximately proportional to scattering in decibels. These results show the same strong maximum for gray nilas as Onstott's results. Another broad minimum is evident for FY ice, after which the scattering undergoes a gradual increase, and finally a strong jump for MY ice. Nazirov and coworkers

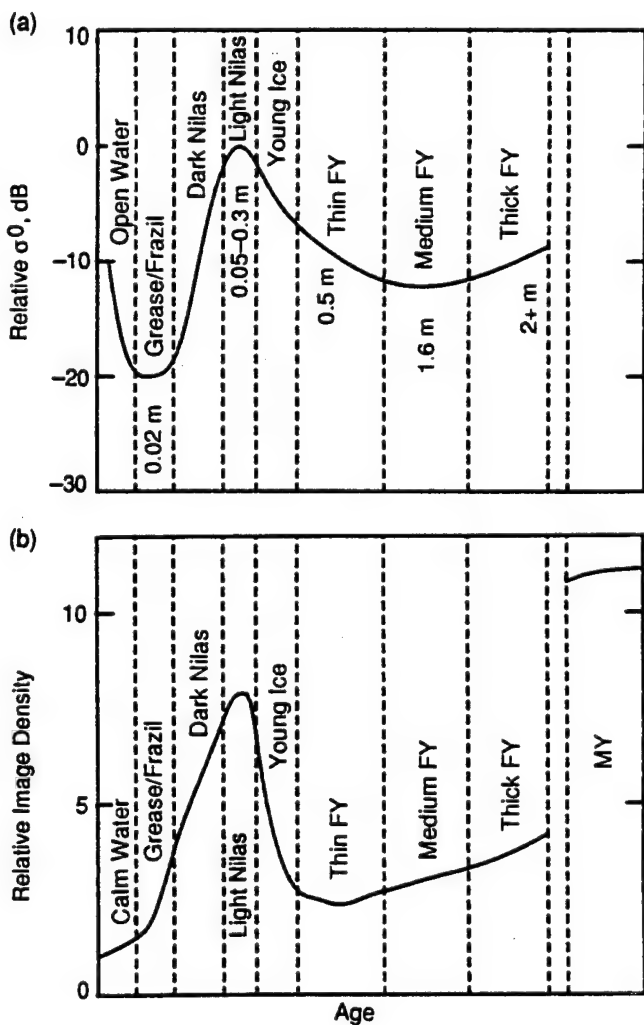


Fig. 14-12. (a) Radar backscatter sequence for FY ice. Combined surface backscatter cross sections at C- and X-bands' VV and HH polarizations showing the progression from open water through thick ice. (b) Satellite real-aperture backscatter observations at 9.7-GHz VV pol from Cosmos 1500 showing the same progression from open water through thick ice. The dynamic range is not reported, but can be inferred relative to the jump from thick FY to MY ice.

quote results for calm open water with lower scattering than for new ice, while Onstott shows results for roughened water.

The maximum for nilas in Figure 14-12(a) is related to the presence of frost flowers whose density can become quite high and blanket the entire surface. The individual flowers (Figure 14-13) are large enough to present a significant cross section to radar radiation, but their density and the size of the dendrites indicates that they should be transparent at frequencies up to at least X-band. However, frost flowers can also affect the near-surface brine distribution [Grenfell and Comiso, 1986; Drinkwater and Crocker, 1988] and are frequently characterized by a lump at the base due to wicking of surrounding brine from the ice surface and subsequent metamorphism (as can be seen directly in Figure 14-13). These structures are sufficiently large and have a high enough dielectric constant to present a significant enhancement in the radar cross section. The second minimum for thicker ice is attributed to further densifying of the frost layer due to snow accumulation combined with an increase in brine volume due to the thermal insulation. This brine could be partly incorporated into the snow by capillary action and would introduce attenuation to mask the rough interface.

Aircraft SAR observations at P-, L-, and C-bands [Drinkwater et al., 1991b; Winebrenner, D. P. and L. D. Farmer, On the L-band polarimetric SAR response to ice thickness in new and thin sea ice types, *Journal of Geophysical Research*, in preparation] were carried out over the Beaufort and Bering Seas during March 1988. These studies confirm the strong influence of frost flowers and indicate that their absence results in the near disappearance of the maximum of σ for nilas. They also show that at

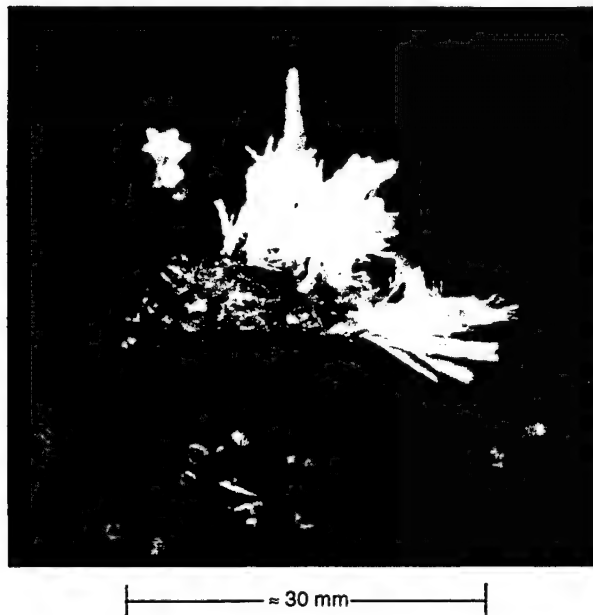


Fig. 14-13. A single frost flower on growing young ice observed during LEADEX'91. (Courtesy of R. G. Onstott.)

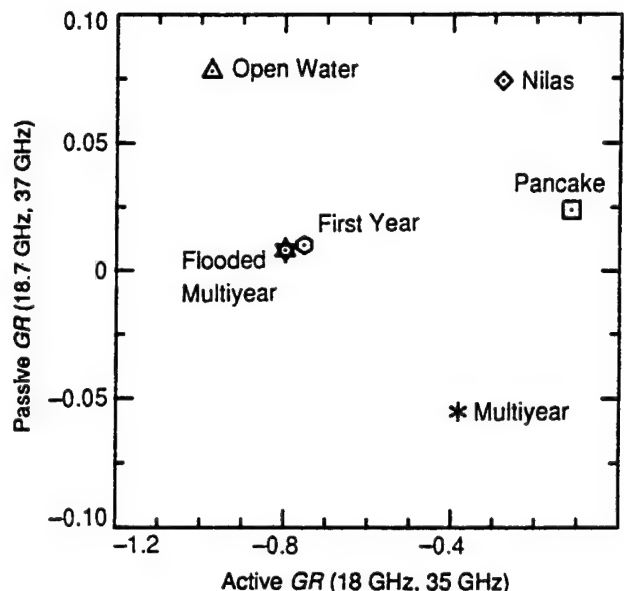


Fig. 14-14. Comparison of microwave observations for selected ice types measured during MIZEX'87 in the northern Greenland Sea in early spring.

L-band, both the ratio of backscatter cross sections, σ_{VV}/σ_{HH} , and the copolar phase are sensitive to certain thin ice types. To first order, the ratio σ_{VV}/σ_{HH} depends on the dielectric constant of the scattering material and not on surface roughness, and values for thin ice are between those of open water and FY ice.

Some surface and aircraft-based comparisons of radiometric and radar data for thin ice from MIZEX'87 [Tucker et al., 1991] show that selected combinations of active and passive gradient ratios appear to separate nilas and pancake ice from open water and FY ice (Figure 14-14). Although these data were for a few selected sites for which the ice properties had been extensively measured, the distinct ice types were clearly identified. More data are needed to test the robustness of this result.

Passive-active comparisons have been reported for the Bering Sea in 1988 from NASA DC-8 observations. Cross-polarization scattering cross section (σ_{HV}) versus T_B (37 GHz, V-pol) reported by Drinkwater et al. [1991a] are shown in Figure 14-15(a). The young ice is separated as indicated from the locus of points for varying concentrations of small first-year floes and open water (squares) by more than 20 K in T_B and 4 dB in σ_{HV} . This locus is curved because the contribution to scattering by floe edges is not directly proportional to concentration and hence to T_B . Dual-frequency radar data at like polarizations, including one very low frequency, also separate out the young ice, Figure 14-15(b). The decrease in scattering cross section by the young ice suggests that frost flowers were not present in this case.

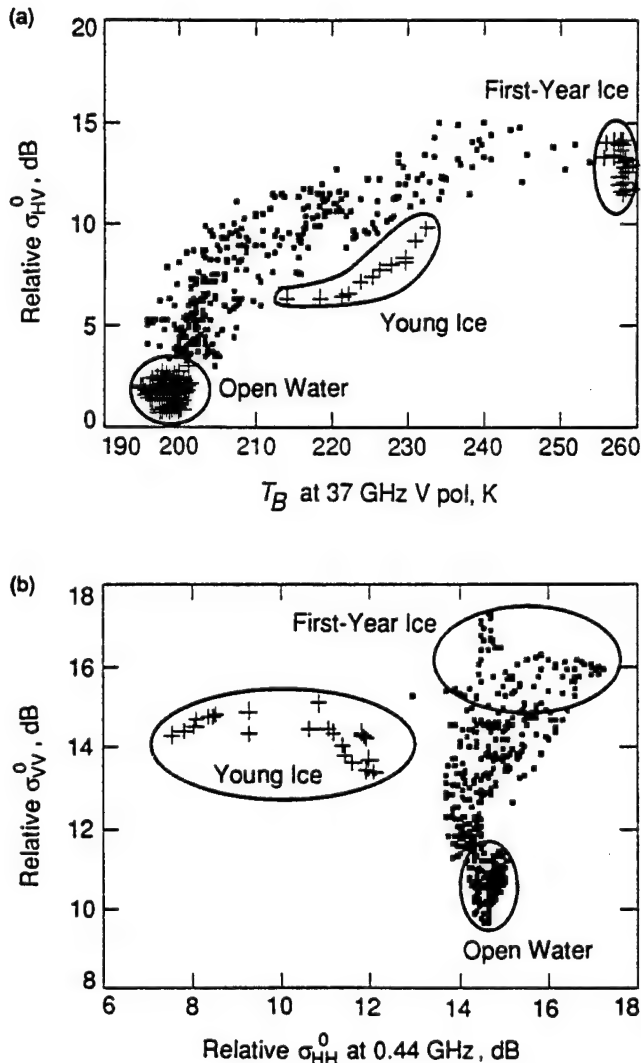


Fig. 14-15. Comparison of relative radar backscatter at 5.3 GHz and (a) HV and (b) VV pol measured by aircraft over the Bering Sea MIZ on March 21, 1988.

14.4.3 The Influence of Ice Structure on Microwave Signatures

In addition to total ice thickness and bulk salinity, several phenomena related to the small-scale structure of the surface layers are important in modulating the microwave signatures of thin ice. The first class of effects includes those that affect the brine volume of the ice that in turn can modify the permittivity quite strongly. These effects combine considerations of both temperature and salinity. One of the most important of these is the existence of a highly saline surface layer where the salinities can exceed 80 ppm. This gives rise to a very high brine content that has produced detectable changes in T_B [Grenfell and Comiso, 1986; Wensnahan et al., 1992]. This surface layer is known to exhibit horizontally spatial inhomogeneity. Other considerations that influence the salinity are the ice growth

rate and whether the growth occurs under quiescent or wavy conditions [Weeks and Ackley, 1986]. A second class of significant effects consists of those that affect the surface roughness, including the growth of frost flowers and the occurrence of ridging or overthrusting.

The importance of snow cover for ice signatures is complex (Chapter 16). Snow cover on thin ice affects both the salinity distribution and the surface roughness. It insulates the ice, increasing the temperature, but also acts to wick up the extra brine, and as metamorphism proceeds can introduce significant surface roughness [Lohanick, personal communication, 1990]. If the snow cover is thick enough, it can submerge the ice and cause flooding [Weeks, 1976; Wadhams et al., 1987; Eicken and Lange, 1989; Tucker et al., 1991]. Recent laboratory measurements have demonstrated that each of these effects can modify the microwave signatures of thin ice (for more detail see Chapter 9), but it remains to show how to characterize the effects in general.

14.5 IMPLICATIONS FOR SATELLITE ALGORITHMS

Operational satellite algorithms that do not account for thin ice can produce significant errors, particularly in MIZ. For example, thin ice has a high enough PR to look like almost 30% open water, and this offers a potential explanation of certain ambiguities in the interpretation of both SMMR and SSM/I data. There are frequent occurrences in the satellite records of low ice concentration events during midwinter persisting over very long time periods compared to known ice growth rates. Present evidence suggests that these low concentration areas may include extensive amounts of thin ice. Thin ice might also account for part of the jump in ice extent during the transition from ESMR to SMMR in the course of the 15-year record of Arctic Sea ice from 1973 to 1987 analyzed by Parkinson and Cavalieri [1989]. This jump is most noticeable in the Kara, Barents, and Greenland Seas and the Sea of Okhotsk where higher abundances of thin ice are expected.

The trajectories of brightness temperature, emissivity, and backscatter cross section for thin ice during growth show behavior that suggests that T_B , e , and σ^0 vary independently to some degree. The maximum scattering coefficients due to frost flower formation, for example, do not appear to have a corresponding expression in the emissivity data.

Even though the number of different processes that can modify the ice structure may appear to be large, satellite imagery suggests that the microwave signatures develop in relatively reproducible orderly sequences, and that some measure of ice thickness resolution is practical. Thus, although the relative importance of the various physical processes is not yet well understood, these processes probably occur in regular progression and give relative statistical homogeneity over large areas.

From the point of view of ice dynamics and mass balance, even a single additional thin ice category would greatly improve our present understanding of the ice. More resolv-

able categories would correspondingly improve the definition of the thickness distribution.

14.6 POTENTIAL FOR MULTISENSOR DATA

These studies of thin ice indicate that additional information is available from radiometer imagery. ESMR and SMMR have identified areas where thin ice should be found, but techniques capable of resolving thin ice types have not yet succeeded in producing unambiguous retrievals. The improved spatial resolution and radiometric precision of SSM/I have produced some promising results, and analysis based on surface observations has also made progress in that regard. Progress in thin ice identification should further benefit, though, by comparison with data from other types of sensors in combination with theoretical studies. On the basis of results presented here, it appears that it is precisely for thin ice that the combination of active and passive imagery has the greatest potential.

Additional sensors exist that should assist in improving the resolution of thin ice types. In the visible and near infrared, ice signatures respond to different physics than at microwave frequencies because the scattering inhomogeneities are much larger than the wavelength. Upwelling solar radiance above the ice is determined primarily by multiple scattering and the entire volume of the ice can contribute. Snow cover is very important and masks the underlying ice if it is thicker than a few centimeters. In the thermal infrared, sea ice and snow act as blackbodies and observations at these wavelengths would be useful for determining the changes in surface temperature associated with ice growth. Visible, infrared, and microwave signatures will not be completely independent, however, because the physical properties that determine them are linked. For example, brine pocket size and density, snow cover, surface roughness, and ice thickness change together as the ice ages.

14.7 FUTURE DIRECTIONS

Thin sea ice can occur in substantial quantities, and it appears that the technology to detect thin ice is becoming available. Ambiguities in interpretation, however, are still present. Current limitations stem from spatial resolution, instrument accuracy, and analysis techniques. Developments in these areas include regional cluster analysis, Kalman filtering analysis, principal component analysis, and image texture analysis (see Chapters 4, 12, and 23).

Understanding the small-scale structure and development of the surface layers with and without snow cover is important in interpreting the microwave signatures of thin ice, but many of the details remain to be investigated. The transition from the signature of young ice to that of FY ice is also poorly understood. These topics should have high priority in future investigations.

Development of new satellite microwave sensors with higher spatial resolution is needed. In addition to SAR, lightweight large-aperture interferometric radiometers are

under development, and they can achieve surface resolutions near one kilometer. Lower-frequency microwave observations should also be explored because of their improved penetration depth, reduced sensitivity to volume scattering by inhomogeneities, and greater sensitivity to the brine content of the ice. The required technology is practical now, and we expect considerable progress in the near future.

REFERENCES

Anderson, D. L., Growth rate of sea ice, *Journal of Glaciology*, 3, pp. 1170-1172, 1961.

Cavalieri, D. J., Preliminary observations of polar sea ice with the special sensor microwave imager, *Proceedings of the IGARSS '88 Symposium*, Edinburgh, Scotland, ESA SP-284, European Space Agency, Noordwijk, Netherlands, August 1988.

Cavalieri, D. J., P. Gloersen, and T. T. Wilheit, Aircraft and satellite passive microwave observations of the Bering Sea ice cover during MIZEX West, *IEEE Transactions on Geoscience and Remote Sensing*, GE-24(3), pp. 368-377, 1986.

Comiso, J. C. and H. J. Zwally, Concentration gradients and growth/decay characteristics of the seasonal sea ice cover, *Journal of Geophysical Research*, 84(C5), pp. 8081-8103, 1984.

Comiso, J. C., T. C. Grenfell, D. L. Bell, M. A. Lange, and S. F. Ackley, Passive microwave in situ observations of winter Weddell sea ice, *Journal of Geophysical Research*, 94(C8), pp. 10,891-10,905, 1989.

Drinkwater, M. R. and G. B. Crocker, Modelling changes in the dielectric and scattering properties of young snow-covered sea ice at GHz frequencies, *Journal of Glaciology*, 34(118), pp. 274-282, 1988.

Drinkwater, M. R., J. P. Crawford, and D. J. Cavalieri, Multi-frequency, multi-polarization SAR and radiometer sea ice classification, *Proceedings of the IGARSS 91*, vol. 1, catalog number 91CH2971-0, pp. 107-111, IEEE, New York, 1991a.

Drinkwater, M. R., R. R. Kwok, D. P. Winebrenner, and E. Rignot, Multifrequency polarimetric Synthetic Aperture Radar observations of sea ice, *Journal of Geophysical Research*, 96(C11), pp. 20,679-20,698, 1991b.

Eicken, H. and M. A. Lange, Development and properties of sea ice in the coastal regime of the southeastern Weddell Sea, *Journal of Geophysical Research*, 94, pp. 8193-8206, 1989.

Gascard, J. C., Deep convection and deep-water formation, *EOS*, 71(49), pp. 1837-1839, December 1990.

Grenfell, T. C., Surface-based passive microwave observations of sea ice in the Bering and Greenland Seas, *IEEE Transactions on Geoscience and Remote Sensing*, GE-24(3), pp. 378-382, 1986.

Grenfell, T. C. and J. C. Comiso, Multifrequency passive microwave observations of first-year sea ice grown in a tank, *IEEE Transactions on Geoscience and Remote Sensing*, GE-24(6), pp. 826-831, 1986.

Lange, M. A. and H. Eicken, The sea ice thickness distribution in the Northwestern Weddell Sea, *Journal of Geophysical Research*, 96, pp. 4821–4838, 1991.

Martin, S. and D. J. Cavalieri, Contributions of the Siberian shelf polynyas to the Arctic Ocean intermediate and deep water, *Journal of Geophysical Research*, 94(C9), pp. 12,725–12,738, 1989.

Maykut, G. A., Energy exchange over young sea ice in the Central Arctic, *Journal of Geophysical Research*, 83, pp. 3646–3658, 1978.

Maykut, G. A., Large-scale heat exchange and ice production in the Central Arctic, *Journal of Geophysical Research*, 87, pp. 7971–7984, 1982.

Maykut, G. A., The surface heat and mass balance, *The Geophysics of Sea Ice*, edited by N. Untersteiner, pp. 395–464, NATO ASI Series B: Physics vol. 146, Plenum Press, New York, 1986.

Morison, J. H., M. G. McPhee, T. Curtin, and C. A. Paulson, The oceanography of leads, *Journal of Geophysical Research*, in press, 1991.

Nazirov, M., A. P. Pichugin, and Yu. G. Spiridonov, *Radar Observations of the Earth's Surface From Space (Radiolokatsiya Poverchnosti Zemli iz Kosmosa)*, edited by L. M. Mitnika and S. V. Viktorova, 200 pp., Gidrometeoizdat (Hydrometeorological Publishing Office), St. Petersburg, 1990.

Parkinson, C. L. and D. J. Cavalieri, Arctic sea ice 1973–1987: seasonal, regional, and interannual variability, *Journal of Geophysical Research*, 94, pp. 14,499–14,523, 1989.

Parkinson, C. L., J. C. Comiso, H. J. Zwally, D. J. Cavalieri, P. Gloersen, and W. J. Campbell, *Arctic sea ice, 1973–1976: Satellite passive-microwave observations*, NASA SP-489, 296 pp., National Aeronautics and Space Administration, Washington, DC, 1987.

Rothrock, D. A., The mechanical behavior of pack ice, *Annual Review of Earth and Planetary Science*, 3, pp. 317–342, 1975.

Rothrock, D. A., Ice thickness distribution—measurement and theory, *The Geophysics of Sea Ice*, edited by N. Untersteiner, pp. 551–576, NATO ASI Series B: Physics vol. 146, Plenum Press, New York, 1986.

Smith, S. D., R. D. Munch, and C. H. Pease, Polynyas and leads: An overview of physical processes and environment, *Journal of Geophysical Research*, 95(C6), pp. 9461–9479, 1990.

Thorndike, A. S., Kinematics of sea ice, *The Geophysics of Sea Ice*, edited by N. Untersteiner, pp. 489–550, NATO ASI Series B: Physics vol. 146, Plenum Press, New York, 1986.

Thorndike, A. S., D. A. Rothrock, G. A. Maykut, and R. Colony, The thickness distribution of sea ice, *Journal of Geophysical Research*, 80(33), pp. 4501–4513, 1975.

Tucker, W. B. III, T. C. Grenfell, R. G. Onstott, D. K. Perovich, A. J. Gow, R. A. Shuchman, and L. L. Sutherland, Microwave and physical properties of sea ice in the winter marginal ice zone, *Journal of Geophysical Research*, 96, pp. 4573–4587, 1991.

Wadhams, P., M. A. Lange, and S. F. Ackley, The ice thickness distribution across the Atlantic sector of the Antarctic Ocean in midwinter, *Journal of Geophysical Research*, 92(C13), pp. 14,535–14,552, 1987.

Weeks, W. F., Sea ice conditions in the Arctic, *AIDJEX Bulletin No. 34*, pp. 173–205, December 1976.

Weeks, W. F. and S. F. Ackley, The growth, structure, and properties of sea ice, *The Geophysics of Sea Ice*, edited by N. Untersteiner, pp. 9–164, NATO ASI Series B: Physics vol. 146, Plenum Press, New York, 1986.

Weller, G., Spatial and temporal variations in the south polar surface energy balance, *Monthly Weather Review*, 108, pp. 2007–2014, 1980.

Wensman, M. R., *Microwave emission from thin saline ice: field observations and implications for remote sensing*, Master's thesis, University of Washington, Seattle, 1991.

Wensnahan, M. R., T. C. Grenfell, D. P. Winebrenner, and G. A. Maykut, Observations and theoretical studies of microwave emission from thin saline ice, *Journal of Geophysical Research*, in press, 1992.

Wittmann, W. I. and J. Schule, Jr., Comments on the mass budget of Arctic pack ice, *Proceedings of the Symposium on the Arctic Heat Budget and Atmospheric Circulation*, edited by J. O. Fletcher, pp. 215–246, Memorandum RM-5233-NSF, Rand Corporation, Santa Monica, California, 1966.

Worby, A. P. and I. Allison, Ocean–atmosphere energy exchange over thin Antarctic pack-ice of variable concentration, *Annals of Glaciology*, 15, in press, 1991.

Zwally, H. J., J. C. Comiso, C. L. Parkinson, W. J. Campbell, F. D. Carsey, and P. Gloersen, *Antarctic sea ice, 1973–1976: Satellite passive-microwave observations*, NASA SP-459, 206 pp., National Aeronautics and Space Administration, Washington, DC, 1983.

Chapter 24. Potential Applications of Polarimetry to the Classification of Sea Ice

MARK R. DRINKWATER, RONALD KWOK, AND ERIC RIGNOT

Jet Propulsion Laboratory, California Institute of Technology, 4800 Oak Grove Drive, Pasadena, California 91109

HANS ISRAELSSON

Department of Radio and Space Sciences, Chalmers University of Technology, S-41296, Göteborg, Sweden

ROBERT G. ONSTOTT

Environmental Research Institute of Michigan, P. O. Box 8618, Ann Arbor, Michigan 48107

DALE P. WINEBRENNER

Polar Science Center, Applied Physics Laboratory, University of Washington, 1013 NE 40th Street, Seattle, Washington 98105

24.1 INTRODUCTION

To date, conventional microwave radar studies of sea ice have enabled scattering characteristics of saline ice to be measured for particular sets of radar parameters, such as frequency, incidence angle (θ_i), and, foremost, polarization. Radar polarimetry employs a methodology that allows simultaneous measurement of the radar backscatter from a given surface at a number of different polarizations. The goals of polarimetry are to improve geophysical property retrievals and, in the near term, improve the estimate accuracy using single-channel radar techniques.

Technology has traditionally limited the number of variable parameters. Generally, a single antenna has been used for both signal transmission and reception (i.e., monostatic radar) with either vertical (v) or horizontal (h) fixed polarization. In most cases, the radar system was incoherent and did not preserve phase information (i.e., recording only the magnitude of the complex scattered field vector). With advances in available technology, practical airborne imaging with polarimetric synthetic aperture radar (SAR) is now being conducted [Zebker and van Zyl, 1991] and new airborne systems are under development [Livingstone et al., 1990]. Not only do these systems have frequency diversity (multiple channels at P-, L-, C-, and X-bands), but they also have polarization diversity (allowing reception of both the transmission polarization and its orthogonal) and polarimetric capability (where phase information is also recorded). Polarimetric radar selects h and v transmission and reception polarizations, simultaneously recording all combinations of linear polarizations (i.e., hh, hv, vh, and vv). Thus, the unknown complex scattered electromagnetic vector is sampled in two orthogonal directions so as to completely characterize the backscattered field.

The wave transmitted by a radar polarimeter can be considered a monochromatic and completely polarized plane wave. In contrast, a scattered signal is seldom completely polarized when observed as a function of time or space. Typically backscatter originates from a statistically random surface made of distributed scattering centers or facets. The resulting polarimetric response then comprises a superposition of a large number of waves with a variety of polarizations. For complete discussions on aspects of wave polarization, the reader is referred to Ulaby and Elachi [1990] and Kong [1990].

24.2 POLARIMETRIC DATA AND DEFINITIONS

For backscattering from a discrete target, the transmitted and received field vectors are uniquely related through the complex scattering matrix $\bar{\mathbf{S}}$, where

$$\bar{\mathbf{S}} = \begin{bmatrix} |S_{hh}| e^{j\phi_{hh}} & |S_{hv}| e^{j\phi_{hv}} \\ |S_{vh}| e^{j\phi_{vh}} & |S_{vv}| e^{j\phi_{vv}} \end{bmatrix} \quad (1)$$

$|S_{rt}|$ is the magnitude of the scattering matrix element, and $e^{j\phi_{rt}}$ is the relative phase information for (t) transmit (r) receive polarization. Since in all operational imaging polarimeters the polarizations are linear and fixed by the antennas, the commonly used subscripts h and v refer to the horizontal and vertical transverse polarized components of the transmitted and received electric field. Each element of the scattering matrix is a function of the frequency and the scattering and illumination angles. A polarimetric radar essentially measures $\bar{\mathbf{S}}$ for every pixel or resolution element within an image

$$\mathbf{E}_s = e^{jkr} (kr)^{-1} \bar{\mathbf{S}} \mathbf{E}_i \quad (2)$$

where k is the wave number, r is range, and \mathbf{E}_i and \mathbf{E}_s are the incident and scattered field vectors, respectively. The backscattered signal from sea ice is a vector sum of waves with a variety of polarizations from numerous randomly positioned scatterers. The SAR polarimeter provides a measure of the mean field components of the resulting partially polarized wave in each pixel. The effective backscattering coefficient σ_{rt}^0 is then defined from elements of the scattering matrix

$$\sigma_{rt}^0 = 4\pi \frac{\langle S_{rt} S_{rt}^* \rangle}{A} \quad (3)$$

where A is the illuminated area, $*$ denotes the complex conjugate, and $\langle \rangle$ denotes the ensemble averages of a number of pixels. Two equivalent forms for displaying the elements of \bar{S} in terms of the SAR-recorded complex polarimetric backscattering information are the Stokes matrix \bar{M} and the covariance matrix \bar{C} —both representations consist of linear combinations of the cross products of the four elements of \bar{S} . Importantly, each form explicitly characterizes the polarimetric scattering properties of the sea ice, thereby enabling synthesis of the backscattered power for arbitrary transmission and reception polarizations. Polarization synthesis expressions are given by Zebker and van Zyl [1991], and further discussion of the Stokes matrix for sea ice is contained in Drinkwater and Kwok [1991].

It is most convenient to convey the backscatter in terms of ensemble averaged properties of a group of pixels in the covariance matrix form

$$\bar{C} = \begin{bmatrix} \langle S_{hh} S_{hh}^* \rangle & \langle S_{hh} S_{hv}^* \rangle & \langle S_{hh} S_{vv}^* \rangle \\ \langle S_{hv} S_{hh}^* \rangle & \langle S_{hv} S_{hv}^* \rangle & \langle S_{hv} S_{vv}^* \rangle \\ \langle S_{vv} S_{hh}^* \rangle & \langle S_{vv} S_{hv}^* \rangle & \langle S_{vv} S_{vv}^* \rangle \end{bmatrix} \quad (4)$$

This three-by-three Hermitian matrix fully characterizes the polarimetric scattering properties of a distributed scattering target such as sea ice. It is assumed that the surface satisfies the reciprocity relation where $S_{hv} = S_{vh}$. For practical purposes, one of the cross-polarized components of the scattering matrix is ignored and the scattering matrix is made symmetrical. In doing so, the mean phase imbalance between transmission and reception (in both h - and v -polarized antennas) is removed. This difference must be recorded for use during subsequent cross-channel phase balancing of images. Such a procedure is typical in generating the standard compressed data format for the National Aeronautics and Space Administration, Jet Propulsion Laboratory (NASA-JPL) synthetic aperture radar (SAR) polarimeter [Zebker and van Zyl, 1991].

24.3 POLARIMETRIC DISCRIMINANTS

Polarimetric parameters in this section are chosen to characterize the polarimetric signature of particular ice

types. The term polarimetric discriminants here applies to combinations of elements of the matrix \bar{C} that describe the polarimetric response. In this section, several discriminants are introduced, namely: span, like-polarized (co-pol) and cross-polarized (cross-pol) power ratios, phase difference, correlation coefficient, and fractional polarization. Multi-frequency data from JPL and the Environmental Research Institute of Michigan (ERIM) SAR polarimeters, acquired in March 1988 and March 1989, respectively, are used to illustrate examples of the variation in these discriminants for particular Arctic ice types.

Figure 24-1 shows a C-band sea ice image with five sample boxes. Contextual clues and the polarimetric response of this Beaufort Sea ice indicates that there is a mixture of multiyear (MY) and first-year (FY) ice. Boxes 1 and 3 are from large MY floes, while box 2 is from an area of ridged and rafted FY ice. The relatively dark response of boxes 4 and 5 indicates mechanically undisturbed and likely smoother FY ice that formed in cracks in the large MY floes. The brighter tones of the MY ice are explained by volume scatter [Drinkwater, 1990; Drinkwater et al., 1991a, 1991b, 1991c], as examples of subsequent polarimetric measures testify. All ice surfaces in this scene are likely covered by a veneer of dry snow [Wen et al., 1989].

Figure 24-2 is an image set illustrating polarization sensitivity at L-band. These images are 10×10 km with a resolution of about 2 m, and θ_i varies from 30° to 65° . Data shown in Figures 24-1 and 24-2 illustrate a range of polarimetric examples spanning frequencies from X-band to P-band, and provide the basis for the analyses contained in following sections.

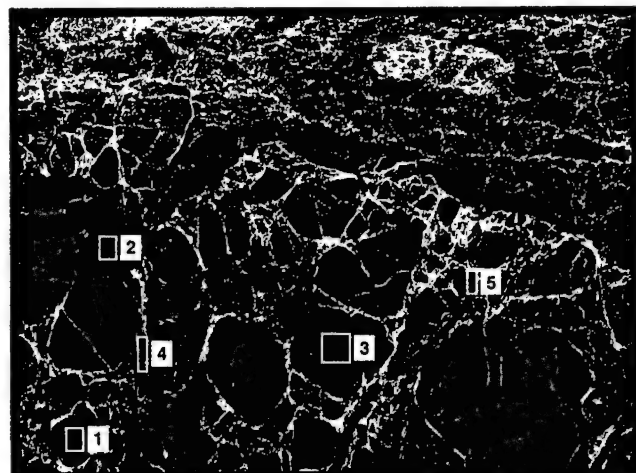


Fig. 24-1. Three-frequency total power image acquired by the JPL polarimeter at the location $73^\circ 13.4' N$ $142^\circ 1.1' W$ at 17:21:26 GMT (i.e., 08:21:26 local time) on March 11, 1988, in the Beaufort Sea [Drinkwater et al., 1991a]. These data are overlaid as a false-color image, with the C-band in blue, L-band in green, and P-band in red.

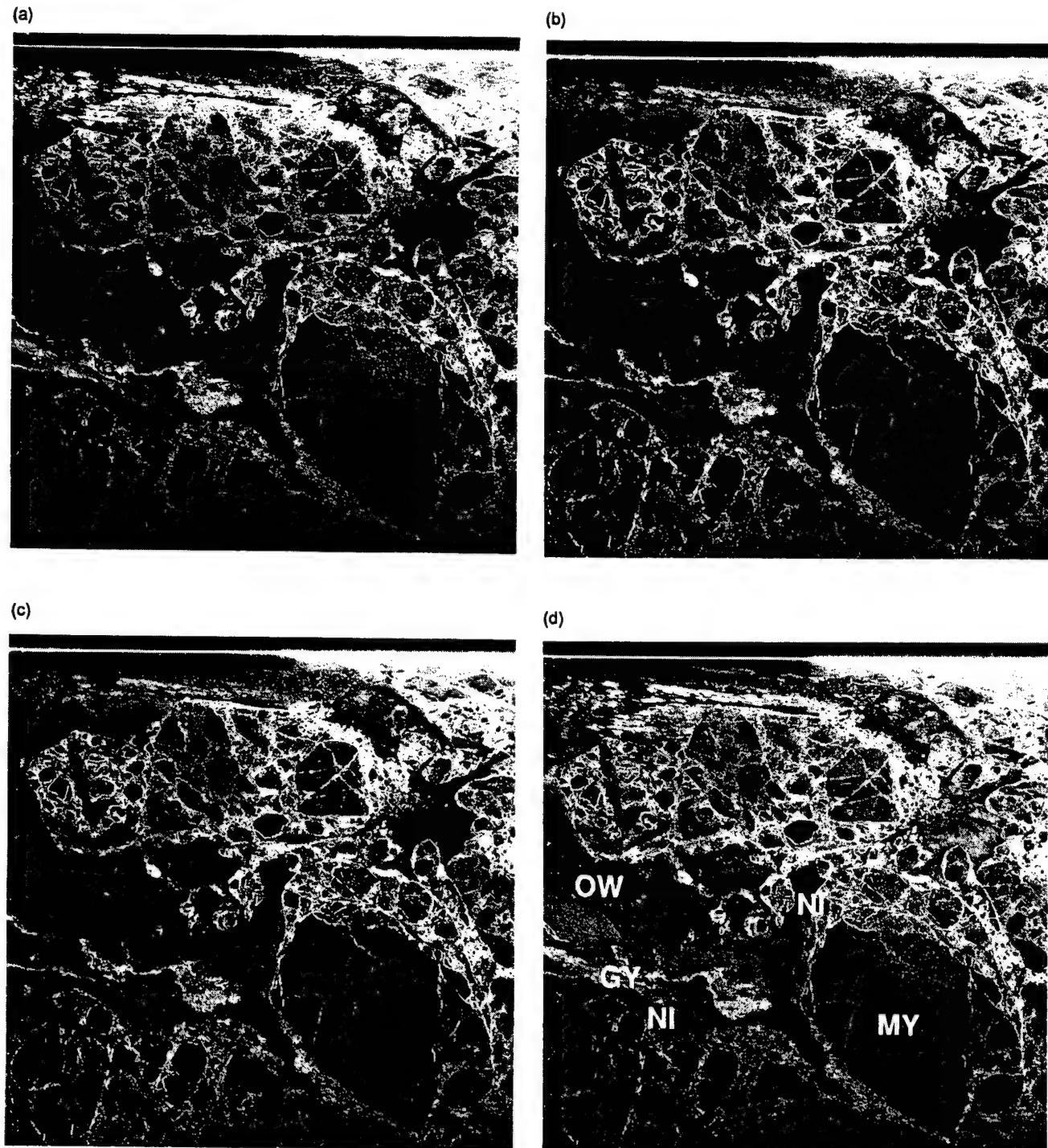


Fig. 24-2. ERIM L-band (1.25-GHz) SAR images of sea ice at (a) hh, (b) hv, (c) vh, and (d) vv polarizations from the Greenland Sea marginal ice zone during March 1989. The surface categories indicated are open water (OW), nilas (NI), grey ice (GY), and multiyear ice (MY).

24.3.1 Total Power

Absolute calibration is not possible for many polarimetric data, owing to the absence of in-scene targets with known backscattering characteristics. Consequently, relative measures are derived using frequency and polarization. One such measure is the span, which represents the total power in the scattered field at a particular frequency

$$SPAN = \langle S_{hh} S_{hh}^* \rangle + \langle S_{vv} S_{vv}^* \rangle + 2 \langle S_{hv} S_{hv}^* \rangle \quad (5)$$

where $\langle \cdot \rangle$ denotes ensemble averaging of a number of pixel values.

Israelsson and Askne [1991] choose examples taken from JPL polarimeter images of Beaufort Sea ice using 200-m² samples. They contrasted the *SPAN* values for FY and MY ice at three frequencies and demonstrated the best discrimination at C-band with a separation of 10 dB. Typically, *SPAN* is greater for MY than FY ice due to the fact that MY ice gives an additional depolarized component of backscatter along with the predominantly co-pol returns from FY ice of equivalent surface roughness (Chapter 8). The proportion of depolarized returns is significantly larger at C-band than at L- or P-band, leading to the hypothesis that some component is derived from multiple scattering by bubbles and inhomogeneities present in the upper layers of old ice in addition to second-order rough surface scattering and volume-surface interaction effects. Supporting evidence for volume scattering is that *SPAN* is less sensitive to the incidence angle at C-band, in direct contrast to *SPAN* values for L- and P-bands, each of which decrease with increasing θ_i . The decrease in L- and P-band *SPAN*'s for MY ice between 25° and 52° is between 10 and 15 dB, in contrast to the 5-dB decrease at C-band.

24.3.2 Power Ratios Between Channels

Polarization signatures are a convenient tool for three-dimensional viewing of the power recorded at each of the polarimeter's transmit and receive combinations [Evans et al., 1988]. However, polarization signatures in Drinkwater et al. [1991a] and Zebker and van Zyl [1991] indicate that sea ice backscattering does not appreciably transform the polarization of linearly polarized transmitted waves. Typically, the linear h- or v-polarization (hereafter abbreviated to h- or v-pol) of the transmitted waves is retained for a large fraction of the backscattered signal. Additionally, circularly polarized transmitted waves produce negligible co-pol returns [Drinkwater et al., 1991a]. For most geophysical media, circularly polarized waves are depolarized most effectively [Zebker et al., 1987]. Since there is some degree of redundancy in the information contained in nonlinear polarizations, linear h- and v- co- and cross-pol channels can be reasonably effective in characterizing the polarization signature of a given sea ice surface.

Heterogeneity of scattering mechanisms between pixels introduces a component of unpolarized or randomly polar-

ized backscatter. This is manifested as a fraction of returns that exhibit diffuse scattering, characterized by rapidly varying polarizations from pixel to pixel (and thus widely differing covariance matrices in adjacent resolution elements). Generally, complex surfaces or anisotropic or multiple-scattering surface layers increase this unpolarized fraction of the backscatter. Another mechanism contributing to such an effect is the presence of system noise, which may occur at low backscatter. This circumstance is only really typical of situations of smooth young ice in the far range [Kwok et al., 1991a].

A more convenient method for using polarization combinations is by applying channel ratios. Ratios quantify the difference in power (in decibels) between specific polarizations and thus characterize the full polarization signature. The ratio between co-pol elements of \bar{C} is

$$R_{hh/vv} = \frac{\langle S_{hh} S_{hh}^* \rangle}{\langle S_{vv} S_{vv}^* \rangle} \quad (6a)$$

Similarly, the cross-pol ratio is

$$R_{hv/vv} = \frac{\langle S_{hv} S_{hv}^* \rangle}{\langle S_{hh} S_{hh}^* \rangle} \quad (6b)$$

The depolarization ratio is defined as the ratio of cross-pol to both co-pol channels

$$R_{depol} = \frac{2 \langle S_{hv} S_{hv}^* \rangle}{\langle S_{hh} S_{hh}^* \rangle + \langle S_{vv} S_{vv}^* \rangle} \quad (6c)$$

24.3.2.1 Co-pol ratio distributions. The co-pol ratio distributions in Figure 24-3 illustrate how the hh- and vv-pol backscatter varies between each ice type with frequency. Individual pixel ratios are shown as a distribution, rather than by deriving a mean ratio using Equation (6a). The ratios are balanced by applying C- and L-band correction factors (-1.8 and 0.6 dB, respectively) based upon hh/vv imbalance calculations from radar calibrations. The resulting distributions are normalized with respect to the total number of pixels used in each sample box. Model predicted ratios, based upon first-order Bragg scattering [Winebrenner et al., 1989], are also made at L-band using typical measured properties of Beaufort Sea ice.

C-band consistently has the widest hh/vv ratio distribution, the lowest peak, and a tail extending to values above 1. This appears to be due to a combination of greater rough surface scattering as the wavelength becomes shorter and the apparent surface roughness increases. Figure 24-3 indicates the broadest spread of ratios in thick FY ice, and the narrowest distributions and lowest mean ratios for thin FY ice. MY ice exhibits an intermediate situation where C-band has the largest variance, but L- and P-bands show similar distributions. Based on this evidence, box 2 conforms to the characteristics of a rough surface scatterer at all

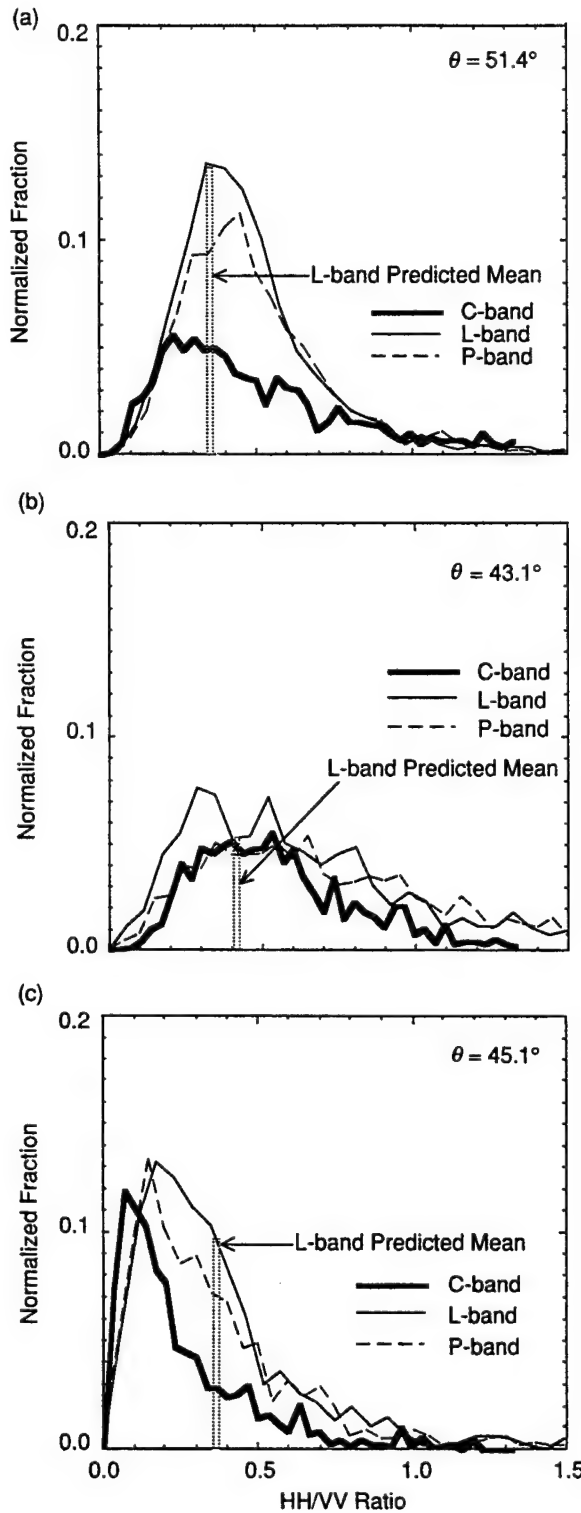


Fig. 24-3. Normalized distributions in the Beaufort Sea of individual hh/vv ratios at each frequency for (a) MY ice in box 1, (b) thick FY ice in box 2, and (c) thin FY ice in box 5. The measured L-band mean ratios are 0.44, 0.6, and 0.37 for Figure 24-1 boxes 1, 2 and 5, respectively; first-order model predictions are shown for comparison.

frequencies [Drinkwater et al., 1991a]. The mean C-band ratio falls close to -2.5 dB (0.6) for samples of this ice, but at L- and P-bands generally indicates slightly higher values. The $R_{hh/vv}$ at L-band is -2.2 dB, which is greater than the predicted value of -3.9 dB (0.41).

In contrast, box 5 (Figure 24-3) appears to be a smoother, higher salinity thin FY ice surface with a clustering of ratios less than 0.5 (-3 dB). Values are consistent with the small-perturbation scattering theory discussed in Chapter 8. First-order predictions suggest that vv-pol backscatter should exceed hh-pol backscatter for smooth surfaces at these incidence angles. The corresponding mean hh/vv ratios at each frequency become smaller as the wavelength or θ_i increases and as the ice salinity and permittivity increases [Winebrenner et al., 1989]. The $R_{hh/vv}$ falls close to predictions at L- and P-bands for smooth ice with a salinity of 15% and brine volume fraction close to 100%.

Box 1 demonstrates an intermediate situation and the L-band model predicts lower mean values than those observed. Penetration depths are greater in MY ice and, consequently, the polarimetric characteristics are somewhat different than those observed for higher salinity surfaces. The most pervasive of all observations to date is that MY signatures are remarkably stable in their polarimetric characteristics at L- and P-bands: backscattered power varies by only a fraction of a decibel.

Figures 24-4(a) and (b) show the trend in $R_{hh/vv}$ for FY and MY ice as θ_i varies from 32° to 52° . In Figure 24-4(a), the C-band ratio rises with increasing θ_i , with the ratio tending to 1 (i.e., 0 dB) at higher angles in FY ice. This trend is consistent with geometric optics scattering from floe edges or slope facets of rough FY ice at higher incidence angles [Livingstone and Drinkwater, 1991]. In contrast, at L-band the ratio falls with θ_i to -4.0 dB at 50° . This is consistent with the predicted L-band ratio at 50° for thick FY ice [Onstott et al., 1991]. The MY ice plot in Figure 24-4(b) shows C-band ratios to have negligible gradient; L-band ratios for the same ice are slightly lower. Both sets of values fall close to the theoretical surface scattering predictions for MY ice. Volume scattering may account for the residual difference and that the C-band ratio is closer to 0 dB. Comparative X-band values of $R_{hh/vv}$ observed for MY by Onstott et al. [1991] indicate a mean ratio of 0 dB. This is also consistent with the general trend towards a mean ratio of 0 dB as the wavelength decreases and the volume scattering increases.

24.3.2.2 Cross-pol ratios. An increase in $R_{hv/hh}$ and second-order scattering effects generally implies anisotropy in the surface roughness or the dielectric structure of the FY ice (e.g., as a consequence of brine-inclusion size and orientation), or air bubbles and inhomogeneities in MY ice. In Figure 24-4(a) there is an increase in the FY ratio with θ_i . The C-band ratio rises from around -15 dB at 32° to -11.5 dB at 52° . Though the L-band ratio is more variable over this range, a similar trend is reproduced with a mean offset of -2 dB throughout the 20° range. Figure 24-4(b)

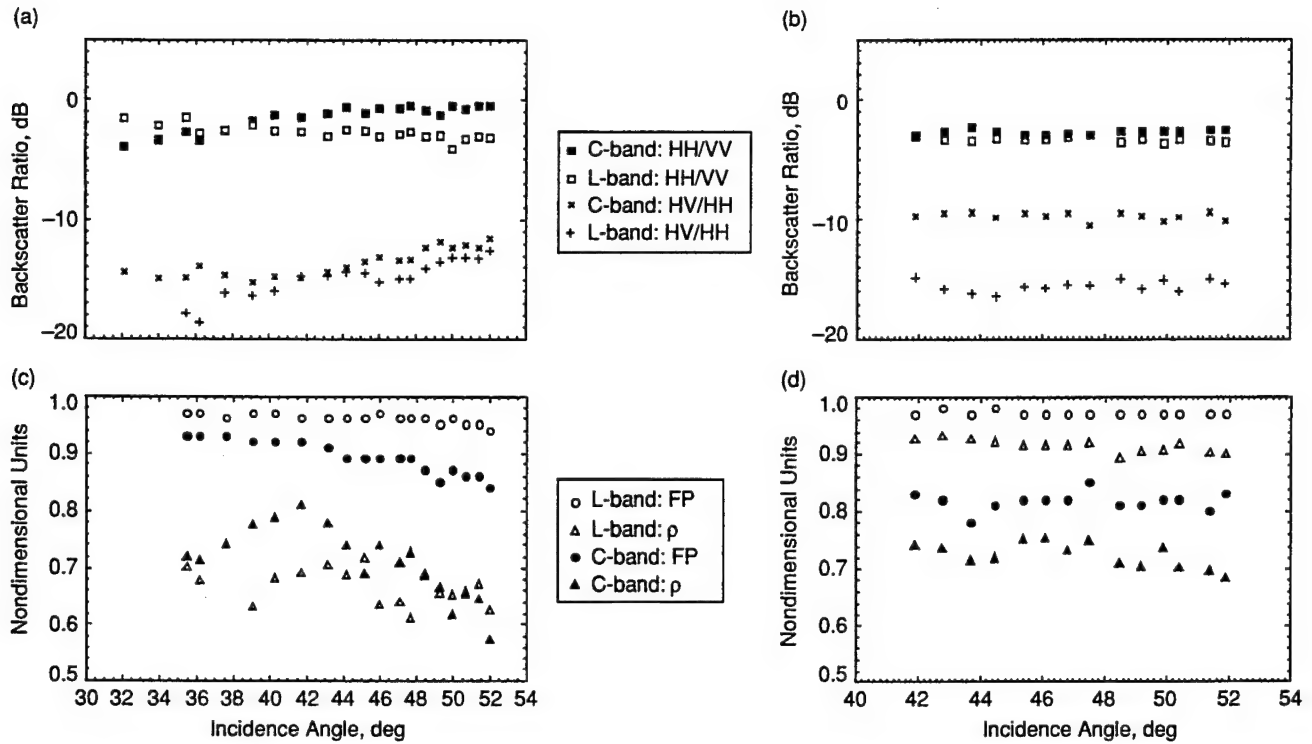


Fig. 24-4. Cross-swath C- and L-band polarimetric discriminant statistics. The upper panels show co- and cross-pol ratios in the Beaufort Sea for (a) FY and (b) MY ice. The lower panels show the correlation coefficient ρ between hh- and vv-pol returns and the corresponding fractional polarization (FP) for samples of (c) FY and (d) MY ice.

shows a contrasting MY situation with almost uniform mean ratios at each frequency: L-band has a mean $R_{hv/hh}$ value of around -15.0 dB, while the C-band mean is around -10.0 dB. Higher C-band MY ice cross-pol ratios of around -9.5 dB are recorded by Drinkwater et al. [1991a]. Notably, some of the highest cross-pol ratios have been observed for thin FY ice in the Beaufort and Bering Seas; certain L- and P-band examples result in values of $R_{hv/hh}$ between -6.9 dB and -9 dB [Drinkwater et al., 1991a]. Box 4 in Figure 24-1 is a particularly good example of high $R_{hv/hh}$, having L- and P-band values of -8.4 and -8.3 dB, respectively. The cross-pol isolation for the JPL radar system is around -27 and -17 dB for C- and L-band, respectively. Thus, these measurements are well within the sensitivity range of the JPL SAR.

At X-band, $R_{hv/hh}$ values are lowest for MY ice and increase as the surface salinity increases [Onstott et al., 1991]. In contrast, the above JPL SAR C-band results show that $R_{hv/hh}$ is highest for MY ice, generally decreasing the greater the salinity of the surface. Thick FY ice has a mean C-band ratio of -13.5 dB, while the lowest mean cross-pol ratios of -14.7 dB were observed for what is suspected to be thin frost-flowered ice [Drinkwater et al., 1991a]. Notably these latter examples also have the largest variability in the ratios. At L-band the reverse is true with MY ice exhibiting the smallest ratios.

24.3.3 Co-pol Correlation and Fractional Polarization

A condition for fully polarized radar backscattering from natural geophysical targets is that the cross-pol magnitude must be zero and hh and vv returns perfectly correlated (i.e., unity). The correlation coefficient between co-pol elements of \bar{C} is

$$\rho_{hhvv} = \left| \frac{(S_{hv} S_{vv}^*)}{\sqrt{(S_{hh} S_{hh}^*) (S_{vv} S_{vv}^*)}} \right| \quad (7)$$

At short wavelengths, FY sea ice typically has high correlation coefficients (tending to 1 at nadir). Figure 24-4(c) illustrates that the C-band correlation coefficient generally falls with θ_i in sea ice that is predominantly surface scattering, and at an increasing rate in higher salinity ice. In Figure 24-4(d), MY ice demonstrates slightly lower C-band values of ρ_{hhvv} than FY ice, due to the depolarization effects mentioned in Section 24.3.2. MY values indicate a much smoother and gradual monotonic decline with θ_i . Generally, the longer the wavelength, the lower the sensitivity of ρ_{hhvv} to surface or volume scattering effects. Figure 24-4(d) illustrates that the highest correlations ($0.89 \leq \rho_{hhvv} \leq 0.93$) are observed at L-band for MY ice.

The fractional polarization (FP) in Figure 24-4 is calculated from a sample by synthetically varying the polarization state and by recording the maximum (P_{max}) and

minimum (P_{\min}) intensities as both transmission and reception polarizations are varied [Zebker et al., 1987]. The value FP is then calculated from

$$FP = \frac{P_{\max} - P_{\min}}{P_{\max} + P_{\min}} \quad (8)$$

where FP is a measure of the polarization purity of the return; thus, for lower values the unpolarized component is greater and ρ_{hhvv} is reduced. Figures 24-4(c) and (d) illustrate that FP is close to unity at L-band for both FY and MY ice, in direct contrast to other geophysical media such as forest vegetation where values of $FP < 0.5$ are typical. Wavelength effects are significant and as the wavelength is reduced to C-band FP is similarly reduced. The value of FP falls with θ_i in FY ice from above 90% to around 82%, while FP in MY ice is consistently lower and relatively insensitive to θ_i . The lowest C-band values of FP (around 0.8) were observed by Drinkwater et al. [1991a] in MY ice. Together with correlation coefficients as low as 0.7, this indicates that the largest fraction of unpolarized returns occurs in lower salinity ice, and is probably due to multiple scattering from bubbles or air-filled inhomogeneities in the upper ice sheet.

24.3.4 Phase Differencing

Relative differences in phase between channels are important because each scattering event, either at reflective horizons or from diffraction by particles in the medium, transforms the relative phase of co-pol waves. The mean hh-vv phase difference is

$$\phi_{hh-vv} = \tan^{-1} \left[\frac{\Im(S_{hh} S_{vv}^*)}{\Re(S_{hh} S_{vv}^*)} \right] \quad (9)$$

where \Re and \Im indicate the real and imaginary parts, respectively. Normal incidence reflection from a highly conductive material such as sea water results in $\phi_{hh-vv} = 0$ and extremely low variability in the individual pixel phase difference. More complex distributed and layered targets such as sea ice often produce multiple reflections and sometimes nonzero values of ϕ_{hh-vv} . The hh-vv phase difference for a planar dielectric is also known to increase with θ_i . This arises from the sensitivity of a given linear polarization orientation to a particular scattering mechanism.

The co-pol phase difference ϕ_{hh-vv} can be estimated from the first-order Bragg scattering model. Assuming Fresnel reflection from a simple planar dielectric interface, Equation (9) reduces to

$$\phi_{hh-vv} = \tan^{-1} \left[\frac{\Im(R_h / R_v)}{\Re(R_h / R_v)} \right] \quad (10)$$

where R is the power reflection coefficient at h and v polarizations. L-band results in Onstott et al. [1991] indicate that for MY ice ϕ_{hh-vv} is predicted to be zero and independent of θ_i . If the surface is lossy, the co-pol phase term becomes negative and with increasing negative phase difference with increasing θ_i . The higher the dielectric constant of the surface, the more rapid this increase becomes. Thus, the co-pol phase difference in the range of 45° to 50° is largest for open water and typically around -5° at L-band [Onstott et al., 1991].

Figures 24-5(a) and (b) contrast distributions of MY and FY ice single pixel values of ϕ_{hh-vv} at C-band, while Figures 24-5(c) and (d) show the same contrast at L-band. Results of comparing MY samples across the swath show that distributions of ϕ_{hh-vv} have zero means and are independent of θ_i , thus making MY a good target for relative phase calibration within a scene [Drinkwater et al., 1991a]. The spread in the MY ice distribution increases with decreasing wavelength, indicating that at sufficiently short wavelengths volume scatter from inhomogeneities introduces mixed phase differences.

Compared with MY ice examples, the FY ice in Figures 24-5(b) and (d) shows more variability in ϕ_{hh-vv} . Sample boxes 2, 4, and 5 from Figure 24-1 indicate means displaced less than 5° from zero, but which are within the expected phase accuracy of ±5°. At C-band the variance in ϕ_{hh-vv} differs negligibly between ice type, but at L-band the distribution is much broader for FY ice than for MY ice.

Values of ρ_{hhvv} shown in Figure 24-4(c) and (d) are closely related to the hh-vv phase distributions in Figure 24-5. Generally, the lower ρ_{hhvv} is, the greater the variance in the phase difference and the smaller FP becomes. This situation is characterized by the differences in variance in L- and C-band MY ice co-pol phase distributions shown in Figures 24-5(a) and (c). Figure 24-4(d) indicates that the higher L-band values of ρ_{hhvv} result in a much narrower distribution of phase difference, as in Figure 24-5(c), while the lower C-band correlation produces a much broader spread, as in Figure 24-5(a).

24.4 GEOPHYSICAL APPLICATIONS OF POLARIMETRY

Multifrequency polarimetric SAR observations, together with passive microwave imagery, will ultimately yield retrievals of important geophysical ice information. In this section, preliminary results of geophysical importance are presented. Firstly, different types of thin ice and open water are identified using polarimetric observations. Secondly, images of sea-ice are classified using the polarimetric characteristics presented. Each result represents an improvement over single-frequency, single-polarization, incoherent radar observations of sea ice.

24.4.1 Thin Ice and Open Water Detection

One of the most significant problems facing single channel microwave techniques is their poor discrimination between

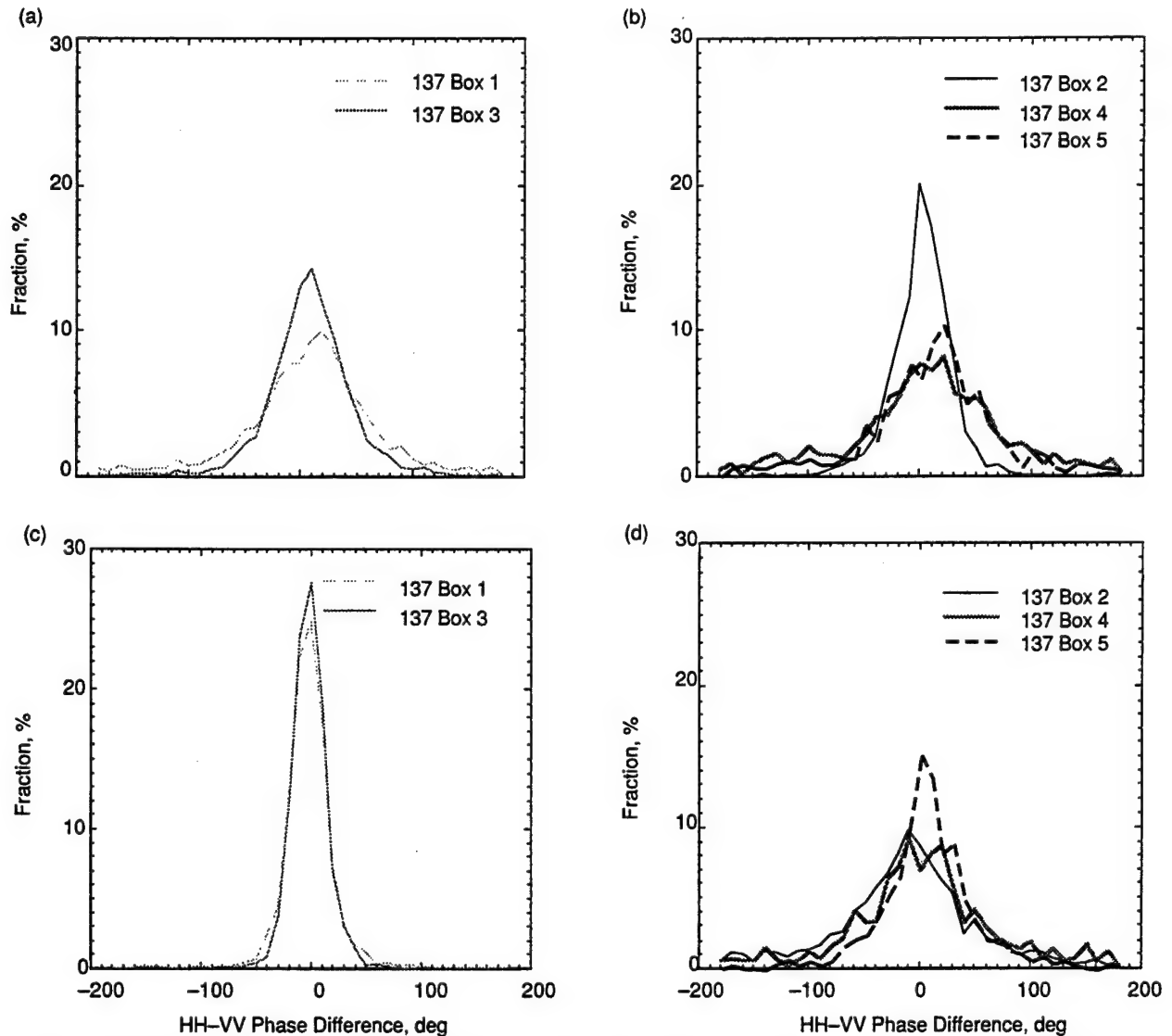


Fig. 24-5. Normalized C- and L-band hh-vv phase difference distributions derived from single pixel values from the boxes in Figure 24-1. Upper panels show C-band distributions for (a) the MY and (b) FY ice; the lower panels contrast L-band distributions of the same (c) MY and (d) FY examples.

open water and new ice. The early ice growth phase is of critical significance in controlling the vigor of heat, salt, and vapor fluxes taking place at the surface of the ocean. Thus, it is of particular importance to establish a technique for studying transformations in the ice during this period.

Polarization ratioing is employed as a means of discriminating between the ice and liquid phases of water [Winebrenner, 1990]. Providing that the sea ice is snow-free, as is typically the case for young or new ice, $R_{vv/hh}$ increases with θ_i at a rate dependent upon the complex dielectric constant. This relationship holds best for L- and P-bands in the range of roughness where the small-perturbation theory is valid (see Chapter 8). At C-band, the model is not valid, except for the smoothest surfaces encountered.

Thus, to first-order, the ratio is independent of roughness and is dependent only on θ_i and the brine volume fraction, and thus the thickness and age of the ice.

Winebrenner [1990] showed that single-pixel hh/vv ratios are noisy, requiring averaging of 100 pixels or more. Kwok et al. [1991a] extended this approach by averaging 20-by-20 pixel windows and using the mean ratio and the co-pol correlation to estimate and correct for additional system noise effects. Examples demonstrate L-band ratios between 2 and 10 dB in the range of 25° to 52°; these values are consistent with theoretical ratios for conditions between open water and thin ice. Confirmation for these findings is provided by collocated 33.6-GHz passive microwave brightness temperatures [Drinkwater et al., 1991b,

1991c]. The mean value of 150 K is well separated from the typical cold MY radiometric temperature (170 K) and is more consistent with the signature of new ice or open water. One example of ice–water discrimination is to use the calibrated L-band ERIM SAR data in Figure 24-2 from the Coordinated Eastern Arctic Experiment. Nilas and open water are each observed to produce weak backscatter at hh pol (−29.6 dB for nilas and −34.6 dB for water). In the vv-pol image where the water return is at its highest, the backscatter for nilas is weaker (−32.1 dB for nilas and −27.9 dB for water) and closer to that observed at hh pol.

Unique thin-ice signatures have been observed in many images acquired in the Beaufort Sea by the JPL SAR. This ice has characteristically bright C-band backscatter approaching that of MY ice, while having relatively low backscatter at L-band. In addition to the high vv/hh ratios noted above, a further effect has been recorded. Thin ice forming in leads is found to cause a significant phase shift between hh and vv returns, particularly at L-band, where values of -15° to -20° were noted by Kwok et al. [1991a]. The typical correlation coefficient for thin ice is also lower at L-band than for those examples observed for thick FY ice in Figure 24-3. At C-band though, ρ_{hhvv} is more consistent, with values for FY and MY ice ranging between 0.7 and 0.8. It is the latter clue that suggests that predominantly rough surface scattering is taking place at C-band while L-band penetrates the ice layer. Phase shifts can only be accounted for by a finite layer thickness effect that enables interference of top- and bottom-scattered signals. Ice salinities required to produce the observed hh/vv ratios and the observed phase effects are high and, since many of the observed ratios fall between the predictions for a thin ice layer and open water, this has led to speculation that the upper ice surface is roughened by frost flowers high in salinity.

24.4.2 Feature Use in Ice Classification

Polarimetric procedures for ice classification have been developed that utilize both magnitude and phase. In this final section, ice classification is broken into two stages: image segmentation using polarimetric image statistics, and labeling or tagging of the subdivided images into surface types.

24.4.2.1 Image segmentation. Polarimetric image segmentation requires no a priori information about sea ice and is simply based on the statistical distribution of the data. Several parameters need to be selected prior to segmentation, e.g., the number of image classes in relation to the number of sea-ice types that can be clearly identified, and the dimension and nature of the feature vector (combining different polarizations and frequencies).

Selection of image classes can be done either in a supervised or unsupervised manner. In the supervised polarimetric selection scheme used by van Zyl [1989], image classes, each corresponding to distinct polarimetric scattering behavior, were limited to single bounce, double

bounce, and diffuse scattering. In Rignot and Drinkwater [1992], selection of the image classes was unsupervised, and was instead based on a multidimensional cluster analysis of the polarimetric covariance matrix data. This technique examines less than 10% of the pixels in the image, is robust to the presence of image speckle, and accounts for the distribution of each sample pixel into more than one image class.

Given distinct image classes and their polarimetric backscatter characteristics, various methods are then available to segment the entire polarimetric radar scene. Scattering behavior [van Zyl, 1989], single discriminants (such as the hh–vv phase difference or the hh/vv ratio), or complete polarimetry can be used. A fully polarimetric maximum likelihood (ML) Bayes classifier was developed by Kong et al. [1988] and Lim et al. [1988] on the basis that polarimetric data are characterized by a multivariate Gaussian distribution. Both show that from Monte Carlo simulations and various images the Bayes classifier produces better results than those obtained using single polarimetric discriminants. Van Zyl and Zebker [1990] used this method for ice in the Beaufort Sea. They found that C-band data alone give excellent discrimination between FY and MY sea ice, but that ridged FY ice is confused with the latter. Though P- and L-band classifications separate pressure ridges from MY and FY ice types better, the most accurate classification of the three surface types is achieved using a combination of all three frequencies. Results obtained from the ML classifier remain noisy, however, and unsatisfactory for most practical applications. Rignot and Chellappa [1992] extended the ML technique with what is termed the maximum a posteriori (MAP) classifier. In the MAP technique, image classes are not assumed to have equal a priori probabilities, and spatial context is used to improve the segmentation results. MAP segmentation accuracy is typically improved by 10 to 20% over the ML classifier. Using the MAP classifier, Rignot and Drinkwater [1992] extended the analysis of van Zyl and Zebker [1990] to the delineation of five surface types: compressed FY ice, MY floes, FY ridges and rubble, undeformed thick FY ice, and thin ice (see Figure 24-6). Compressed FY ice, which is the deformed FY matrix that holds together MY ice floes, and the hummocks present in the MY ice floes are clearly separated from other ice types based on polarimetric data and coincident passive microwave measurements. Such compressed ice is probably extremely thick, rafted FY ice that has deformed then desalinated due to its higher freeboard. The best overall classification results are in discriminating these five distinct ice types (>90% estimated accuracy) using combined L- and C-band fully polarimetric data. Notwithstanding this result, certain combinations of two frequencies at a single polarization, or of two polarizations at a single frequency, yield classification accuracies that are only slightly lower (84% classification accuracy using L-band hh and vv pol and 89% classification accuracy using L-band hh pol and C-band vv pol).

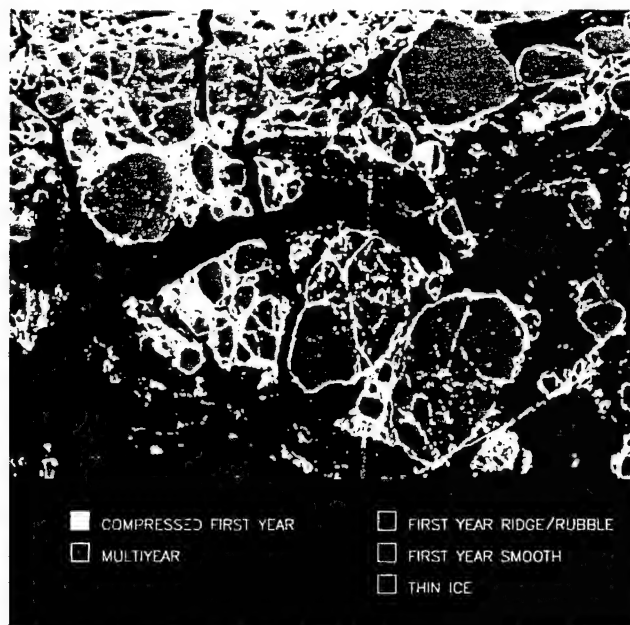


Fig. 24-6. Fully polarimetric C- and L-band MAP classification of five ice types [Rignot and Drinkwater, 1992].

24.4.2.2 Improvements in the labeling of segmented images. The final classification procedure requires labeling of segmented images. Identifying ice that demonstrates similar polarimetric characteristics requires a priori information about surface properties and scattering mechanisms. Most segmentations are labeled by deductive reasoning incorporating minimal surface data collected at ice camps, contextual information from patterns and the shape of features within the images, and experience from image analysis.

In the future, the required a priori ice information may be derived from two sources: surface measurements and model simulation data (i.e., a lookup table of the polarimetric backscatter characteristics of different ice types). Classifiers need to be constructed such that modeled polarimetric responses may be incorporated in the classification procedure. This will enable not only classification of broad classes of ice with different properties, but also extraction of geophysically important ice variables.

24.5 DISCUSSION

Knowledge of the Stokes or covariance matrices allows us to synthesize the scattering cross-section for all possible transmission and reception polarizations. Polarization signatures are not unique in that different combinations of scattering mechanisms may yield the same polarization response. However, the results from additional polarizations increase our present capability to solve for the geomet-

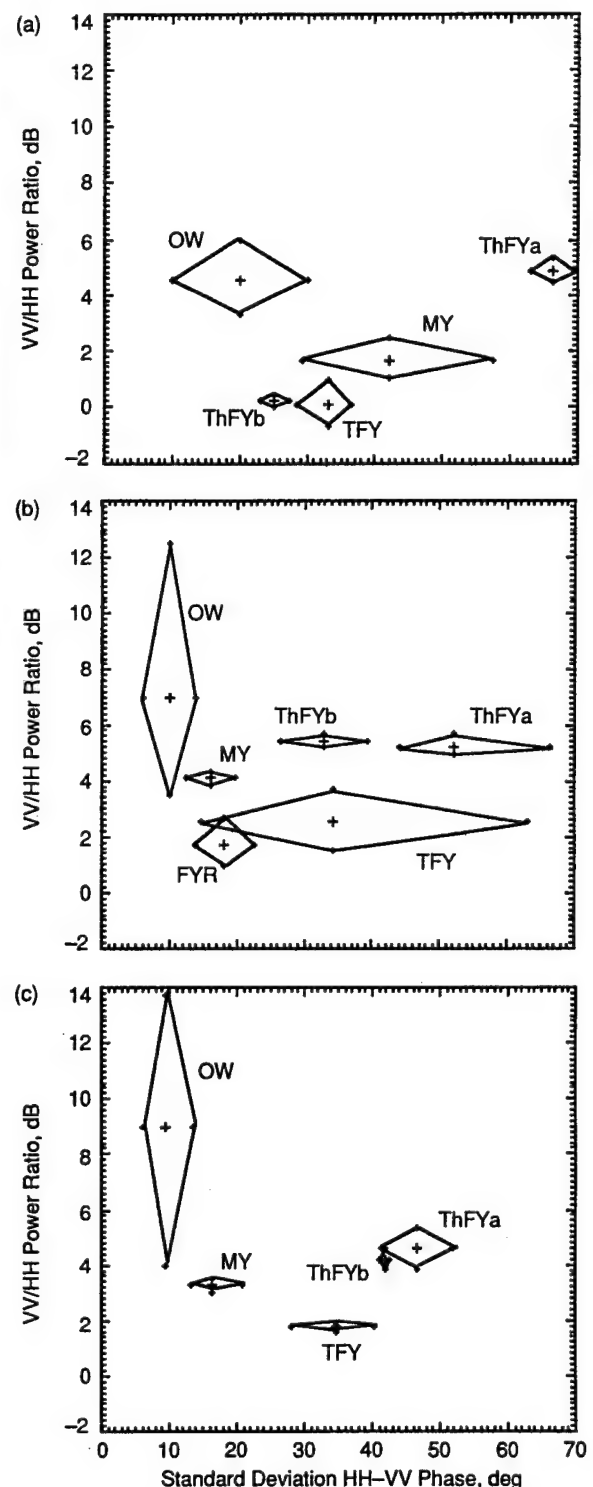


Fig. 24-7. Classification feature space for (a) C-band, (b) L-band, and (c) P-band, indicating the separability of ice types and open water using a polarimetric feature combining the spread in the hh-vv phase difference and the vv/hh power ratio. The categories are thin first-year ice (ThFYb), anomalous thin ice surfaces (ThFYa), thick first-year ice (TFY), rough Bering Sea first-year ice (FYR), multiyear ice (MY), and open water (OW).

ric structure of sea ice surfaces and dielectric properties of the main scatterers. This gives us a more flexible tool for identifying the dominant scattering mechanisms within an ice scene.

Measurement of the complete polarization response allows more rigorous testing of contemporary scattering models. These models must not only predict the backscatter coefficient as a function of θ_i or properties of the scatterer, but also as a function of the polarization of the transmitting and receiving antenna.

Results demonstrate that the essence of polarimetry is not simply in the added benefit of selectable polarization, so much as in the additional phase information embedded in correlations between differently polarized waves. The results of plotting the two single most effective discriminants are shown in Figure 24-7. This two-dimensional feature space incorporates the mean co-pol ratio $R_{vv/hh}$ and the standard deviation of the co-pol phase difference ϕ_{hh-vv} . Segmented clusters are labelled with the aid of Ka-band passive-microwave images and contextual information within radar images from the Beaufort and Bering Seas [Drinkwater et al., 1991a]. Discrimination of the three principal ice types (MY and thin and thick FY) is possible along with separation of all ice from open water. Clearly one of the main obstacles of single channel radar is overcome, namely, separating ice from open water. One of the more interesting observations is that anomalous thin FY ice returns, supposedly from frost-flowered new ice, are very different from other thin ice surfaces at short wavelengths. These two signatures become similar at P-band. Multiyear ice provides a tight cluster at L- and P-bands, when volume scattering is negligible, while thick FY ice shows its greatest variability at L-band.

With a demonstrated capability, in particular for identifying the early stages of thin ice formation, monitoring new ice by high-resolution radar polarimeter will become of critical interest in those regions of intense air-ice-ocean interaction (Chapters 12, 13, 14, and 15). A future spaceborne polarimetric SAR, such as the proposed EOS-SAR, offers the observational capability at the necessary scale and resolution to provide information about the influence of such key regions upon global climate.

REFERENCES

Drinkwater, M. R., Multi-frequency imaging radar polarimetry of sea ice, *Ice Technology for Polar Operations*, edited by T. K. S. Murthy, J. G. Paren, W. M. Sackinger, and P. Wadhams, pp. 365-376, Computational Mechanics Publications, Southampton, UK, 1990.

Drinkwater, M. R. and R. Kwok, Stokes matrix statistics in sea ice polarimetric SAR images, *Proceedings of the IGARSS'91 Symposium*, vol. 1, pp. 99-102, IEEE catalog no. 91CH2971-0, IEEE, New York, 1991.

Drinkwater, M. R., R. Kwok, D. P. Winebrenner, and E. Rignot, Multifrequency polarimetric synthetic aperture radar observations of sea ice, *Journal of Geophysical Research*, 96(C11), pp. 20,679-20,698, 1991a.

Drinkwater, M. R., J. P. Crawford, D. J. Cavalieri, B. Holt, and F. D. Carsey, *Comparison of Active and Passive Microwave Signatures of Arctic Sea Ice*, JPL Publication 90-56, Jet Propulsion Laboratory, California Institute of Technology, Pasadena, California, pp. 29-36, 1991b.

Drinkwater, M. R., J. P. Crawford, and D. J. Cavalieri, Multi-frequency, multi-polarization SAR and radiometer sea ice classification, *Proceedings of the IGARSS'91 Symposium*, vol. 1, pp. 107-111, IEEE catalog no. 91CH2971-0, IEEE, New York, 1991c.

Evans, D. L., T. G. Farr, J. J. van Zyl, and H. A. Zebker, Radar polarimetry: Analysis tools and applications, *IEEE Transactions on Geoscience and Remote Sensing*, GE-26, pp. 774-789, 1988.

Israelsson, H. and J. Askne, Analysis of polarimetric SAR observations of sea ice, *Proceedings of the IGARSS'91 Symposium*, vol. 1, IEEE catalog no. 91CH2971-0, pp. 89-92, IEEE, New York, 1991.

Kong, J. A. (editor), *Polarimetric Remote Sensing, Progress in Electromagnetic Research*, vol. 3, 520 pp., Elsevier Science Publishers, New York, 1990.

Kong, J. A., A. A. Swartz, H. A. Yueh, L. M. Novak, and R. T. Shin, Identification of terrain cover using the optimum polarimetric classifier, *Journal of Electromagnetic Wave Application*, 2(2), pp. 171-194, 1988.

Kwok, R., M. R. Drinkwater, A. Pang, and E. Rignot, Characterization and classification of sea ice in polarimetric SAR data, *Proceedings of the IGARSS'91 Symposium*, vol. 1, IEEE catalog no. 91CH2971-0, pp. 81-84, IEEE, New York, 1991a.

Lim, H. H., A. A. Swartz, H. A. Yueh, J. A. Kong, R. T. Shin, and J. J. van Zyl, Classification of Earth terrain using polarimetric synthetic aperture radar images, *Journal of Geophysical Research*, 94, pp. 7049-7057, 1989.

Livingstone, C. E. and M. R. Drinkwater, Springtime C-band SAR backscatter signatures of Labrador Sea marginal ice: Measurements versus modelling predictions, *IEEE Transactions on Geoscience and Remote Sensing*, 29(1), pp. 29-41, 1991. (Correction, *IEEE Transactions on Geoscience and Remote Sensing*, 29(3), p. 472, 1991.)

Livingstone, C. E., T. I. Lukowski, M. T. Rey, J. R. C. Lafontaine, J. W. Campbell, R. Saper, and R. Wintjes, CCRS/DREO synthetic aperture radar polarimetry—status report, *Proceedings of the IGARSS'90 Symposium*, vol. 2, IEEE catalog no. 90CH2825-8, pp. 1671-1674, IEEE, New York, 1990.

Onstott, R. G., T. C. Grenfell, C. Mätzler, C. A. Luther, and E. A. Svendsen, Evolution of microwave sea ice signatures during early summer and midsummer in the marginal ice zone, *Journal of Geophysical Research*, 92(C7), pp. 6825-6835, 1987.

Onstott, R. G., R. A. Shuchman, and C. C. Wackerman, Polarimetric radar measurements of Arctic sea ice during the Coordinated Eastern Arctic Experiment, *Proceedings of the IGARSS'91 Symposium, vol. 1*, pp. 93-97, IEEE catalog no. 91CH2971-0, IEEE, New York, 1991.

Rignot, E. J. M. and R. Chellappa, Segmentation of polarimetric synthetic aperture radar data, *IEEE Transactions on Geoscience and Remote Sensing*, in press, July 1992.

Rignot, E. J. M. and M. R. Drinkwater, On the application of polarimetric radar observations for sea ice classification, *Proceedings of the IGARSS'92 Symposium*, in press, Houston, 1992.

Ulaby, F. T. and C. Elachi, *Radar Polarimetry for Geoscience Applications*, 364 pp., Artech House, Dedham, Massachusetts, 1990.

van Zyl, J. J., Unsupervised classification of scattering behavior using radar polarimetry data, *IEEE Transactions on Geoscience and Remote Sensing*, 27(1), pp. 36-45, 1989.

van Zyl, J. J. and H. A. Zebker, Imaging radar polarimetry, *Polarimetric Remote Sensing, Progress in Electromagnetics Research*, vol. 3, edited by J. A. Kong, 520 pp., Elsevier Science Publishers, New York, 1990.

Wen, T., W. J. Felton, J. C. Luby, W. L. J. Fox, and K. L. Kientz, *Environmental Measurements in the Beaufort Sea, Spring 1988*, Technical report APL-UWTR 8822, 34 pp., Applied Physics Laboratory, University of Washington, Seattle, 1989.

Winebrenner, D. P., Accuracy of thin ice/open water classification using multi-polarization SAR, *Proceedings of the IGARSS'90 Symposium, vol. 1*, IEEE catalog no. 90CH2825-8, pp. 2237-2240, IEEE, New York, 1990.

Winebrenner, D. P., L. Tsang, B. Wen, and R. West, Sea-ice characterization measurements needed for testing of microwave remote sensing models, *IEEE Journal of Oceanic Engineering*, 14(2), pp. 149-158, 1989.

Zebker, H. and J. J. van Zyl, Imaging radar polarimetry: A review, *Proceedings of the IEEE*, 79(11), pp. 1583-1606, 1991.

Zebker, H. A., J. J. van Zyl, and D. N. Held, Imaging radar polarimetry from wave synthesis, *Journal of Geophysical Research*, 92, pp. 683-701, 1987.

Investigation of the Effects of Summer Melt on the Calculation of Sea Ice Concentration Using Active and Passive Microwave Data

DONALD J. CAVALIERI

Laboratory for Oceans, NASA Goddard Space Flight Center, Greenbelt, Maryland

BARBARA A. BURNS AND ROBERT G. ONSTOTT

Radar Science Laboratory, Environmental Research Institute of Michigan, Ann Arbor

Active and passive microwave data sets acquired during the 1984 Marginal Ice Zone (MIZ) Experiment aircraft flights in the Fram Strait region are used to examine the effects of ice surface melt on microwave signatures and their resulting error in the calculation of sea ice concentration. Conditions examined with the active-passive data set include ice floes with moist and dry snow cover and both heavily ponded and ridged surfaces. Passive sensors on the NASA CV-990 aircraft included the aircraft electrically scanning microwave radiometer (ESMR) operating at 19.4 GHz and aircraft multichannel microwave radiometer (AMMR) operating at 10.7, 18.0, 21.0, and 37.0 GHz. Active microwave sensors flown on the Canadian Centre for Remote Sensing CV-580 aircraft included the Environmental Research Institute of Michigan synthetic aperture radar (SAR) operating at 1.2 and 9.4 GHz. Coincident AMMR and SAR measurements of individual floes identified in aerial photography are used to describe the effects of surface melt on the calculation of sea ice concentration, and in particular, the response of the passive microwave polarization and spectral gradient characteristics to different stages of surface melt. Although the onset and progression of summer melt are not uniform throughout the Arctic, the stages of summer melt observed in the MIZ are also observed on a large-scale in the central Arctic. This is demonstrated using Nimbus 7 SMMR data and Arctic Ocean buoy temperature data over one annual cycle. Finally, the potential of optimally combining both active and passive microwave data in an effort to ameliorate these surface melt effects during the summer months is also explored.

1. INTRODUCTION

The importance of having a long-term passive microwave data set of known accuracy for obtaining climatologically important ice parameters on both global and regional scales is well recognized. The Nimbus 7 scanning multichannel microwave radiometer (SMMR) has provided almost 9 years of global sea ice concentrations and numerous case studies have been carried out to determine the accuracy of these concentrations primarily under winter and premelt conditions [e.g., Martin *et al.*, 1987; Steffen and Maslanik, 1988]. Summer sea ice concentrations are more uncertain because of the presence of moist snow, wet ice surfaces, and the collection of free water in depressions (i.e., meltponds), and of temperature-dependent variations in ice emissivity near the melt point [Cavalieri *et al.*, 1984; Onstott *et al.*, 1987].

Problems associated with the interpretation of passive microwave data during summer months were recognized early on. Areas of low microwave radiance observed during summer in the central Arctic with the Nimbus 5 electrically scanning microwave radiometer (ESMR) were interpreted as low ice concentration areas [Gloersen *et al.*, 1978; Campbell *et al.*, 1980], whereas Crane *et al.* [1982] suggested an alternative explanation in terms of melt ponding effects. This problem was revisited by Campbell *et al.* [1984], who argued that the low radiance areas are primarily due to open leads and polynyas. A first attempt at actually mapping melt pond fractional coverage using microwave data was made by Carsey [1985]. From lead area estimates and from Nimbus 5

ESMR brightness temperature time series, Carsey argued that the time of minimum brightness (mid-July) corresponds to maximum pond coverage, but also noted that other surface phenomena cannot be unambiguously distinguished from the ponding maximum. Clearly, these areas of low radiances observed in passive microwave data will remain ambiguous in the absence of additional information. Recently, in a study of late summer Nimbus 7 SMMR brightness temperature variations in the Canadian Basin for the period 1979-1984, Barry and Maslanik [1989] used Defense Meteorological Satellite Program (DMSP) optical line scanner and NOAA advanced very high resolution radiometer (AVHRR) visible imagery as their additional source of information to establish that areas of low brightness temperature and increased polarization corresponded to areas of actual reduced ice concentration in 4 of the 6 years studied.

Since passive microwave satellite observations alone cannot distinguish between the collection of meltwater on an ice surface and the water between ice floes, a means is needed to estimate the areal extent of ponding within floe boundaries. This paper explores the potential of synthetic aperture radar (SAR) to provide the additional information needed to supplement the passive microwave data in order to unambiguously discriminate between open water areas and ponded floes. Previously, high-resolution aircraft SAR data have been used to discern individual floes and to provide information concerning the state of melt pool development and its areal extent [Burns *et al.*, 1984, 1985; Onstott and Moore, 1984; Holt and Digby, 1985].

A previous study of summer ice concentrations [Burns *et al.*, 1987] utilized active and passive microwave aircraft sensors flown during the 1984 Marginal Ice Zone Experiment

Copyright 1990 by the American Geophysical Union.

Paper number 89JC03158.
0148-0227/90/89JC-0315\$05.00

(MIZEX). The passive sensors on the NASA CV-990 aircraft included an ESMR operating at 19.4 GHz and an aircraft multichannel microwave radiometer (AMMR) operating at 10.7, 18.0, 21.0, and 37.0 GHz. The fixed-beam AMMR radiometers measured both horizontally and vertically polarized radiances at all frequencies except 21 GHz. The active microwave sensor included the Environmental Research Institute of Michigan (ERIM) SAR operating at 1.2 and 9.4 GHz on the Canadian Centre for Remote Sensing (CCRS) CV-580 aircraft. A detailed description of these sensors may be found in the Burns et al. paper.

A comparison of ice concentrations derived from the single-frequency (9.4 GHz) active and single-frequency (19.0 GHz) passive microwave aircraft imagery showed that they agreed to within 13%. It was determined that the primary cause of the discrepancy was ice signature variations of the X-band SAR. The SAR image statistics for an entire scene showed little bimodality; a broad ice intensity distribution resulted from variations in surface conditions including moist or saturated snow cover and wet ice surfaces, although local areas showed good ice/water discrimination. Speckle noise was also a contributing factor. This was in contrast to the 19 GHz passive microwave imagery which showed a distinct brightness distribution with two broad peaks.

Sea ice concentrations were also obtained from coincident aerial photography. Both the SAR and AMMR ice concentrations agreed to within 13–14% of the concentrations from the aerial photographs. Concentrations from the digitized photographic imagery, also subject to various uncertainties, were treated not as “ground truth,” but simply as another remotely-sensed measurement of ice concentration.

In the same study, a comparison of SAR and AMMR ice concentration measurements, which spanned a range between 45% and 56%, showed a mean difference of 3.5%. In contrast to the single-channel ESMR concentrations, the AMMR algorithm results exhibited much less variability (5.6% versus 17.5% for ESMR) which was attributed in part to the sensor's lower spatial resolution (see Table 1 of Burns et al. [1987]) and in part to the ability of the algorithm to accommodate variations in ice surface emissivity. The rms difference between the concentrations from the AMMR and the photography was 10.4% for three of the four areas sampled, while the rms difference between the SAR and photography was 15.8%. The SAR and AMMR gave identical results (56%) for the fourth sample, in contrast to 83% derived from the digital photographic image. Interestingly, both the photograph and the SAR image showed evidence of surface melt.

In the present study we examine in much greater detail the effect of surface melt on microwave signatures and the resulting error in the calculation of sea ice concentration. We also explore the potential of optimally combining both active and passive microwave data in an effort to ameliorate the effects of melt ponding on the calculation of ice concentration during the summer months. As in the Burns et al. [1987] study, we use both the active and passive microwave data sets acquired during the 1984 MIZEX aircraft flights (see Figure 1). An overview of the large-scale sea ice conditions encountered during the experiment is provided by Campbell et al. [1987]. Conditions in the coincident active/passive microwave aircraft data set under consideration include ice floes with dry, moist and saturated snow covers and with both heavily ponded and ridged surfaces. A related study by

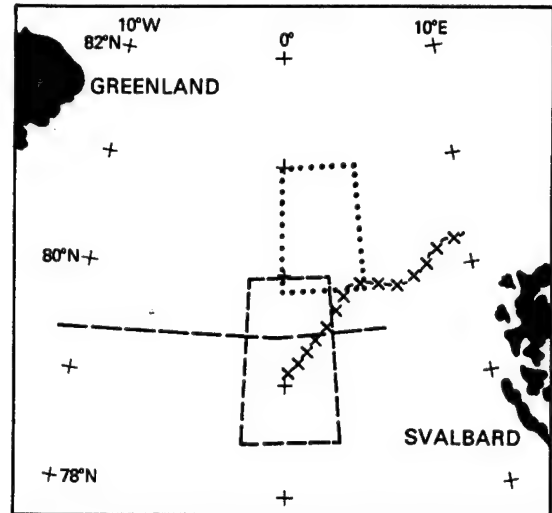


Fig. 1. Map of the Fram Strait region showing the location of the aircraft coverage used in this study. The two boxes indicate the SAR coverage on June 29 (dotted lines) and on June 30 (dashed lines). The E-W track (dashed line) gives the northern most leg of ESMR and AMMR coverage on June 30. The June 30 ice-edge position as determined from SMMR imagery is indicated by the cross-hatched line.

Gloersen and Campbell [1988] examined the influence of surface melt on the calculation of multiyear ice concentration. The emphasis in this study is on the dual-polarized, multifrequency passive microwave sensors and the single-channel SAR as these will be the types of satellite sensors providing coincident or nearly coincident data in the near future.

2. MICROWAVE CALCULATION OF SEA ICE CONCENTRATION

2.1. Passive Microwave

In contrast to the simple linear ice concentration algorithm used with the 19 GHz ESMR, the AMMR sea ice algorithm uses the 18 and 37 GHz channels to calculate both total and multiyear sea ice concentration. Two ratios of radiances serve as the independent variables. These ratios are the polarization ratio PR and the spectral gradient ratio GR defined by

$$PR(f) = \frac{TBv(f) - TBh(f)}{TBv(f) + TBh(f)} \quad (1)$$

$$GR(18, 37) = \frac{TBv(37) - TBv(18)}{TBv(37) + TBv(18)} \quad (2)$$

where f is frequency (18 GHz is used in this study), and TBv and TBh are the observed microwave brightness temperatures at vertical and at horizontal polarization, respectively. The advantage of using these ratios is that they are almost orthogonal in the sense that variations in PR reflect mostly changes in ice concentration and are largely independent of ice type (first-year or multiyear), whereas variations in GR reflect mostly changes in ice type. GR is also used to minimize weather-related effects including the microwave emission by atmospheric water vapor, cloud liquid water and wind-roughened seas which are known to result in false

indications of sea ice over open oceans [Gloersen and Cavalieri, 1986]. Under summer melt conditions, multiyear ice type discrimination becomes indeterminable; nevertheless, the orthogonal nature of these independent variables provides a mechanism for overcoming the effects of early melt on the calculation of total ice concentration as will be illustrated in section 4 below.

The expression for the total sea ice concentration (C) is actually a sum of the first-year (C_{FY}) and multiyear (C_{MY}) ice concentrations calculated as follows:

$$C_{FY} = \frac{F_0 + F_1 PR + F_2 GR + F_3 (PR)(GR)}{D_0 + D_1 PR + D_2 GR + D_3 (PR)(GR)} \quad (3)$$

$$C_{MY} = \frac{M_0 + M_1 PR + M_2 GR + M_3 (PR)(GR)}{D_0 + D_1 PR + D_2 GR + D_3 (PR)(GR)} \quad (4)$$

$$C = C_{FY} + C_{MY} \quad (5)$$

The algorithm is discussed in detail by Cavalieri *et al.* [1984] and further by Gloersen and Cavalieri [1986]. The values of the constants F_i , M_i and D_i ($i = 0$ to 3) are as follows:

$$F_0 = 2284.36 \quad F_1 = -21,403.00$$

$$F_2 = 16,003.92 \quad F_3 = 1424.94$$

$$M_0 = -561.20 \quad M_1 = 16,023.66$$

$$M_2 = -22,386.97 \quad M_3 = -38,971.83$$

$$D_0 = 1424.94 \quad D_1 = 8715.30$$

$$D_2 = -4125.98 \quad D_3 = -11,416.34$$

Note that the corresponding coefficients given in Gloersen and Cavalieri differ slightly from these due to a numerical error discovered after publication.

2.2. Active Microwave

The sea ice concentration algorithm used with the single-channel 9.4 GHz SAR data is the same as in the Burns *et al.* [1987] study, that is, a linear interpolation between the radar backscatter of open water and sea ice. As stated there this technique was adopted as an attempt to account for the ice signature variability and not because we are treating a mixed-pixel situation. In fact, because of the high resolution of the SAR, most pixels can be assumed to represent areas of 100% ice or 100% water, and mixed pixels covering both surface types are expected only at the ice/water boundaries. Here location at a boundary, the finite time-response of the sensor, and the smoothing effect of digital post-processing (geometric rectification and speckle reduction) all contribute to this situation which is clearly most frequent in the marginal ice zone. Even for SARs with ERS-1 resolution, this mixed-pixel situation would be minimal in pack ice areas.

The linear expression for sea ice concentration $C(I)$ is:

$$C(I) = (I - I_w) / (I_I - I_w) \quad (6)$$

where I is the backscatter intensity for a given pixel, and I_I and I_w are the mean values of sea ice and of open water intensities, respectively, with $I_I > I_w$. Conditions other than those encountered during the summer MIZEX can result in

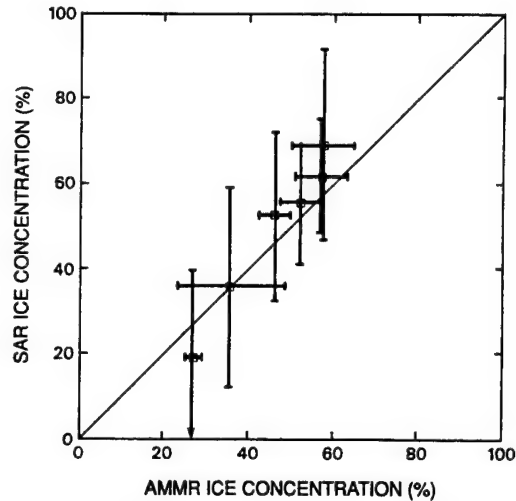


Fig. 2. Comparison of Greenland Sea MIZ ice concentrations derived using X-band SAR and AMMR measurements for six areas. The vertical and horizontal lines represent the standard deviation of the SAR and AMMR measurements respectively.

signature ambiguities that would lead to errors in ice concentration using this algorithm. One example is the presence of grease ice (soupy layer of coagulated ice crystals on the water surface) which has a signature similar to calm open water [Gray *et al.*, 1982]. Another is wind-roughened water which at low-incidence angles can appear brighter than the surrounding ice [Askne and Ulander, 1989]. In these cases, information in addition to image intensity must be used to obtain concentration estimates.

This algorithm was applied on a pixel-by-pixel basis to the 9.4 GHz SAR data which had been radiometrically rectified (although not calibrated) to remove intensity variations dependent on radar range. Only the 9.4 GHz data were used because of the more uniform ice signature at this frequency versus the 1.2 GHz data (see below). Further discussion of the algorithm is given by Burns *et al.* [1985, 1987].

2.3. Comparison

Six areas each of 6 km^2 in size were identified as having coincident SAR and AMMR coverage. The observations from these sensors were registered using both the NASA CV-990 and the Canadian CV-580 aerial photography. For each area, mean concentration values and their standard deviations were calculated from the SAR and AMMR data and are shown in Figure 2. The calculated ice concentrations for these six areas range from approximately 20% to approximately 70%. Examination of the figure shows that the SAR concentration estimates are on average 3.8% higher than the AMMR estimates and have an intrascene variability approximately three times greater. Similar results were obtained in the previous study by Burns *et al.* [1987, Table 6] which showed for four samples a mean difference of 3.5% between SAR and AMMR estimates. The lower AMMR measurements may be attributable in part to the lower resolution of the AMMR sensor through contamination by peripheral areas of open water seen by the wings of the relatively wide antenna pattern of the sensor itself. The large difference in the magnitude of the standard deviations results from the greater variability of the SAR ice signatures, from the ability

of the AMMR algorithm to accommodate some of the passive microwave signature variability, and to some degree from the higher spatial resolution of the SAR.

3. MICROWAVE SIGNATURES OF MELT EFFECTS

In this section we review briefly the characteristics of microwave sea ice signatures observed during the 1984 MIZEX and then show using Nimbus 7 SMMR data and Arctic Ocean buoy temperatures that the progression of summer melt observed in the MIZ is also observed in the central Arctic.

The snow and sea ice conditions and associated microwave signatures during the 1984 MIZEX have been discussed previously by *Onstott et al.* [1987]. They observed that during the experiment the sea ice and its snow cover underwent a transition from late spring to summer when air temperatures were within 2°C of the freezing point. As the air temperature increases, the snow cover becomes progressively moist, until in early summer it has become thoroughly moistened and free water percolates to the snow/ice interface where it collects to form subsurface pools. As the season progresses, surface melt ponds form and at about midsummer begin to drain.

Because of the considerable difference in the microwave emissivities of water and ice, the effect of this evolution of surface conditions on the microwave emission is a deviation from the winter signatures in proportion to the amount of free water present. As the liquid water content of the snow cover increases from 0 to 0.5%, the penetration depth will decrease by more than an order of magnitude [Ulaby *et al.*, 1982]. During winter when the snow cover is dry and the underlying sea ice is cold, the microwave emission for first-year ice is almost independent of frequency, while multiyear ice emission decreases with increasing frequency [e.g., *Cavalieri et al.*, 1984]. With the snow cover becoming moist in late spring, the multiyear ice signature becomes indistinguishable from that of first-year ice [e.g., *Comiso*, 1983]. In some instances during the early stages of summer melt, the radiometric brightness temperature of multiyear ice becomes greater than that of first-year ice [Grenfell and Lohanick, 1985]. Because this increase of free water is neither temporally or spatially uniform during this time of year, the overall distribution of multiyear pack ice may look quite different than during midwinter. As the snow cover becomes progressively wet, the microwave signatures become progressively less variable. This is because the average microwave emission is determined by conditions within the frequency dependent penetration depth, which in this period corresponds to a layer of moist snow with an emissivity close to unity. Thus the microwave emission is high at all frequencies and resembles that of winter first-year ice, making the differentiation of ice type indiscriminate [*Cavalieri et al.*, 1984; *Onstott et al.*, 1987]. Beginning about midsummer as surface melt ponds form and drain, the microwave emissivity becomes extremely variable reflecting the great spatial variability of surface conditions. In late summer and early fall the ice types once again become radiometrically distinguishable and their signatures approach their winter values.

Ice type discrimination is also lost during the first half of summer in the radar signature because the backscattering process is dominated by surface scattering and/or absorption

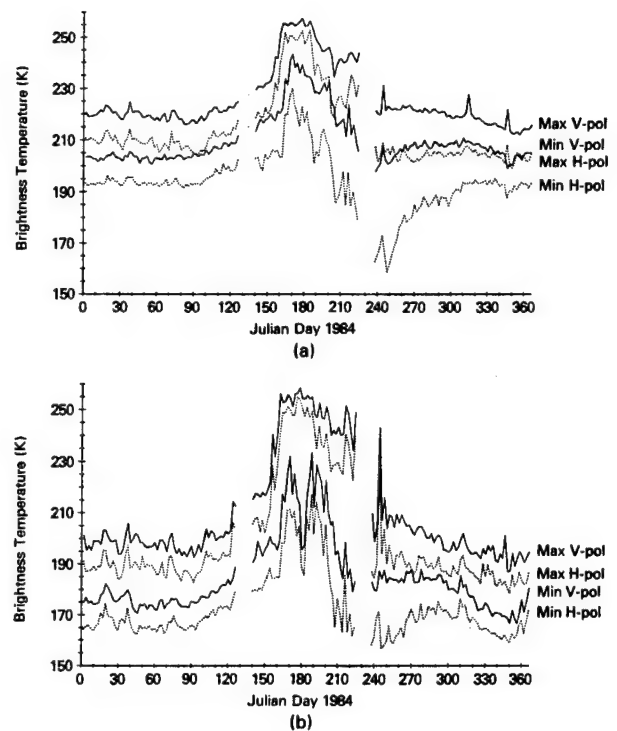


Fig. 3. Maximum and minimum (a) 18 GHz H and V and (b) 37 GHz H and V SMMR brightness temperatures for a $600 \times 600 \text{ km}^2$ region north of the Canadian archipelago for 1984.

in the moist snow pack resulting in a loss of ice type classification [*Livingstone et al.*, 1987a, b]. Large intensity variability is still present, though, due to different degrees of surface wetness and amounts of snow cover. By early to midsummer the snowpack has experienced considerable melt and depressions in the ice or ice with a lower freeboard will have collected varying quantities of meltwater. Fully open water meltponds will appear as extremely low return areas at both 1.2 and 9.4 GHz. In areas where melt pools are still forming and the snow has been transformed into mixtures of snow, ice, and water, very strong returns are produced in the SAR imagery. For areas of thick snow, weak returns are produced at both frequencies, and the ice surface topography is well masked. As the frequency decreases, the contrast between areas with heavy and thin snow cover increases. In areas where melting has produced both a thin snow cover and small-scale surface roughness (of the order of 1–3 cm for first-year ice), enhanced returns are produced, especially at 1.2 GHz. Thus in late summer, as the ice surface is exposed and surface melt ponds drain, the radar backscatter, as well as the microwave emission, again reflects ice type differences.

This progression of surface melt conditions observed in the MIZ by *Onstott et al.* [1987] is also observed on a larger scale in the central Arctic. The change in the minimum and maximum sea ice brightness temperatures from the Nimbus 7 SMMR 18 and 37 GHz horizontal and vertical polarization channels over one annual cycle is illustrated in Figures 3a and 3b for a $600 \times 600 \text{ km}^2$ area in the central Arctic north of the Canadian archipelago. From an examination of Figure 3 we observe that the discrimination between the 18 and 37 GHz radiances throughout winter and early spring is well defined. The actual difference between the two signatures is

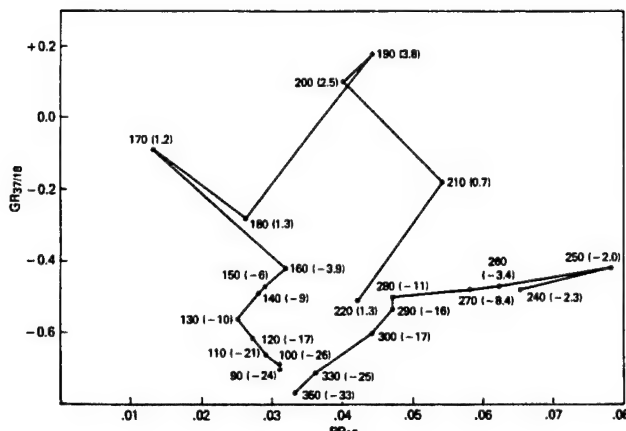


Fig. 4. Average values of GR and PR plotted every 10th day in 1984 from Julian day 90 through Julian day 350 together with corresponding Arctic Ocean buoy temperatures shown in parenthesis for the same Arctic region as for Figure 3.

a measure of the relative amounts of first-year and multiyear sea ice. This spectral difference, measured in terms of the spectral gradient ratio defined by (2), is used to obtain ice type concentrations. Beginning about Julian day (JD) 100 (April 9), all the brightness temperatures begin to increase as a result of the general seasonal warming. On or about JD 170 (June 18) there is a very sharp increase in the temperatures indicating the onset of summer melt. During summer the well-defined discrimination between the 18 and 37 GHz channels is lost as is the corresponding ice type information. Starting about JD 270 (September 26) the signatures begin to diverge and assume their characteristic winter values.

The average PR and GR values for this same central Arctic region are plotted every 10 days in 1984 from JD 90 through JD 350 and are shown in Figure 4. The gap between JD 220 and JD 240 is due to missing data. Each point also has associated with it a temperature shown in parentheses obtained from Arctic Ocean buoys 3835 and 3849 located within the $600 \times 600 \text{ km}^2$ region. Although the reported temperatures [Colony and Munoz, 1986] are from a sensor within the buoy, they are believed to be within a few degrees of the ambient air temperature [Martin and Clarke, 1978]. From March (JD 90) through May (JD 150) the temperatures are well below freezing, but by mid-June the temperatures reach the freezing point and the PR and GR values approach zero (JD 170). This is consistent with the sequence of events described earlier whereby at some time in early to midsummer there is a period when the snow cover becomes very nearly a perfect blackbody emitter. Interestingly, in a related study of SMMR brightness temperature data and Arctic Ocean buoy temperature data for the summers of 1979 through 1982, Maslanik and Barry [1989] find that the rapid increase in brightness temperature typically occurs around June 20 (JD 171) which is within a day of what is shown in Figure 4. By June 28 (JD 180) the PR value has increased to wintertime values, but GR is appreciably greater indicating a loss of ice type information. Because polarization information remains largely intact, but with larger uncertainties, we can still derive useful total ice concentration information. From JD 180 until mid-September (JD 260) there is considerable variability in both PR and GR indicating a complicated mix of surface conditions including wet snow, surface

melt ponding, and open water. From September to mid-December the temperature decreases and the PRs and GRs return to their wintertime values.

4. EFFECTS OF SUMMER MELT ON CONCENTRATION CALCULATIONS

We now examine the microwave signatures of three ice floes which illustrate the progression of summer melt from early spring to late summer for the purpose of understanding the effect that these characteristics have on the calculated ice concentrations. These floes were identified with the aid of the NASA CV-990 aerial photograph record for the June 30 flight and are shown in Figure 5. The three images were taken with a KS87-B metric camera from an altitude of 33,000 feet and each frame has a field-of-view of approximately 10 km along the direction of flight (right to left). The across-track (up and down) distortion results from the camera looking off to the right of nadir at an angle of 45°.

The first floe, floe A, appears to the right of center in Figure 5a and is a composite floe made up of primarily multiyear ice. Cloud shadows are visible against the bright snow cover on the floe. The location of this floe was over 200 km west of the main ice edge (see Figure 1) where the local environmental conditions were closer to winter than summer. The CV-990 infrared radiometer (PRT-5) measurements gave surface water temperatures of -1.6°C to -2.1°C . There were also visual sightings of grease ice formation between floes [Gloersen *et al.*, 1985], another indication of cold surface conditions. From an examination of an enlarged Figure 5a there appears to be a heavy snow cover and considerable ridging. From a survey of the physical properties of the ice in the experiment region during June and July, Tucker *et al.* [1987] found that of the 40 floes sampled, 27 were identified as multiyear, 9 as first-year, and 4 as composite floes of first-year and multiyear ice. Their measurements of snow depth revealed that multiyear floes had a significantly deeper snow cover averaging 28.5 cm as compared with first-year ice, which had an average cover of only 8 cm.

The second floe, floe B, is a large floe made up of smaller multiyear floes cemented together (Figure 5b). There are also some thin first-year ice areas, the areas that are grey in appearance. This floe was observed from the aircraft, and a few melt areas were reported to be visible [Gloersen *et al.*, 1985]. An examination of the image shows that there is some evidence of melt ponds beginning to form in the right of center of the floe. The floe was located approximately 100 km west of the ice edge. Ships in the general vicinity reported surface air temperatures hovering around 0°C .

The third floe, floe C, is another large composite floe similar to floe B but shows a more advanced stage of melt as indicated by the small dark grey areas which are more or less evenly distributed across the floe (Figure 5c). This floe was located just inside the ice edge and an icebreaker located just west of the floe well within the pack ice reported surface air temperatures just above freezing.

Floe C was the only one of the three floes which was imaged coincidentally by the active and passive sensors on June 30. In Figure 6 we show the 1.2 GHz and the 9.4 GHz SAR images which include a portion of this large floe. Observed differences result from the distortion produced by the side-looking camera on the CV-990 and the side-looking

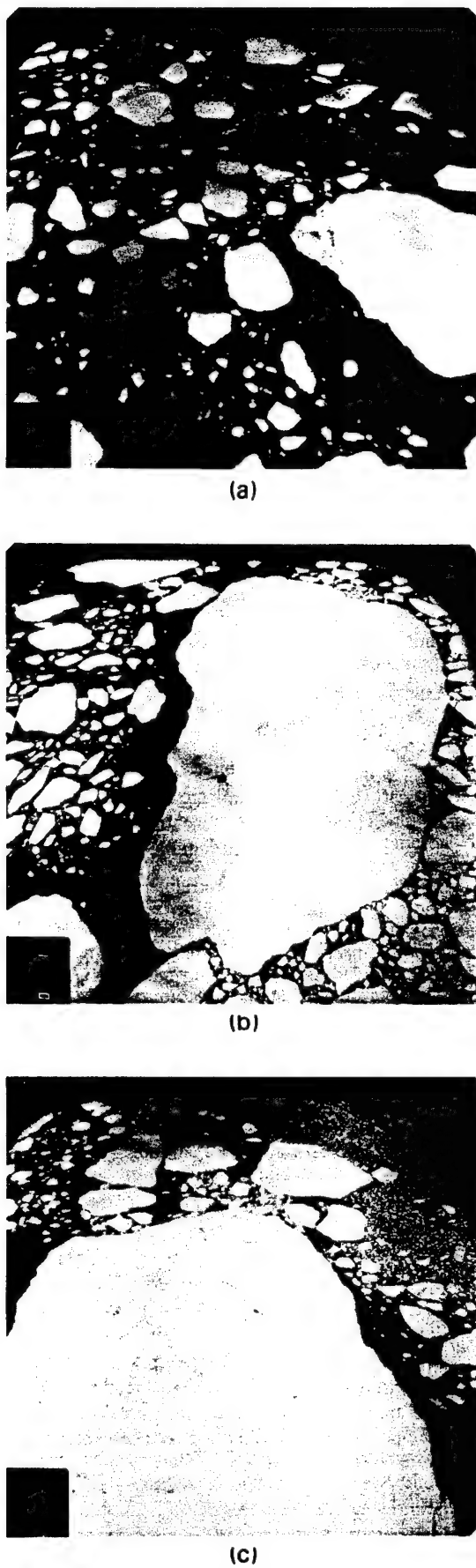


Fig. 5. NASA Convair-990 aerial photographs of floes (a) A, (b) B, and (c) C.

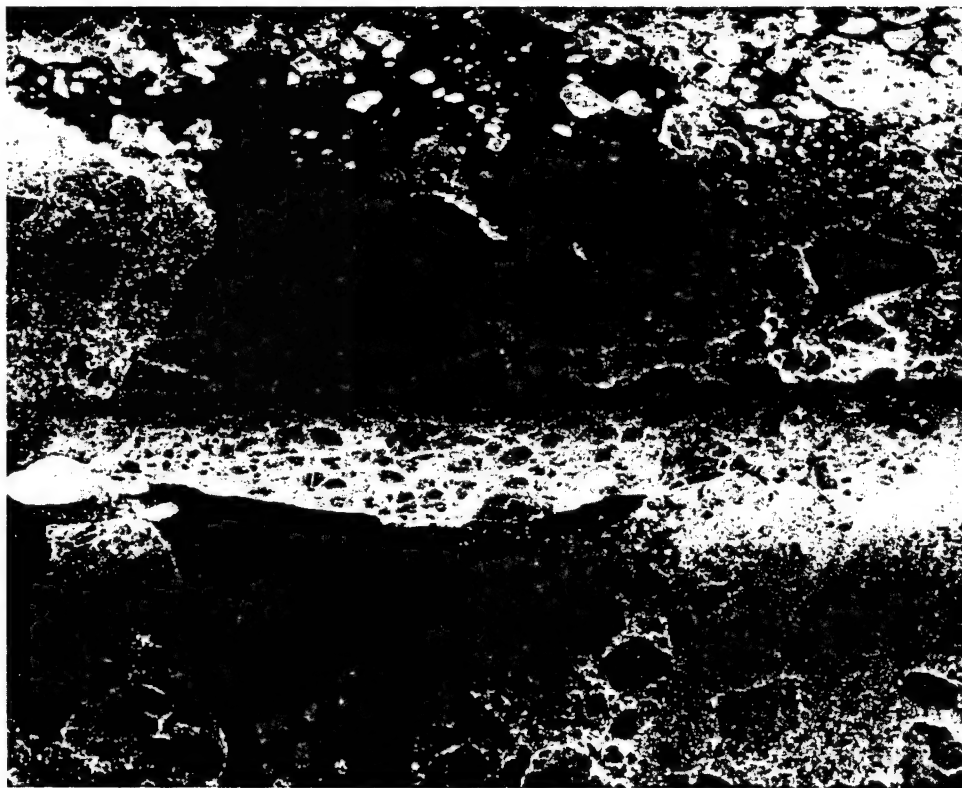
radar, and from actual ice motion during the time between the two aircraft overflights. Comparison with the aerial photography (Figure 5c) shows that the 1.2 GHz image most closely reflects the floe structure seen in the photograph, the areas of young ice or advanced melt areas appear brighter than the surrounding areas, which with a thick and moist snow cover produce a weaker backscatter. Some of these areas also produced strong returns in the 9.4 GHz data, but, in general, at this frequency the floe interior was more uniform in appearance than at 1.2 GHz due to the absorptivity of the moist snow cover. This image illustrates both the lower sensitivity of the 9.4 GHz data to variations in surface conditions as observed during early to midsummer throughout the MIZ, and the large intensity variability of floes in the ice field at this time.

PR and GR values calculated from the AMMR measured radiances on June 30 for the three floes shown in Figure 5 are plotted in Figure 7. The clusters of measurements corresponding to these floes are labeled "A," "B," and "C." The PR and GR values corresponding to the multichannel SMMR algorithm constants for open water (OW), first-year (FY), and multiyear (MY) sea ice are also plotted for reference and are indicated by open squares.

The cluster of points labeled A have PR and GR values typical of consolidated midwinter MY ice. The two observations of floe B have microwave signatures close to first-year ice and correspond to a concentration of about 90%. Factors which may have contributed to the less than 100% concentration include wet snow cover, ponding, and contamination from adjacent open water areas by the low-resolution field of view of the aircraft radiometer. The degree to which we can attribute the relative position of the B cluster along the FY-MY line to actual ice type or surface wetness is uncertain, but the key point is that the wetness that is observed has not affected the computation of the concentration by more than 10%. The cluster of points labeled "C" corresponds to a calculated concentration of between 60% and 65%, which is considerably less than 100%. The low calculated concentration is attributed to the wet ice surfaces, the numerous open water melt ponds, and to areas of snow-ice-water mixtures.

Image statistics derived from the 9.4 GHz SAR image data for Figure 6 are shown in Figure 8. Here mean backscatter amplitude is plotted versus standard deviation for 60×60 m subimages of floe C and adjacent ice and water areas. This plot demonstrates the two main sources of error in the single channel SAR ice concentration algorithm. First, the ice exhibits a much greater signature variability than the water as seen from the greater scatter in the mean values in Figure 8. For these data the standard deviation of the ice means is approximately one third of the difference between the mean ice intensity (I_I) and the mean water intensity (I_W) used as tie points in the algorithm (section 2.2). By assuming that the distribution of ice signatures is Gaussian about the mean value, it can be shown that the error in the calculated concentration is directly proportional to the ratio of the standard deviation of the ice signatures to the difference between ice and water mean intensities. Using the values from Figure 8, this predicts underestimates of about 2% for 10% concentration and almost 20% for 100% concentration. This effect is seen in Figure 9a where estimates over floe C fall between 75% and 85%.

The second source of error, also illustrated in Figure 8, is



(A)



(B)

Fig. 6. SAR imagery of floe C obtained on 30 June for (a) 1.2 GHz (23 cm) and (b) 9.4 GHz (3.2 cm).

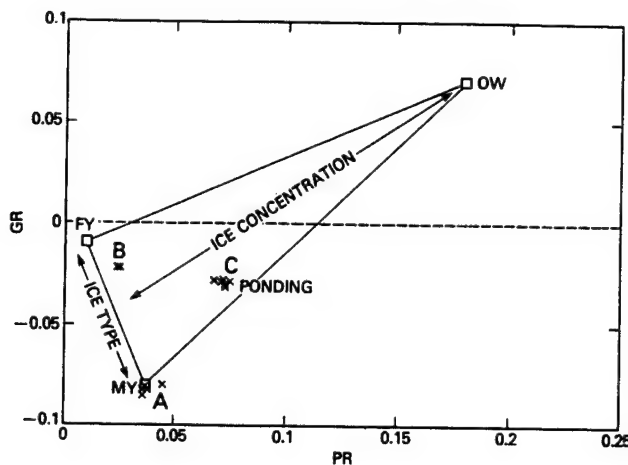


Fig. 7. GR versus PR plot for 30 June, 1984, showing clusters of measurements corresponding to floes A, B, and C shown in Figure 5.

that the standard deviation for the water signatures is much smaller than for the ice. This is due to the speckle noise inherent in the SAR imaging process which introduces a variance equal to the square of the mean divided by N , where N is the number of "looks" [Burns and Lyzenga, 1984]. In addition, the standard deviation of pixel values within ice subimages, induced mainly by speckle, is greater than that of the mean backscatter values for all the subimages. Because this algorithm calculates concentration on a pixel-by-pixel basis, it effectively resolves the speckle noise which thereby contributes directly to the large uncertainty in the concentration estimates (Figure 2).

There are two main implications of this analysis of the errors in the SAR algorithm: (1) pixel-by-pixel evaluation of concentration is not suitable for these high-resolution data and (2) specification of an ice tie point is not appropriate given the large signature variability. The linear interpolation algorithm, applied on a pixel-by-pixel basis, cannot therefore adequately account for this variability, as seen from the results. Simple thresholding on a pixel-by-pixel basis, al-

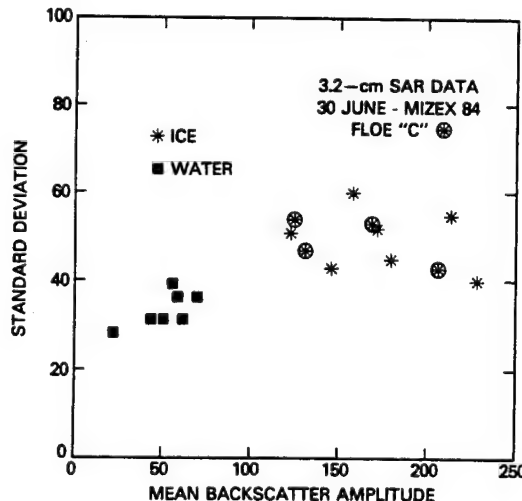
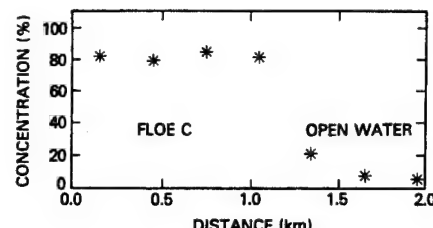
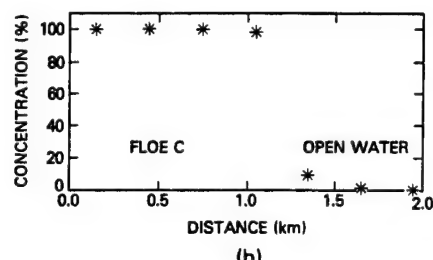


Fig. 8. SAR X-band (3.2 cm) image statistics for floe C area based on 60×60 m sample area.



(a)



(b)

Fig. 9. Mean concentration estimates for 900×300 m areas across floe C and open water calculated using two SAR techniques: (a) linear interpolation and (b) neighborhood classification.

though more appropriate to the high-resolution case, also results in misclassification of ice as water again because of the large ice signature variability aggravated by speckle noise.

A better method that would avoid resolving the variability and still take advantage of the relatively high SAR resolution would be to evaluate concentration on a neighborhood basis using an intensity decision rule based on the water mean intensity value alone. Such a scheme has been used to calculate ice concentration over a portion of the floe C area. Using a 10×10 pixel (30×30 m) neighborhood and an intensity threshold equal to the water mean plus one standard deviation, each neighborhood is classified either as ice or as water on the basis of the majority of pixels having intensity values above or below the threshold, respectively. Once ice and water are detected in this way, concentration estimates at any spatial scale greater than the size of the neighborhood can be obtained. The results for the floe C area are shown in Figure 9b and indicate the significant improvement over the linear interpolation method. Although this algorithm needs to be tested on more data sets with a range of concentration and seasonal conditions, it clearly has potential for providing relatively accurate SAR estimates over consolidated ice areas under melt conditions where AMMR estimates are poorest.

5. POTENTIAL SOLUTION

A possible solution to the problem of reduced passive microwave concentrations due to surface melt effects may be obtained through the use of SAR imagery to estimate floe areas that are comprised of moist snow and areas of snow-ice-water mixtures. In this section our working hypothesis will be that the interior floe surface conditions may be acquired using 9.4 GHz SAR. If this hypothesis is valid, it may be possible to obtain, at least in a statistical sense, a measure of the ice surface area in a given region which is

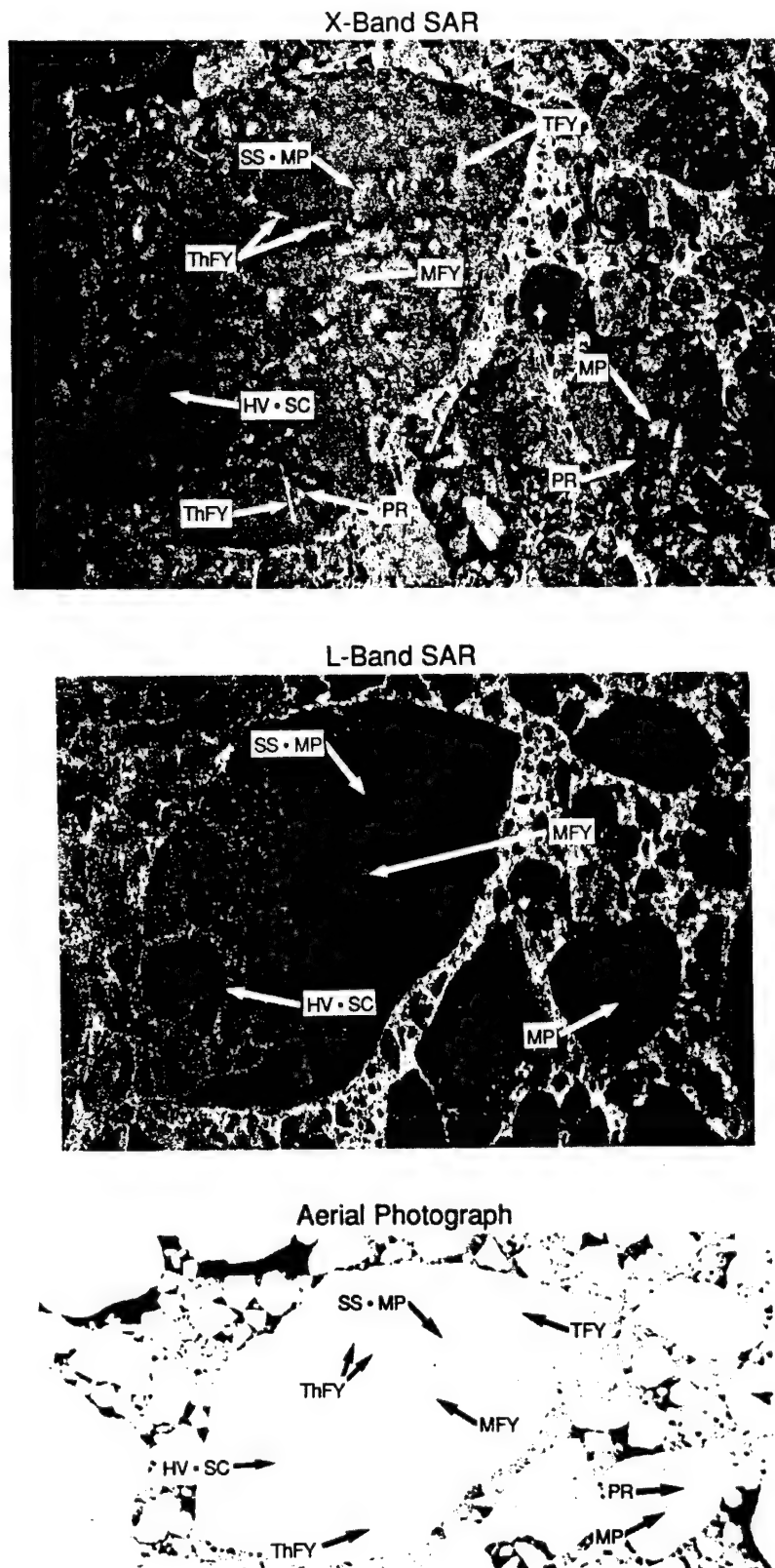


Fig. 10. Annotated ice floe imagery obtained on 29 June, 1984, with the ERIM X-band (9.4 GHz) and L-band (1.2 GHz) SAR and the CCRS aerial camera on the CV-580. Surface features include snow-covered ice (SCI); heavy-snow covered ice (HV.SC); thick (TFY), medium (MFY), and thin (ThFY) first-year ice; pressure ridges (PR); subsurface melt ponds (SS.MP); and melt ponds (MP).

ponded or sufficiently wetted to adversely affect the passive microwave ice concentrations.

To test this hypothesis, we examine a flow which was surveyed at the surface and imaged with the CV-580 SAR on June 29, 1984. Unfortunately, the poor image contrast and low signal-to-noise ratio of the floe C SAR image (Figure 6), prevented its use for testing this hypothesis. The 9.4 GHz (X-band) and 1.2 GHz (L-band) SAR images and an aerial photograph of the June 29 floe are shown in Figure 10 together with annotations of surface features. Areas identified include thick (TFY), medium (MFY), and thin (ThFY) first-year ice areas, heavy-snow covered ice (HV.SC), pressure ridges (PR), subsurface melt ponds (SS.MP) and melt ponds (MP). The snow-ice-water mixtures cover a considerable portion of the surface of this floe and also produce emission more similar to water than to ice. The procedure for testing this hypothesis is as follows. The surface areas of the floe were divided into two categories: mixed regions of snow-ice-water and areas of moist snow. SAR backscatter intensity thresholds were defined to separate the returns from these two types of areas. Their means are separated by 4 dB. With this technique it was determined that 70% of the floe area was snow-covered ice (SCI) and 30% was melt ponds (SS.MP and MP).

These results suggest that SAR can be used to estimate the fraction of developing meltponds which also cause the passive microwave sensor to measure a microwave signature more like water than like ice. An approach that may be developed would use the high-resolution capability of SAR first, to identify a statistically significant number of floes in a given region; second, to determine the state of melt pool development (i.e., to determine the period when the passive microwave sensor is sensing a water signature for the meltponds); and finally, to determine the areal extent of melt ponds on the floes for that region. For example, if the results of the analysis for the floe imaged on June 29 were applicable to floe C, we could increment by 30% the ice concentration as determined by the passive microwave measurements (see Figure 7). This correction would bring the floe C concentration up to 90–95%, similar to the value obtained for floe B. Since this approach is believed to be independent of regional characteristics, developing a grid system across the Arctic Basin for which SAR melt-ponding statistics are obtained, areal ponding estimates for each grid may be used to adjust the synoptic passive microwave estimates of ice concentration.

6. SUMMARY

This paper describes the effects of summer melt on both active and passive microwave signatures of sea ice and on the calculation of sea ice concentrations. The progression of surface melt from late spring to midsummer in the central Arctic is observed to follow that in the MIZ and as such may contribute significantly to the uncertainty in the calculated sea ice concentrations from passive microwave satellite observations. We have demonstrated the advantage of utilizing both polarization and spectral gradient information from multichannel microwave sensors for calculating sea ice concentrations under conditions of surface melt. We have found that by using ratios of radiances, early changes in the free water content of the snow cover can be accommodated by the multichannel algorithm to the extent that variations in

the free water content alter the spectral gradient ratio and thus appear as variations in the relative proportion of "first-year" and "multiyear" ice types. Under conditions of substantial surface ponding the polarization information will change significantly and the algorithm will underestimate the ice concentration.

With respect to the active sensors, we have shown that the large ice signature variability in the SAR data is responsible for the underestimates produced with the single-channel linear algorithm, and that the large estimate variances result from the algorithm being applied on a pixel-by-pixel basis. To avoid resolving the signature variability, a neighborhood segmentation algorithm was suggested and used on a ponded floe to demonstrate the potential for improved SAR concentration estimates during surface melt conditions. We have further demonstrated using high-resolution aircraft data that high-resolution SAR imagery can be used to obtain an areal measure of the degree to which individual floes have wetted surfaces and open melt ponds. This suggests that a combined active-passive microwave system of sensors may provide a means for improving the accuracy of the ice concentration determinations during the summer melt period through the development of a "microwave surface melt climatology" for different regions.

Acknowledgments. The authors thank James Maslanik for his very helpful review of this paper and two anonymous reviewers for their comments and suggestions. We also thank Per Gloersen, NASA aircraft scientist during MIZEX; Robert Shuchman of ERIM; and the crews of the NASA CV-990 and CCRS CV-580 aircraft for their efforts in the collection of the microwave aircraft data and surface information. This work was supported by the National Aeronautics and Space Administration Oceanic Processes Branch and by the Office of Naval Research (ONR). The ONR support for two of us (B.A.B. and R.G.O.) under contract N00014-81-C-0295 was monitored by Charles Luther.

REFERENCES

- Askne, J., and L. Ulander, Azimuth dependence in SAR-imaging of open water leads in ice infested areas, *Proceedings of IGARSS'89*, 12th Canadian Symposium on Remote Sensing, IEEE 89CH2768-0, Inst. of Elec. and Electron. Eng., New York, 1989.
- Barry, R. G., and J. Maslanik, Arctic sea ice characteristics and associated atmosphere-ice interactions in summer inferred from SMMR data and drifting buoys: 1979–1984, *GeoJournal*, 18(1), 35–44, 1989.
- Burns, B. A., and D. R. Lyzenga, Textural analysis as a SAR classification tool, *Electromagnetics*, 4, 309–322, 1984.
- Burns, B. A., R. A. Shuchman, P. L. Jackson, J. D. Lyden, and C. E. Livingstone, SAR measurement of sea ice properties during MIZEX 1983, *Eur. Space Agency Spec. Publ., ESA SP 215*, 347–351, 1984.
- Burns, B. A., R. R. Jentz, C. G. Caruthers, J. D. Lyden, and P. L. Jackson, Computer assisted techniques for geophysical analysis of SAR sea ice imagery, in *Proceedings of the Nineteenth International Symposium on Remote Sensing of the Environment*, pp. 947–959, Environmental Research Institute of Michigan, Ann Arbor, 1985.
- Burns, B. A., D. J. Cavalieri, M. R. Keller, W. J. Campbell, T. C. Grenfell, G. A. Maykut, and P. Gloersen, Multisensor comparison of ice concentration estimates in the marginal ice zone, *J. Geophys. Res.*, 92, 6843–6856, 1987.
- Campbell, W. J., R. O. Ramseier, H. J. Zwally, and P. Gloersen, Arctic sea-ice variations from time-lapse passive microwave imagery, *Boundary Layer Meteorol.*, 13, 99–106, 1980.
- Campbell, W. J., P. Gloersen, and H. J. Zwally, Aspects of Arctic sea ice observable by sequential passive microwave observations from the Nimbus 5 satellite, in *Arctic Technology and Policy*,

Proceedings of the Second Annual MIT Sea Grant College Program Lecture and Seminar, edited by I. Dyer and C. Chrysostomidis, pp. 197–222, Hemisphere, New York, 1984.

Campbell, W. J., P. Gloersen, E. G. Josberger, O. M. Johannessen, P. S. Guest, N. Mognard, R. Shuchman, B. A. Burns, N. Lannelongue, and K. L. Davidson, Variations of mesoscale and large-scale sea ice morphology in the 1984 Marginal Ice Zone Experiment as observed by microwave remote sensing, *J. Geophys. Res.*, 92, 6805–6824, 1987.

Carsey, F. D., Summer Arctic sea ice character from satellite microwave data, *J. Geophys. Res.*, 90, 5015–5034, 1985.

Cavalieri, D. J., P. Gloersen, and W. J. Campbell, Determination of sea ice parameters with the Nimbus 7 SMMR, *J. Geophys. Res.*, 89, 5355–5369, 1984.

Colony, R., and E. A. Munoz, Arctic Ocean Buoy Program, data report, Polar Sci. Center, Appl. Phys. Lab., Univ. of Wash., Seattle, 1986.

Comiso, J. C., Sea ice effective microwave emissivities from satellite passive microwave and infrared observations, *J. Geophys. Res.*, 88, 7686–7704, 1983.

Crane, R. G., R. G. Barry, and H. J. Zwally, Analysis of atmosphere-sea ice interactions in the Arctic Basin using ESMR microwave data, *Int. J. Remote Sens.*, 3, 259–276, 1982.

Gloersen, P., and W. J. Campbell, Satellite and aircraft passive microwave observations during the marginal ice zone experiment in 1984, *J. Geophys. Res.*, 93, 6837–6846, 1988.

Gloersen, P., and D. J. Cavalieri, Reduction of weather effects in the calculation of sea ice concentration from microwave radiances, *J. Geophys. Res.*, 91, 3913–3919, 1986.

Gloersen, P., Zwally, H. J., A. T. C. Chang, D. K. Hall, W. J. Campbell, and R. O. Ramseier, Time-dependence of sea ice concentration and multiyear ice fraction in the Arctic Basin, *Boundary Layer Meteorol.*, 13, 339–360, 1978.

Gloersen, P., E. Mollo-Christensen, T. Wilheit, T. Dod, R. Kutz, and W. J. Campbell, MIZEX '84 NASA CV-990 flight report, *NASA Tech. Memo.*, 86216, 149 pp., May 1985.

Gray, A. L., R. K. Hawkins, C. E. Livingstone, L. Drapier-Arsenault, and W. M. Johnstone, Simultaneous scatterometer and radiometer measurements of sea ice microwave signatures, *IEEE J. Oceanic Eng.*, OE-7(1), 20–33, 1982.

Grenfell, T. C., and A. W. Lohanick, Temporal variations of the microwave signatures of sea ice during the late spring and early summer near Mould Bay NWT, *J. Geophys. Res.*, 90, 5063–5074, 1985.

Holt, B., and S. A. Digby, Processes and imagery of first-year fast sea ice during the melt season, *J. Geophys. Res.*, 90, 5045–5062, 1985.

Livingstone, C. E., K. P. Singh, L. Drapier-Arsenault, and A. L. Gray, Seasonal and regional variations of active/passive microwave signatures of sea ice, *IEEE Trans. Geosci. Remote Sens.*, GE-25, 159–173, 1987a.

Livingstone, C. E., R. G. Onstott, L. Drapier-Arsenault, A. L. Gray, and K. P. Singh, Microwave sea-ice signatures near the onset of melt, *IEEE Trans. Geosci. Remote Sens.*, GE-25, 174–187, 1987b.

Martin, P. C., and M. Clarke, A test of barometric pressure and temperature measurements from ADRAMS buoys, *AIDJEX Bull.* 40, pp. 61–82, Univ. of Wash., Seattle, 1978.

Martin, S., B. Holt, D. J. Cavalieri, and V. Squire, Shuttle imaging radar B (SIR-B) Weddell Sea ice observations: A comparison of SIR-B and scanning multichannel radiometer ice concentrations, *J. Geophys. Res.*, 92, 7173–7179, 1987.

Maslanik, J., and R. G. Barry, Short-term interactions between atmospheric synoptic conditions and sea-ice behavior in the Arctic, *Ann. Glaciol.*, 12, 113–117, 1989.

Onstott, R. G., and R. K. Moore, Active microwave measurements of sea ice in the marginal ice zone under summer conditions, *Eur. Space Agency Spec. Publ.*, ESA SP 215, 359–363, 1984.

Onstott, R. G., T. C. Grenfell, C. Matzler, C. A. Luther, and E. A. Svendsen, Evolution of microwave sea ice signatures during early summer and midsummer in the marginal ice zone, *J. Geophys. Res.*, 92, 6825–6835, 1987.

Steffen, K., and J. A. Maslanik, Comparison of Nimbus 7 scanning multichannel radiometer radiance and derived sea ice concentrations with Landsat imagery for the North Water area of Baffin Bay, *J. Geophys. Res.*, 93, 10,769–10,781, 1988.

Tucker, W. B. III, A. J. Gow, and W. F. Weeks, Physical properties of summer sea ice in Fram Strait, *J. Geophys. Res.*, 92, 6787–6803, 1987.

Ulaby, F. T., R. K. Moore, A. K. Fung, *Microwave Remote Sensing Active and Passive*, vol. 2, Addison-Wesley, Reading, Mass., 1982.

B. A. Burns and R. G. Onstott, Radar Science Laboratory, Environmental Research Institute of Michigan, Ann Arbor, MI 48107.

D. J. Cavalieri, Laboratory for Oceans, NASA Goddard Space Flight Center, Greenbelt, MD 20771.

(Received May 11, 1989;
accepted July 14, 1989.)

Microwave and Physical Properties of Sea Ice in the Winter Marginal Ice Zone

W. B. TUCKER III,¹ T. C. GRENFELL,² R. G. ONSTOTT,³ D. K. PEROVICH,¹ A. J. GOW,¹ R. A. SHUCHMAN,³ AND L. L. SUTHERLAND³

Surface-based active and passive microwave measurements were made in conjunction with ice property measurements for several distinct ice types in the Fram Strait during March and April 1987. Synthetic aperture radar imagery downlinked from an aircraft was used to select study sites. The surface-based radar scattering cross section and emissivity spectra generally support previously inferred qualitative relationships between ice types, exhibiting expected separation between young, first-year and multiyear ice. Gradient ratios, calculated for both active and passive data, appear to allow clear separation of ice types when used jointly. Surface flooding of multiyear floes, resulting from excessive loading and perhaps wave action, causes both active and passive signatures to resemble those of first-year ice. This effect could possibly cause estimates of ice type percentages in the marginal ice zone to be in error when derived from aircraft- or satellite-borne sensors.

INTRODUCTION

The final field program of the Marginal Ice Zone Experiment (MIZEX) took place in March and April 1987. As with previous MIZEX field investigations, this experiment was carried out primarily in the Fram Strait. This particular program consisted of the winter phase of the experiment whose primary objective was to examine ice-ocean-atmosphere MIZ processes during the period of maximum ice extent. A detailed description of MIZEX objectives is presented by *Wadhams et al.* [1981]. Many of the results from the summer MIZEX programs are described in the special Marginal Ice Zone Research issue of the *Journal of Geophysical Research* (volume 92, number C7, 1987).

The objectives of the investigation described here were to determine, under winter conditions in the MIZ, active and passive microwave signatures for a variety of characteristic ice types and to relate these signatures to the physical properties of the ice. These joint measurements were conducted from the ice-strengthened Norwegian vessel *Polar Circle*. At selected sites, a variety of measurements were made, the most basic of which included documentation of the ice physical properties. Snow thickness surveys and pits excavated in the snow were used to furnish snow depths and physical properties. Radar backscatter and passive microwave measurements were made at a variety of frequencies, polarizations, and incidence angles. Both active and passive microwave systems were also routinely operated as the ship moved through the ice, thereby obtaining a large set of data encompassing a variety of ice conditions in the MIZ. Occasionally, the passive microwave system was mounted on a sled which was pulled across the floe in order to assess the small-scale within-floe variations.

¹U.S. Army Cold Regions Research and Engineering Laboratory, Hanover, New Hampshire.

²Department of Atmospheric Sciences, University of Washington, Seattle.

³Environmental Research Institute of Michigan, Ann Arbor.

Copyright 1991 by the American Geophysical Union.

Paper number 90JC02269.
0148-0227/91/90JC-02269\$05.00

INSTRUMENTS AND MEASUREMENTS

Synthetic Aperture Radar

Synthetic aperture radar (SAR) data collection missions were flown on a daily basis throughout MIZEX '87 using the Intera STAR systems. The Intera STAR 1 and STAR 2 are *X* band (0.032-m wavelength) *HH* polarization radars with resolutions ranging from 4 to 24 m. The high/low resolution swath width is 23/43 km for STAR 1 and 17/63 km for STAR 2. Each mission covered approximately a 200 by 200 km area surrounding the *Polar Circle*. During overflights, SAR data were transmitted via radio link to the *Polar Circle*, where they were used to select sites for the comprehensive microwave and physical properties investigations.

Ice Physical Properties

The physical properties description consisted of a detailed characterization of the snow cover and the underlying sea ice. Snow characterization entailed a snow thickness survey and an examination of the snowpack stratigraphy. The surveys typically consisted of snow depths measured on a grid of 25 or more locations spaced at 3 to 5 m. Snow stratigraphy was investigated by excavating a snow pit and measuring vertical profiles of snow temperature, density, ionic conductivity, and crystal size and type. In addition, solid snow specimens were prepared for later, more detailed structural studies, by filling the pore spaces of a sample with dimethyl phthalate and freezing the sample.

Our description of each site included floe size and qualitative surface topography information. At least one 80-mm-diameter ice core was taken through the entire thickness of each floe to enable analysis of the ice structural and physical properties. These cores were used to determine vertical profiles of ice temperature, salinity, density, and crystalline structure for successive 10-cm increments of core. Brine and air volumes were calculated using the measured parameters and the relationships formulated by *Cox and Weeks* [1983].

Passive Microwave

Passive microwave measurements were obtained at 10, 18, 37, and 90 GHz (*X*, *K*, *K_a*, and *W* bands) at a nadir angle of 50°, alternating between vertical and horizontal polariza-

tions. While the ship was moving, the four radiometers were mounted approximately 15 m above the ice, and continuous traverses of brightness temperature were recorded. At the ice stations when the ship was stationary against the selected floe, the radiometers were mounted on a sled, and traverses across the ice floe were carried out with the antenna pointed at 50° from nadir.

The effective emissivity at frequency ν for polarization p is determined from the formula [Grenfell and Comiso, 1986]

$$e_{\nu}(p, \theta) = (T_B - T_{\text{sky}})/(T_s - T_{\text{sky}}) \quad (1)$$

where T_B is the brightness temperature of the surface at a nadir angle θ , T_{sky} is the brightness temperature of the sky at zenith angle θ , and T_s is the physical temperature at the snow-ice interface. This formula is appropriate for the determination of emissivity for a surface based measuring system in that it includes the entire atmospheric contribution to the sky radiation.

Present models calculate the microwave emissivity from the physical structure of the medium in terms of the relationship

$$e_{\nu}(p, \theta) = 1 - R_{\nu}(p, \theta) - S_{\nu}(p, \theta) \quad (2)$$

where R is the effective surface reflectance and S is an angular integration of the surface and volume scattering. Each of these quantities is a function of frequency, polarization, and angle of observation. A distinction is made between reflectance and surface scattering in that the reflectance consists of the relative intensity of the coherent reflected field where surface scattering refers to the incoherently scattered field. R is determined largely by the bulk dielectric properties of the medium, while S (surface and volume scattering) is dependent on the distribution of inhomogeneities in the medium as well as the bulk dielectric constant.

Radar Backscatter

The backscatter measurements were obtained using two radar scatterometer systems operating from the rail of the upper decks of the *Polar Circle*, about 15 m above the ice. Backscatter data were acquired at 1.5, 5.25, 9.38, 18, and 35 GHz (L , C , X , K_u , and K_a bands), although logistical considerations sometimes made it necessary to restrict the frequencies to 18 and 35 GHz only. In this paper we present results only from VV polarization, as it was the only polarization for which a complete set of measurements was obtained. Where other polarizations were available, corresponding values for HH polarization were usually found to be about 2–4 dB lower, while cross polarization was typically 20–30 dB lower. Data were collected at fixed angles as the ship transited the ice, while angular response measurements were made at selected stationary sites.

We use the conventional definition of radar scattering coefficient (σ_{vv}^0) as the average scattering cross section per unit area. The subscripts denote the received and transmitted polarizations respectively, and σ_{vv}^0 is given by the following expression [Ulaby *et al.*, 1982, equation 11.2]

$$\sigma_{vv}^0 = \pi R^2 P_{vv}/AP_{vv} \quad (3)$$

where R is the range to the target, P_{vv} is the total power scattered at V polarization by an equivalent isotropic scat-

terer in the direction of the receiver, P_{vv} is the transmitted power density at V polarization, and A is the illuminated area. Since only VV polarization results are presented here, we adopt the convention that σ^0 implies σ_{vv}^0 .

Except for near-nadir viewing, where the backscatter is influenced predominantly by total scattering and surface reflection effects, the radar return is dominated by the combination of surface and volume scattering. Spatial fluctuations in the dielectric properties of the medium determine the magnitude of the scattering.

RESULTS

Combined measurements of ice and microwave properties were made at about 25 floes. Five specific sites representing the distinctive ice types observed during the experiment were selected for this investigation (Figure 1). The selected ice types consisted of pancake (P), multiyear (M), flooded multiyear (MF), first-year (F) and very young (50–100 mm thick) ice or nilas (N). Our observations indicated that the various ice types are fairly well intermixed throughout the Fram Strait MIZ. The major exception is pancake ice, which was generally found close to the ice edge, where the wave action needed to form this kind of ice is prevalent.

Figure 2 is a SAR mosaic of an area of the ice in Fram Strait, approximately 400 × 180 km. This particular image was collected on April 4, 1987, roughly the midpoint of the experiment. The area encompassed by the image is outlined in Figure 1. Typical ice types are identified on the SAR image. In general, bright tones on the image correspond to multiyear ice, while the darker tones are various stages of young ice. The blackest signatures are indicative of open water. We place a high degree of certainty on the identification of the designated ice types because they were identified directly by helicopter reconnaissance. This entailed carrying the downlinked SAR image on helicopter flights shortly after the actual SAR flight and locating recognizable features on the image (i.e., leads, large floes, etc). Ice in the vicinity of recognizable features was also identified as to type, concentration and mixture. This information has been used for the development of SAR interpretation algorithms [Shuchman *et al.*, 1989; Wackerman *et al.*, 1988].

No attempts were made to extract SAR backscatter values for the detailed study sites because sites were often located on floes that could not be distinctly identified on the image. Also, the SAR was not calibrated in an absolute sense, which leads to difficulty in attempting to compare backscatter values for particular ice types between different SAR flights.

Nilas, April 8, 1987

Figure 3 contains composite results of the nilas investigation site. The photograph (Figure 3a) shows the vast expanse (~5–10 km) of 20- to 60-mm-thick nilas ice that was examined. Small ice sheet overthrusts ranging from 15 to 20 mm high occurred every 0.2 to 0.5 m. At this particular site, both thermal growth and the subsequent rafting were responsible for increasing the ice thickness. Indeed, that case is suggested by the vertical thin section photograph of 30-mm-thick nilas shown (Figure 3b), which shows a mixed structure of granular and small columnar crystals, generally a type of structure that precedes purely congelation ice

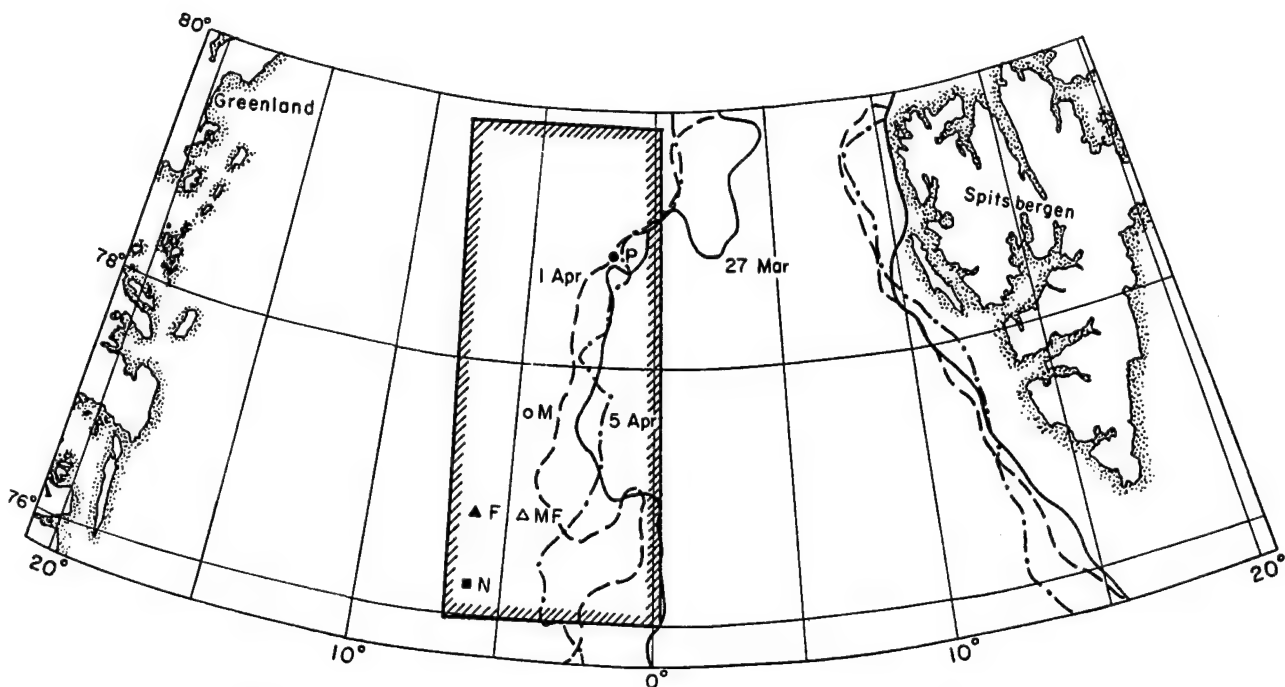


Fig. 1. Sampling sites in the Fram Strait with approximate location of the ice edge on March 27, April 1 and April 5, 1987. Sites are designated by ice type for first-year (F), nilas (N), pancake (P), multiyear (M), and flooded multiyear (MF). Box indicates approximate area covered by SAR image shown in Figure 2.

growth. The structural discontinuity in the middle of the sample is attributed to rafting of one sheet upon another. The high salinities, ranging from 14.3 to 16.2‰, were a result of rapid freezing and hence brine retention within the granular ice structure. Density was also relatively high, about 0.92 Mg m^{-3} , indicating minimal entrapment of air in the ice.

The emissivity spectra for this case (Figure 3c) represent averages over a distance of several hundred meters and show a strong increase from 10 to 90 GHz at both vertical and horizontal polarizations. Also shown for reference are the spectra measured for open water. The error bars represent standard deviations, or uncertainty in the measurements. The spectra are intermediate between that of open water and that of thick first-year ice. This probably results from a combination of two effects. The real part of the dielectric constant of brine decreases with increasing frequency, giving the lowest ice-air surface reflectivity at 90 GHz. According to Table 1, where optical thicknesses have been estimated for first-year ice types, at lower frequencies the ice is not optically thick, so the underlying water significantly increases the net reflectivity at 10 and 18 GHz. The difference in slopes between *V* and *H* polarization is most likely due to the presence of small-scale surface roughness elements on a size scale which would scatter weakly at 37 GHz but significantly more at 90 GHz.

Backscatter coefficients for nilas (Figure 3d) are the smallest of all the ice types investigated in this study. The σ^0 values presented here, however, are up to 30 dB higher for K_u band over incidence angles of 30° to 50° than results of Onstott and Shuchman [1988] for undisturbed nilas. The increase shown here is probably due to the backscatter from the numerous exposed edges created by overthrusting, and possibly, the higher surface dielectric due to flooding with seawater. The scattering coefficients for nilas decreased

rapidly with increasing nadir angle from -5 dB at 20° to between -15 and -17 dB at 50° at both K_u and K_a bands.

Pancake Ice, March 29, 1987

Pancakes existed in both loosely aggregated and closely packed forms at this site (Figure 4a). The individual pancakes ranged in size from 0.3 to over 1.5 m in diameter and 50 to 130 mm in thickness. The raised edges or rims, which ranged in height from 10 to 50 mm above the relatively flat surface, resulted from collisions between individual pancakes and from the freezing of seawater and frazil which splashed onto the edges of the pancakes. As the thin section in Figure 4b indicates, the structure of this ice is very similar to that of the previously described nilas. Specifically, the texture appears to consist of closely packed platey-type crystals. This type of structure has been observed in young ice forming in a disturbed water column [Eicken and Lange, 1989]. This is certainly reasonable in this case because pancake formation itself is indicative of growth in a disturbed or wind-whipped sea. Salinity of the pancakes ranged from 9 to 12‰, somewhat less than that of the nilas. However, bulk ice density was the same as the nilas, 0.92 Mg m^{-3} .

The emissivity spectra for pancake ice (Figure 4c) are again spatial averages and represent a composite of the pancakes and the open water surrounding them. In accordance with Table 1, the ice is optically thick at all frequencies except 10 GHz, which results in a higher, flatter spectrum than for nilas. The rather high degree of polarization (defined as $[e_v(V, \theta) - e_v(H, \theta)]/[e_v(V, \theta) + e_v(H, \theta)]$) is probably due to the contribution of the open water but may also be indicative of a smooth ice surface.

Backscatter coefficients for the pancake ice are quite

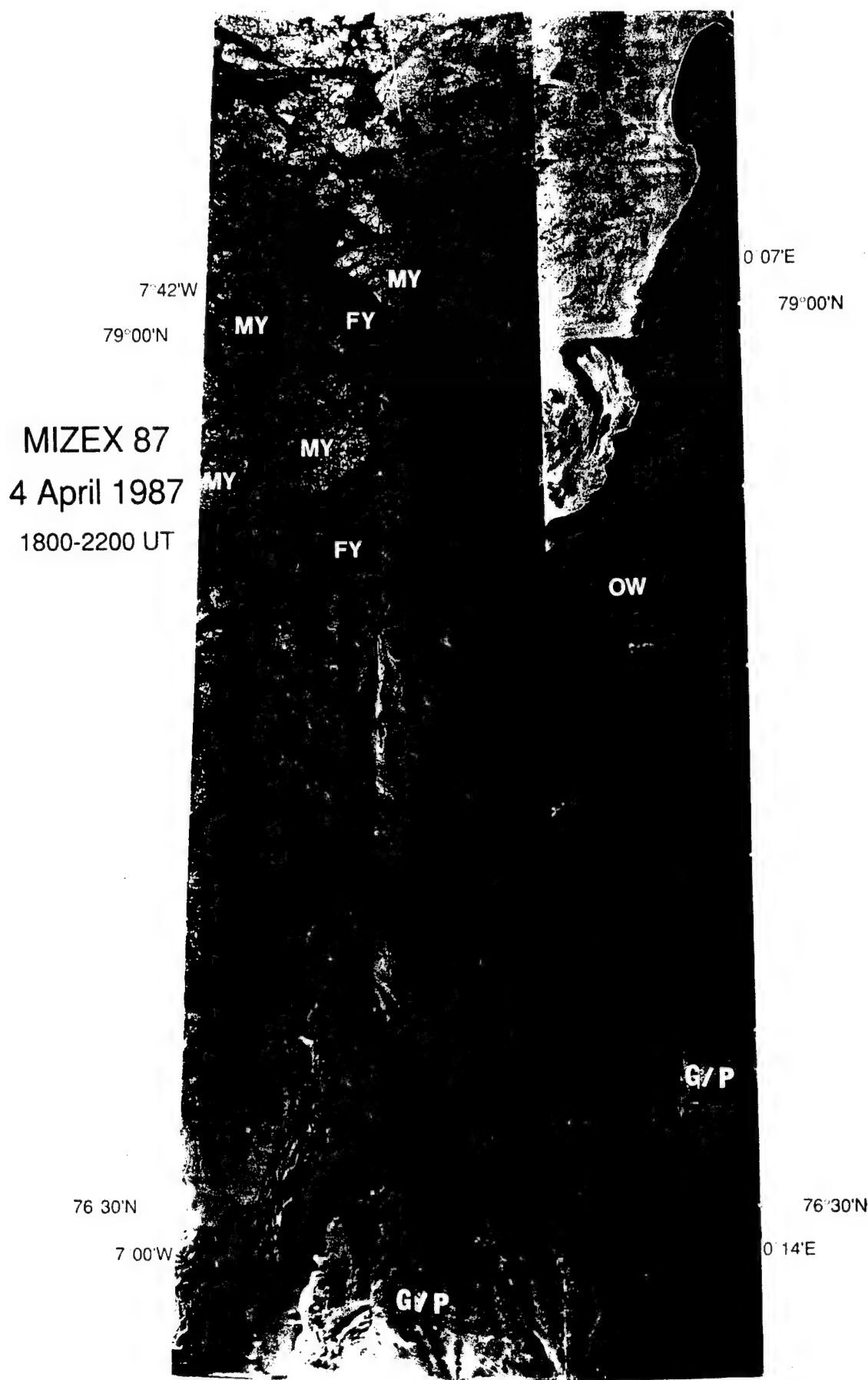


Fig. 2. SAR image mosaic of the Fram Strait marginal ice zone on April 4, 1987. Typical ice types identified by helicopter reconnaissance are multiyear (MY), first-year (FY), and grease and pancake (G/P) ice and open water (OW).

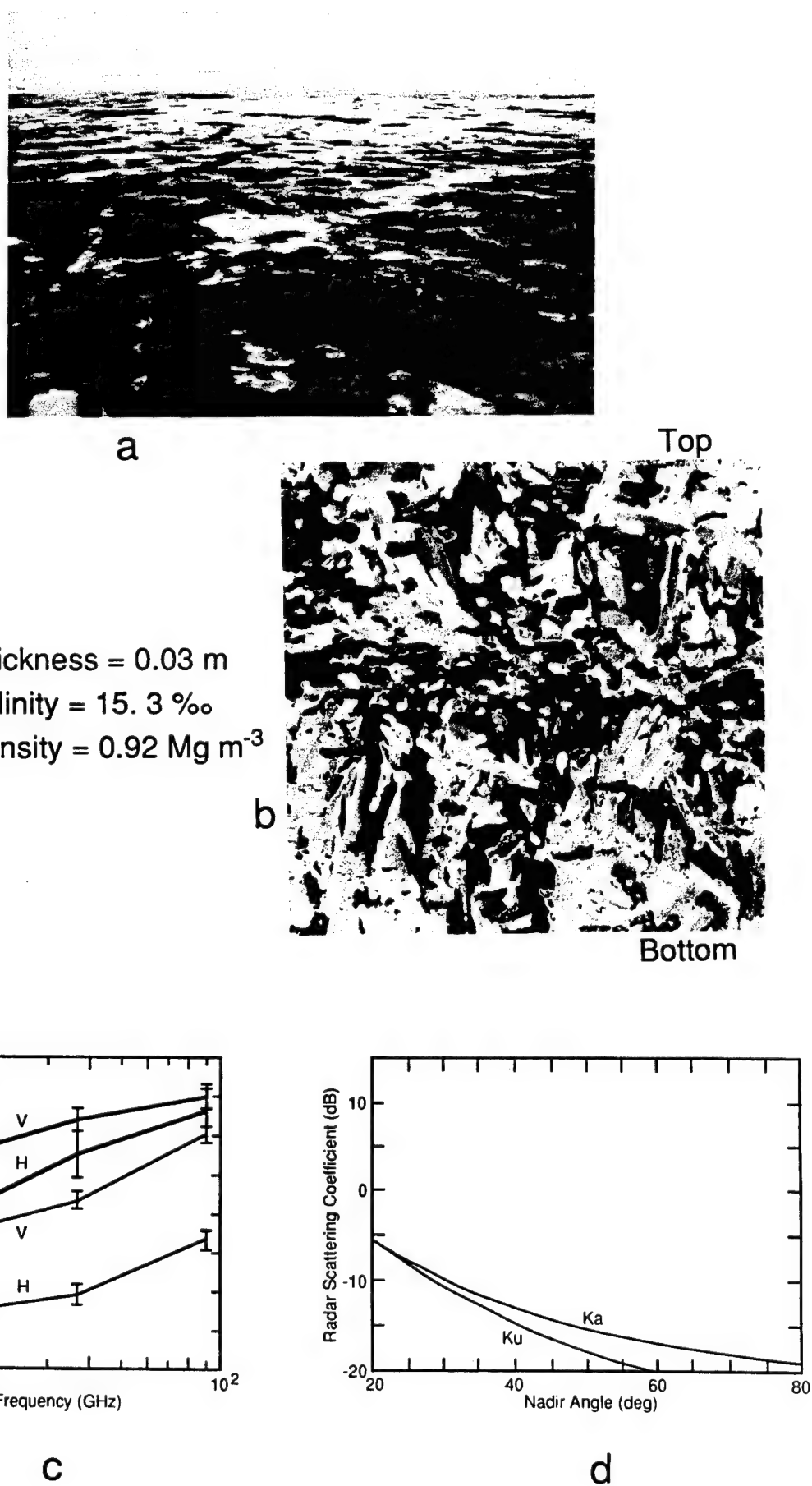


Fig. 3. Nilas ice, April 8, 1987: (a) photograph of site, (b) vertical thin section of ice, (c) passive microwave emissivity for vertical and horizontal polarizations, and (d) radar backscatter coefficient. Emissivities are also shown for open water.

TABLE 1. Optical Depths as a Function of Frequency for Thin Ice Types

	Optical Depth τ			
	10 GHz	18.7 GHz	37 GHz	90 GHz
30-mm nilas	1.2	3.4	6	12
50-mm pancakes	2	5.7	10	20
1-m first-year ice	40	114	200	400

Uncertainty in optical thicknesses is estimated to be 50%, depending on fluctuations in brine volume. Optical depths τ are estimated from the results of Grenfell [1986] and Grenfell and Comiso [1986]. Estimates for the 1-m ice assume salinities consistent with thinner ice; thus optical depths may be slightly high. Ice is referred to as being optically thick if τ exceeds 4, for which 98.2% of the incident radiation on the layer would be absorbed.

variable owing to differences in the heights of the rims surrounding the pans. Results for two cases at the pancake ice site are shown in Figure 4d. The solid lines are for the predominant pancake type ice, and the crosses are from an area of thicker and rougher pancake ice. For the case represented by the solid curves, the pan rims were rather small, and σ^0 values at K_u and K_a bands are only slightly above the values for nilas. The angular dependence was also similar, including the crossover at nadir angles of 20° to 25°. Scattering at X band, however, was from 7 to 15 dB greater than that at K_a and K_u bands. For the rougher pancakes, the σ^0 at 40° was enhanced by about 17 dB at K_a band, and the difference between K_a and K_u increased to about 8 dB.

First-Year Ice, April 6, 1987

This site was located on a 100-m-diameter floe contained within a several-kilometer expanse of thin first-year ice (Figure 5a). The ice at the coring site measured 0.36 m thick and was overlain by 100 mm of snow. The snow had a density of 0.09 Mg m^{-3} and consisted of 0.25- to 1.00-mm needle and stellar crystals. This area was free of major ridges, although many small cracks and some rafting were evident once the snow cover was removed. The ice surface consisted of raised edges 10 to 100 mm high, occurring every 5 to 10 m. The crystalline texture (Figure 5b) through the entire ice thickness consisted of fine-grained columnar ice crystals indicating that growth had occurred under relatively calm conditions. The salinity of the ice ranged from 7 to 9.8‰ with a bulk salinity of 8.6‰. Bulk density of the ice was 0.92 Mg m^{-3} . The combination of thin ice and the insulating effect of the thick snow cover resulted in a relatively warm ice surface temperature of -3.5°C .

The emissivities for this case (Figure 5c) are very close to unity, the spectra are quite flat, and the difference between vertical and horizontal polarizations is small, consistent with a variety of observations made to date from the surface, aircraft, and satellites [Grenfell, 1986; Cavalieri *et al.*, 1984a, b]. The ice was optically thick (Table 1), implying that emission was primarily from the surface. The smaller difference between $e_\nu(V, 50)$ and $e_\nu(H, 50)$ as compared with younger ice types was probably a result of influences of the snow layer and lower salinity. This may also account for the slight decrease at 90 GHz. The spectra of thick first-year ice seem to be rather insensitive to ice conditions and have been used as a benchmark point for almost all sea ice work to date.

The backscatter coefficients (Figure 5d) are indicative of first-year ice having a surface roughness of the order of a few millimeters [Kim *et al.*, 1985; Onstott *et al.*, 1979]. This small roughness was not detected by our properties measurements, however. The backscatter coefficients at K_u and K_a band are 10 and 18 dB greater, respectively, at 25° than those for pancake ice, and σ^0 decreases almost linearly with frequency. Sigma values at all frequencies decrease more slowly with increasing nadir angle than for either pancakes or nilas.

Multiyear Ice, April 3, 1987

This site was located on a 100 × 200 m floe embedded in a loosely concentrated field of similar sized floes (Figure 6a). The floe had a hummocky surface with general relief of about 0.5 m and also featured a 4-m-high ridge on one side (not shown in the photograph of Figure 6a). It appeared that the floe contained a substantial amount of deformed ice. This was verified by three thickness measurements which ranged from 3.01 m at the coring location near the center of the floe to 4.46 m on the flank of the ridge. A thorough snow survey revealed a rather thick layer with depths ranging from 0.14 to 1.20 m, about a mean of 0.40 m. The snowpack consisted of a 60-mm surface layer of 1- to 2-mm-long delicate needles with a density of 0.09 Mg m^{-3} . The surface layer was underlain by a layer varying in thickness containing 0.3- to 0.5-mm-diameter rounded grains with density of 0.31 Mg m^{-3} . The crystal structure of the underlying ice (Figure 6b) was primarily columnar, with only a 0.20-m-thick layer of granular ice at the surface and a mixed congelation and granular ice layer from 1.0 to 1.2 m below the surface. There was, however, a significant amount of inclined columnar ice in this core, indicating previous deformation or ridging. During normal undisturbed ice growth, columnar crystals are oriented vertically; thus the occurrence of inclined crystals in a vertically drilled core usually implies the presence of tilted ice blocks. The salinity of this floe was quite low, being typical or multiyear ice, with a bulk salinity of 2.9‰. Discontinuities in the salinity profile may correspond either to structural breaks or to annual transitions. It is logical for salinity discontinuities to appear in deformed (ridged) ice because normal vertical drainage patterns are likely to be interrupted by the existence of an inclined block-granular ice structure. Also typical of multiyear ice is the low-density ice constituting the upper layers. Such structure results from the desalination and thermal modification of the upper layers during summer, leading to increased porosities and, consequently, lowered densities in near surface ice.

The present measurements represent our first surface-based radiometric observations over winter multiyear ice. For this case, several spectra were obtained (Figure 6c). They show a pronounced negative spectral gradient ($\text{de}_\nu(p, \theta)/d\nu$) considered characteristic on the basis of previous aircraft and satellite observations [Cavalieri *et al.*, 1984b; Troy *et al.*, 1981]. This might be due to strong volume scattering in the low-loss, desalinated, near-surface layers. The light solid and dashed spectra were obtained from different locations on this floe. The increase in emissivity between 37 and 90 GHz is unexpected and results from the very thick snow layer which is not transparent at 90 GHz. Variations at 90 GHz over snow covered ice will, in general,

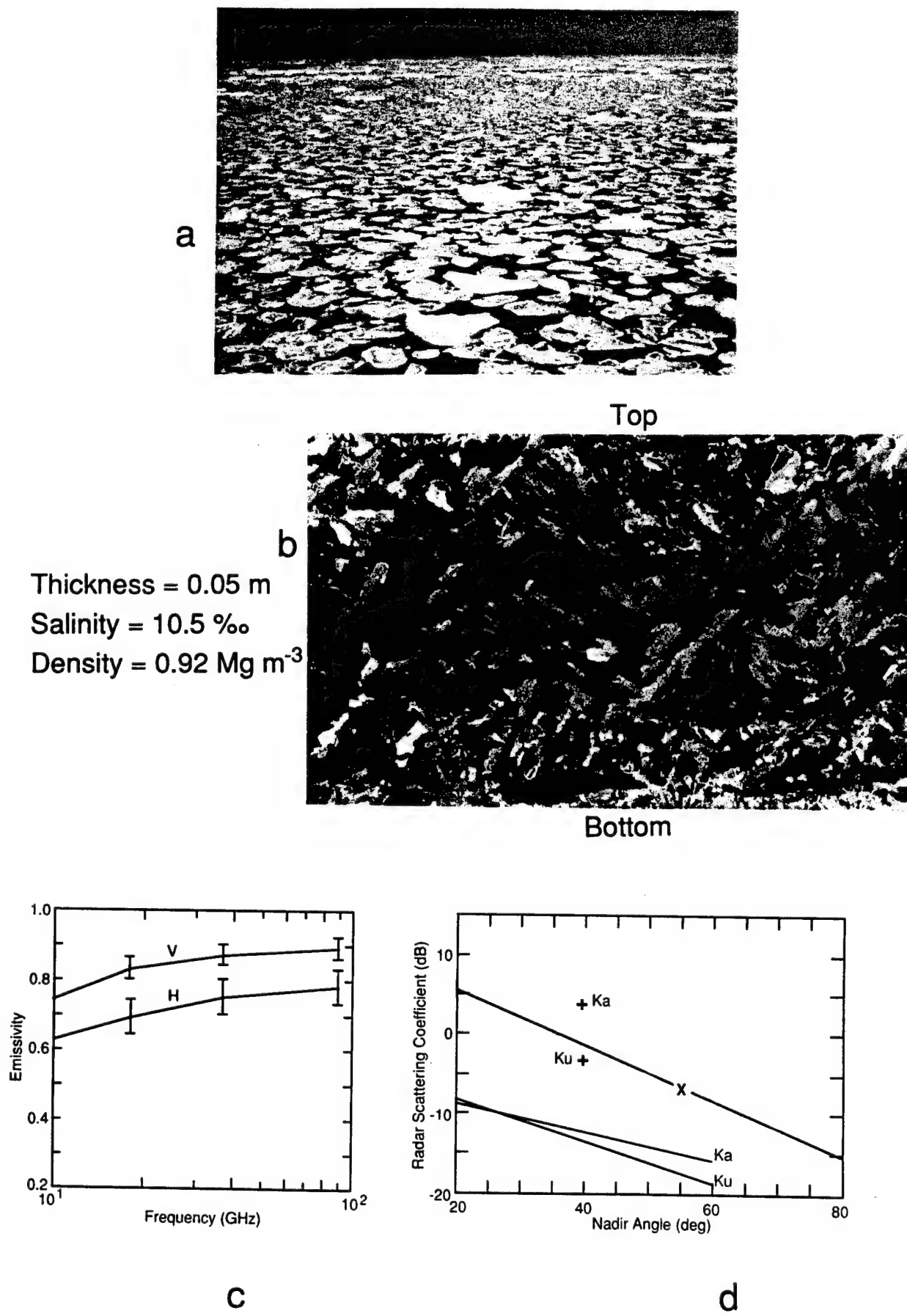
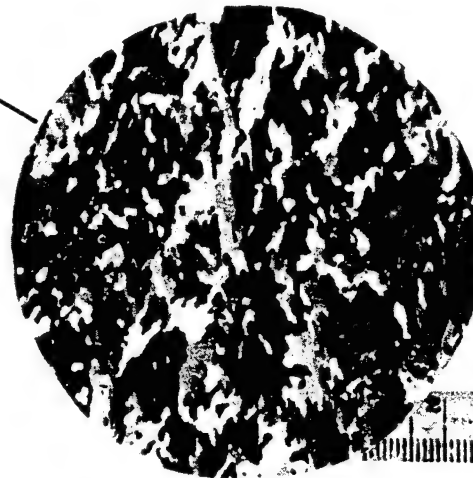
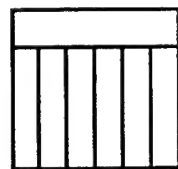
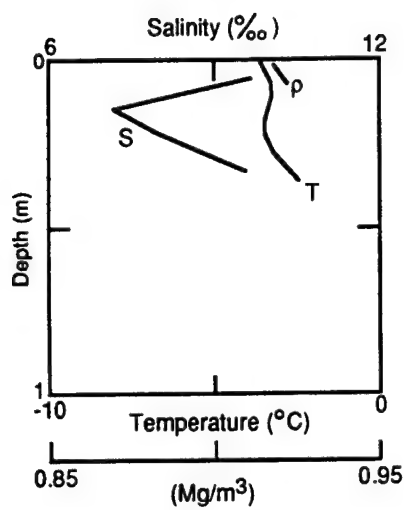


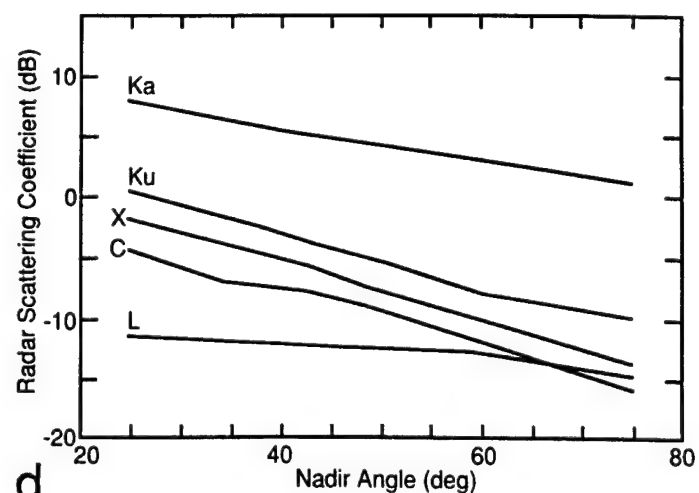
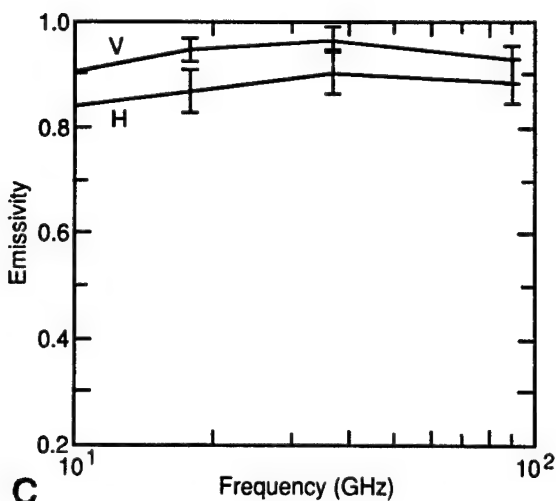
Fig. 4. Pancake ice, March 29, 1987: (a) photograph of typical pancake conditions, (b) vertical thin section, (c) emissivity, and (d) backscatter coefficient. Data indicated by crosses on the backscatter plot are from an area of thicker and rougher pancakes.



a



b



d

Fig. 5. First-year ice, April 6, 1987: (a) photograph of site, (b) properties and structural profile, (c) emissivity, and (d) backscatter coefficient. Curves labeled S, T, and ρ on the properties profile are salinity, temperature, and density.

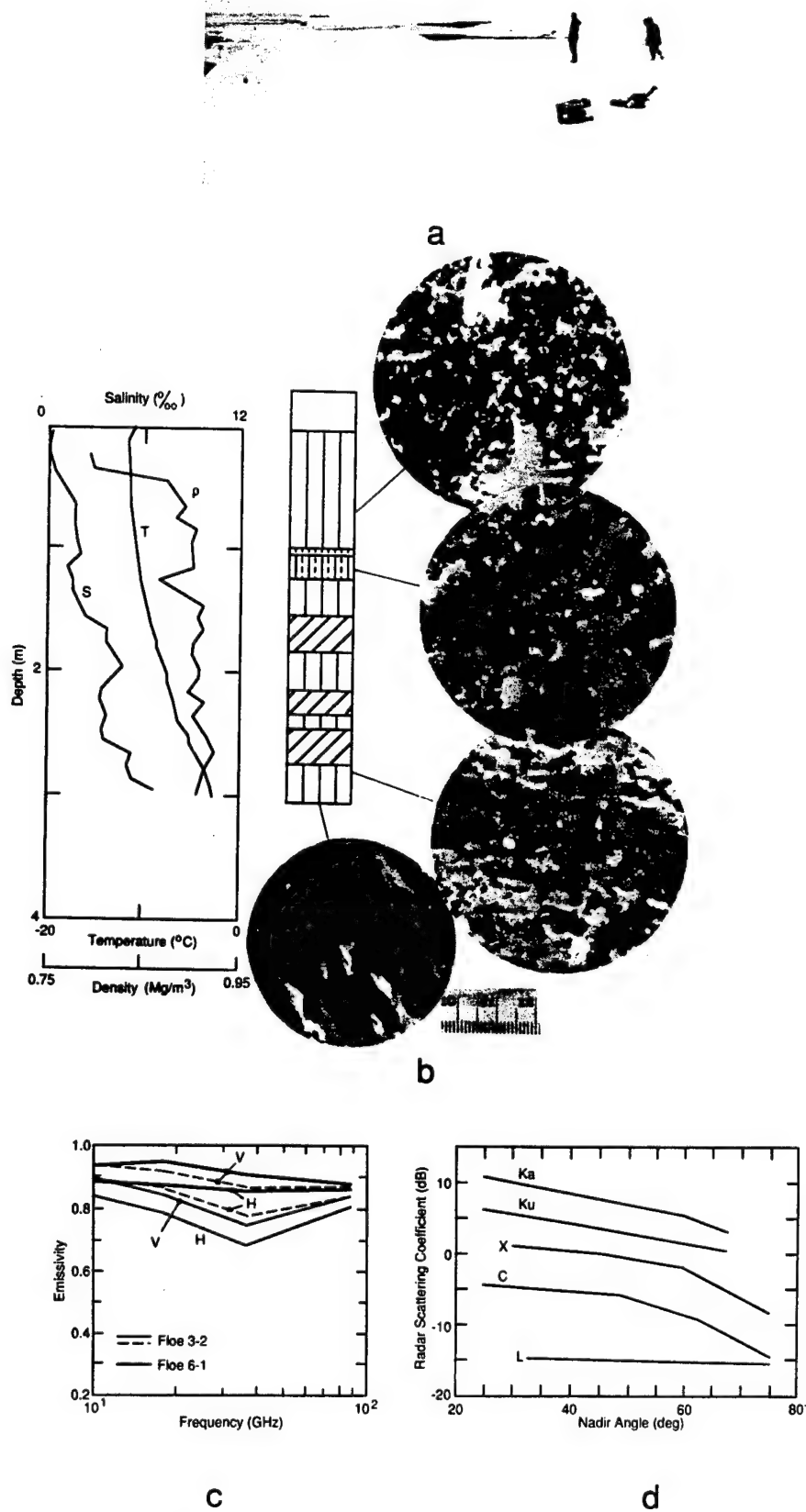


Fig. 6. Multiyear ice, April 3, 1987: (a) photograph of site (b) properties and structural profile, (c) emissivity, and (d) backscatter coefficient. Two emissivity spectra are presented for this site (3-2) in addition to that from another multiyear site (6-1).

be sensitive to snow grain size and density. The dark solid curve, obtained from a hummock on a different floe, shows a weak negative spectral gradient.

Multiyear ice produced the strongest backscatter (Figure 6d) of the ice types considered in this investigation. This is consistent with observations made under cold conditions in other geographic areas [Onstott *et al.*, 1982]. The angular response of the radar scattering coefficients at frequencies from 1.5 to 35 GHz is smooth, the scattering increases uniformly with frequency, and the curves are evenly spaced with respect to each other. In fact, the backscatter intensity (calculated as $10^{[\sigma(\text{dB})/10]}$) is proportional to the square of the frequency. Such a uniform increase suggests that the backscatter originates from the same roughness elements and internal inhomogeneities (e.g., air bubbles).

Flooded Multiyear Ice, April 7, 1987

The photograph in Figure 7a shows the 50×70 m multiyear floe on which flooding of the surface by seawater significantly altered the physical and microwave properties. This floe was covered by snow averaging 0.84 m thick, one of the thickest snow covers observed on the experiment. The snowpack consisted of three distinct layers. The top layer was 0.08 m of new snow composed of 1.0- to 1.5-mm stellar dendrites of density 0.07 Mg m^{-3} . At the bottom was a 0.14-m layer of 0.31 Mg m^{-3} density depth hoar consisting of 3- to 4-mm scrolls. The remainder of the snowpack was 0.40 Mg m^{-3} density, 0.2- to 0.5-mm rounded grains. Ice thickness at the coring location was 4.10 m. Surface topography was consistently low, with generally less than 0.3 m relief. Ice structure, as shown in Figure 7b, was a mixture of columnar, inclined columnar and granular. Granular ice made up 32% of the entire core. The presence of inclined columnar ice in conjunction with granular ice in the structural profile implies that this ice had undergone deformation at some point during evolution [Tucker *et al.*, 1987].

The most unusual feature of this multiyear floe was the very high salinity values in the upper 0.4 m. Salinities of 6 to 10‰ are normally associated with first-year ice. We attribute high salinities in this instance to flooding of the surface by seawater which seeped into and became trapped in the porous upper layers. The flooding likely resulted from depression of the floe by the excessive snow load and associated wave action. This situation was supported by the observation that at the time of coring there was less than 10 mm of freeboard in the core hole. Once again the low density of the ice near the surface, so typical of multiyear floes, was evident here. The depressed freeboard and possibly the intrusion of seawater appear to have warmed the ice. The lowest temperature was slightly below -5°C , whereas for the dry multiyear floe, described earlier, the minimum ice temperature was about -12°C .

Representative emissivity spectra for two flooded multiyear ice sites are shown in Figure 7c. These are essentially indistinguishable from that of first-year ice. This results from the modified high salinity layer at the base of the snow and in the upper 0.4 m of the ice. The two pairs of curves show results from sites with differing snow characteristics; the curves from the April 7 floe (Figure 7c, floe 7-1) described here had thicker snow. The values at 90 GHz are controlled by the characteristics of the overlying snow layer. Consequently, for the thicker snow, they are the same as for the case of dry multiyear ice.

The flooding of snow-covered multiyear ice by seawater has a dramatic effect on the backscattering properties. The flooded multiyear ice has a signature similar to that of typical first-year ice. As can be seen by comparing Figure 7d with Figure 6d, the dry multiyear ice, the σ^0 values are reduced by 4 and 10 dB at 35 and 18 GHz, respectively, for the flooded floe. The difference in reduction suggests that the snow layer contributes significantly to the backscattering at 35 GHz.

DISCUSSION

The greatest difference between first-year and multiyear ice backscatter levels is produced at a frequency of 18 GHz; however, the differences in emissivity are greatest at 37 GHz. Although this difference may be attributed to the possibility that the active and passive sensors were focused on slightly different areas of the same floe, it may also be due to cracks or other surface inhomogeneities in the first-year ice, which produce enhanced backscattering at 37 GHz but which have little effect on the integrated scattering. The smooth increase in scattering with frequency for multiyear ice appears to be consistent with the emissivity spectra.

The radar contrast between multiyear and rough first-year ice is least in the angular region near 25° . For frequencies between 5 and 35 GHz, the contrast ranges between 2.5 and 7.5 dB. At 1.5 GHz, these ice types show similar backscatter levels, with the first-year ice returns higher by 1 to 2 dB. This may have been the result of greater surface roughness on the 0.10- to 0.30-m scale for the first-year ice.

The changes between multiyear and flooded multiyear in the emissivity spectra and the backscattering appear consistent. At K_a band the backscatter at large nadir angles was reduced significantly on the flooded multiyear, while the emissivity increased measurably. At 18 GHz, however, the reduction in backscatter was larger than that at 35 GHz, yet no effect was measurable in $e_\nu(V, 50)$. This seems consistent with the notion that the snow-ice interface was very strongly absorbing and that the snow cover was almost transparent at 18 GHz but much less so at 37 GHz.

Within the present levels of accuracy, the emissivity spectra found in the Greenland Sea MIZ for the younger ice types are at least qualitatively consistent with corresponding observations in other locations at similar times of year. We do not know if this is true for winter multiyear ice, however, because we have no previous data for comparison. Both the present observations and aircraft data [Troy *et al.*, 1981] show that the multiyear spectra are quite variable, even on a single floe (Figure 6c). Although the multiyear ice in the MIZ is structurally similar to multiyear ice in the eastern Arctic, the increase in snow cover modifies the microwave signatures directly because it represents a significant extra scattering layer whose structural properties can evolve rapidly during warming events. A thick snow cover also has an indirect effect in that it provides enough additional mass to make surface flooding relatively common in the presence of ocean swell.

We are interested in assessing which of the physical properties besides snow cover that were measured significantly affect the microwave properties. There are, of course, extremely important properties that were beyond the scope of our measurement program. As was previously inferred, surface roughness is very important. Also, the distribution of

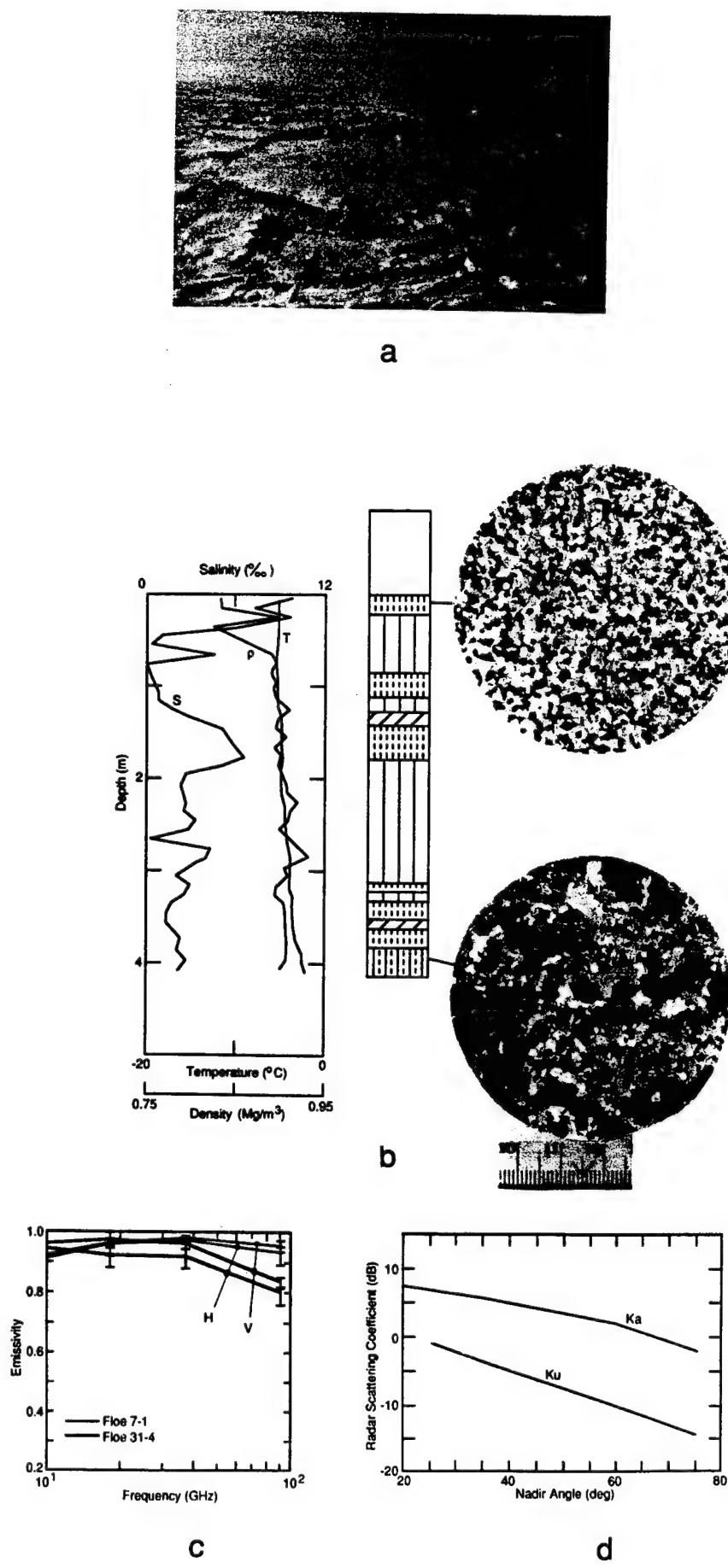


Fig. 7. Flooded multiyear ice, April 7, 1987: (a) photograph of floe, (b) properties and structural profile, (c) emissivity, and (d) backscatter coefficient. Emissivity spectra are shown for this site plus an additional flooded multiyear floe.

TABLE 2. Summary of Basic Ice Properties for Each Ice Type With Passive Microwave Polarization and Gradient Ratios and Active Microwave Gradient Ratios

	Nilas	Pancake	First-Year	Multiyear	Flooded Multiyear
Date	April 8	March 29	April 6	April 3	April 7
Latitude (North)	76°15.0'	78°50.3'	76°44.8'	77°36.9'	76°49.5'
Longitude (West)	6°03.0'	1°39.8'	6°16.8'	4°54.8'	4°44.2'
Physical properties					
Snow depth, m	0.00	0.00	0.10	0.40	0.84
Ice thickness, m	0.03	0.05	0.36	3.01	4.10
Density (top 0.1 m), Mg m ⁻³	0.92	0.92	0.92	0.79	0.84
Bulk salinity, %	15.30	10.50	8.60	2.76	3.21
Percent granular	100	100	0	2	32
Percent columnar	0	0	100	62	62
Percent inclined	0	0	0	30	6
Passive microwave					
PR (18 GHz)	0.220	0.092	0.044	0.041	0.032
GR (37, 18 GHz)	0.074	0.024	0.010	-0.055	0.008
Active microwave					
GR (K_u, K_a)	-0.280	-0.115	-0.753	-0.383	-0.798

liquid and vapor within the ice determines the degree of volume scattering [Tsang and Kong, 1981; Stogryn, 1985, 1987]. Clearly, the dielectric properties of sea ice play a large role in determining the microwave signatures. Since the bulk dielectric constants of sea ice and snow are strongly modulated by the amount and distribution of liquid (both brine and fresh water), the salinity and temperature of the ice are of primary importance. Therefore it is meaningful to compare the microwave signatures with the first-order properties of the ice that were measured.

In Table 2 we present a synopsis of the important physical data that were documented in this investigation. The table also contains ratios which are useful in summarizing important results of the microwave signatures. For the microwave radiometry we show the gradient ratio GR and the polarization ratio PR used in the scanning multichannel microwave radiometer (SMMR) "team algorithm" for the determination of concentration and the identification of first-year/multiyear ice type distribution [Cavalieri *et al.*, 1984b]. These ratios are given by

$$PR(18) = \frac{e_{18}(V, 50) - e_{18}(H, 50)}{e_{18}(V, 50) + e_{18}(H, 50)} \quad (4)$$

$$GR(37, 18) = \frac{e_{37}(V, 50) - e_{18}(V, 50)}{e_{37}(V, 50) + e_{18}(V, 50)} \quad (5)$$

Similarly, a gradient ratio has been calculated for the radar backscatter for K_u and K_a bands (18 and 35 GHz) at a nadir angle of 40° from the following definition:

$$GR (K_u, K_a) = \frac{I(\sigma^0 K_u) - I(\sigma^0 K_a)}{I(\sigma^0 K_u) + I(\sigma^0 K_a)} \quad (6)$$

where $I(\sigma^0)$ are the backscattered intensities determined from the transformation $I = 10^{(\sigma \text{dB}/10)}$. The order of the frequencies has also been reversed from those in the passive gradient ratio (equation (5)). In this manner, the radar gradient ratio varies in the same sense as the passive; that is, greater scattering at higher frequency gives a more negative value of GR. While this parameter may not be useful for the first generation of single-frequency radar satellites, it is introduced here because it very likely provides a measure of

the size distribution of scattering inhomogeneities either in the ice or on the surface. Thus we feel that GR(K_u, K_a) should be useful for improving the capability of distinguishing ice types when appropriate instrumentation becomes available.

In Table 2, PR(18) shows a steady decrease with ice age from initial formation through thick first-year ice, while the differences between first-year, dry multiyear, and flooded multiyear are small. GR(37, 18) decreases consistently with the age of the ice with exception of the flooded multiyear ice, whose value is very nearly that of first-year ice.

The large negative values of the radar gradient ratio, GR(K_u, K_a), are anticipated because radar scattering cross sections typically increase with increasing frequency; both theory and observations support this trend. The differences between nilas and pancake cases are nearly indistinguishable. The raised edges of the pancakes and overthrust edges of nilas were large relative to the K_u and K_a band wavelengths (about 17 and 8.7 mm, respectively), and they appear to have produced similar backscatter intensities. With its very large negative value, first-year ice is quite distinct from dry multiyear or the new ice types. It is important to note that the gradient ratios for first-year and flooded multiyear are similar, which implies that even this active microwave ratio is masked by flooding.

Table 2 also indicates that the passive microwave gradient ratios can be related to the age of the ice. The passive ratios also appear to correlate well with the salinity, generally decreasing when the salinity decreases, thus reinforcing the relationship to the age of the ice. While a relationship between ice age or salinity and the radar gradient ratio is not apparent, there are distinct differences between thick first-year, multiyear, and young ice types. In the case of the flooded multiyear, the increased brine volume in upper layers resets the salinity to be practically the same as that of first-year ice, and the observed microwave signatures are consistent with this "effective" age.

Contrasts between emissivity and backscatter cross sections at Ka band are shown in Figure 8. Similar behavior was observed at 18 GHz. The points are ordered by increasing σ^0 and range from open water through dry multiyear ice. The points for open water were taken from Grenfell and Comiso

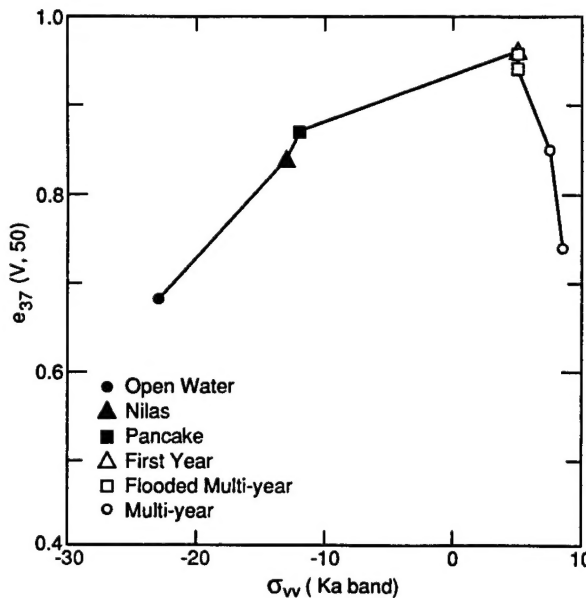


Fig. 8. Emissivity at 37 GHz versus radar backscatter at K_a band for open water, nilas, pancake, first-year, two flooded multiyear, and two multiyear sites.

[1986] and from *Onstott and Shuchman* [1988]. There appear to be two correlation regimes. The first covers the thin ice types through first-year ice where both e , and σ^0 increase together, and the second includes the first-year and multiyear cases for which e , decreases with further increase in σ^0 . In the first regime we believe that the emissivity is increasing because of decreasing reflectivity as the ice thickens while scattering increases owing to the development of surface roughness. In the second regime it is our opinion that scattering becomes dominant and emissivity decreases as scattering increases. First-year and flooded multiyear ice are located at the apex where scattering begins to contribute significantly to the emissivity.

Although using the combination of emissivity and back-

scatter at a single frequency (Figure 8) to distinguish between ice types is superior to using either separately, results are less than satisfactory. The ice type separation shown in Figure 8 is apparently similar to radiometric cluster plots [e.g., *Cavalieri et al.*, 1984b]. More information appears to be provided if we include the polarization and gradient ratio values from Table 2. Two likely representations are shown in Figures 9 and 10, where we have plotted the passive gradient and polarization ratios, respectively, against the active gradient ratio.

In Figure 9, the active gradient ratio separates open water from nilas and pancakes from first-year ice, showing that these pairs which are unresolved by $GR(37, 18)$, have very different scattering characteristics. The passive gradient

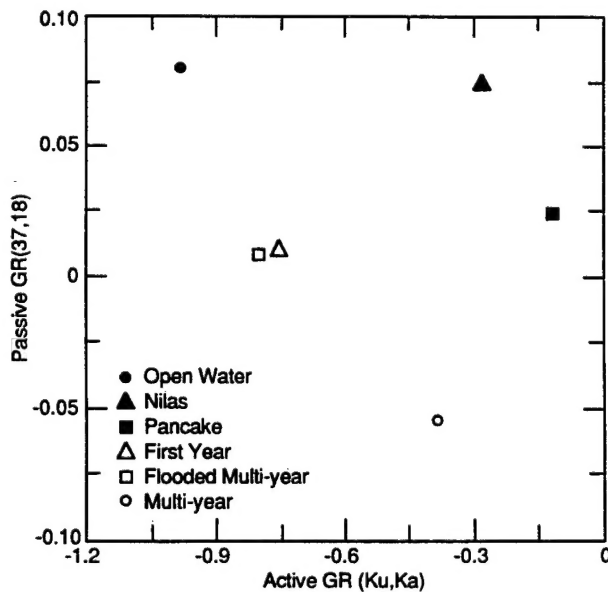


Fig. 9. Passive gradient ratio, $GR(37, 18)$, versus active gradient ratio, $GR(K_u, K_a)$, for the different ice types.

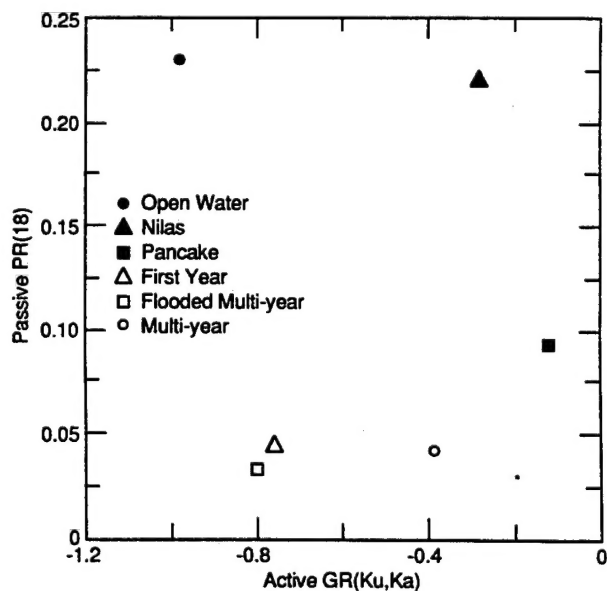


Fig. 10. Passive polarization ratio, $PR(18)$, versus active gradient ratio, $GR(K_u, K_a)$, for the different ice types.

ratio clearly separates the dry multiyear ice from the other categories and the pancakes from the nilas. Neither measure is adequate for distinguishing the first-year from the flooded multiyear ice, however. The polarization ratio, shown in Figure 10, provides three resolved groups: (1) open water and nilas, (2) pancakes, and (3) the first-year and multiyear ice types. Combined with $GR(K_u, K_a)$, all ice types except the first-year and flooded multiyear are separable.

It appears that similar information can be obtained from either of the two representations (Figures 9 and 10). In both cases the ability to distinguish between ice types is improved over the combination of emissivity and backscatter at a single frequency (Figure 8). The information contained in Figures 9 and 10 appears to have at least one additional degree of freedom.

CONCLUSIONS

The major thrust of this paper has been to examine microwave properties for a variety of ice types whose signatures were recorded in conjunction with a first-order characterization of ice properties. The ultimate goal is, of course, to use airborne or satellite-derived remote sensing data to differentiate between distinct ice types. Microwave signatures are affected by the properties of the ice including surface roughness, brine and liquid content, void distribution, as well as properties of the snow cover. Although the properties within single ice types can have large spatial and temporal variability, we found that certain ice types have characteristic microwave signatures.

For young and first-year ice types, emissivities are consistent with other observations that have been made. The emissivity spectra for pancake ice is slightly higher and flatter than that for nilas. The radar backscattering cross sections for pancake and nilas are very similar, however. The distinction between thicker first-year ice and the thinner ice types is quite clear for both the passive and active microwave signatures. The emissivity of thicker first-year ice at all frequencies is close to unity, while the backscatter coefficients for this ice type are larger at K_u and K_a bands than for new ice.

The emissivities over snow covered multiyear ice were found to have a negative spectral gradient, consistent with results from aircraft measurements in the central Arctic although with somewhat less gradient. Radar backscatter was the strongest of any ice type examined, and the scattering increased uniformly with frequency. For flooded multiyear ice, however, both emissivities and backscatter were nearly indistinguishable from first-year ice.

Snow covers were thicker in the eastern Arctic than have been found in other parts of the Arctic. A thicker snow cover will certainly affect the microwave signatures directly, but more importantly, they are sometimes thick enough to depress the floe and cause flooding. If flooded multiyear ice makes up a significant percentage of the multiyear ice fraction within the marginal ice zone, this may have a profound impact on the concentration of first-year/multiyear ice percentages derived from airborne and satellite-borne radars and radiometers. This may explain a significant part of the apparent discrepancy between SMMR and surface and submarine observations [Cavalieri *et al.*, 1984b] of multiyear/first-year ice percentages.

Ice type separation is clearly improved using a combina-

tion of active and passive microwave signatures. The separation becomes even more distinct if gradient and polarization ratios for emissivity are contrasted to a gradient ratio calculated for the active microwave backscatter. Using this method, all ice types examined in this study were separable except first-year and flooded multiyear.

Although we have presented only a few cases, they are generally representative of the ice types found in the Greenland Sea marginal ice zone. Further study will be necessary to determine uncertainties in the signatures and to fully understand the relationships between the microwave signatures and more detailed ice properties.

Acknowledgments. This work was made possible by funding from the Arctic Program, Office of Naval Research, and from the Oceanic Processes Branch, National Aeronautics and Space Administration. We gratefully acknowledge this support.

REFERENCES

- Cavalieri, D. J., P. Gloersen, T. T. Wilheit, and C. Calhoun, Passive microwave characteristics of the Bering Sea ice cover during MIZEX-West, *IEEE Trans. Geosci. Remote Sens.*, **GE-24**, 3-37, 1984a.
- Cavalieri, D. J., P. Gloersen, and W. J. Campbell, Determination of sea ice parameters with Nimbus 7 SMMR, *J. Geophys. Res.*, **89**, 5355-5369, 1984b.
- Cox, G. F. N., and W. F. Weeks, Equations for determining the gas and brine volumes in sea ice samples, *J. Glaciol.*, **29**, 306-316, 1983.
- Eicken, H., and M. A. Lange, Development and properties of sea ice in the coastal regime of the southeastern Weddell Sea, *J. Geophys. Res.*, **94**, 8193-8206, 1989.
- Grenfell, T. C., Surface based passive microwave observations of sea ice in the Bering and Greenland Seas, *IEEE Trans. Geosci. Remote Sens.*, **GE-24**, 378-382, 1986.
- Grenfell, T. C., and J. C. Comiso, Multifrequency passive microwave observations of first-year sea ice grown in a tank, *IEEE Trans. Geosci. Remote Sens.*, **GE-24**, 826-831, 1986.
- Kim, Y. S., R. K. Moore, R. G. Onstott, and S. Gogineni, Towards identification of optimum radar parameters for sea ice monitoring, *J. Glaciol.*, **31**, 214-219, 1985.
- Onstott, R. G., and R. A. Shuchman, Radar backscatter of sea ice during winter, in *Proceedings of International Geoscience and Remote Sensing Symposium (IGARSS '88)*, vol. II, pp. 1115-1118, European Space Agency Publications Division, Noordwijk, Netherlands, 1988.
- Onstott, R. G., R. K. Moore, and W. F. Weeks, Surface based scatterometer results of Arctic sea ice, *IEEE Trans. Geosci. Remote Sens.*, **GE-17**, 74-85, 1979.
- Onstott, R. G., R. K. Moore, S. Gogineni, and C. V. Delker, Four years of low altitude sea ice broadband backscatter measurements, *IEEE J. Oceanic Eng.*, **OE-7(1)**, 44-50, 1982.
- Shuchman, R. A., C. C. Wackerman, A. L. Maffett, R. G. Onstott, and L. L. Sutherland, The discrimination of sea ice types using SAR backscatter statistics, paper presented at International Geoscience and Remote Sensing Symposium (IGARSS '89), IEEE, Vancouver, Canada, 1989.
- Stogryn, A., Strong fluctuation theory for moist granular media, *IEEE Trans. Geosci. Remote Sens.*, **GE-23**, 78-83, 1985.
- Stogryn, A., An analysis of the tensor dielectric constant of sea ice at microwave frequencies, *IEEE Trans. Geosci. Remote Sens.*, **GE-25**, 147-158, 1987.
- Troy, B. E., J. Q. Hollinger, R. M. Lerner, and M. M. Wisler, Measurements of microwave properties of sea ice at 90 GHz and lower frequencies, *J. Geophys. Res.*, **86**, 4283-4289, 1981.
- Tsang, L., and J. A. Kong, Application of strong fluctuation random medium theory to scattering from vegetation-like half space, *IEEE Trans. Geosci. Remote Sens.*, **GE-19**, 62-69, 1981.
- Tucker, W. B., III, A. J. Gow, and W. F. Weeks, Physical properties of summer sea ice in the Fram Strait, *J. Geophys. Res.*, **92**, 6787-6803, 1987.
- Ulaby, F. T., R. K. Moore, and A. K. Fong, *Microwave Remote*

Sensing: Active and Passive, vol. 2, *Radar Remote Sensing and Surface Scattering and Emission Theory*, pp. 457–1064, Addison Wesley, Reading, Mass., 1982.

Wackerman, C. C., R. R. Jentz, and R. A. Shuchman, Sea ice type classification of SAR imagery, in *Proceedings of International Geoscience and Remote Sensing Symposium (IGARSS '88)*, vol. I, pp. 425–428, European Space Agency Publications Division, Noordwijk, Netherlands, 1988.

Wadhams, P., S. Martin, O. M. Johannessen, W. D. Hibler III, and W. J. Campbell, MIZEX: A program for mesoscale air-ice-ocean interaction experiments, in *Arctic Marginal Ice Zones, I, Research Strategy*, *CRREL Spec. Rep. 81-19*, pp. 1–20, U.S. Army Cold Reg. Res. and Eng. Lab., Hanover, N. H., 1981.

A. J. Gow, D. K. Perovich, and W. B. Tucker III, U.S. Army Cold Regions Research and Engineering Laboratory, Lyme Road, Hanover, NH 03755.

T. C. Grenfell, Department of Atmospheric Sciences, AK-40, University of Washington, Seattle, WA 98195.

R. G. Onstott, R. A. Shuchman, and L. L. Sutherland, Environmental Research Institute of Michigan, Ann Arbor, MI 48107.

(Received March 26, 1990;
revised September 14, 1990;
accepted July 26, 1990.)